Safe Flight Envelope Prediction and Experimental Validation of Multirotor UAV

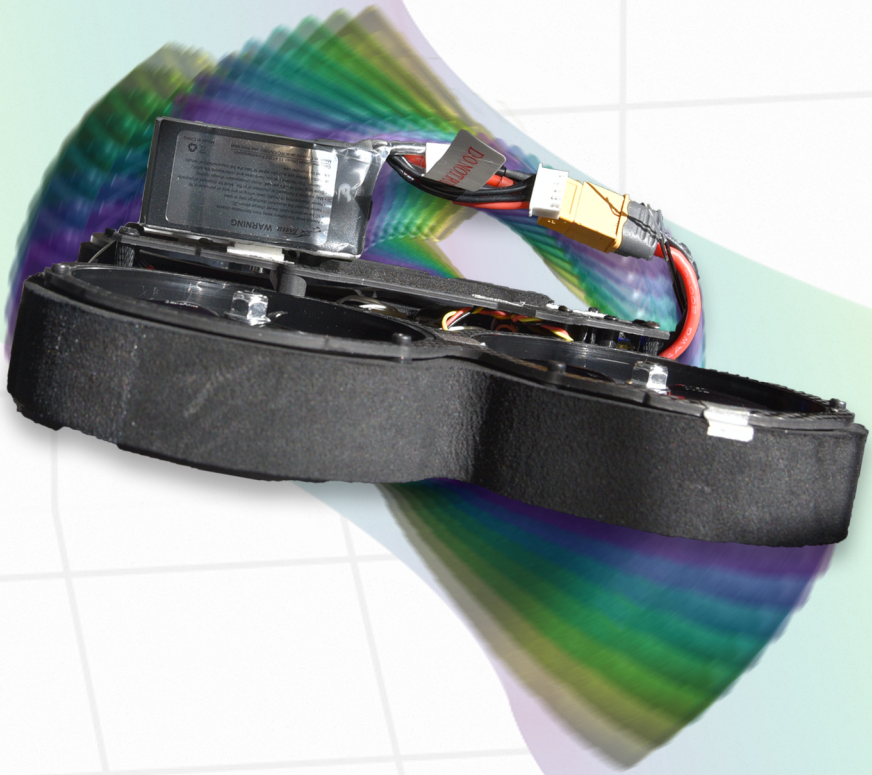

An Analysis on the Effects of Longitudinal Center of Gravity Position and Actuator Dynamics on Quadcopter Flight Envelopes

MSc. Thesis
Lauren Cécile Kaffa

TU Delft

Safe Flight Envelope Prediction and Experimental Validation of Multirotor UAV

An Analysis on the Effects of Longitudinal Center of Gravity Position and Actuator Dynamics on Quadcopter Flight Envelopes

by

Lauren Cécile Kaffa

to obtain the degree of Master of Science
at Delft University of Technology.

Defence Date (Public): Friday 7th of July 2023, 13:00

Student Number:	4546792	
Supervisor:	Dr. ir. Coen de Visser	
Project Duration:	19 April 2022 - 7 July 2023	
Institution:	Delft University of Technology	
Faculty:	Faculty of Aerospace Engineering	
Track and Profile:	Control & Operations, Control & Simulation	
Thesis Committee:	Dr. ir. C.C. de Visser	TU Delft, Control & Simulation
	Dr. M.D. Pavel	TU Delft, Control & Simulation
	Dr. ir. E. Mooij	TU Delft, Space Engineering
	Ir. P. Solanki	TU Delft, Control & Simulation

TU Delft

Preface

This thesis report contains all the results of the research work to obtain the degree of Master of Science at the faculty of Aerospace Engineering within the Control & Simulation section. Readers who are especially interested in an overall document containing all relevant research information can find this in the thesis paper in Part I of this document.

First and foremost, I would like to thank my supervisor, Coen de Visser, for helping, supporting and guiding me throughout the thesis process which helped me to deliver valuable research work. Furthermore, I would like to thank Jasper van Beers, Prashant Solanki and Till Blaha for all the help, discussions and feedback that they have offered me. Without them I would not have achieved as much as I have accomplished in this work. Last but not least, I would like to thank Andries Muis and Till Blaha for all the support they have given me. I could always count on them which helped me through the tough times.

With the completion of this work my time as a student at the TU Delft comes to an end. I can happily and with satisfaction reflect back on the years in which I have learned a lot about engineering and grown as a person. It was an honor to spend my last years as a student at the Control & Simulation section, which felt home to me. I would like to thank all my friends, fellow SIM0.08 students and C&S staff members for the countless hours in the coffee corner, accompanied with lots of humor. Finally, I would like to thank my parents for all the mental and financial support, without them I would not have made it so far.

Lauren Cécile Kaffa
Delft, June 2023

Abstract

Loss of control (LOC) is the primary cause of failure of Unmanned Aerial Vehicles (UAV). The safety of these systems can be largely improved by facilitating techniques to prevent LOC to occur, such as Flight Envelope Protection, enabling controllers to keep the system within the Safe Flight Envelope (SFE).

The aim of this work is to examine the behaviour of the global SFE of a quadcopter subjected to varying system dynamics, including the effects of longitudinal center of gravity displacements and actuator dynamics.

The analysis has been split into the forward reachable set (FRS) and the backward reachable set (BRS). The FRS is estimated through an optimized Monte-Carlo (MC) simulation approach. Verification shows that the system specific optimized MC simulation approximates the true reachable sets with high accuracy, while exceeding performance on both accuracy as well as computation time compared to the Level-Set method. The BRS is derived from the FRS directly using a minimum-time optimal control (MTOC) routine including actuator dynamics. This approach guarantees that the BRS is contained within the FRS and bypasses the need to simulate the dynamics backwards in time. Both methods exploit the control *affine* system structure from which it can be derived that the MTOC for both the FRS and BRS is *bang-bang* control, which drastically reduces the sampling space and optimal control complexity.

The results show that both the location of the centroid of the FRS and the return time distribution of the BRS are a function of the offset position. A large decrease in the FRS area is seen for larger center of gravity offset positions. Furthermore, the actuator dynamics reduce the FRS by 85%, irrespective of center of gravity location, while the BRS without actuator modelling shows impractical return times as a result of unfeasible instantaneous rotor speed changes. A novel experimental validation procedure on the quadcopter FRS has been performed. The results show a general overestimation with respect to the flight data, which is expected when comparing an open-loop simulation with closed-loop performed flight maneuvers.

The results from this research provide valuable information on quadcopter reachability analysis. This information can be further used in the application of (probabilistic) FEP for LOC prevention on quadcopters, subjected to varying system dynamics. Additionally, the results show that it might be feasible to interpolate the reachable sets subjected to varying center of gravity locations, actuator dynamics and varying time-windows. This supports the possibility of a data-base driven approach for (real-time) envelope prediction and protection. The MC simulation and minimum-time optimal control routine, as developed in this work, have shown to be promising methods to be used in future work in the framework of reachability analysis of quadcopter drones.

Contents

Nomenclature

ϵ	Model residual
$\hat{\theta}$	Parameter vector
κ_0	Rotor property coefficient
μ	Mean
ω_i	Rotational speed of motor i
σ	Standard deviation
τ	Time constant
τ_0	Rotor torque coefficient
	Mass moment of inertia matrix around the body i-axis
I	Mass moment of inertia matrix
θ	Pitch angle (about the body Y-axis)
$\vec{F}$	Resultant force vector
$\vec{G}$	Gravity vector
$\vec{M}$	Resultant moment vector
$\vec{u}$	Input vector
$\vec{x_0}$	Initial state vector
$\vec{x}$	State vector
$\vec{y}$	Measurement vector
A	Regression matrix
b	Distance to center of gravity along body Y-axis
d	Polynomial degree
dt	Time step
f	System dynamics
l	Distance to center of gravity along body X-axis
m	Mass
M_i	$0i^{i<0\text{ th}}$ model parameter
N	Number of realizations / Number of data points
n	Number of independent states
N_{switch}	Number of control input sampling occasions
N_{traj}	Number of trajectories
P	Regressor function
p	Angular velocity about the body X-axis

p_c	Tuning parameter
q	Angular velocity about the body Y-axis
r	Angular velocity about the body Z-axis
R^2	Coefficient of determination
T	Resultant thrust
T	Time-window
t	Time
u	Airspeed component along the body X-axis / Input
u_0	Initial input
U_q	Control pitching moment
v	Airspeed component along the body Y-axis
w	Airspeed component along the body Z-axis
BRS	Backward Reachable Set
CFD	Computational Fluid Dynamics
CNN	Convolutional Neural Network
FCL	Flight Control Law
FE	Flight Envelope
FEP	Flight Envelope Protection
FRS	Forward Reachable Set
HJ	Hamilton-Jacobi
HJ PDE	Hamilton-Jacobi Partial Differential Equation
HJB PDE	Hamilton-Jabobi-Bellman Partial Differential Equation
HJI PDE	Hamilton-Jacobi-Isaac Partial Differential Equation
IMU	Inertial Measurement Unit
LOC	Loss of Control
LOC-I	Loss of Control In Flight
MC	Monte-Carlo
MPC	Model-Based Predictive Control
NRMSE	Normalized Root Mean Square Error
ODE	Ordinary Differantial Equation
PCA	Principal Component Analysis
PID	Proportional Integral Derivative
ROA	Region of Attraction
SFE	Safe Flight Envelope
SNR	Signal-to-Noise Ratio
UAV	Unmanned Aerial Vehicle
ZKF	Zonotopic Kalman Filter

1 Introduction

The use and applications of Unmanned Areal Vehicles (UAV) are expected to grow rapidly in the near future [1]. Currently Loss of control (LOC) is the main cause of failures for UAVs [2]. In order to improve safety of these systems, development of LOC prevention techniques are of utmost importance. A way to prevent LOC is through the use of flight envelope protection (FEP) which enables controllers to keep the system within the Safe Flight Envelope (SFE). The SFE indicates the state-space in which the vehicle can be safely operated, operating outside the SFE is linked to LOC [3][4]. The SFE can be defined as *the set of states that can be reached, within a certain time-window, for which a trajectory exist to return to a safe flight condition within a predefined time-window* [5][6][7][8]. This research focuses on predicting the SFE of multirotor UAVs to allow for FEP implementation and development for LOC prevention and thereby facilitating in improving the safety of these systems. The prediction is focused on the global flight envelope, rather than local boundary prediction, as it has the advantage to apply global FEP techniques to balance safety and performance for the specific application.

The aim of this work is to examine the behaviour of the global SFE of a quadcopter subjected to varying system dynamics, including the effects of longitudinal center of gravity displacements and actuator dynamics. The analysis has been split into the forward reachable set (FRS), which contains all the states the system can reach from a set of initial states within a given time-window, and the backward reachable set (BRS), which contains the states from which the system can return to the initial set of states within an arbitrary time-window. The multirotor UAV considered in this study is a quadcopter model because these models are widely used in various applications, easily accessible and suitable for conducting (indoor) flight experiments. The dynamics of the quadcopter for various center of gravity positions are captured via a data-driven approach using model identification on flight data. The prediction of the forward reachable sets are obtained using a Monte-Carlo (MC) approach rather than the prevailing Level-Set method. The MC simulation approach is a promising method for quadcopter flight envelope prediction as it can be applied on higher dimensional nonlinear systems [8], it has a lower computational load with increased number of dimensions compared to the Level-Set method [9], and is recently successfully applied on quadcopter models [10]. The BRS is derived from the FRS directly using a minimum-time optimal control (MTOC) routine including actuator dynamics. This approach guarantees that the BRS is contained within the FRS and bypasses the need to simulate the dynamics backwards in time. Both methods exploit the control *affine* system structure from which it can be derived that the MTOC for both the FRS and BRS is *bang-bang* control, which drastically reduces the sampling space and optimal control complexity. The methods are verified and an experimental validation procedure is performed to validate the FRS estimations.

The thesis report is structured as follows: in chapter 2 an overview of the thesis project is covered including the research motivation, objective, research contributions and the scope and limitations of the work. In Part I the thesis paper is presented which contains all relevant information of the research. The findings from the literature review study, carried out before the thesis project, can be found in Part II. In Part III the conclusions and recommendations of the research are summarized in chapter 8.

2

Thesis Project Overview

This research focuses on improving and extending knowledge on (the prediction of) the Safe Flight Envelope (SFE) of a quadcopter model motivated by the promising findings in recent (fixed-wing) aircraft literature in the framework of SFE prediction and protection (FEP) for loss of control (LOC) prevention. Hereby contributing to the improvement of the safety of aircraft. Furthermore, research on application of this reachability framework on quadcopters is limited [11] and hence this research directly adds knowledge to the body of literature. The flight envelopes considered in this work include both the forward reachable set (FRS) and the backward reachable set (BRS). These sets can be combined to define the SFE which can be used in SFE protection techniques for LOC prevention. In this chapter the research motivation and a summary of the literature review can be found in section 2.1. The research objective and research questions are discussed in section 2.2. The contributions of this research are summarized in section 2.3 followed by the scope and limitations in section 2.4.

2.1. Research Motivation and Summary of Gaps in Literature

From the literature research it has been identified that a major factor playing a role in fatal accidents of UAVs involves LOC [2]. Since the use of (commerical) UAVs has been rising and is expected to grow even more in the future [1], it is of utmost importance to prevent LOC conditions to improve UAV safety [12]. Operating outside the Safe Flight Envelope (SFE) of an aircraft is linked to loss of control (LOC) [3][4], which is the main cause of failures for UAVs [2][12]. The SFE is defined as all the possible states which an aircraft can both reach from- and be controlled back to a set of initial flight conditions within a given time-window [8]. A promising technique that prevents the system to violate the SFE boundaries is called Flight Envelope Protection (FEP). For this research it is decided to focus on global flight envelope prediction because having prior knowledge on the global envelope has the advantage to develop FEP systems to balance safety and performance for the specific application.

From the literature research it can be concluded that treating the boundaries of the SFE as probabilistic is preferred. The reason is because classical deterministic flight envelopes tend to overestimate envelopes leading to dangerously optimistic FEP systems [13][14]. Furthermore, in Yin et al. [8] it was shown that the envelopes change shape and size when changing the (fixed-wing) aircraft system dynamics. Therefore, when including system model uncertainties, it is more suitable to model the envelope boundaries as probabilistic. Moreover, an advantage of treating the boundaries as probabilistic allows for earlier responses and gentler protective FEP measures as shown in Yin et al. [8].

The behaviour of the SFE boundaries of a multirotor UAV under varying configurations is yet to be explored. Therefore, a sensitivity analysis generates knowledge on the behaviour of the boundaries under varying multirotor UAV configurations which directly adds information to the body of literature of multirotor UAVs. Varying multirotor UAV configurations can be considered as a form of model uncertainty, thus the analysis of the behaviour of the boundaries will generate knowledge on boundary prediction in a probabilistic way. Consequently, this could enhance the integration of SFE protection systems on multirotor UAVs to balance safety and performance with novel probabilistic protection strategies [8].

The current mainstream method for flight envelope prediction found in literature is through (a model-based) reachability analysis, often involved with finding a solution to the Hamilton-Jacobi partial differential equation (HJ PDE). The main disadvantage of this method is that the numerical methods for solving the PDE, such as the widely used Level-Set method, suffer from the curse of dimensionality

as it scales exponentially with the number of states and becomes impractical to use for more than four states [5][11][15][16]. Furthermore, the Level-Set method tends to produce underestimated sets which are not desirable as it prevents to exploit the ability of highly maneuverable flight which multirotor UAV systems have to offer [13][14]. Therefore, application of this method is not preferred for high dimensional nonlinear multirotor UAV applications. To conquer these limitations, the Monte-Carlo (MC) simulation seems to be the most promising method to be used as it can be applied on higher dimensional nonlinear systems and is recently successfully applied on quadcopter models [8][11]. In Sun et al. [11] it is shown that this method is able to solve a 6 dimensional reachability problem for a quadcopter model in a matter of seconds and is more computational efficient than the Level-Set method [8]. Although in Terrell et al. [9] it was shown that the MC simulation also suffers from the curse of dimensionality, however less than the Level-Set method. It should be noted that extreme control effectiveness methods, such as bang-bang control [11], should be employed to mainly reach the boundary states, prevent conservative results and reduce the amount of simulations required. Also it should be noted that the probability distribution of the input determines the probability distribution of the corresponding output [8]. Furthermore, the time-window used for reachability analysis has a large influence on the obtained results and is system and application specific.

It should be kept in mind that the results from this model based approach heavily relies on the model quality and model validity used in the reachability analysis. System identification is a technique often used for model identification of nonlinear systems [17].

Knowledge on the behaviour of SFE boundaries under varying system dynamics allows for further investigation into methods to interpolate envelopes for different configurations of the system. Interpolation of envelopes bypasses the need for recalculation of computational expensive envelope prediction methods and hence could allow for real-time application. This enables further exploration in the feasibility of the promising database approach for real-time flight envelope prediction for multirotor UAVs [5]. In Zhang [5] flight data are used to classify a certain aircraft damage case, and consequently use onboard stored pre-calculated flight envelopes which are interpolated online based on the flight condition and damage case scenario. This paper showed promising results on flight envelope interpolation approximating the result of the Level-Set method and encourages to investigate and apply this database approach to (damaged) drones [5].

2.2. Research Objective

The thesis project focuses on enhancing the knowledge on the behaviour of the Safe Flight Envelope (SFE) boundaries of a multirotor UAV under varying system dynamics. The results directly add knowledge to the body of literature of multirotor UAV on probabilistic boundary prediction with regards to varying system dynamics. This could be used to improve (probabilistic) SFE protection systems for balancing safety and performance. Furthermore, the obtained knowledge from the research could be used to investigate interpolation techniques to support a database-driven technique to enable real-time SFE prediction for quadcopters [5].

The objective for the research is defined as follows:

Research Objective

The objective of this thesis work is to assess the behaviour of the boundaries of the Safe Flight Envelope (SFE) of a quadcopter subjected to varying system dynamics.

With the research objective defined, the following research question is formulated:

Research Question

How do the boundaries of the Safe Flight Envelope (SFE) of a quadcopter change subjected to varying system dynamics?

Important to emphasize is the definition of the SFE used in this research, which is as follows:

The Safe Flight Envelope (SFE) Definition

The Safe Flight Envelope (SFE) can be defined as the set of states that can be reached, within a certain time-window, for which a trajectory exist to return to a safe flight condition within a predefined time-window [5][6][7][8].

In this research the SFE is divided into two sets: 1) the forward reachable set (FRS), which defines all the states that the system can reach within a time-window, and, 2) the backward reachable set (BRS), which defines all states from which the system can return to the (initial) safe (set of) state(s) within an arbitrary time-window. In this work the BRS is found directly from the FRS which guarantees that the BRS is contained within the FRS.

The varying system dynamics in this research include the effects of **varying the center of gravity position** and the effects of **actuator dynamics** on the reachable set. Additionally, the effect of varying the **time-window** on the reachable sets are analyzed as well to further explore the possibility of interpolating envelopes for varying time-windows.

The main research question is further divided into multiple subquestions. The subquestions are formulated as follows:

1. How does the FRS vary subjected to:
   (a) Displacing the center of gravity position?
   (b) Actuator dynamics?
   (c) Varying the time-window of the reachable set analysis?
2. How does the BRS vary subjected to:
   (a) Displacing the center of gravity position?
   (b) Actuator dynamics?
   (c) Varying the time-window of the reachable set analysis?
3. To what extend is interpolation of the reachable sets feasible to support a data-base driven approach for (real-time) envelope prediction and protection?

This research uses a *Monte-Carlo approach* for forward reachable set estimation and a *minimum-time optimal control routine* is developed for backward reachable set analysis, both methods are subjected to an elaborate verification analysis. Furthermore, a validation procedure is performed to *experimentally validate* the results of the forward reachable set estimates. Since a model-based reachability approach is taken, the models of the quadcopter dynamics are determined using a data-driven approach. System identification is applied to determine the parameters of the (polynomial) model structure using ordinary least-squares regression (OLS). An overview of the main project phases and their relative connections are shown in Figure 2.1.

2.3. Research Contributions

This research contributes to the literature as follows:

1. This research adds knowledge on the behaviour of the SFE of a quadcopter subjected to varying center of gravity position. It produces results on the quadcopter performance in terms of both the forward reachable set (FRS) and the backward reachable set (BRS). The results allow further research into the feasibility of interpolating envelopes, for example for application in a database-driven approach for (real-time) FEP [5].
2. The results on the reachable sets as a function of center of gravity position can be used to quantify as model uncertainty. This uncertainty can be used to model the SFE in a probabilistic way, for example for applications in which the center of gravity of the quadcopter could vary.
3. This research includes the actuator dynamics in the reachability analysis and shows its relevance, whereas the actuator dynamics are often neglected in quadcopter literature.
4. The results on the reachable sets obtained from the Monte-Carlo (MC) approach can be used for further research into probabilistic SFE analysis and protection in the application of quadcopters [8].

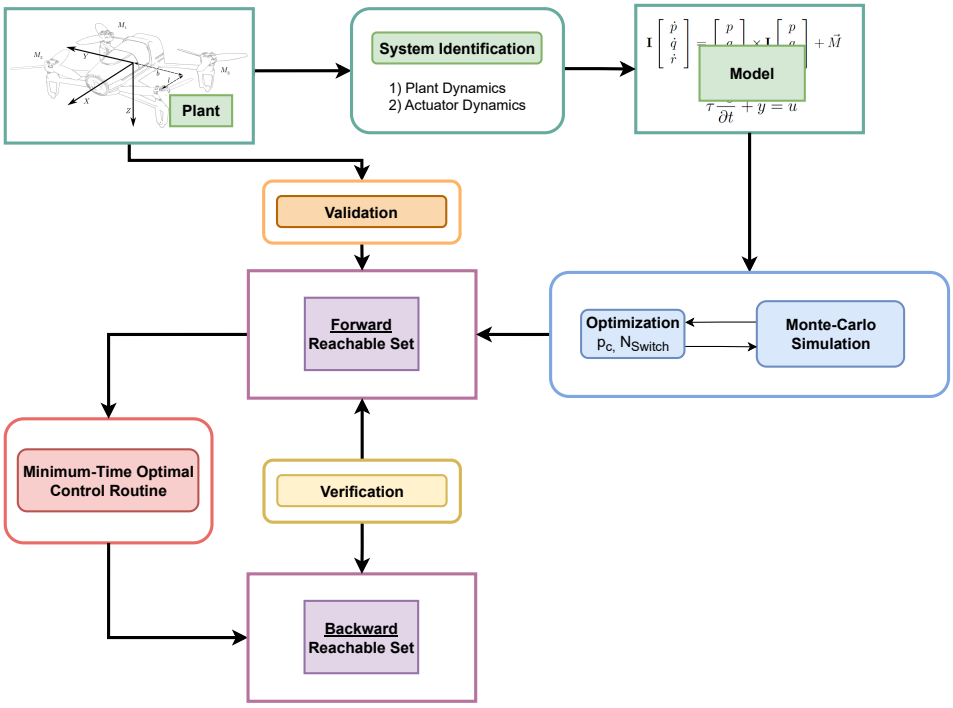

Figure 2.1: Overview of the research project subdivided in various project modules with their relative connections indicated by arrows.

5. An optimization routine is applied on the MC simulation parameters of which the results and insights can be used in further research on quadcopter reachable set estimation using a MC approach.
6. A verification on the performance of the MC simulation on reachable set estimation produces knowledge and insights for future use of the MC approach for reachability analysis. Furthermore, the MC simulation approach is briefly benchmarked with the *Level-set Toolbox* [18].
7. A novel backward reachable set estimation approach is explored. The BRS is derived from the FRS directly using a minimum-time optimal control routine. This approach guarantees that the BRS is contained within the FRS and bypasses the need to simulate the dynamics backwards in time.
8. A minimum-time optimal control routine is developed to control the attitude and angular velocity of the quadcopter *including actuator dynamics* to any desired orientation in minimum-time. The resulting *bang-bang* controller shows a sliding-mode control behaviour. This routine can be (re)used and further developed in other research into (optimal) control applications of quadcopters.
9. An experimental validation on the reachable set of a quadcopter is conducted to validate the FRS through flight experiments. The analysis produces validation results and valuable experience for future implementations.

2.4. Research Scope & Limitations

This research is limited to or restricted by the following elements:

- The quadcopter dynamics and reachable sets are limited to the longitudinal dynamics, which includes rotations around the pitching axis (Y-axis) only. Any cross-coupling effects between the longitudinal and lateral axes are excluded.
- Crosswinds, wind gusts, ground effects, propwash and high (wind)speeds are not included in the modelling. The results presented in this work are therefore only valid in the near-hover regime which is below 2 to 5 m/s [17][19].
- The effects of gravity due to the mass unbalance with respect to the rotor plane center are only modelled for pitch angles between ± 90 degrees by a constant bias. The results in this work with

exceeding pitch angles should be interpreted with care.

- The reachable set analysis is centered around the hover condition, which is defined as the straight and level flight condition in which the quadcopter has no pitch angle, rate or acceleration ($\dot{q}$ = q = θ = 0). This condition is defined as the safe set from which the reachability analysis is applied.
- The structure of the system dynamics model is control *affine*.
- It is assumed that the (forward) reachable sets are both closed and bounded.
- The analysis focuses on forward reachable sets with time-windows up to 0.2 seconds.

Part I

Thesis Paper

Safe Flight Envelope Prediction and Experimental Validation of Multirotor UAV

L.C. Kaffa
MSc. Student, Control & Simulation
TU Delft, Aerospace Engineering
Delft, The Netherlands
l.c.kaffa@student.tudelft.nl

Dr. ir. C.C. de Visser
Associate Professor, Control & Simulation
TU Delft, Aerospace Engineering
Delft, The Netherlands
c.c.devisser@tudelft.nl

***Abstract*—Loss of control (LOC) is the primary cause of failure of Unmanned Aerial Vehicles (UAV). The safety of these systems can be largely improved by facilitating techniques to prevent LOC to occur, such as Flight Envelope Protection, enabling controllers to keep the system within the Safe Flight Envelope (SFE).**

The aim of this work is to examine the behaviour of the global SFE of a quadcopter subjected to varying system dynamics, including the effects of longitudinal center of gravity displacements and actuator dynamics.

The analysis has been split into the forward reachable set (FRS) and the backward reachable set (BRS). The FRS is estimated through an optimized Monte-Carlo (MC) simulation approach. Verification shows that the system specific optimized MC simulation approximates the true reachable sets with high accuracy, while exceeding performance on both accuracy as well as computation time compared to the Level-Set method. The BRS is derived from the FRS directly using a minimum-time optimal control (MTOC) routine including actuator dynamics. This approach guarantees that the BRS is contained within the FRS and bypasses the need to simulate the dynamics backwards in time. Both methods exploit the control *affine* system structure from which it can be derived that the MTOC for both the FRS and BRS is *bang-bang* control, which drastically reduces the sampling space and optimal control complexity.

The results show that both the location of the centroid of the FRS and the return time distribution of the BRS are a function of the offset position. A large decrease in the FRS area is seen for larger center of gravity offset positions. Furthermore, the actuator dynamics reduce the FRS by 85%, irrespective of center of gravity location, while the BRS without actuator modelling shows impractical return times as a result of unfeasible instantaneous rotor speed changes. A novel experimental validation procedure on the quadcopter FRS has been performed. The results show a general overestimation with respect to the flight data, which is expected when comparing an open-loop simulation with closed-loop performed flight maneuvers.

***Index Terms*—Bang-Bang Control, Safe Flight Envelope Prediction, Level-set Method, Minimum-Time Optimal Control, Monte-Carlo Simulation, Quadcopter, Reachability Analysis, Sliding Mode Control**

I. Introduction

The use and applications of Unmanned Areal Vehicles (UAV) are expected to grow rapidly in the near future [1]. Currently Loss of control (LOC) is the main cause of failure for UAVs [2]. In order to improve safety of these systems, development of LOC prevention techniques are of utmost importance. A way to prevent LOC is through the use of flight envelope protection (FEP) which enables controllers to keep the system within the Safe Flight Envelope (SFE). The SFE indicates the state-space in which the vehicle can be safely operated, operating outside the SFE is linked to LOC [3][4]. The SFE can be defined as *the set of states that can be reached, within a certain time-window, for which a trajectory exist to return to a safe flight condition within a predefined time-window* [5][6][7][8]. This research focuses on predicting the SFE of multirotor UAVs to allow for FEP implementation and development for LOC prevention and thereby facilitating in improving the safety of these systems. The prediction is focused on the global flight envelope, rather than local boundary prediction, as it has the advantage to apply global FEP techniques to balance safety and performance for the specific application.

The aim of this work is to examine the behaviour of the global SFE of a quadcopter subjected to varying system dynamics, including the effects of longitudinal center of gravity displacements and actuator dynamics. The analysis has been split into the forward reachable set (FRS), which contains all the states the system can reach from a set of initial states within a given time-window, and the backward reachable set (BRS), which contains the states from which the system can return to the initial set of states within an arbitrary time-window. The multirotor UAV considered in this study is a quadcopter model because these models are widely used in various applications, easily accessible and suitable for conducting (indoor) flight experiments. The dynamics of the quadcopter for various center of gravity positions are captured via a data-driven approach using model identification on flight data. The prediction of the forward reachable sets are obtained using a Monte-Carlo (MC) approach rather than the prevailing Level-Set method. The MC simulation approach is a promising method for quadcopter flight envelope prediction as it can be applied on higher dimensional nonlinear systems [8], it has a lower computational load with increased number of dimensions compared to the Level-Set method [9], and is recently successfully applied on quadcopter models [10]. The BRS is derived from the FRS directly using a minimum-time optimal control (MTOC) routine including actuator dynamics. This approach guarantees that the BRS is contained within the FRS and bypasses the need to simulate the dynamics backwards in time. Both methods exploit the control *affine*

system structure from which it can be derived that the MTOC for both the FRS and BRS is *bang-bang* control, which drastically reduces the sampling space and optimal control complexity. The methods are verified and an experimental validation procedure is performed to validate the FRS estimations.

In Chapter II information on the literature background on the topic of reachability analysis can be found. The specific contributions and limitations of this research are summarized in Chapter III. Details on the quadcopter modelling can be found in Chapter IV. The MC approach in the framework of reachability analysis is covered in Chapter V, followed by a derivation of the minimum-time optimal control routine for backward reachable set estimation in Chapter VI. The results on both the forward and backward reachable set can be found in Chapter VIII. A verification on the MC simulation and optimal control routine is presented in Chapter VII and the forward reachable sets are validated in Chapter IX. Finally, the conclusions and recommendations on the research findings are presented in Chapter X and Chapter XI. An overview of the research project with references to the chapters can be found in Fig. 1.

II. Literature Background

Loss of control (LOC) is the main cause of failure for Unmanned Aerial Vehicles [2]. LOC can occur as a result of a system failure, insufficient controller performance, or as a result of entering an upset condition when violating the flight envelope in which the system can be safely operated. In the occasion of system failures, *fault-tolerant control systems* are developed making use of a closed-loop control system and a (real-time) fault detection and diagnostics system [11]. To improve stability and control, a large amount of quadcopter literature is dedicated towards developing *robust controllers* [12][13]. In order to prevent LOC to occur when the system enters an upset condition, *upset recovery techniques* are developed. Although literature on upset recovery for multirotor UAVs is limited, it has been shown that recovering from upset conditions is possible [14][15][16][17].

In the (fixed-wing) aircraft literature of the past decade, an increase in the amount of research can be observed into the prediction of the Safe Flight Envelope (SFE). The SFE can be defined as *the set of states that can be reached, within a certain time-window, for which a trajectory exist to return to a safe flight condition within a predefined time-window* [5][6][7][8]. The prediction of the SFE in fixed-wing literature is often incorporated with adaptive capabilities under various damage case scenarios. The damaged aircraft dynamics are captured using online system identification techniques, as presented by Belcasto et. al [18] and Van Oort [6], which used the aircraft trim envelope as the a-priori safe set. This research area has been continued by the work of Lombaerts et. al [7][19][20]. The feasibility of interpolation of envelopes was shown by Nabi et. al [21]. In the work of Zhang [5] a database-driven approach is introduced which interpolates offline estimated SFEs for various damage case scenarios, showing quick prediction capabilities with high accuracy results for flight envelope protection (FEP). Zhang [5] recommends to investigate application of this framework on (damaged) drones. In Yin et. al [8] this date-base driven approach has been applied, but instead of using deterministic boundaries, a probabilistic envelope estimation method is used based on the Monte-Carlo (MC) simulation with kernel density estimation resulting in fuzzy sets. This work shows that using probabilistic SFE boundaries results in earlier and more gentle FEP measures [8]. This research is motivated by the promising findings by the research summarized above to extend knowledge on SFE prediction and protection in the framework of quadcopters for safety improvement.

Many methods can be identified in literature for predicting the SFE. The initial flight envelopes were determined by using windtunnel test and computational fluid dynamics (CFD) analysis, which were verified by expensive flight tests [22]. With improved computational power, the focus turned towards numerical simulations to predict nonlinear (aircraft) dynamics and instabilities. A very important development to allow for flight envelope prediction were the bifurcation and continuation methods introduced by Carroll et al. [23]. With these methods it is possible to compute steady-state solutions for all possible control inputs and were mainly used as an analysis tool for the design of flight control laws and flight envelopes [6]. This further branched into the reachability analysis. The most prevailing method used in reachability analysis is the Level-Set method, which solves the optimal control problem by numerically approximating the solution to the Hamilton-Jacobi partial differential equation on a grid. A fundamental disadvantage of the Level-Set method is the computational inefficiency. It suffers from the curse of dimensionality as it scales exponential with the number of states and it becomes impractical to use for systems with more than four states [5][10][24][25]. An alternative method for reachable set estimation is by using a MC simulation. In Sun et al. [10] it has been shown that this method is able to solve a 6-dimensional reachability problem for a quadcopter model in a matter of seconds and is more computational efficient than the Level-Set method [8]. Although in Terrell et al. [9] it has been shown that the MC simulation also suffers from the curse of dimensionality however less than the Level-Set method. It should be noted that extreme control effectiveness methods, such as *bang-bang* control [26], should be employed to mainly reach the boundary states, prevent conservative results and reduce the amount of simulations required. It should be noted that the probability distribution of the input determines the probability distribution of the corresponding output [8]. In this research a model-based reachability analysis is applied using a MC approach supported by the findings described above. In the next section a summary of the research contributions of this work can be found, together with the scope and limitations of the research.

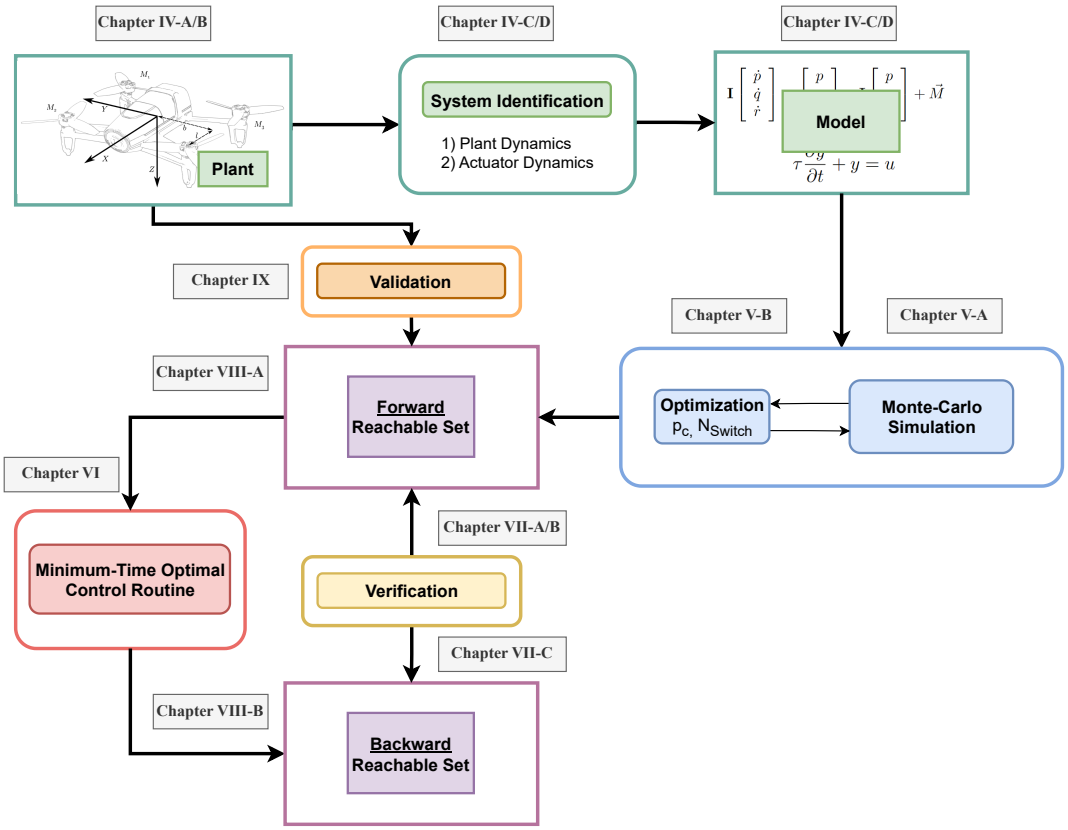

Fig. 1. Overview of the research project with references to the specific chapters.

III. Research Contributions & Limitations

This research focuses on improving and extending knowledge on (the prediction of) the Safe Flight Envelope (SFE) of a quadcopter model motivated by the promising findings in recent (fixed-wing) aircraft literature in the framework of SFE prediction and protection (FEP) for loss of control (LOC) prevention, and thereby improving the safety of aircraft. Furthermore, research of application of this reachability framework on quadcopters is limited [26] and hence this research directly adds knowledge to the body of literature for quadcopter safety improvement. This research contributes to the literature as follows:

1) This research adds knowledge on the behaviour of the SFE of a quadcopter subjected to varying center of gravity position. It produces results on the quadcopter performance in terms of both the forward reachable set (FRS) and the backward reachable set (BRS). The results allow further research into the feasibility of interpolating envelopes, for example for application in a database-driven approach for (real-time) FEP [5].
2) The results on the reachable sets as a function of center of gravity position can be used to quantify as model uncertainty. This uncertainty can be used to model the SFE in a probabilistic way, for example for applications in which the center of gravity of the quadcopter could vary.
3) This research includes the actuator dynamics in the reachability analysis and shows its relevance, whereas the actuator dynamics are often neglected in quadcopter literature.
4) The results on the reachable sets obtained from the Monte-Carlo (MC) approach can be used for further research into probabilistic SFE analysis and protection in the application of quadcopters [8].
5) An optimization routine is applied on the MC simulation parameters of which the results and insights can be used in further research on quadcopter reachable set estimation using a MC approach.
6) A verification on the performance of the MC simulation on reachable set estimation produces knowledge and insights for future use of the MC approach for reachability analysis. Furthermore, the MC simulation approach is briefly benchmarked with the *Level-set Toolbox* [27].
7) A novel backward reachable set estimation approach is explored. The BRS is derived from the FRS directly using a minimum-time optimal control routine. This approach guarantees that the BRS is contained within the FRS and bypasses the need to simulate the dynamics backwards in time.

8) A minimum-time optimal control routine is developed to control the attitude and angular velocity of the quadcopter *including actuator dynamics* to any desired orientation in minimum-time. The resulting *bang-bang* controller shows a sliding-mode control behaviour. This routine can be (re)used and further developed in other research into (optimal) control applications of quadcopters.
9) An experimental validation on the reachable set of a quadcopter is conducted to validate the FRS through flight experiments. The analysis produces validation results and valuable experience for future implementations.

This research is limited to or restricted by the following elements:

- The quadcopter dynamics and reachable sets are limited to the longitudinal dynamics, which includes rotations around the pitching axis (Y-axis) only. Any cross-coupling effects between the longitudinal and lateral axes are excluded.
- Crosswinds, wind gusts, ground effects, propwash and high (wind)speeds are not included in the modelling. The results presented in this work are therefore only valid in the near-hover regime which is below 2 to 5 m/s [28][29].
- The effects of gravity due to the mass unbalance with respect to the rotor plane center are only modelled for pitch angles between ± 90 degrees by a constant bias. The results in this work with exceeding pitch angles should be interpreted with care.
- The reachable set analysis is centered around the hover condition, which is defined as the straight and level flight condition in which the quadcopter has no pitch angle, rate or acceleration ($\dot{q} = q = \theta = 0$). This condition is defined as the safe set from which the reachability analysis is applied.
- The structure of the system dynamics model is control *affine*.
- It is assumed that the (forward) reachable sets are both closed and bounded.
- The analysis focuses on forward reachable sets with time-windows up to 0.2 seconds.

IV. Quadcopter Modelling

For the model-based approach of flight envelope prediction, a dynamic quadcopter model has been established. The definition of the body reference frame relative to the quadcopter frame is illustrated in Fig. 2.

Since the physical principles of modelling a quadcopter system are known, a gray-box model structure is used. Assuming that the quadcopter is a rigid body and using Newton's laws of motion, the following linear and rotational dynamic equations can be derived:

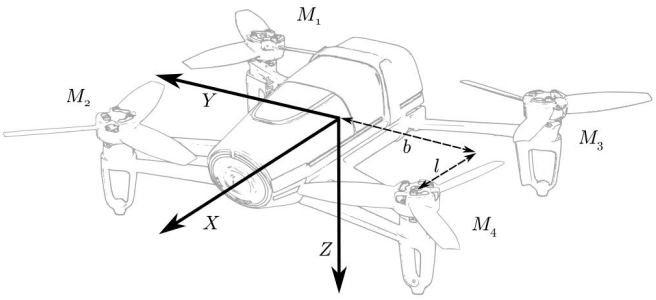

Fig. 2. The definition of the body reference frame with origin at the center of gravity location [13] (adjusted the motor numbering). Roll, pitch and yaw rotations are defined as the rotations around the X, Y, Z axes respectively with right-handed conventions. The motors are labeled by number from one to four.

$$m \begin{bmatrix} \dot{u} \\ \dot{v} \\ \dot{w} \end{bmatrix} = m \begin{bmatrix} p \\ q \\ r \end{bmatrix} \times \begin{bmatrix} u \\ v \\ w \end{bmatrix} + \vec{G} + \vec{F} \tag{1}$$

$$\mathbf{I} \begin{bmatrix} \dot{p} \\ \dot{q} \\ \dot{r} \end{bmatrix} = \begin{bmatrix} p \\ q \\ r \end{bmatrix} \times \mathbf{I} \begin{bmatrix} p \\ q \\ r \end{bmatrix} + \vec{M} \tag{2}$$

With m the mass of the quadcopter, u, v, w and $\dot{u}, \dot{v}, \dot{w}$ the body linear speeds and accelerations along the X, Y and Z axis. $\vec{G}$ and $\vec{F}$ represent the gravity vector and the resultant force vector (excluding gravity) in the body frame. The body angular rates and accelerations are represented by p, q, r and $\dot{p}, \dot{q}, \dot{r}$ which rotate around the X, Y, and Z axis respectively. $\vec{M}$ represents the resultant moment vector on the quadcopter in the body frame and $\vec{I}$ represents the inertia matrix.

The forces and moments that act on the quadcopter can be split into the effects of the rotors ($\vec{F_r}$ and $\vec{M_r}$) and the aerodynamic effects ($\vec{F_a}$ and $\vec{M_a}$) as follows:

$$\vec{F} = \vec{F_r} + \vec{F_a} \tag{3}$$

$$\vec{M} = \vec{M_r} + \vec{M_a} \tag{4}$$

In Sun et al. [29] this gray-box model has been used and the results show great improvements in the prediction ability compared to the basic quadcopter dynamic model. The basic quadcopter model includes the effect of the rotor dynamics but neglects the aerodynamic effects. The pitching moment induced by the rotors can be described by the pitch control and is induced by differential thrust of the motors as follows:

$$\vec{M_y} = l\kappa_0(\omega_4^2 + \omega_2^2 - \omega_3^2 - \omega_1^2) \tag{5}$$

With ω_i the rotor speeds per motor number i and l the longitudinal distance to the center of rotation (along the X-axis), which is equal to the center of gravity location when assuming a uniform gravitational field around the quadcopter. κ_0 is a rotor property coefficient dependent on the air density and can be assumed to be constant [29][30][31].

While previous research suggests that non-rotor aerodynamic effects are significant [29][28], this work focuses on the near-hover regime where they are negligible up until 2 m/s [28]. Any (external) aerodynamic effects are not included in the model. The results in Sun et. al [28][29] show that this model deteriorates above 5 m/s. Therefore it should be kept in mind that the results presented in this work are only valid in the near-hover regime which is below 2 to 5 m/s [28][29].

This research addresses the effects on varying dynamics as a result of center of gravity offsets from the rotor plane center. Consequently, the effects on the forces and moments on the quadcopter dynamics have to be captured. For this reason an altered model structure is used compared to Eq. 37, which assumes that the center of gravity coincides with the rotor plane center. To quantify the offset effects, a data-driven modelling approach is taken. In this approach the forces and moments are modelled by fitting the parameters of a designed model structure to flight data through parameter identification. Note that in this research only the longitudinal center of gravity position (along the X-axis) is considered. It is assumed that the lateral placements (along the Y-axis) are constant. Furthermore, this work solely focuses on the effects of the pitching moment. Hence only the modelling of the pitching moment, M_y, is included in the model identification.

In order to preserve control over the structure of the model and to be able to perform an analysis on the identified parameter values, a white-box model with a polynomial model structure is used. Ordinary least-squares (OLS) regression is used to fit parameters of the linear-in-the-parameters model structure to the flight data.

The flight data are obtained by performing (indoor) quadcopter flights, details on the quadcopter hardware and the flight experiment set-up can be found in Section IV-A. In Section IV-B information is provided on the data acquisition and data processing applied on the measurements before model identification. In Section IV-C the model structure design and the results from the parameter identification are presented. The identified quadcopter models are independent of actuator dynamics, therefore a separate model identification routine is performed for modelling the actuator dynamics in Section IV-D.

A. Flight Experiment Set-Up & Hardware Details

The flight data have been obtained from manual (line-of-sight) indoor flights with a 3-inch sized quadcopter frame. Details on the platform and the hardware can be found in Table I.

To vary the center of gravity position, the battery on top of the quadcopter frame has been varied. In total five battery configurations have been considered: a battery at the center of the quadcopter rotor frame (the neutral configuration), an extreme aft position (aft configuration), an extreme forward position (forward configuration), and two half positions in between (half aft and half forward configuration). The various configurations are illustrated in Fig. 3. Note the exceptional displacement of the battery forward configuration compared to the battery aft position. With each battery configuration manual (indoor) flights have been performed. In order to excite the pitching moment dynamics, low- and high frequency pitching maneuvers have been performed, as well as rapid alternating back-and-forth flying. For the modelling of the actuator dynamics (see Section IV-D) throttle pulse maneuvers have been included in the flights.

TABLE I
HARDWARE DETAILS OF THE QUADCOPTER PLATFORM.

Mass (incl. battery)	388.24 gram
Frame Kit	Metal Beetle (3 inch)
IMU	MPU6000-V1.2
Flight Controller	Holybro Kakute F7
Propeller Type	3052 Three Blades
Electronic Speed Controller	Aikon Race Dragon BLHeli32
Battery	R-line 850 mAh
Flight Control Software	Betaflight

Varying the location of the battery changes the (mass) moment of inertia, thus for each configuration the moment of inertia has been experimentally determined using a bifilar pendulum. It is assumed that the quadcopter has two mass-planes of symmetry, hence all products of inertia are zero. Moreover, the exact center of gravity position has been measured as well. The results on the measured moment of inertia around the pitch axis (Y-axis) and the longitudinal position of the center of gravity (along the X-axis) for each configuration can be found in Table II. Note that indeed the the battery forward configuration has the largest moment of inertia and largest center of gravity offset with respect to the neutral configuration. More information on the moment of inertia and center of gravity position measurements can be found in Appendix A.

TABLE II
RESULTS OF THE EXPERIMENTALLY MEASURED MOMENT OF INERTIA AROUND THE Y-AXIS, AND CENTER OF GRAVITY POSITION ALONG THE X-AXIS FOR EACH BATTERY CONFIGURATION. x_n IS THE DISTANCE FROM THE NEUTRAL CENTER OF GRAVITY. x_c IS THE DISTANCE FROM THE ROTOR PLANE CENTER TO THE CENTER OF GRAVITY POSITION.

Battery Position	$\mathbf{I_{yy}}$ $[kgm^2]$	**%**	$\mathbf{x_n}$ $[cm]$	$\mathbf{x_c}$ $[cm]$
Aft	0.00112	22.3%	-1.0	-1.2
Half Aft	0.000951	3.8%	-0.9	-1.1
Neutral	0.000916	0%	0	-0.2
Half Forward	0.000979	6.9%	0.9	0.7
Forward	0.00133	45.2%	1.9	1.7

B. Data Processing

The flight data have been obtained from the onboard IMU, which include angular velocity measurements from a MEMS gyro, required for the identification of the pitching moment models. Furthermore, the rotational speeds of the four rotors are logged from the bidirectional DSHOT telemetry. For identification of the actuator model, the commanded rotor speed signals are obtained as well, for more information on the actuator dynamics modelling see Section IV-D. In order to improve the quality of the models, state estimation with an

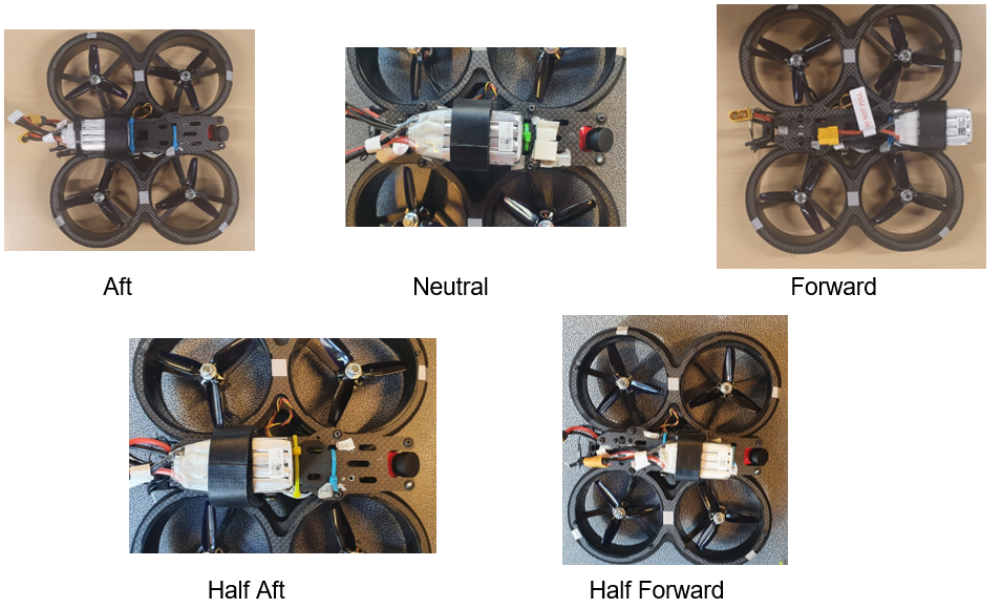

Fig. 3. The five battery positions used in the reachability analysis. Note that the battery aft configuration has a smaller displacement than the battery forward configuration, which is due to practical constraints. Note that in this research only the longitudinal center of gravity position (along the X-axis) is considered. It is assumed that the lateral and vertical placements (along the Y-axis and Z-axis) are constant.

extended Kalman filter has been applied on the data in order to mitigate any bias originating from measurement (and/or process) noise. More information on the data processing can be found in Appendix B. The data have been split into training datasets, which are used for model parameter estimation, and validation datasets, which are used to test the identified model. For each quadcopter configuration, two sets of flight data have been collected which both contain similar maneuvers. The take-off and landing (or crashing) phases of the flights have been excluded from the datasets. Since this work is primarily focused on modelling the pitching moment, the predominant pitching maneuvers have been partitioned from the flight data. The partitioning has been conducted by finding the absolute peaks in the pitching moment data. The data before and after the exciting maneuver have been included to capture the (relevant) dynamics prior and after the excitation maneuvers. An example of a partitioned dataset is displayed in Fig. 4. It should be noted, however, that although similar maneuvers are performed, they are not exactly identical as a result of manual piloted flights. Therefore, the datasets can differ in the reached pitching moment range. Consequently, it is impractical to use a fixed partitioning threshold for all flight datasets. Therefore, for each dataset a balanced threshold has been set manually and the dataset with most sustained pitching maneuvers has been selected as the training dataset. An overview of the total duration of the training and validation data after partitioning can be found in Table III.

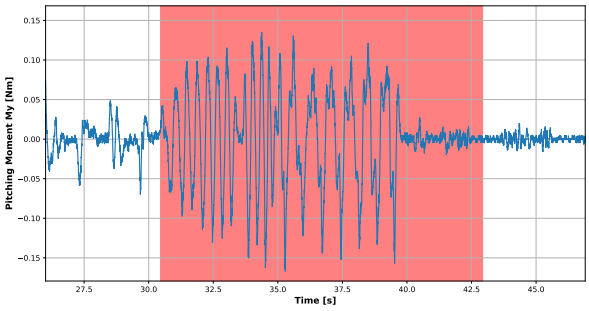

Fig. 4. Example of data partitioning of the pitching moment data to isolate relevant maneuvers which excite the pitching moment dynamics. Note that some data after the maneuver have been included to capture the steady-state effects.

C. Model Structure and Parameter Identification

This work is limited to the longitudinal pitching dynamics of a quadcopter, hence the primary focus is on obtaining models for the pitching moment M_y. The model structure consists of polynomial regressors which have shown to perform well for quadcopter forces and moments modelling [28][12]. For the selection of the model regressors, various sources have been conducted which include patterns in the flight data, a stepwise regression analysis and the basic quadcopter hover model structure Eq. 37. More information on the regressor selection can be found in Appendix D.

The model structure of the pitching moment model has been determined to consist of a *bias term* M_0 and *control pitching moment* term U_q. The control pitching moment is defined as the sum of the front rotors minus the aft rotors: $U_q = \omega_2 + \omega_4 - \omega_1 - \omega_3$. The control moment is split into separate terms each modelling the positive U_q^+ and negative U_q^- control moment independently. When the control input

TABLE III

OVERVIEW OF THE TOTAL AMOUNT OF DATA, MEASURED IN FLIGHT MINUTES OF EXCITATION MANEUVERS, WHICH ARE USED IN THE SYSTEM IDENTIFICATION. THE FLIGHT DATA WITH MOST SUSTAINED PITCHING MANEUVERS HAS BEEN SELECT AS TRAINING DATASET. THE DATA HAVE BEEN MORE OR LESS EQUALLY SPLIT, THE TRAINING DATASETS HAVE A TOTAL DURATION OF 214.64 SECONDS AND THE VALIDATION DATASETS HAVE A TOTAL DURATION OF 254.4 SECONDS.

	Training Datasets	
Battery Position	*Total Excitation Duration [s]*	*% of Full Dataset*
Aft	42.2	60.26
Half Aft	56.7	60.99
Neutral	34.0	28.98
Half Forward	51.18	54.56
Forward	30.06	31.37
	Validation Datasets	
Battery Position	*Total Excitation Duration [s]*	*% of Full Dataset*
Aft	55.51	65.27
Half Aft	37.36	44.8
Neutral	40.44	34.17
Half Forward	77.11	81.17
Forward	43.5	44.0

moment is positive, U_q^- is set to zero and vice versa for a negative control input moment. The resulting model structure can be summarized as follows:

$$M_y = M_0 + M_1 U_q^+ + M_2 U_q^- \tag{6}$$

The bias term captures the differences in dynamics as a result of the center of gravity offsets from the rotor plane center, while the control pitching moment parameters model the possible differences in rotor effectiveness with respect to pitching direction in combination with the center of gravity offset. The coupled and nonlinear regressor terms found from the stepwise regression routine are excluded from the model structure in order to keep the models simple and preserve a physically explainable model structure. Since any (external) aerodynamic effects have not been included, this model is only valid in the low speed regime which is below 2 to 5 m/s [28][29].

The model parameters M_0, M_1 and M_2 are determined using the OLS regression method:

$$\hat{\theta} = (A^T A)^{-1} A^T z \tag{7}$$

With $\hat{\theta}$ the optimal parameter estimate to minimize the model residual, $A = [1, U_q^+, U_q^-] \in R^N$ the regression matrix with N the number of measurement data points, and $z \in R^N$ the measurement vector. The optimal parameter estimates found from the training datasets are summarized in Table IV. Additionally, the parameter (co)variances are included, which represent the noise sensitivity, or variability, of the estimator. The parameter covariances are estimated as follows:

$$cov(\hat{\theta}) = \sigma^2 (A^T A)^{-1} \approx \hat{\sigma}^2 (A^T A)^{-1} = \frac{\epsilon^T \epsilon}{N-k} (A^T A)^{-1} \tag{8}$$

With ϵ the model residual which is the difference between the target and the estimated signal values, N the number of measurement data points, and k the number of regressor terms.

The metrics for estimation performance include the normalized root-mean square error (NRMSE), normalized with the range of the target data, and the adjusted coefficient of determination (Adjusted R^2). The metrics are defined as follows:

$$\text{NRMSE} = \frac{\text{RMSE}}{(y_{max} - y_{min})} = \frac{\sqrt{\sum_{i=1}^{N} \frac{(\hat{y}_i - y_i)^2}{N}}}{(y_{max} - y_{min})} \tag{9}$$

$$R^2_{Adjusted} = 1 - \left(\frac{(1 - R^2)(N-1)}{(N-k-1)} \right) \tag{10}$$

With k the number of regressors, excluding the bias term, and R^2 as:

$$R^2 = 1 - \frac{\sum_{i=1}^{N} (\hat{y}_i - y_i)^2}{\sum_{i=1}^{N} (y_i - \bar{y})^2} \tag{11}$$

With y the target signal, $\bar{y}$ the mean of the target signal, and $\hat{y}$ the predicted signal. The metric values of all pitching moment models can be found in Table V. The identified models show good approximation power and accuracy with respect to the validation data with an average $R^2_{Adjusted}$ = 0.83 and average NRMSE = 0.05. More information on the identified models including a brief model response analysis can be found in Appendix C. More information on the system identification procedure, including the regressor selection procedure, and a model residual analysis, can be found in Appendix D.

TABLE IV

SUMMARY OF THE OPTIMAL PARAMETER ESTIMATES FOR EACH BATTERY CONFIGURATION. ADDITIONALLY, THE PARAMETER VARIANCES (THE ELEMENTS ON THE MAIN DIAGONAL OF THE COVARIANCE MATRIX) ARE SHOWN REPRESENTING THE NOISE SENSITIVITY (OR VARIABILITY) OF THE ESTIMATOR. THE BIAS HAS THE LARGEST PARAMETER VARIANCE, INDICATING THAT THIS PARAMETER HAS THE LARGEST VARIABILITY OF ITS ESTIMATE WITH RESPECT TO VARIATIONS IN THE NOISE REALIZATIONS.

	$\mathbf{M_0}$		
Bias	$\hat{\theta}$	$cov(\hat{\theta})$	$100cov(\hat{\theta})/\hat{\theta}$
Battery Aft	0.045714	5.612698e-08	0.000123
Battery Half Aft	0.028478	2.492080e-08	0.000088
Battery Neutral	0.001716	3.739539e-08	0.002179
Battery Half Forward	-0.026671	2.666699e-08	-0.000100
Battery Forward	-0.060630	3.170904e-08	-0.000052
	$\mathbf{M_1}$		
$\mathbf{U_q^+}$	$\hat{\theta}$	$cov(\hat{\theta})$	$100cov(\hat{\theta})/\hat{\theta}$
Battery Aft	0.000111	1.165452e-12	1.048731e-06
Battery Half Aft	0.000108	3.518097e-13	3.268488e-07
Battery Neutral	0.000098	2.673546e-13	2.740386e-07
Battery Half Forward	0.000093	8.573101e-14	9.187859e-08
Battery Forward	0.000078	2.665912e-14	3.397296e-08
	$\mathbf{M_2}$		
$\mathbf{U_q^-}$	$\hat{\theta}$	$cov(\hat{\theta})$	$100cov(\hat{\theta})/\hat{\theta}$
Battery Aft	0.000077	6.980824e-14	9.012239e-08
Battery Half Aft	0.000093	7.449741e-14	7.974035e-08
Battery Neutral	0.000104	2.297720e-13	2.208843e-07
Battery Half Forward	0.000102	3.144075e-13	3.087665e-07
Battery Forward	0.000099	4.669925e-13	4.703377e-07

TABLE V
NORMALIZED RMSE AND ADJUSTED R^2 VALUES FOR EACH QUADCOPTER CONFIGURATION MODELS ON BOTH THE TRAINING- AND VALIDATION DATASET. NOTE THAT THE METRICS FOLLOW FROM THE PARTITIONED DATASETS.

	NRMSE		
	Train	*Validation*	*Total*
Battery Aft	0.0568	0.0623	0.0512
Battery Half Aft	0.0444	0.0584	0.0480
Battery Neutral	0.0482	0.0442	0.0533
Battery Half Forward	0.0394	0.0621	0.0411
Battery Forward	0.0350	0.0549	0.0469
	Adjusted $\mathbf{R^2}$		
	Train	*Validation*	*Total*
Battery Aft	0.8733	0.7896	0.7901
Battery Half Aft	0.8951	0.8073	0.7782
Battery Neutral	0.8952	0.9066	0.7230
Battery Half Forward	0.9014	0.8020	0.8165
Battery Forward	0.9626	0.8631	0.8344

TABLE VI
VALIDATION RESULTS - ACTUATOR TIME CONSTANTS IDENTIFICATION USING AN EQUAL SPLIT OF TRAINING AND VALIDATION DATA.

		NRMSE		**Adjusted $\mathbf{R^2}$**	
Motor	τ	*Train*	*Validation*	*Train*	*Validation*
1	0.0518	0.0473	0.0460	0.9020	0.9116
2	0.0794	0.0647	0.0497	0.8511	0.9102
3	0.0485	0.0465	0.0443	0.9015	0.9113
4	0.0580	0.0492	0.0505	0.8967	0.9012

TABLE VII
FINAL RESULTS - ACTUATOR TIME CONSTANTS IDENTIFICATION USING ALL FLIGHT DATA.

Motor	τ	$100\mathbf{cov}(\hat{\theta})/\hat{\theta}$	**NRMSE (Train)**	**Adjusted $\mathbf{R^2}$ (Train)**
0	0.0510	0.0221 %	0.0473	0.9102
1	0.0800	0.0173 %	0.0612	0.8704
2	0.0490	0.0232 %	0.0467	0.9075
3	0.0563	0.0193 %	0.0494	0.9012

D. Modelling of Actuator Dynamics

Based on the behaviour of the rotor speeds in response to commanded inputs as observed in the measurement data, the actuator dynamics are modelled by a first order lag function, which in time-domain (12) and frequency-domain (13) has the following structure:

$$\tau \frac{dy}{dt} + y = u \tag{12}$$

$$H(s) = \frac{1}{\tau s + 1} \tag{13}$$

With y the rotor speed, u the commanded rotor speed and τ the time constant. Determination of the time constant τ follows from estimation of the lag (or time-delay) between the rotor speed commanded signal and the actual rotor speed signal measured. By separating $\frac{dy}{dt}$ in Eq. 12 and numerically differentiating the rotor speed measurements y, the parameter $\frac{1}{\tau}$ is estimated using OLS, after forward-backward filtering both signals at 10 rad/s. The time constant τ is obtained by taking the reciprocal of the estimated parameter.

The data used for identification involves all the flight data as discussed in Section IV-B as well as dedicated throttle pulses flights containing 12 throttle pulse maneuvers in total. It is assumed that the actuator dynamics do not change with varying battery configurations. The data have been split into training and validation data equally. The model performance on both training and validation data can be found in Table VI which shows a validation performance of $R^2_{Adjusted} > 0.9$ and NRMSE < 0.05 for all time constants. The time constants estimated, using all flight data available, are summarized in Table VII. These time constants are used in subsequent quadcopter actuator dynamics modelling.

V. REACHABLE SET ESTIMATION: A MONTE-CARLO APPROACH

To obtain an estimate of the forward reachable set, a the Monte-Carlo (MC) simulation approach is used. This approach consists of simulating numerous trajectories from an initial (set of) state(s) while randomly varying the control inputs along the time horizon of a trajectory. Sampling the input randomly from the entire input space results in an extensive amount of simulations (which is called brute force). By considering optimal control for reachability analysis, this sampling space can be drastically reduced. A well-established method for reachable set computations is through the Hamilton-Jacobi reachability analysis in which the goal is to find a control sequence that minimizes a cost function by solving for a value function. Solving the value function via dynamic programming results into the renowned Hamilton-Jacobi-Bellman (HJB) equation. Solving this partial differential equation (PDE) results in a solution to the minimum-time optimal control problem. The PDE has the following form:

$$D_t V(x,t) + H\left(x, t, V, \nabla\phi, D_x^2 V\right) = 0 \text{ for } x \text{ in } \mathbb{R}^n, t \geq 0 \tag{14}$$

Subjected to the initial condition:

$$V(x,t) = V_0(x) \text{ for } x \in \mathbb{R}^n \tag{15}$$

With V the value (or level-set) function, D_t is the partial derivative of V with time t, ∇V is the gradient of V with respect to the state variables x and D_x^2 is the Hessian matrix of the second partial derivatives with respect to x. An appropriate weak solution of the HJB PDE is the so-called *viscocity solution* which has the differential form as shown in Eq. 16. The part to be minimized, in case of finding the backward reachable set (or maximized in case of finding the forward reachable set), is called the *Hamiltonian*.

$$\frac{\partial V}{\partial t} + \min_u [\nabla V(x,t) \cdot f(x,t,u)] \ = 0 \tag{16}$$

With $f(x,t,u)$ the system of equations describing the dynamics of the system. In the case of a control *affine* system the *Hamiltonian* term can be written as [26]:

$$\min_u [\nabla V(x,t) \cdot (f(x,t) + g(x,t)u)] \ = 0 \tag{17}$$

For this type of system the following term can be isolated:

$$\lambda(x,t) = \frac{\partial V}{\partial x}(x,t) g(x,t) \in \mathbb{R}^m \tag{18}$$

Consequently, the solution to the minimum-time optimal control problem is to maximize the input in case $\lambda(x,t) < 0$ and minimize when $\lambda(x,t) > 0$. Vice versa for the case of finding the forward reachable set. When the control input space ranges from a minimum control input, u^-, to a maximum control input, u^+, the found control strategy for the minimum-time optimal control problem can be formally formulated as [26]:

$$u_i^*(x,t) = \begin{cases} u_i^+ & \text{if } \lambda_i(x,t) < 0 \\ u_i^- & \text{if } \lambda_i(x,t) > 0 \end{cases} \tag{19}$$

As a result, the optimum control to solve for reachable sets is located near the control constraints of the system in the case $\lambda_i \neq 0$. With this knowledge, the control input in the MC simulation can be sampled along the ranges of the control input space reducing the sampling space substantially. This control strategy is called *bang-bang* control. Note that this sampling strategy can only be effectively used for control *affine* systems. In case a system is control *nonaffine* the optimal control strategy for MC simulation sampling remains unknown.

To control the extend to which the MC simulation trajectories reach the boundary of the reachable set, thereby controlling the amount of trajectories required for accurate boundary estimation, a tuning parameter p_c is defined as introduced in Sun et. al [26]. It describes the chance of switching the control input from one extreme control input to the other:

$$p_c = (1 - p_s)^N \tag{20}$$

The larger the p_c value, the higher the chance the control input remains constant, while a small p_c indicates a large chance of switching the input. With p_s representing:

$$p_s = 1 - P[u_i(K+h) = u_i(k)] \tag{21}$$

N represents the number of segments the trajectory time-window, T, is divided into. At every segment a control input is sampled. This results in the number of switching times N_{switch}, with a stepsize equal to $h = T/N$. In this work the stepsize is set equal to the time-step $h = dt$ which is kept constant. The N_{switch} is then expressed in the percentage of time-steps at which a control input switch is sampled. For example, $N_{switch} = 100\%$ indicates that at every time-step a control input is sampled, while with $N_{switch} = 50\%$ at only half of the time-steps an input is sampled, i.e. every two time-steps along the trajectory. In Fig. 5 and Fig. 6 the effects of the tuning parameter and switching time are illustrated.

The optimal MC simulation settings, thus the values of p_c and N_{switch}, to estimate a reachable set closest to the true set are dependent on the system dynamics. Therefore a dedicated optimization routine has been developed for obtaining the p_c and N_{switch} resulting in the closest approximation to the true set per quadcopter configuration. A general overview of the MC simulation pipeline can be found in Section V-A. Details about and results from the MC optimization performed on the quadcopter models can be found in Section V-B.

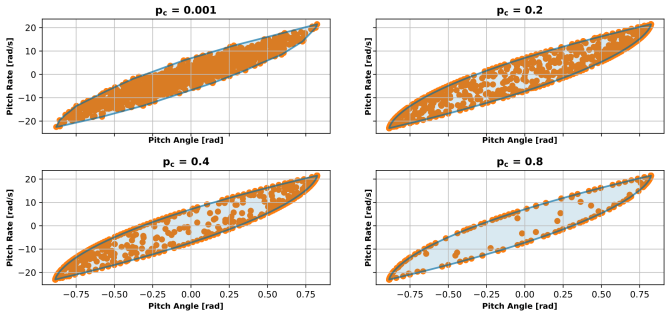

Fig. 5. The influence of the tuning parameter on the trajectory simulations for T = 0.1 s for the battery neutral configuration with N_{traj} = 1000. The higher the p_c the smaller the chance the input switches from input direction and hence the more trajectories reach the boundary of the reachable set. The solid line indicates the estimation of the boundary of the set.

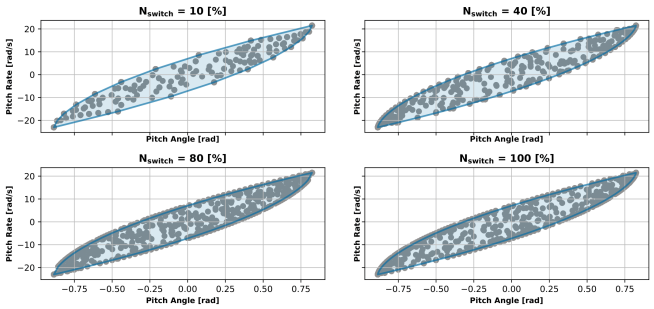

Fig. 6. The influence of sampling time interval on the trajectory simulations for T = 0.1 seconds for the battery neutral configuration with N_{traj} = 1000. Switching intervals are indicated in percentage of the amount of timesteps at which input sampling occurs. The smaller the N_{switch} the less sampling, which results in a higher chance that trajectories end up at the same end state, while increasing the amount of sampling results in more diverse end state trajectories. The solid line indicates the estimation of the boundary of the set.

A. The Monte-Carlo Simulation Environment

An overview of the complete simulation loop can be found in Fig. 7. The simulation uses an open-loop controller, which sets the commanded inputs to the actuator dynamics directly equal to the reference rotor speeds. The actuator dynamics are modelled as a first order lag and saturates the rotor speeds such that these are bounded between the maximum and minimum

obtainable rotor speeds. For numerical integration the forward Euler integration method is used.

Both the forward reachable set (FRS) and backward reachable set (BRS) estimation routines are illustrated in the simulation overview. For FRS estimation a MC sampling routine is performed prior to the trajectory simulation. In this sampling routine the rotor speed references are sampled to either provide a maximum pitch up control moment or a pitch down control moment along the simulation trajectory, based on the p_c and N_{switch} values. At the end of a trajectory simulation the end states are stored and this process is repeated for a number of trajectories N_{traj}. Finally, a convex hull is fitted around the end states using the `alphashape` function from the Alpha Shape Toolbox[1], which completes the FRS estimation. An explanation of the minimum-time optimal control routine used for BRS estimation can be found in Chapter VI.

B. Monte-Carlo Simulation Optimization Routine & Results

The optimal tuning parameter p_c and the optimal time interval between, or the frequency at which, the control inputs are sampled N_{switch}, are unknown and system specific. Therefore an optimization procedure is performed to find the optimum parameters. The MC optimization procedure is performed for each quadcopter configuration model separately in order to ensure optimum reachable set estimation for each center of gravity position model. Since the true reachable sets are unkown, the optimization procedure is designed to maximize the total area of the obtained forward reachable set, as well as maximizing the largest obtained state value, and, minimizing the minimum state value. As a result, the optimization procedure optimizes for obtaining sets that minimize underestimation of the true reachable set. The procedure consists of dividing the simulation parameters into arbitrary discrete values. For each value a MC simulation is performed over a time-window of T = 0.1 s for N_{traj} = 1000. The end state values are stored and used to estimate the boundary of the reachable set by fitting a convex hull shape around the states. See Fig. 7 for a graphical illustration of the FRS estimation routine. This procedure is repeated for a number of realizations to document variability in the results. The routine first optimizes the tuning parameter p_c, subsequently the N_{switch} parameter is optimized. The optimization and simulation settings are summarized in Table VIII.

The MC parameter values, which result in the maximum estimated set area, given that a convergence in the maximum and minimum pitch angle and pitch rate has occurred, are selected as the optimum values. The found optimum p_c and N_{switch} from the MC optimization routine on the forward reachable set for all quadcopter configurations are summarized in Table IX. For demonstration purposes, the MC optimization results for the battery forward model are presented. The area of the estimated reachable sets per tuning and switching parameter can be found in Fig. 8. The maximum and minimum pitch rate from the estimated reachable sets can be found in Fig. 9 (identical trends are found for the pitch angle). It can be observed that the performance of the estimated reachable sets are predominantly determined by the tuning parameter p_c.

[1]https://pypi.org/project/alphashape

TABLE VIII
MC SIMULATION SETTINGS AND PARAMETER VALUES CONSIDERED IN THE OPTIMIZATION ROUTINE.

Trajectories N_{traj}	1000
Time-Window T	0.1 [s]
Time-Step dt	0.001 [s]
Maximum U_q	3800 [eRPM]
Control Strategy	Bang-bang control
Actuator Dynamics	True
N	10
Alpha Parameter	0.001
p_c [-]	0.001, 0.01, 0.1, 0.2, 0.3, 0.4, 0.5, 0.6, 0.7, 0.8, 0.9
N_{switch} [%]	10, 20, 30, 40, 50, 60, 70, 80, 90, 100
Optimizing Set Type	Forward Reachable Set

TABLE IX
SUMMARY OF THE OPTIMAL MC SIMULATION PARAMETERS FOR EACH QUADCOPTER CONFIGURATION.

	Forward Reachable Set	
	p_c	N_{switch}
Battery Aft	0.3	90%
Battery Half Aft	0.4	90%
Battery Neutral	0.5	100%
Battery Half Forward	0.5	100%
Battery Forward	0.4	90%

Since the optimization has been applied on one time-window (T = 0.1 s) only, the set estimation performance of the MC simulation for different time-windows is analyzed as well. The performance of the estimations for various time-windows and number of trajectories of the FRS can be found in Fig. 10 for the battery forward configuration. As expected, the longer the time-window, the larger the forward reachable set, hence the more trajectories are required to retain the estimation performance and reduce the variance among realizations. By increasing the amount of simulated trajectories, the variability of a realization of an estimated set can be controlled per time-window. It can be observed that for about $N_{traj} > 100$ the total set area starts to converge for up to T = 0.2 s. Due to the optimized MC simulation settings, p_c in particular, the maximum and minimum angle and rate obtained already converge for N_{traj} = 25 (only the maximum pitch rate is shown for illustration in Fig. 10). It can be concluded that the optimized MC simulation with N_{traj} = 1000 results in realizations with sufficient convergence for time-windows up to T = 0.2 s. Hence, in further analysis on reachable sets, N_{traj} = 1000 is used as a baseline for reachable set estimation.

Moreover, the maximum and minimum pitch angle and rate obtained from the MC estimated reachable sets can be verified with a simulated trajectory of the quadcopter models over time. In the simulated trajectory the same maximum control pitching moment is applied to the models as used in the MC simulation for reachable set estimation. The results from the

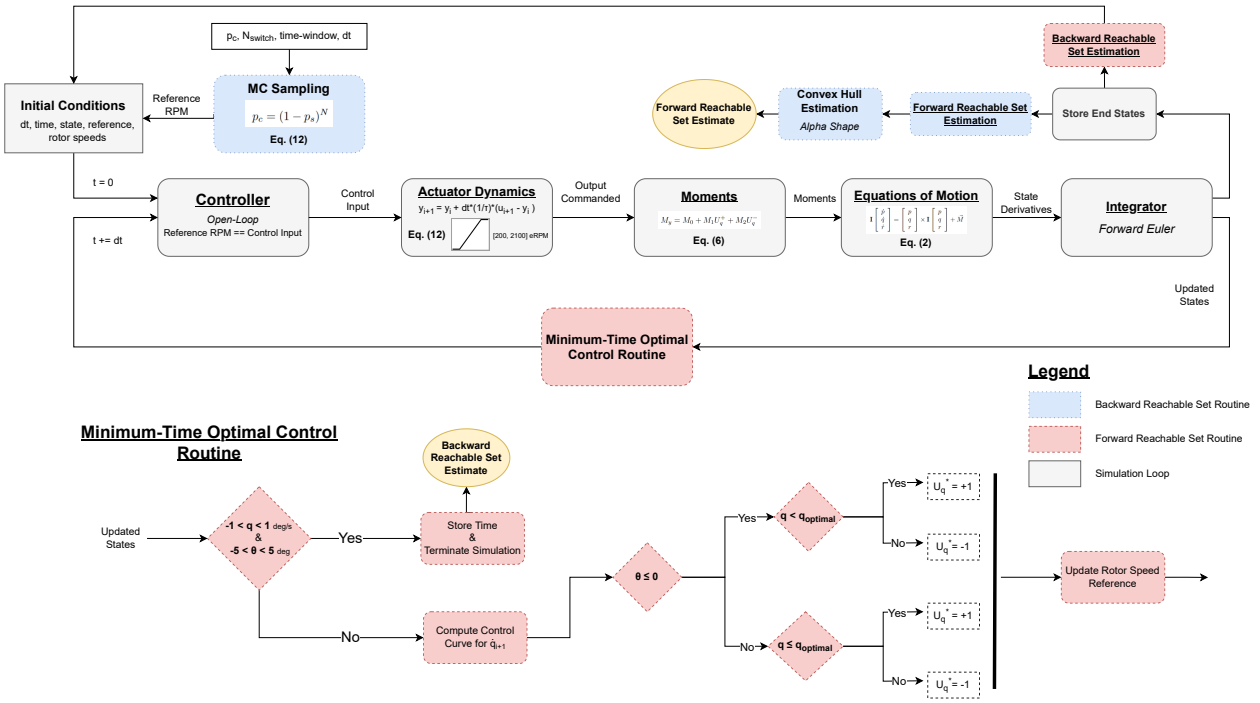

Fig. 7. Overview of the entire simulation loop. For forward reachable set estimation a MC sampling routine is performed prior to the simulation to sample the rotor speed references used along the simulation trajectory. For backward reachable set estimation the end states from the forward reachable set simulations are used and the reference rotor speeds are determined, and updated during simulation, based on the minimum-time optimal control routine. An input of +1 indicates a maximum control pitch *up* moment and -1 a maximum control pitch *down*.

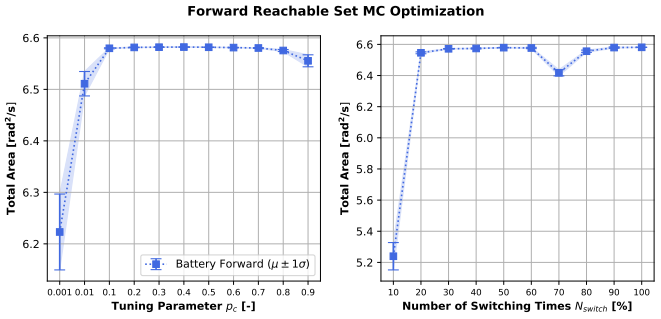

Fig. 8. The total area of the forward reachable set estimates of 10 realizations for varying tuning parameters and switching parameters. The results of the switching parameter are for the case that $p_c = 0.4$. Note the relative large variability at low tuning parameter values. For the battery forward configuration the selected values are $p_c = 0.4$ with N_{switch} = 90%.

MC simulation and the simulated trajectories up to T = 0.2 s are shown in Fig. 11. The differences, displayed in Fig. 12, are negligibly low which verify that the MC simulation provides a converged reachable set estimate for all the models.

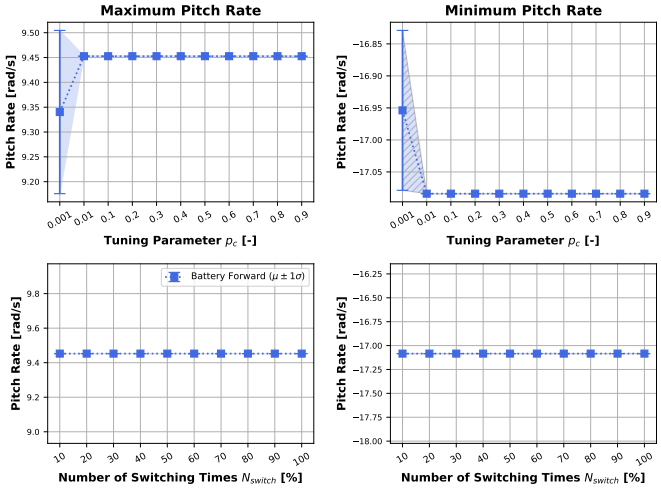

Fig. 9. The maximum and minimum pitch rate obtained from the reachable set estimates of 10 realizations for varying tuning parameters and switching parameter. The results of the switching parameter are for the case that $p_c = 0.4$. Note that both the maximum and minimum pitch rate obtained from the reachable sets have converged for the selected p_c. For the battery forward configuration the selected values are $p_c = 0.4$ with N_{switch} = 90%.

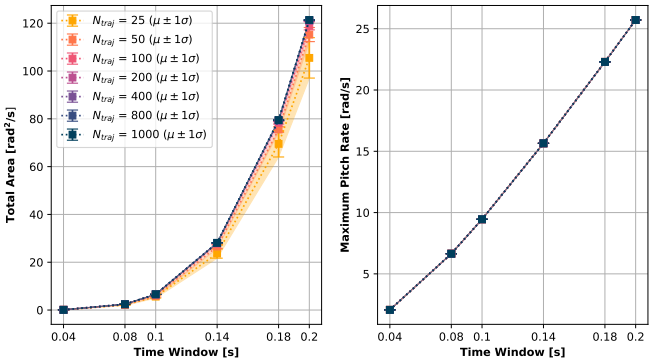

Fig. 10. The performance of the reachable set estimates (N = 10) for various time-windows and number of trajectories for the battery forward configuration. For about $N_{traj} > 100$ the total area of the reachable set estimates starts to converge for time-windows up to T = 0.2 s. Due to the optimized MC simulation settings, p_c in particular, the maximum and minimum angle and rate obtained already converge for N_{traj} = 25.

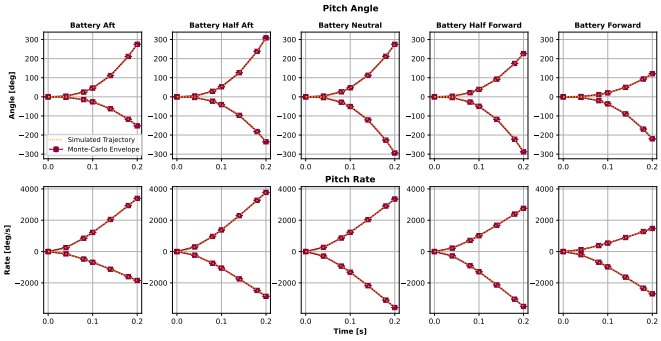

Fig. 11. The maximum pitch angles and rates from the estimated reachable sets from the MC simulation (N_{traj} = 1000) and simulated trajectories are shown together for all quadcopter configurations. The simulated trajectories are obtained with the same maximum control pitching moment input as used in the MC simulation.

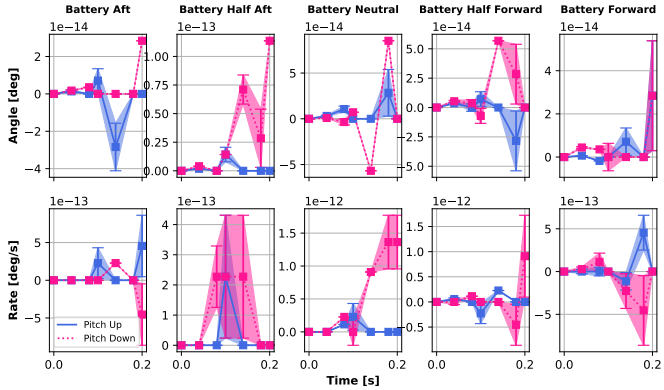

Fig. 12. The differences between the MC simulation reachable set (N_{traj} = 1000) results and simulated trajectories as displayed in Fig. 11. The differences are negligibly low which verify that the MC simulation provides a converged estimate of the reachable set of the models.

VI. Quadcopter Backward Reachable Set Estimation using Optimal Control (Including Actuator Dynamics)

The Safe Flight Envelope (SFE) definition as used in this work is defined as the set of states to- and from which the system can go- and return to a predefined (set of) safe state(s) within an arbitrary time-window. Instead of finding the backward reachable set (BRS) separately and intersecting the set with the forward reachable set (FRS), as often done in literature, this work directly calculates the BRS from the FRS. This approach guarantees that the BRS is contained within the FRS and bypasses the need to simulate the dynamics backwards in time.

To return to the initial safe state (in this work the hover condition) from a state in the FRS, the quadcopter needs to generate a pitch maneuver. In terms of attitude control, this amounts to controlling the change of the quadcopter rotational rate over time, which is equivalent to controlling a double integrator system. The solution to the minimum-time optimal control problem for a double integrator system has been proven in Chapter V to be *bang-bang* control as it is a control *affine* system. This means that the optimal control solution is to provide a maximum acceleration towards the target state, and at some critical state provide a maximum opposite acceleration which will bring the system precisely at the target state. This critical curve, or optimal control curve, in the state-space of the double integrator system can be derived by integration of the system equations and equating the states to the desired (end state) values:

$$\ddot{x} = u \tag{22}$$

$$\dot{x} = \dot{x}(0) + ut \tag{23}$$

$$x = x(0) + \dot{x}(0)t + \frac{1}{2}ut^2 \tag{24}$$

With x the system state and u the input. Setting the position and velocity state to zero, as desired, $\dot{x} = x = 0$ results into the following *optimal control curve*:

$$\dot{x}(0) = \pm\sqrt{2 \cdot u \cdot x(0)} \tag{25}$$

For the longitudinal quadcopter system x and $\dot{x}$ are the pitch angle and rate respectively. The input u amounts to the change in pitch rate over time which is equal to:

$$\dot{q} = \frac{M_y}{I_{yy}} \tag{26}$$

Since the M_y models, as found in Chapter IV, for the various quadcopter battery configurations have a bias as a result of the center of gravity offset with the rotor plane center, the maximum reachable pitch up and pitch down moment are not equal. Consequently, the optimal control curve for the quadcopter models are asymmetrical. A graphical representation of these curves for each quadcopter configuration are shown in Fig. 13. Indeed, for the battery aft position, for example, a higher pitch up moment can be generated.

Consequently, when this model has a positive pitch angle with a pitch rate which is above the optimal control curve, it can generate a negative pitch rate until the optimal control curve has been reached after which a pitch up moment is generated. The aft configuration can extend its negative pitch rate to larger critical rates than the battery forward position as a result of the larger obtainable pitch up moment due to the bias. And vice versa for the battery forward position, which can generate a larger pitch down moment.

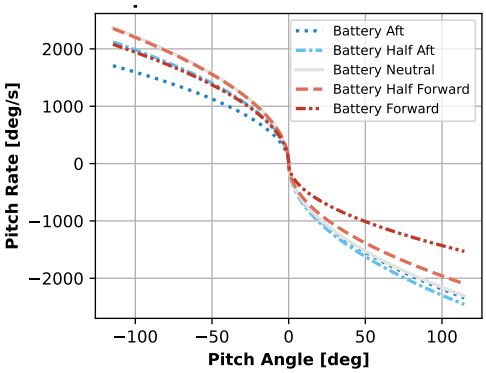

Fig. 13. The optimal control curves which are used to determine the *bang-bang* input to return to zero pitch angle and rate in minimum-time. When the quadcopter has a negative pitch angle and is below the optimal control curve, a pitch up moment input is commanded, if it is at, or above the curve, a pitch down moment input is commanded (note in the latter case the quadcopter will overshoot the target state). A similar but opposite input sequence applies for positive pitch angles. The curves are generated with U_q = 3800 eRPM.

The above derivation applies to a system that assumes that an instantaneous change in rotational rate can be applied: that is in the case without actuator dynamics. When including the actuator dynamics, modelled as a first order lag, the system equations are:

$$\ddot{x} = \begin{cases} \ddot{x_1} \\ \ddot{x_2} \end{cases} = \begin{cases} u_0 + (u - u_0) \cdot (1 - e^{-\frac{t}{\tau}}) & \text{if } t \leq t_s \\ \ddot{x_1}(t_s) \cdot (e^{-\frac{(t-t_s)}{\tau}}) & \text{if } t > t_s \end{cases} \tag{27}$$

$$\dot{x} = \begin{cases} \dot{x_1} \\ \dot{x_2} \end{cases} = \begin{cases} \dot{x_0} + \int_0^t \ddot{x_1}(t)\,dt & \text{if } t \leq t_s \\ \dot{x_1}(t_s) + \int_{t_s}^t \ddot{x_2}(t)\,dt & \text{if } t > t_s \end{cases} \tag{28}$$

$$x = \begin{cases} x_1 \\ x_2 \end{cases} = \begin{cases} x_0 + \int_0^t \dot{x_1}(t)\,dt & \text{if } t \leq t_s \\ x_1(t_s) + \int_{t_s}^t \dot{x_2}(t)\,dt & \text{if } t > t_s \end{cases} \tag{29}$$

With u_0 the initial rotational acceleration and τ the time constant of the actuator dynamics. Note that if τ = 0, Eq. 27 reduces to the case without actuator dynamics.

The dynamics of the rotational acceleration have been split into two phases separated by a switch-off time t_s. The first phase (t $\leq t_s$) accounts for the dynamics of a rotational acceleration input of a quadcopter including actuator dynamics. The second phase (t $> t_s$) accounts for the dynamics after which the rotor speeds are commanded to the hover speeds to ensure no rotational acceleration is present at the target state.

The same derivation of the optimal control curve applies as previously shown for the system without actuator dynamics by setting $\dot{x_2} = x_2 = 0$ in the limit of $t \to \infty$ and solving for $\dot{x_0}$ and x_0.

Without actuator dynamics these optimal control curves are only dependent on the maximum possible rotational acceleration (or maximum moment) that can be generated by the system. However, when introducing actuator dynamics, the optimal control curves are also a function of u_0, τ and t_s. Consequently, instead of optimal control curves, an *optimal control surface* is obtained. Determining the optimum *bang-bang* control to the system depends on the position of the system in state-space with respect to this surface. A visualization of this optimal control surface for the battery neutral configuration can be found in Fig. 14. A graphical illustration of the minimum-time optimal control routine based on the optimal control surface can be found in Fig. 7.

In case the quadcopter has a negative pitch angle and is below the surface, the optimal control routine commands a pitch up moment, if it is above the surface it commands a pitch down moment. Vice versa for the case of a positive pitch angle. Once the system intersects the surface it will command a pitch down moment in the negative angle case and a pitch up moment for the positive angle case. Furthermore, the routine stores the corresponding t_s used to determine the time at which the rotors are set to hover speed. After implementation in simulation, the resulting optimal control routine also works without using the t_s. This is because after t_s, the system enters the second phase (see Eq. 27) in which the optimal control surface is independent of u_0. The optimal control surface reduces to an optimal control curve along the pitch angle and rate plane. The optimal *bang-bang* control results in a sliding-mode controller which makes the system oscillate along this optimal control curve. See Fig. 15 and Fig. 16 for a trajectory example. Note that the average time constant of all four motors is used for τ.

The derived optimal *bang-bang* control solution will always bring the system back to hover condition, however since the quadcopter is able to fully rotate ±360 degrees and because the optimal control strategy depends on the sign of the pitch angle, the found solution is not always the optimal solution. This is because the pitch angle loops around an arbitrary range in simulation. In this work the pitch angle loops between [-180, +180] degrees and is kept fixed. For future reference it is recommended to loop the pitch angle range for an integer amount of variations and select the control trajectory with the smallest return time.

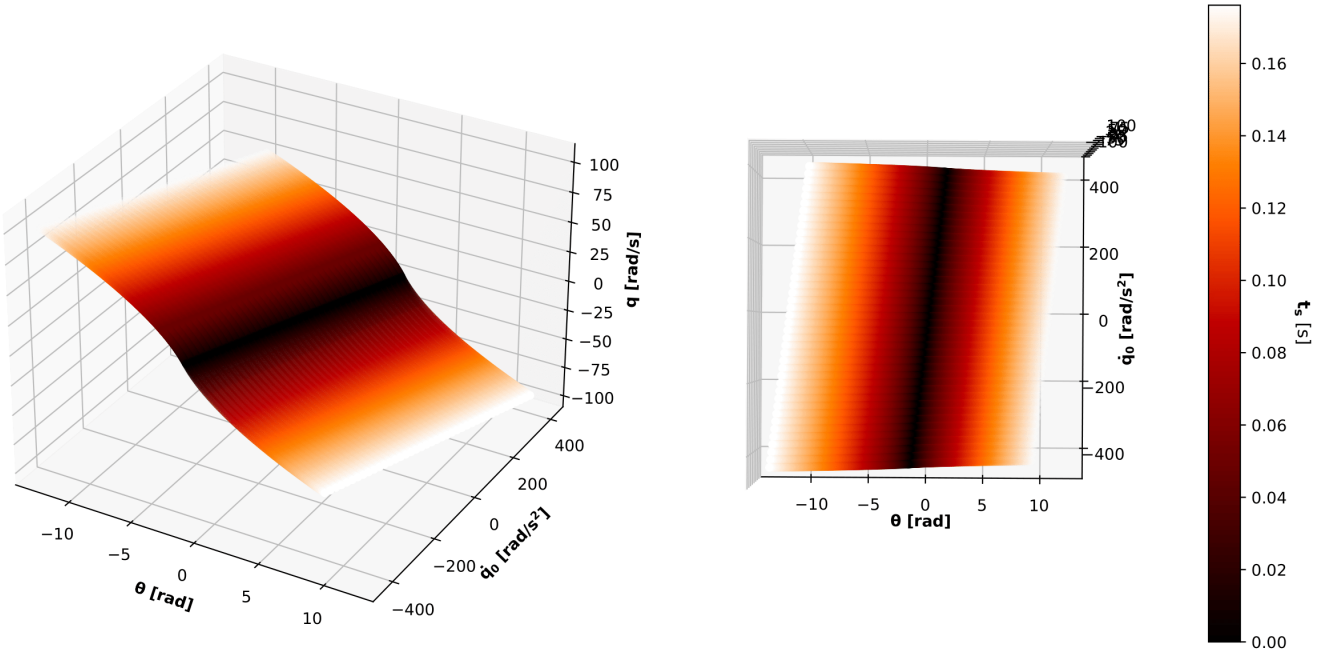

Fig. 14. The *optimal control surface* of the battery neutral configuration used to determine the *bang-bang* input based on the position of the system in state-space with respect to this surface. Due to the actuator dynamics, the optimal control curves are not only dependent on the maximum moment that can be applied to the system, but also on its initial rotational acceleration $u_0 = \dot{q}_0$, τ and t_s, extending the optimal control curve to an optimal control surface. The surface is generated with U_q = 3800 eRPM.

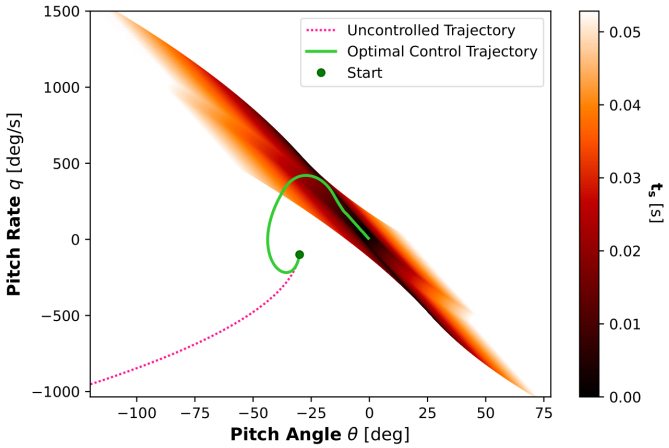

Fig. 15. An example of the optimal control trajectory for a quadcopter with an end state of θ = -30 deg, q = -100 deg, and M_{y_0}= -0.21 Nm. The battery forward configuration model is used. The optimal control routine returns the quadcopter back to hover while the uncontrolled case results in a trajectory with increasing rotational rates. See Fig. 16 for more details on the states over time.

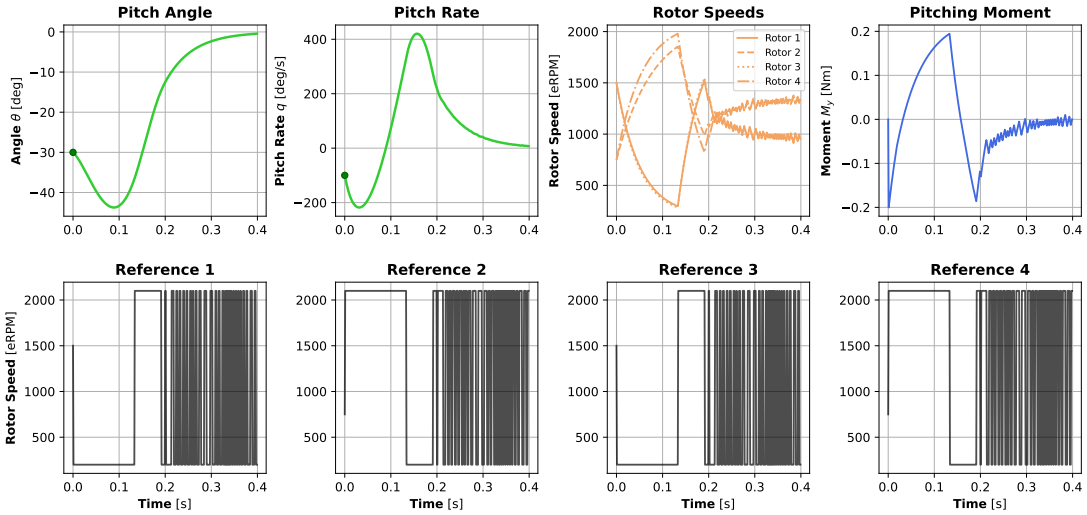

Fig. 16. An example of the optimal control trajectory for a quadcopter with an end state of θ = -30 deg, q = -100 deg, and M_{y_0}= -0.21 Nm. The battery forward configuration model is used. Note the sliding mode control behaviour near the end of the trajectory which results in rotor speeds approximating the hover speeds, resulting in a zero pitching moment.

VII. Verification of the Monte-Carlo Simulation and Optimal Control Method

Before diving into the results on the quadcopter reachable sets, first the methods for estimating the sets are verified. Readers who are primarily interested in the quadcopter reachability results are advised to continue to Chapter VIII.

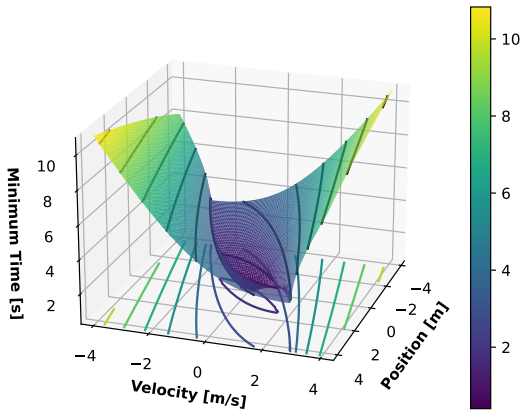

Fig. 17. Analytical forward reachable sets of the double integrator system. The color bar indicates the reachable set time-window.

Both the Monte-Carlo (MC) simulation method, for estimating the forward reachable set (FRS), and the minimum-time optimal control routine as described in Chapter VI, used to estimate the return time for backward reachable set (BRS) estimation, are verified with the analytically obtainable reachable sets of the double integrator system. The double integrator system, often modelled as a cart on a rail system, has the following equation of motion in state-space form:

$$\begin{bmatrix} \dot{x_1} \\ \dot{x_2} \end{bmatrix} = \begin{bmatrix} 0 & 1 \\ 0 & 0 \end{bmatrix} \boldsymbol{x} + \begin{bmatrix} 0 \\ 1 \end{bmatrix} u \tag{30}$$

With x_1 the position, x_2 the velocity of the system and u the input, defined as the force acting on the system divided by the mass of the system. The positive force direction is defined into the positive direction of the states. The double integrator system has an analytical solution for its reachable sets, as first derived by Althans et. al [32]. Given that the origin is the target or the initial set, the forward reachable set solution can be defined as:

$$\phi(\vec{x}) = \begin{cases} -x_2 + \sqrt{4x_1 + 2x_2^2} & \text{if } x_1 > \frac{1}{2} x_2 \left| x_2 \right| \\ x_2 + \sqrt{-4x_1 + 2x_2^2} & \text{if } x_1 < \frac{1}{2} x_2 \left| x_2 \right| \\ \left| x_2 \right| & \text{if } x_1 = \frac{1}{2} x_2 \left| x_2 \right| \end{cases} \tag{31}$$

And the backward reachable set can be defined as:

$$\phi(\vec{x}) = \begin{cases} x_2 + \sqrt{4x_1 + 2x_2^2} & \text{if } x_1 > \frac{1}{2} x_2 \left| x_2 \right| \\ -x_2 + \sqrt{-4x_1 + 2x_2^2} & \text{if } x_1 < \frac{1}{2} x_2 \left| x_2 \right| \\ \left| x_2 \right| & \text{if } x_1 = -\frac{1}{2} x_2 \left| x_2 \right| \end{cases} \tag{32}$$

Note that both curves have a local discontinuity defined by the switch curves. The reachable set at any given time t can be found by solving for $\phi = t$. A visualization of the forward reachable set curve can be found in Fig. 17 with reachable sets at various times projected as contours onto the position-velocity plane.

Verification is performed on both the FRS in Section VII-A and the BRS in Section VII-C. Furthermore, a brief verification

analysis is done on the well-established *Level-Set Toolbox* in Section VII-B in order to benchmark the performance of the MC simulation with the performance of the toolbox.

A. Verification of the Forward Reachable Set Estimation

For the verification of the FRS estimates from the MC simulation, the MC simulation settings are optimized for the double integrator system. The same optimization procedure has been applied as described in Section V-B. However, since the analytical sets are available, the MC optimization has been performed with respect to these true sets by optimizing for the minimum *Hausdorff distance*. The *Hausdorff distance* is a metric used to quantify how close sets are with respect to one another in terms of a (non-euclidean) distance. When two sets are equal, the *Hausdorff distance* is zero. The found optimum MC settings for the double integrator system (at T = 2 s) are p_c = 0.1 and N_{switch} = 100%.

The performance of the reachable set estimation of the MC simulation for various time-windows is measured by analyzing the *Hausdorff distance* and the area *error percentage* for various amount of simulation trajectories. The area *error percentage* is defined as the percentage of the difference between the union and the intersection of the estimated and the true set, with the true set. Since the *Hausdorff distance* grows with increasing set size over time, the metric is normalized with the area of the analytical set per time-window. The results are summarized in Fig. 20. It can be observed that for t = 1 s the variance among the realizations is negligibly low indicating a converged set estimation for the given time-window. For increasing time-windows the variance of the estimated sets increases, while increasing the number of trajectories decreases the variance as expected. Hence, the variance of the metrics can be used to determine whether the MC simulation estimates have converged for a given time-window and number of trajectories. Convergence seems to have occurred for N_{traj} = 2000 and N_{traj} = 4000 up until t = 2.5 seconds. Increasing the amount of trajectories does not increase the performance of the set estimate for the analyzed time-windows. The area *error percentage* converges in these converged cases towards the numerical inaccuracies as a result of numerical integration. Decreasing the simulation integration step size by an order of magnitude results in lowering the total area *error percentage* with about an order of magnitude, as displayed in Fig. 19. For the double integrator system the MC simulation shows a worst case average area *error percentage* of about 3.84% for a time-window between 1 and 2.5 seconds and N_{traj} = 500. For visualization purposes the estimated and the true sets are plotted in Fig. 21 for one simulation realization per time-window with N_{traj} = 500. A visualization with the MC simulation end states can be found in Fig. 18.

From this verification analysis it can be concluded that the (system specific) optimized MC simulation approximates the true forward reachable set with high accuracy, as demonstrated for the double integrator system. Increasing the number of trajectories results in an improved estimation of the true set. However, this is only valid up until a certain number

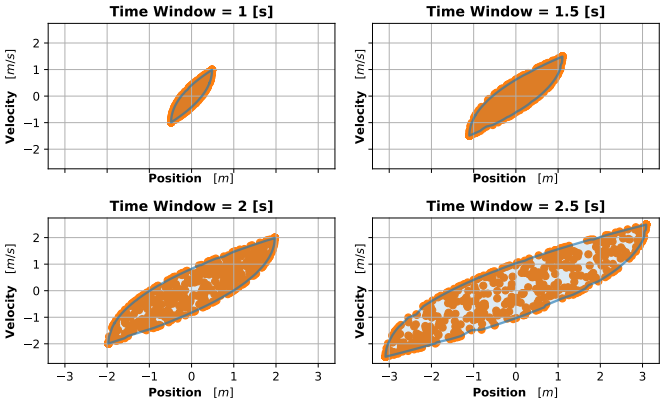

Fig. 18. Example of the reachable set estimates for various time-windows including the simulation end-states and reachable set boundary estimates for N_{traj} = 500 and dt = 0.01.

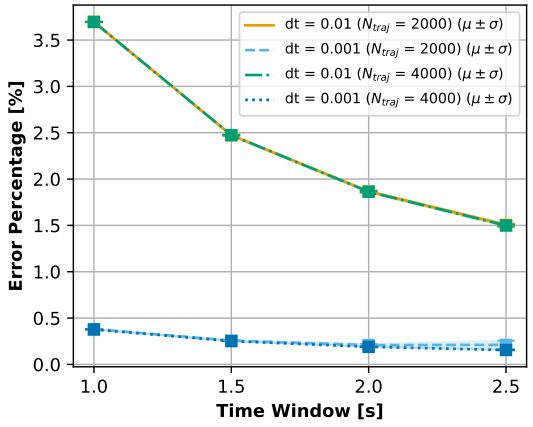

Fig. 19. Increasing the amount of trajectories does not reduce the reachable set area error after some number of trajectories. The error has converged to the errors due to numerical inaccuracies in the simulation. The accuracy of the converged sets can be improved by decreasing the numerical integration time-step. The simulation results are of reachable sets of 10 realizations.

of trajectories after which no improvement can be observed and the error converges towards the errors due to numerical inaccuracies. The accuracy of the converged sets can be improved by decreasing the numerical integration time-step.

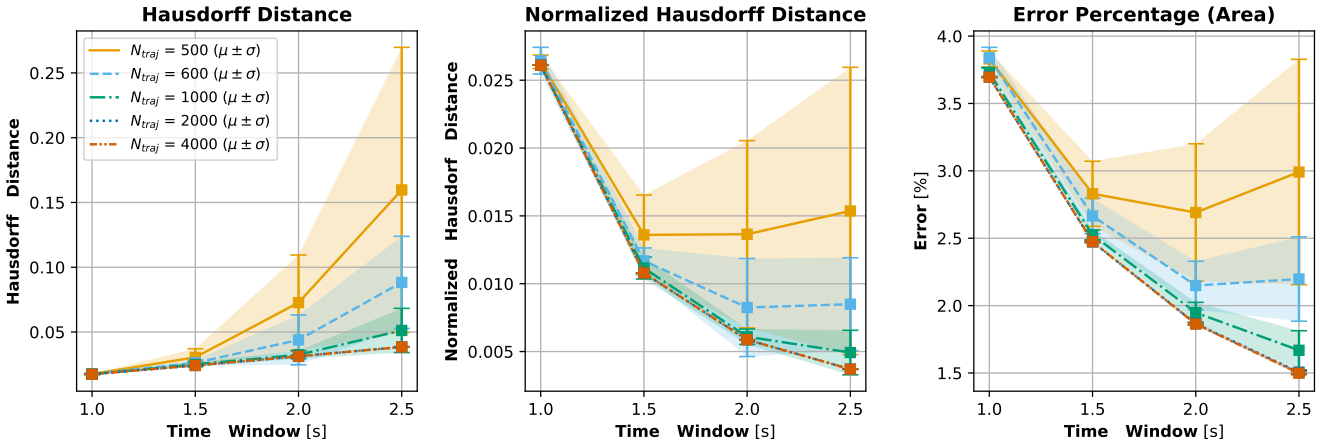

Fig. 20. The performance of the optimized MC simulation for various time-windows and number of trajectories of the double integrator system. The performance metrics include the (normalized) *Hausdorff distance* and the area *error percentage* with respect to the analytical (true) sets. The normalized *Hausdorff distance* is normalized with the area of the analytical set per time-window. As expected, the more simulated trajectories are included, the more the reachable set estimates converge to the true set. Note that for more than 1000 trajectories no noticeable performance increase is visible. The data shown are for N = 10 and dt = 0.01 s.

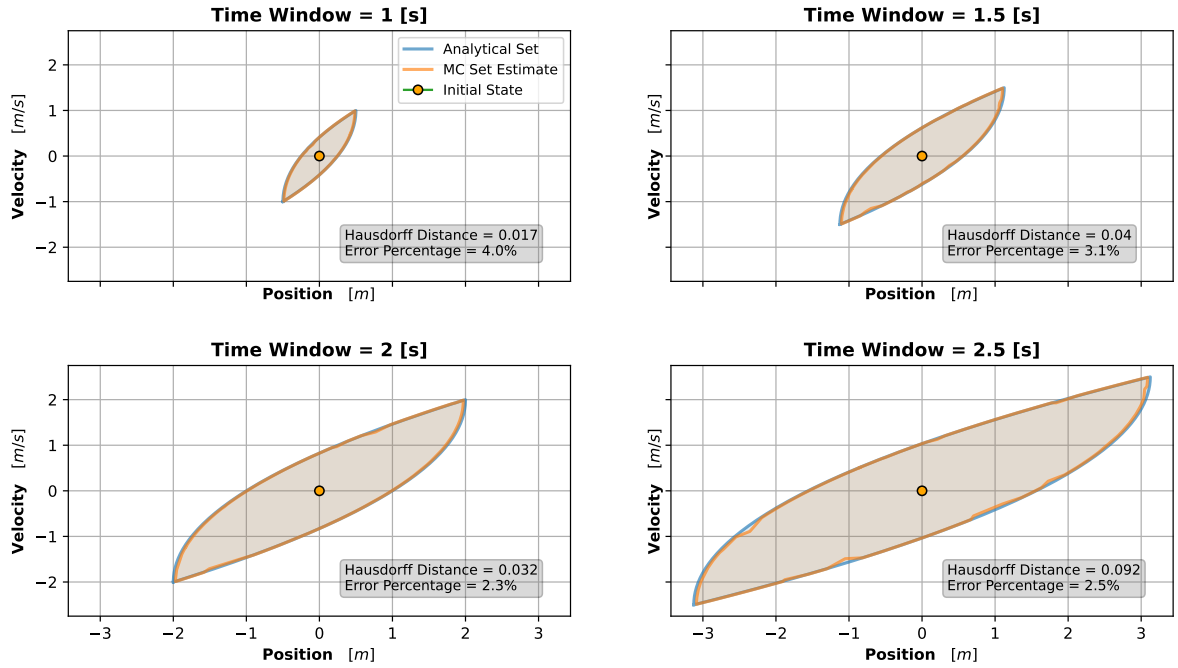

Fig. 21. Example of one realization of a MC reachable set estimate for various time-windows with the analytical sets. The worst performing estimating setting of N_{traj} = 500 is plotted, which already shows almost no differences with the analytical set. Time-step used is dt = 0.01 s.

B. Verification of the Level-Set Toolbox (benchmark)

The *Level-Set Toolbox* [27] is a numerical solver for the Hamilton-Jacobi partial differential equation to find the reachable set using optimal control. In order to benchmark the results of the MC simulation approach for reachable set estimates, the toolbox is also verified with the analytical set of the double integrator. Various numerical accuracy options are available. The accuracy VERY HIGH has been used, which uses a third-order scheme which averages three steps forward in time. For the spatial scheme a fifth order accurate weighted "Hamilton-Jacobi Essentially Non-oscillatory" scheme is used. The results of the reachable set estimates from the toolbox for various time-windows together with the analytical sets can be found in Fig. 22. The accuracy of the results from the toolbox is dependent on the the grid size that is used. The toolbox provides underestimated reachable sets, despite the fact that the toolbox uses a set of initial states, instead of the origin as used in the derivation for the analytical sets. The underestimation primarily occurs near the edges of the envelope. This can be explained by the switch curves in the analytical solution as seen in Eq. 31 and Eq. 32. The switch curve defines the critical condition in state-space at which the system control strategy switches its direction (i.e. application of a force into the opposite direction). Since the toolbox uses a grid, the extend to which the location of this switch curve can be identified depends on the accuracy of the grid. A coarse grid will result into wrong estimations of the spatial gradient resulting into an incorrect optimal control strategy. Since the switch curve occurs near the upper and lower edges, the toolbox provides poor set estimations at these locations [33]. For N_{grid} = 800 the estimation approaches the performance of the worst MC simulation estimate with 500 trajectories, however the estimates perform worse for $t > 1$ second. Besides the poor performance, additionally the computation time required for the toolbox to obtain a similar set is in the order of tens of minutes for t = 1 with N_{grid} = 600, and around an hour for t = 2.5 with N_{grid} = 800, while the MC simulation only requires a computation time in the order of a few seconds on the same machine. From the analysis it can be concluded that the MC simulation exceeds the performance of the *Level-Set Toolbox* in both accuracy as well as computation time[2].

C. Verification of the Optimal Control Routine for Backward Reachable Set Estimation

The backward reachable set of the double integrator system includes all the states from which the system can return to the origin within an arbitrary time-window. The solution to the optimal control for minimum-time to reach the origin has been derived in Section V-B to be *bang-bang* control. In order to verify whether the minimum-time optimal control routine has been implemented correctly, the obtained set is compared to the boundaries of the analytical backward reachable set of the double integrator. Note that since the optimal control input is determined relative to curves in state-space (the optimal control curves), the numerical resolution of the simulation has an influence on the accuracy of the estimated backward reachable set.

For the verification analysis a grid in the state-space is generated. For each grid point the optimal control strategy is applied to return the system to the origin. The time it takes for the system to reach the origin, within one time-step dt size for both the position and velocity state, is documented. It should be noted that the critical curve contains a margin, $velocity \pm n \cdot dt$, to account for limited floating point precision. The analysis shows that both the margin size n, as well as the simulation integration time-step dt influence the estimation performance. A summary of the results of various simulation conditions can be found in Table X. The optimal margin resulting in the lowest amount of incorrectly predicted return times is $\pm 2 \cdot dt$. An illustration of the results with this margin and $\Delta_{grid} = 0.1$ can be found in Fig. 23.

To explore the distribution of the errors, the erroneous time estimates from all simulations with the settings in Table X are plotted together in Fig. 24. The distribution of the errors are mostly centered around the upper and lower corners. This underestimation near the corners also occurred for the set estimates from the *Level-Set Toolbox* in which the inaccuracies near the corners emerged from the inability to estimate a discontinuity on a grid. The same approach is used in the optimal control routine resulting in similar incorrect set estimates. The top corner of the BRS estimate from the toolbox with $N_{grid} = 800$ together with the optimal control estimates has been highlighted in Fig. 25. Although the optimal control estimate results in errors near the corners, the resulting expected underestimation of the optimal control routine with the true set is less compared to the underestimation of the *Level-Set Toolbox* estimate. Furthermore, as noticed in the analysis of the forward reachable set verification, the optimal control routine has a much lower computational time required compared to *Level-Set Toolbox* for obtaining BRS estimates with similar accuracy.

TABLE X
THE TOTAL AMOUNT OF INCORRECTLY PREDICTED BACKWARD REACHABLE STATES, ALSO AS A PERCENTAGE OF THE TOTAL AMOUNT OF PREDICTED STATES WITHIN ALL ANALYTICAL SETS OF T = 1, 1.5, 2, 2.5 S.

	$\Delta_{\mathbf{grid}}$ **= 0.1**			
Margin	$\pm 1 \cdot dt$	$\pm 2 \cdot dt$	$\pm 3 \cdot dt$	$\pm 4 \cdot dt$
dt = 0.01	290 (9.97%)	52 (1.79%)	84 (2.89%)	174 (5.98%)
dt = 0.001	86 (2.96%)	10 (0.34%)	28 (0.96%)	44 (1.51%)
	$\Delta_{\mathbf{grid}}$ **= 0.05**			
Margin	$\pm 1 \cdot dt$	$\pm 2 \cdot dt$	$\pm 3 \cdot dt$	$\pm 4 \cdot dt$
dt = 0.01	1074 (9.41%)	144 (1.26%)	246 (2.15%)	642 (5.61%)
dt = 0.001	378 (3.31%)	38 (0.33%)	38 (0.33%)	98 (0.86%)

[2]A thorough time complexity analysis on both the toolbox and the MC simulation has not been performed and is recommended.

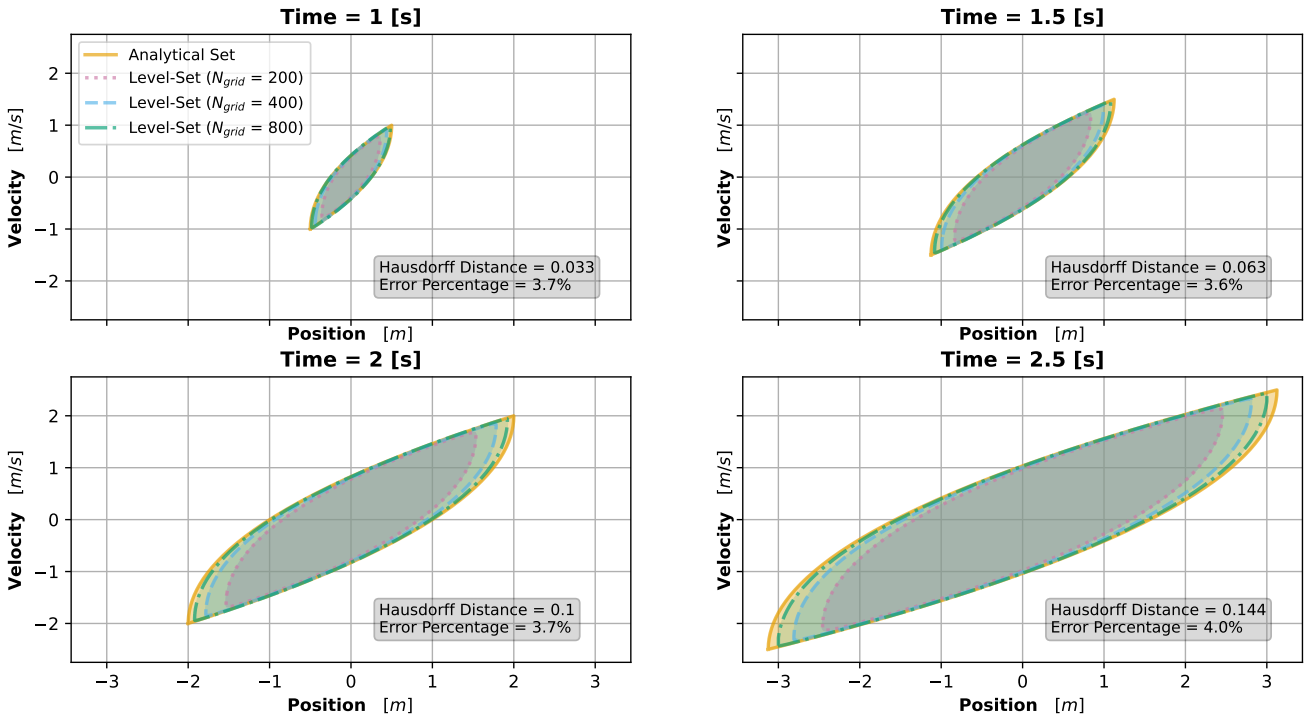

Fig. 22. The reachable set results from the *Level-Set Toolbox* with the analytical sets for various time-windows. The toolbox provides underestimated sets which improves with increased grid resolution. Results are from a simulation with a time-step of dt = 0.01 seconds and a grid ranging from [-3, 3] in both position and velocity direction. The initial set is contained within a circle of radius 0.01 around the origin. The *Hausdorff distances* and *error percentages* displayed in the plots are for the toolbox results with N_{grid} = 800.

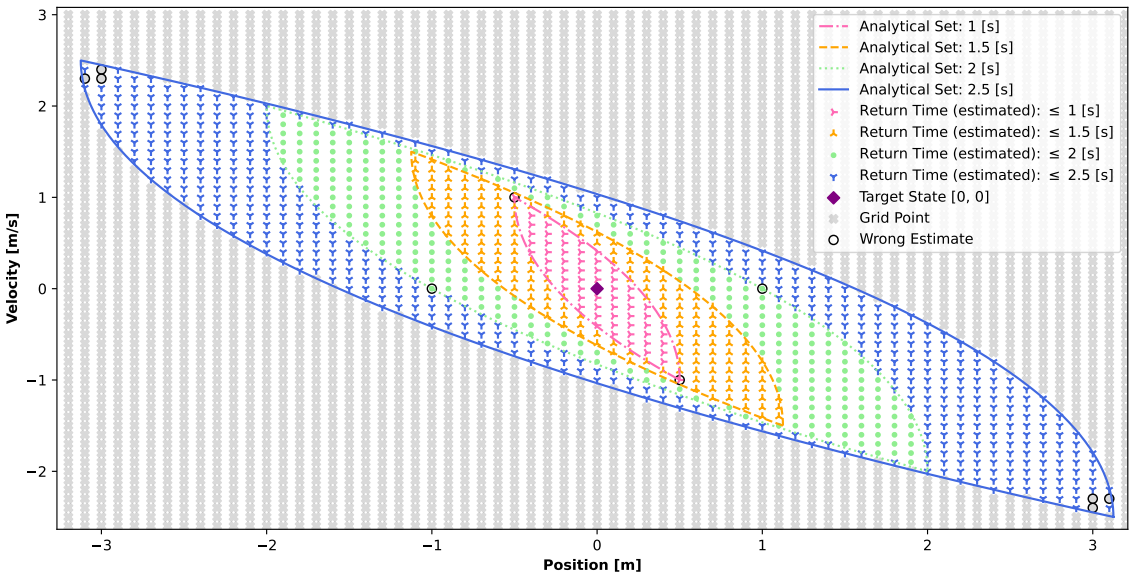

Fig. 23. Illustration of the backward reachable set estimation from the optimal control routine performed on states on a grid with step size [0.1, 0.1] in both directions. The estimations are with a margin of $2 \cdot dt$ and step size of dt = 0.001 s.

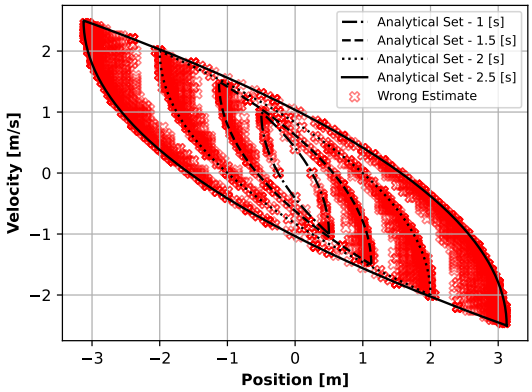

Fig. 24. A plot of all the states for which an incorrect BRS time estimate was predicted from the simulations as summarized in Table X. A total of 3426 invalid estimates, out of 114,730 predicted grid points within the analytical sets, are shown. Note that most errors are distributed around the corners of the reachable sets.

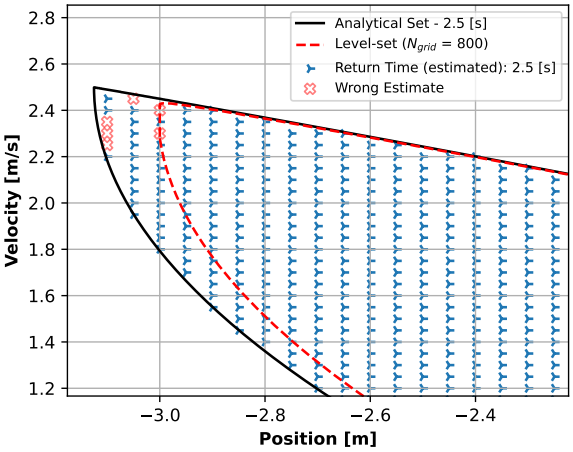

Fig. 25. The (incorrect) BRS estimates from the optimal control routine (with margin of $2 \cdot dt$, dt = 0.001 s and Δ_{grid} = 0.05), together with the estimated reachable set from the *Level-Set Toolbox* (with N_{grid} = 800 and dt = 0.01 s) and the analytical set. Although the optimal control estimate results in errors near the corners, the resulting expected underestimation of the optimal control routine with the true set is less compared to the underestimation of the *Level-Set Toolbox* estimate.

To conclude, the verification shows that the minimum-time optimal control routine for BRS estimation, with an optimal control curve margin of $\pm 2 \cdot dt$ and a time-step of dt = 0.001, results in BRS estimates with more than 99.5% accuracy for the time-windows analyzed. The errors occur near the upper- and lower corners which could result in a slight underestimated backward reachable set which increases with increasing time-windows as can be observed in Fig. 24. The resulting underestimation of the estimated set is expected to be smaller than the underestimated backward reachable sets from the *Level-Set Toolbox*.

VIII. Results

In this chapter the results on the quadcopter forward reachable sets (FRS) and backward reachable sets (BRS) are presented which are analyzed separately in Section VIII-A and Section VIII-B. The effects of varying the center of gravity position, varying the trajectory time-windows and the influence of actuator dynamics on the reachable sets are explored. The simulation settings, from which the sets are obtained, are identical to the settings as used during the Monte-Carlo (MC) optimization routine, summarized in Table VIII. Furthermore, the found optimized MC parameters are used as summarized in Table IX.

A. Results on the Forward Reachable Set

The forward reachable set contains all the states that the quadcopter can reach within a certain time-window. The FRS is estimated by simulating (random) trajectories with the optimized MC simulation settings, storing the end states and fitting a convex hull to the data. The resulting set is dependent on the system dynamics, and will grow as the time-window increases. The effect of the center of gravity position, varying time-windows and the effect of actuator dynamics on the FRS are explored individually.

1) The Effect of Battery Position: To observe the effect of varying the center of gravity position on the reachable set, the FRS estimation routine has been applied on all quadcopter configurations for a fixed time-window of T = 0.1 s. The estimated reachable sets can be found in Fig. 26 and Fig. 27. Information on the properties of the reachable sets per configuration for relative comparison is summarized in Table XI.

The following observations can be made:

- *The larger the displacement of the center of gravity from the rotor plane center, the smaller the reachable set area.* Compared to the battery neutral position the aft battery position has a set area which is about 45% smaller, while the battery forward configuration has a reachable set area which is reduced by about 65%. The reduction is due to the increased moment of intertia as a result of the battery displacement. The increase in inertia is largest for the forward configuration, resulting in the largest decrease in reachable set area.
- *The location of the centroid of the reachable set is a function of the center of gravity position.* The centroid of the reachable set moves into the rotation direction of the pitching moment bias. This is the result of the center of gravity offset with the rotor plane center resulting in a bias offset in the pitching moment. The battery neutral configuration has the smallest absolute pitching moment bias, which results into a set with a centroid closest towards the origin. The battery aft configuration has a centroid shifted into the positive rotation direction (due to the positive bias) and the battery forward configuration towards the negative pitching direction (negative bias).

- *The neutral battery position acquires the largest reachable set area.* Furthermore, it reaches the largest minimum pitch angle and rate compared to the other configurations. Although the displaced battery positions from the neutral position result in a larger bias in the pitching moment, the increased moment of inertia restraints the obtainable pitch rates within the fixed time-window.
- *The half aft configuration obtains the largest maximum pitch angle and rate.* An exception to above observation is the battery half aft configuration, which exceeds the maximum pitch angle and rate for all configurations. This can be explained by the fact that this configuration has the smallest increase in moment of inertia, while at the same time it has a larger bias towards the positive pitch direction than the neutral configuration. This combination results in obtaining a larger pitch up angle and rate compared to the other configurations. Vice versa applies to the half forward configuration, however this configuration has a larger moment of inertia increase than the half aft position (compared to the neutral), resulting in a slightly lower minimum reachable pitch angle and rate than the neutral configuration.
- *The forward battery position has a smaller reachable set compared to the aft set.* This is the direct result from a larger center of gravity displacement for the forward battery configuration than the aft configuration. Consequently, the quadcopter has a larger moment of inertia, which reduces the change in rotational rate over time, which shrinks the reachable set, despite the larger bias in the pitching moment.

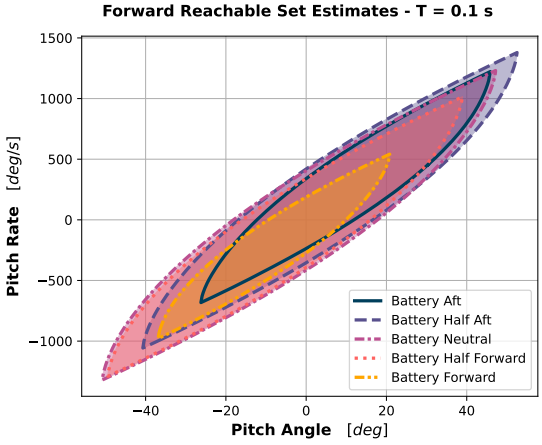

Fig. 26. Forward reachable set estimates for each battery configuration for a time-window of T = 0.1 s. The overlay of the sets highlight the dissimilarities between the battery configuration reachable set estimates.

2) The Effect of Time: When increasing the time-window, the reachable set naturally grows. To quantify the effect on the reachable set as a function of time, the forward sets are estimated for T = 0.05, 0.1, 0.15 and 0.2 s for all quadcopter configurations. The results of the sets can be found in Fig. 28 and Fig. 29. The effect of the time-window on the area, the minimum and maximum pitch angles and rates are quantified by computing the percentage difference with respect to the set obtained at T = 0.1 s. The percentages per time-window and configuration can be found in Fig. 30.

The following observations can be made:

- *The reachable set expands as a function of time.* The area of the set grows with increasing time-window. Due to the double integrator like dynamics, the maximum and minimum pitch angle and pitch rate obtained from the reachable set increases quadratically and linearly with respect to time.
- *The expansion of the reachable set per unit of time is dependent on the system dynamics.* The area increases more for the battery aft and forward position, with less than 1% more compared to the neutral and half positions at T = 0.05 s, about 15% more at T = 0.15 s, and 50% more at T = 0.2 s. The minimum pitch angle and rates expand more for the battery forward position, with less than 1% more at T = 0.05 s, about 5% and 3% more at T = 0.15 s, and 15% and 5% at T = 0.2 s. A larger expansion is observed in maximum angle and rate for the battery aft configuration, about 5% more at T = 0.15 s, 15% and 6% more at T = 0.2 s.
- *The quadcopter system is a very fast system.* When considering the battery neutral configuration, it can be observed that at T = 0.1 s a maximum pitch angle of 47 degree with a pitch rate of 1230 deg/s can be obtained. If this time-window is only increased by a fraction of a second, to T = 0.2 s, the pitch angle reached is almost 6 times larger, 275 degree, and the pitch rate is almost 3 times larger, 3357 degree/s.
- *The reachable set expands in time in a similar fashion as a double integrator system.* The similarities are observed in the the verification part of this work in Chapter VII. This is because the pitch angle and pitch rate dynamics of a quadcopter essentially are a double integrator system and hence the set is similar to the reachable sets of this system.

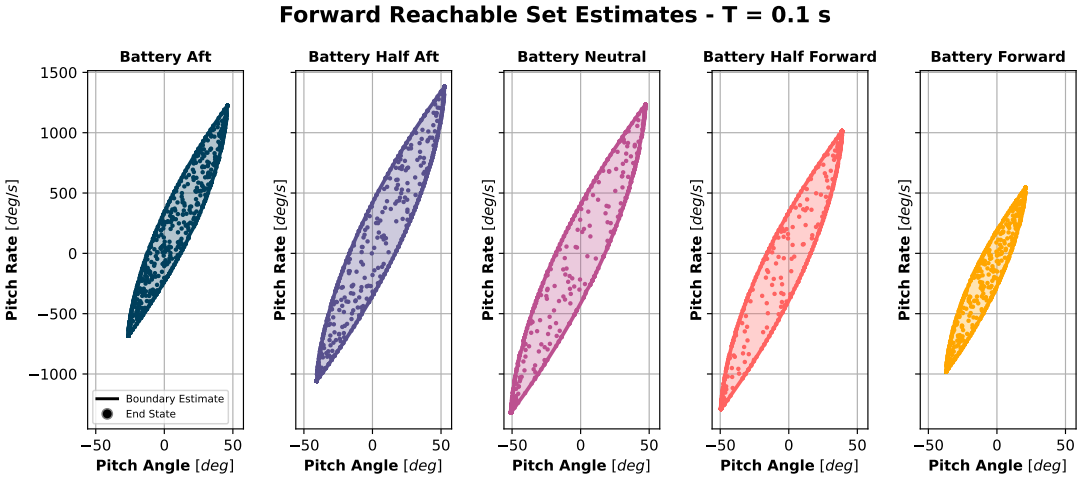

Fig. 27. Forward reachable set estimates for each configuration including the simulation end states and the boundary estimates for a time-window of T = 0.1 s. Note the evident area size variations and centroid offsets among the battery configurations.

TABLE XI
PERFORMANCE COMPARISON OF THE FRS FOR THE VARIOUS BATTERY CONFIGURATIONS.

Battery Position	**Area** $[deg^2/s]$		**Min.** θ [deg]		**Max.** θ [deg]		**Min.** q [deg/s]		**Max.** q [deg/s]		**Centroid** [θ, **q**]	
Aft	10.31	-45.29%	-26.22	+48.34%	45.87	-2.79%	-682.34	+48.31%	1222.54	-0.69%	10.39	273.07
Half Aft	17.10	-9.25%	-40.69	+19.83%	52.55	+11.35%	-1057.10	+19.92%	1379.57	+12.06%	6.22	162.97
Neutral	18.85	0%	-50.75	0%	47.19	0%	-1320.00	0%	1231.08	0%	-1.92	-45.23
Half Forward	15.32	-18.70%	-49.41	+2.66%	38.88	-17.61%	-1290.12	+2.26%	1013.84	-17.65%	-5.43	-139.17
Forward	6.58	-65.07%	-36.89	+27.32%	20.82	-55.88%	-978.84	+25.85%	541.60	-56.01%	-8.32	-219.86

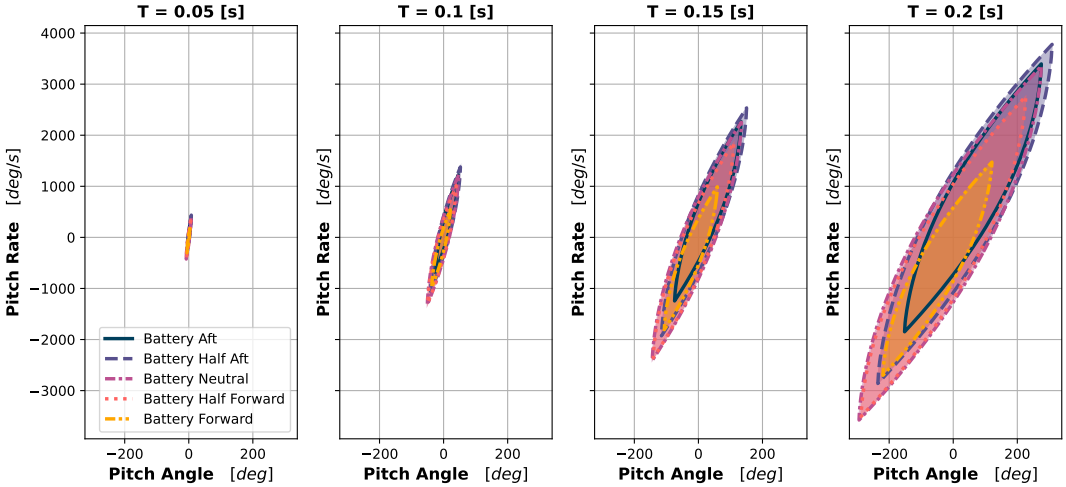

Fig. 28. The FRS as a function of time for all battery configurations plotted together.

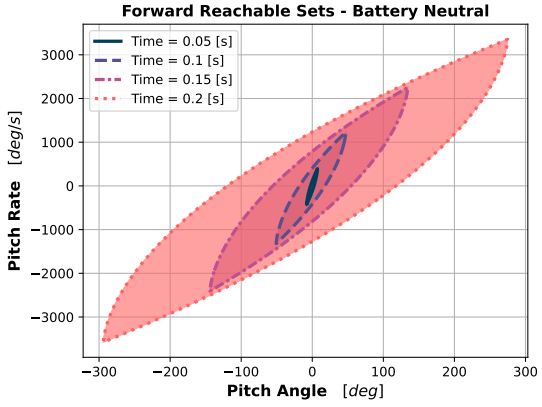

Fig. 29. The FRS as a function of time for the battery neutral configuration. Note the similarities between the reachable sets of the double integrator system as discussed in Chapter VII.

3) The Effect of Actuator Dynamics: The reachable set is a function of the dynamics of the quadcopter model, hence including or excluding the actuator dynamics in the modelling has an effect on the reachable set. To explore the effects of the actuator dynamics, the forward reachable sets are estimated for each configuration with and without actuator dynamics modelling for a fixed time-window of T = 0.1 s. The results of the reachable sets per configuration can be found in Fig. 31. Numerical information of the properties of the reachable sets, including the percentage difference with respect to the set without actuator dynamics, is summarized in Table XII. The following observations can be made:

- *The reachable set area reduces substantially when including actuator dynamics.* The area of the set with actuator dynamics reduces about 85% in size compared to the set without actuator dynamics.
- *Maximum and minimum pitch angle and pitch rate reduces substantially with actuator dynamics included.* The minimum and maximum pitch angle and rate are reduced by about 60% and 47% respectively.
- *The effect of the actuator dynamics on the set is independent of the battery configuration.* The extend to which the actuator dynamics affect the reachable sets is mostly the same for each quadcopter configuration (about $\pm$1%-2% difference).

B. Results on the Backward Reachable Set

The backward reachable set is obtained from the forward reachable set directly by applying the optimal control routine as described in Chapter VI. The optimal control routine is applied on every FRS end state, and the amount of time required to return to the safe state is stored. A quadcopter is considered to be at the safe state (hover condition) in the case -5 deg $< \theta <$ 5 deg and -1 deg/s $< q <$ 1 deg/s. As a result, for every end state in the FRS, the amount of time is found which describes how much time it takes to return to the safe state, on top of the time required to reach the end state. In this work the distribution of return times on the FRS is referred to as the BRS. The effect of the center of gravity position, varying time-windows and the effect of actuator dynamics on the backward reachable sets are explored individually.

1) The Effect of Battery Position: To observe the effects of the center of gravity position, the optimal control routine has been applied on the forward reachable set of each battery configuration, with a fixed time-window of T = 0.1 s. In Fig. 32 the results can be found, with the time to return to the safe state specified in color. The following observation can be made:

- *The distribution of the return time over the entire FRS set is a function of battery position.* For the battery neutral position this distribution seems almost symmetric, while for the extreme battery positions larger return times are found near one of the edges of the FRS. This can be explained by the pitching moment bias as a result of the center of gravity offset with the rotor plane center, due to which higher pitching moments are reached into the direction of this bias. Moreover, a higher moment of inertia restricts large changes in rotational rates, which increases the return time.

2) The Effect of Time: To observe the effects of varying the time-windows on the BRS, the FRS for various time-windows have been obtained and the optimal control routine is applied on these sets. The results of the BRS for varying FRS time-windows can be found in Fig. 33 for each battery configuration. To highlight the effects of varying the time-window on the return time distribution, the BRS results for various time-windows for the battery neutral configuration only are shown in Fig. 34. The following observation can be made:

- *The time to return to the safe state generally requires (substantially) more time than the time-window used to obtain the FRS.* A forward reachable set, with time-window of T = 0.1 s, results in a BRS with return times up to 0.7 seconds. This is due to the sampling along the maximum input range to estimate the boundary of the FRS. These extreme inputs result in trajectory end states with high rotational rates and accelerations from which the quadcopter needs to recover. Moreover, due to the modelling of the actuator dynamics, an additional delay is introduced to change the (direction of the) rotor

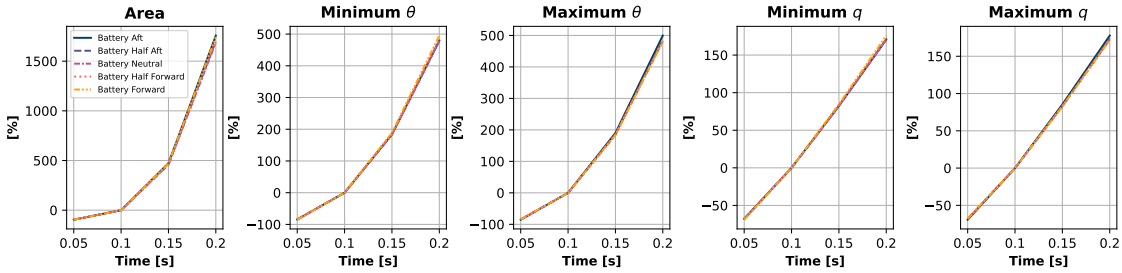

Fig. 30. The percentage difference of the reachable set for various time-windows with respect to T = 0.1 s.

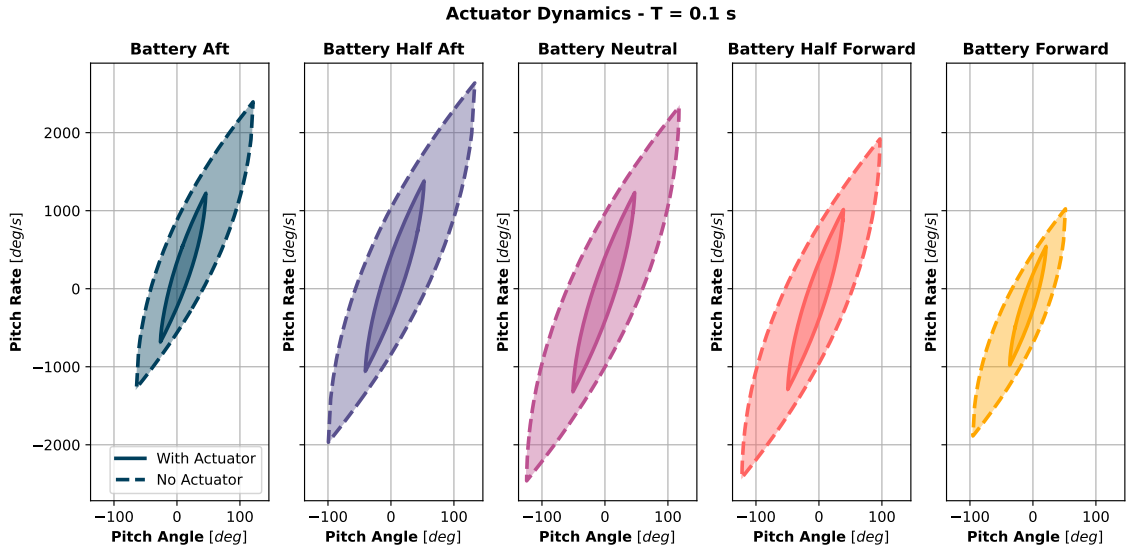

Fig. 31. The FRS with and without actuator dynamics for each battery configuration at T = 0.1 s. Note the substantial reachable set reduction when actuator dynamics are included in the modelling.

TABLE XII
PERFORMANCE COMPARISON OF THE FRS WITH AND WITHOUT ACTUATOR DYNAMICS FOR THE EACH BATTERY CONFIGURATIONS

	Area$[deg^2/s]$			**Min.** θ [deg]			**Max.** θ [deg]			**Min.** q [deg/s]			**Max.** q [deg/s]		
Battery Position	*With*	*Without*	*%*	*With*	*Without*	*%*	*With*	*Without*	*%*	*With*	*Without*	*%*	*With*	*Without*	*%*
Aft	68.11	10.31	-84.86%	-64.23	-26.22	+59.18%	120.91	45.87	-62.06%	-1271.92	-682.34	+46.35%	2394.18	1222.54	-48.94%
Half Aft	107.32	17.10	-84.07%	-99.35	-40.69	+59.05%	133.11	52.55	-60.52%	-1967.32	-1057.10	+46.27%	2635.83	1379.57	-47.66%
Neutral	116.52	18.85	-83.82%	-124.32	-50.75	+59.18%	117.65	47.19	-59.89%	-2461.80	-1320.00	+46.38%	2329.66	1231.08	-47.16%
Half Forward	95.59	15.32	-83.97%	-122.24	-49.41	+59.58%	96.91	38.88	-59.88%	-2420.67	-1290.12	+46.70%	1919.04	1013.84	-47.17%
Forward	42.90	6.58	-84.66%	-95.27	-36.89	+61.28%	51.68	20.82	-59.71%	-1886.57	-978.84	+48.12%	1023.41	541.60	-47.08%

speeds and generate rotational accelerations towards the safe state.

- *The return time increases with increasing FRS time-window, until a specific time, after which the return time distribution shows a repeating pattern along the FRS.* The repeating return time pattern occurs from T = 0.15 s for angles around- and greater than 100 degrees when considering all configurations. The repeating pattern can be explained by the looping of the pitch angle in the simulation. As described in Chapter VI, the optimal control routine depends on the sign of the pitch angle, which loops around an arbitrary range. As a result, the found optimal control solution does not always result in the global optimum. When the pitch angle approaches the end of the angle range and it has sufficient pitch rate and $\dot{q}_0$ into the direction of this range, the quadcopter can exceed the looping angle and the sign of the pitch angle is switched. Consequently, the optimal control routine input is switched as well, which happens to result in a faster time to reach the safe state. As proposed before, it is recommended to loop the pitch angle interval for an integer amount of variations and select the routine resulting in the minimum return time for each end state considered.

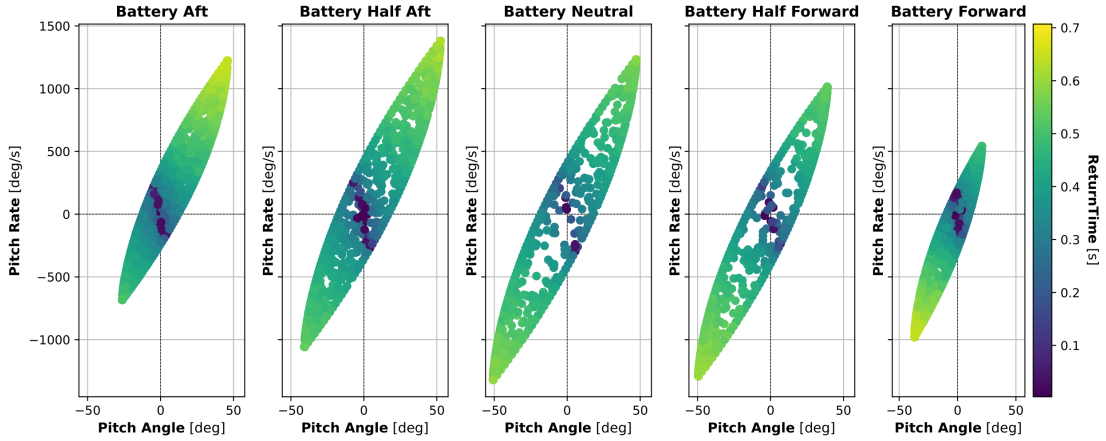

Fig. 32. The effect of center of gravity position on the return times in the BRS. The FRS are obtained for a time-window of T = 0.1 s and the number of trajectories are increased to N_{traj} = 2000 for illustration purposes. Note the distribution of the return times along the FRS which seems to be a function of the center of gravity position.

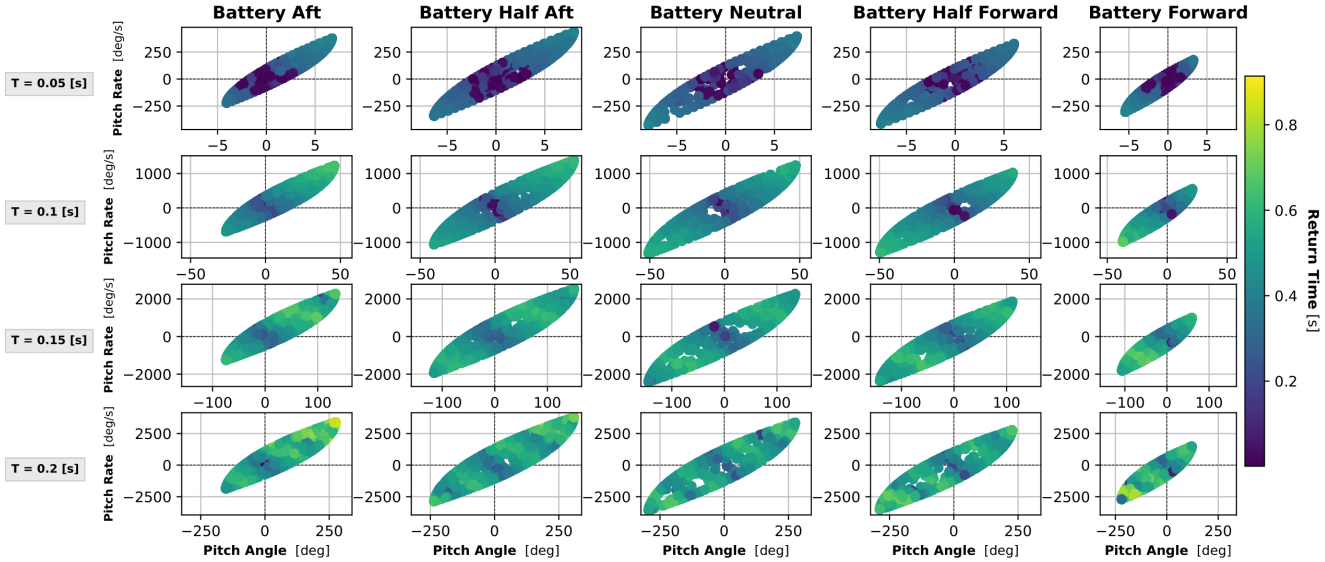

Fig. 33. The effect of the time-window of the FRS on the return times in the BRS for each battery configuration. With increasing FRS time-windows the return times increases as well, after T = 0.1 s a pattern emerges along the FRS set. Note that the ranges of the axes of the plots are not the same.

3) The Effect of Actuator Dynamics: The effect of the actuator dynamics on the BRS is analyzed by comparing the BRS sets for T = 0.1 s for each configuration with and without actuator dynamics modelling. Note that for the simulations without actuator dynamics, the optimal control routine reduces from using the optimal control surface to the optimal control curves as displayed in Fig. 13. The results for all configurations can be found in Fig. 35. The following observation can be made:

- *The BRS without actuator dynamics has a considerably larger FRS with reduced return times.* The quadcopters without actuator dynamics modelling obtain larger FRS as well as a BRS with much lower return times. For a FRS of T = 0.1 s the largest distribution of the return time of the set without actuator dynamics ranges up to about 0.3 seconds, despite the larger pitch angles and pitch rates obtained in the FRS. This is because a system without actuator dynamics can apply a rotational acceleration instantaneously, while the actuator dynamics introduce a lag, making the system respond slower. Note that the repeating return time distribution as observed before is already visible in the BRS without actuator dynamics as larger pitch angles and rates are obtained in the FRS within the same time-window.

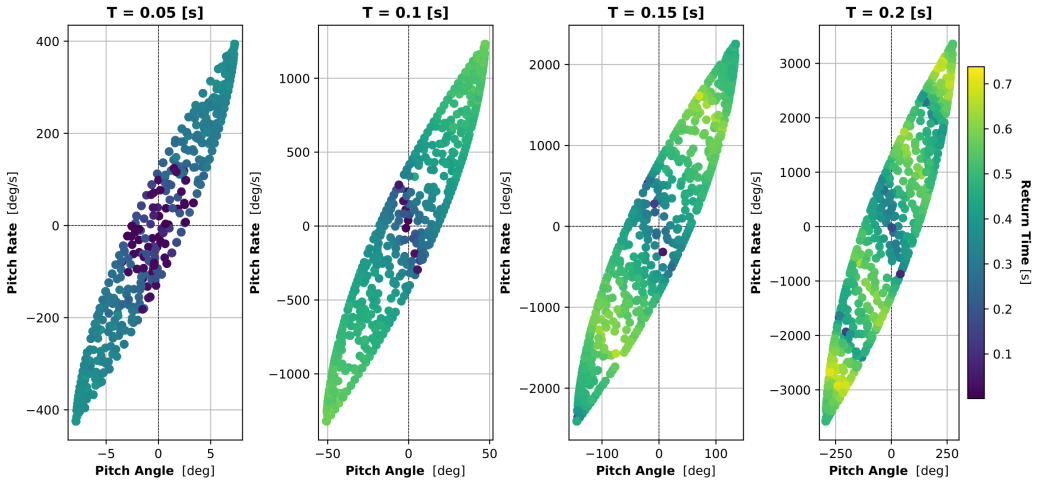

Fig. 34. The distribution of the return times for various FRS time-windows for the battery neutral configuration. After T = 0.1 s a repeating pattern of the return times can be observed along the FRS. Note that the ranges of the axes of the plots are not identical.

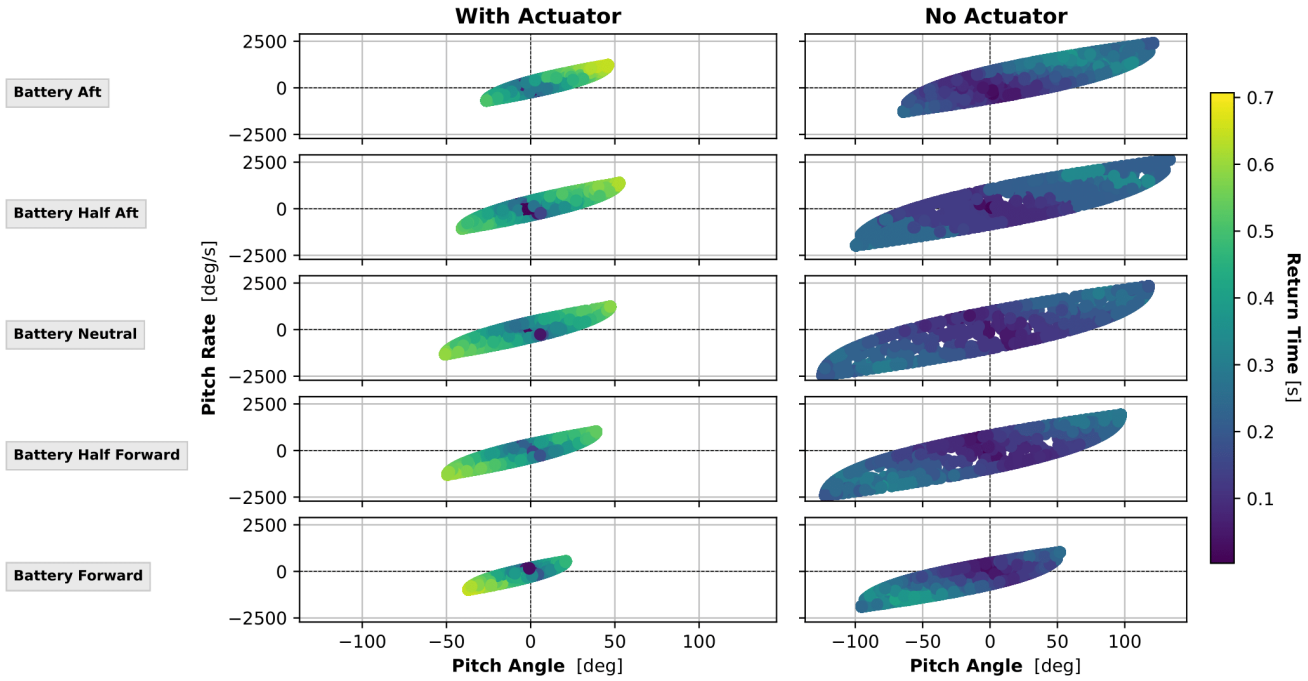

Fig. 35. The effect of actuator dynamics on the FRS and the BRS for each battery configuration for a FRS time-window of T = 0.1 s, N_{traj} = 2000. Note that the BRS without actuator dynamics have much smaller return times and that the repeating pattern is already visible.

The results on the FRS and BRS generate knowledge on the capabilities of the quadcopter in the framework of reachability analysis. So far, the reachable sets are separated into the FRS and BRS respectively. In order to determine the SFE, it is required to define the amount of time the quadcopter is allowed to go from- and return to the safe state (hover condition). This particular time-window is application specific and dependent on the safety and performance requirements. For further implementation of the results in the framework of the SFE, it is recommended to further investigate the application specific safety requirements (e.g. in terms of time-windows) which can then be co-implemented with a controller for flight envelope protection.

IX. Experimental Validation of the Forward Reachable Sets

To validate the results on the forward reachable set (FRS) as presented in Chapter VIII, the FRS estimations from the Monte-Carlo (MC) simulation are compared to flight data. In this work the edge case scenarios of reaching the maximum and minimum pitch angle and rate (the top and bottom corners of the envelopes) as a function of time are considered. For each quadcopter battery configuration, maximum commanded pitch up and pitch down maneuvers are manually performed. The resulting angles and rates over time are compared to the maximum angles and rates of the reachable set estimates.

A. Experiment Set-up

The validation flights have been conducted indoors above a net to capture the quadcopter after each maneuver. The quadcopter has been flown manually in a line-of-sight fashion. Since there was no available method to directly control the rotors in an open-loop fashion, a rate controller has been used and adjusted to approximate a step-input as much as the software could allow[3]. This resulted in a full stick deflection mapping to a pitch rate command of 2000 deg/s, which extended the maximum control moment input over time as much as possible before the quadcopter approached the commanded input rate. To reduce any unintentional roll and yaw inputs, the roll and yaw commands were limited to a maximum of 2 deg/s at full stick deflection. An overview of the commanded pitch rate signals for all maneuvers can be found in Fig. 36. More details on the experiment set-up can be found in Appendix E.

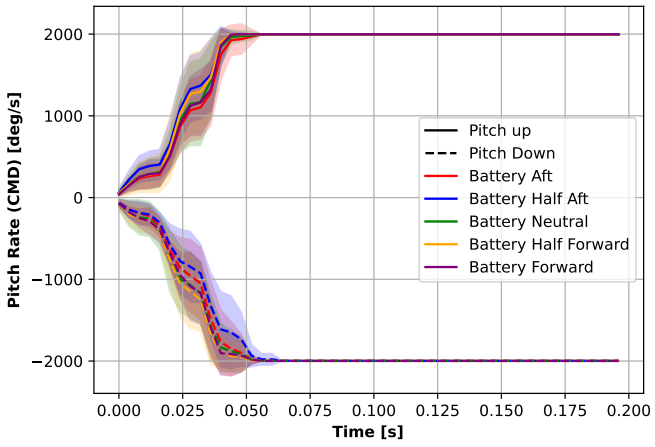

Fig. 36. The mean $\pm$ one standard deviation of the pitch rate commanded signals for both pitch up and pitch down maneuvers. For both maneuver directions the absolute pitch rate commanded at full stick deflection is 2000 deg/s. Note that the input is not a pure step-input.

B. Validation Data

To perform the validation analysis, the rotor speeds, pitch angles and pitch rates of all flight maneuvers are required. The pitch rate data have been obtained from the onboard MEMS gyro, while the pitch angles are obtained from both the quadcopter software, which integrates the pitch rate over time, and an external motion capture system (OptiTrack[4]). An overview of the amount of maneuvers included in the analysis can be found in Table XIII. The measurement results of all pitch maneuvers are plotted in Fig. 37.

TABLE XIII
Overview of the maneuver count per direction and quadcopter configuration.

	Number of Maneuvers	
	Pitch Up	*Pitch Down*
Battery Aft	10	15
Battery Half Aft	13	14
Battery Neutral	16	17
Battery Half Forward	14	15
Battery Forward	13	15

Note that the expected differences between the quadcopter configurations can be noticed in the measured pitch angles and rates over time. Especially the battery forward configuration noticeably obtains much smaller pitch angles and rates over time for the pitch up maneuvers and vice versa for the battery aft configuration. Also note that indeed the battery half aft configuration shows a larger obtainable maximum pitch up angle and rate compared to the other configurations, which was also found in the FRS analysis in Chapter VIII.

The results of the OptriTrack measurements together with the pitch angle data from the onboard software are plotted in Fig. 38 for the battery neutral configuration. The onboard pitch angle data show to be periodic about ± 90 degrees. Due to the high pitch angles and rates reached during the maneuvers, the OptiTrack system systematically lost track of the rigid body after around ± 60 degrees (the signal remains constant after tracking loss). Furthermore, the onboard pitch angle underestimates the pitch up maneuvers, and overestimates the pitch down maneuvers with respect to the OptiTrack system for the battery neutral configuration measurements. In order to obtain a clean pitch angle reference, the gyro data have been integrated over time. The pitch angle from the OptiTrack system has been used as the initial pitch angle at the start of the maneuver due to the external fashion and high accuracy capabilities of the system. The resulting integrated pitch angle signal, also plotted in Fig. 38, averages the under- and overestimation of the onboard pitch angle measurements and OptiTrack measurements. This integrated pitch angle signal is further used as reference in the validation analysis.

Another observation from the flight data is an asymmetry of the control pitching moment with respect to the direction of the maneuver. The pitch up maneuvers generally obtain higher control moments (around 3000 eRPM) than the pitch down maneuvers (around 3800 eRPM). This becomes more apparent when plotting the distribution of the rotor speeds as shown in Fig. 39. A possible explanation of this phenomenon could be

[3]BetaFlight Configurator V10.8.0

[4]https://optitrack.com/

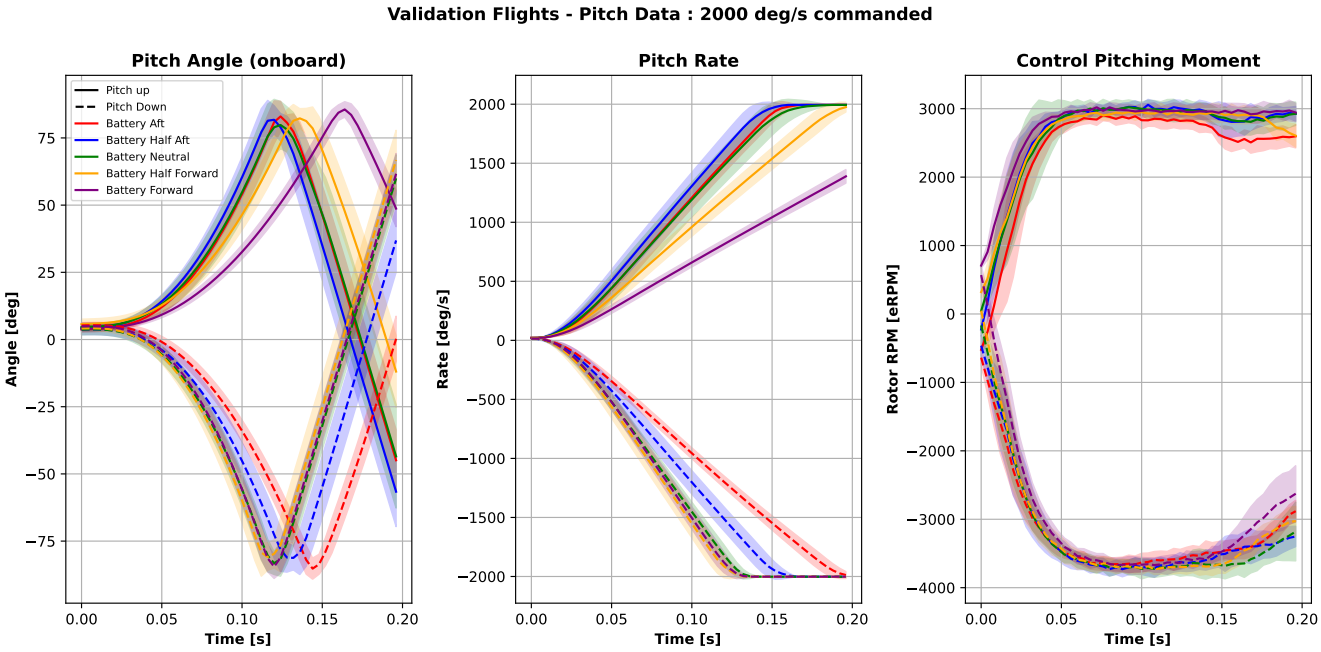

Fig. 37. The mean ± one standard deviation of the pitch angle, pitch rate and control pitching moment of all maneuvers and quadcopter configurations. Note the expected differences in obtained pitch angle and rate over time, especially noticeable for the pitch up maneuver of the battery forward configuration, which obtains a smaller pitch angle and rate over time compared to the other configurations. Also note the asymmetry in the control pitching moment between the pitch up and pitch down maneuvers.

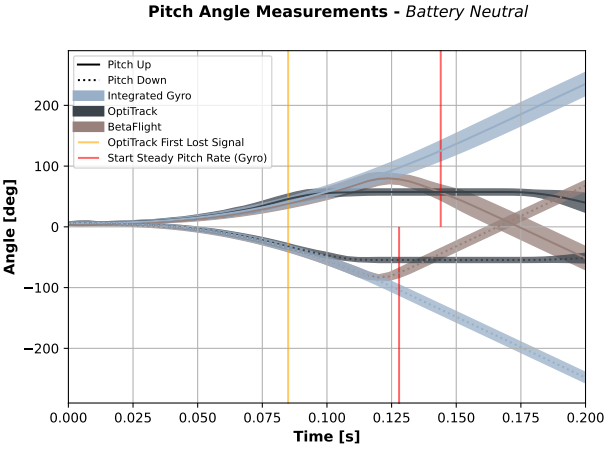

Fig. 38. The mean ± one standard deviation of the pitch angle measurements over time from both the onboard datalogging (BetaFlight), which show to be periodic about ±90 degrees, and the external measurement system (OptiTrack), which show tracking loss. The first vertical line indicates the first signal loss of the OptiTrack system, the next two vertical lines indicate the moment a steady-state pitch rate has been obtained for the pitch up and down maneuvers. Note that the pitch angle integrated from the gyro signal, using the initial pitch angle from the OptiTrack system, is plotted as well, which is the signal used as reference in the validation analysis.

as a result of asymmetrical rotor blades and/or functionality of the motors. It is recommended to investigate the cause of this asymmetry as symmetrical control moment inputs would benefit the validation analysis.

C. Validation Results

Before the validation flight data can be compared to the simulation results, the control moment applied in the simulations must match those as observed during the validation flights, in order to obtain a fair comparison. Since the control moment distributions are asymmetric with maneuver direction, for each maneuver direction a dedicated control moment is selected which is used in the MC simulation for envelope prediction. The maximum front and aft rotor speeds, as used in the simulations, are selected by averaging the means of the rotors speeds of all configurations, per pitch up and down maneuver as displayed in Fig. 39. A summary of the selected rotor speeds, as well as the MC simulation settings can be found in Table XIV.

The validation results show that the quadcopter models consistently underestimate the flight data, as presented in Fig. 40. The actuator dynamics model, as identified in Chapter IV (referred to as the default actuator model), has a noticeably slower performance than what the flight data show. A re-identification of the time constants on the validation data only shows that indeed the updated time constant values are reduced by more than half compared to the default time constant values. The time constants identified on the validation flight

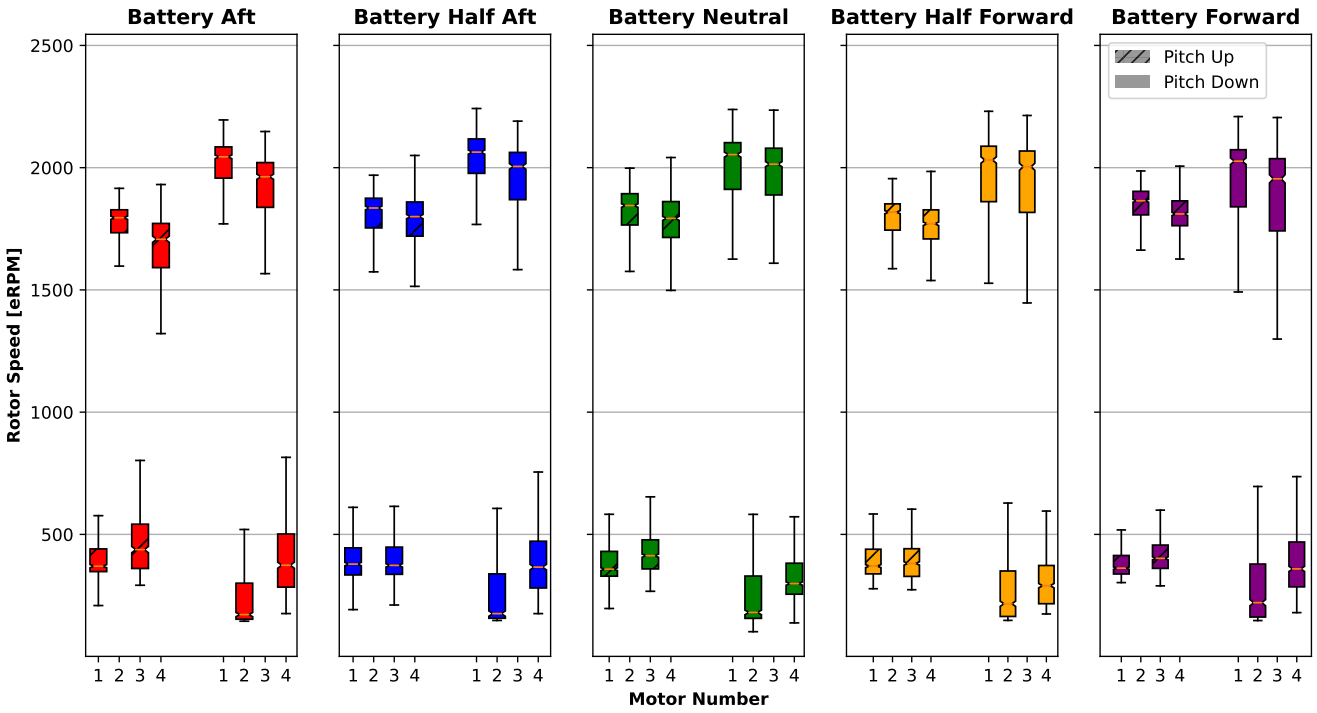

Fig. 39. The rotor speed distributions of each rotor for all validation flight maneuvers. An asymmetry in the obtained maximum and minimum rotor speeds between the pitch up and pitch down maneuvers can be observed. The average rotor speeds for the pitch up and pitch down maneuvers are taken and used as separate cases in the simulations for the validation analysis.

TABLE XIV
SUMMARY OF THE ROTOR SPEEDS USED IN THE MC SIMULATION, TOGETHER WITH THE SIMULATION SETTINGS TO OBTAIN THE REACHABLE SET ESTIMATES FOR COMPARISON WITH THE VALIDATION FLIGHT DATA.

Simulation Settings	
Pitch Up [min, max]	[384.1, 1803.4] eRPM
Pitch Down [min, max]	[264.3, 2015.4] eRPM
dt [s]	0.001
$TimeWindows$ [s]	0.04, 0.08, 0.1, 0.14, 0.18, 0.2
$N_{trajectory}$	1000
p_c, N_{switch}	Optimized Parameters
N	10

data (referred to as the updated actuator model) can be found in Table XV. A possible explanation for these differences is that the default actuator dynamics are identified on data from a quadcopter flown in "angle mode", while the validation flights have been performed in "rate mode". The "angle mode" has an additional control loop including data from the accelerometer for angle control. The additional control loop possibly results in larger delays, resulting in slower actuator dynamics on the default model. Moreover, the commanded inputs to the rotors may be different as well. The feedback loop oriented "angle mode" controller leads to less aggressive inputs than the feedforward oriented "rate mode" controller. Since the rotor speed commands change faster, the rotor speed output changes more aggressively in "rate mode" and hence a smaller time constant is found. Another possible source for the differences is the observed difference in scaling of the commanded and measured rotor speeds in the flight controller software which directly influences the parameter estimation as well.

The validation errors, which are the differences between the MC simulation results and the validation measurements, for both actuator models are shown in Fig. 41. Note that the regions in which the gyro data have obtained a steady-state value are highlighted because in that case the comparison with the simulation data is invalid. Also note that the variance in the errors (indicated as a bound of one standard deviation) mainly originate from the variations in the validation flight data.

For time-windows up to T = 0.1 s the mean and standard deviation of the validation error, as well as the percentages with respect to the validation data are summarized in tables. The data with the default actuator model for the pitch angle and rate can be found in Table XVI and Table XVII respectively. The data with the updated actuator model for the pitch angle and rate can be found in Table XVIII and Table IX-C respectively. Note that the validation data have an initial positive pitch angle and pitch rate at the start of the maneuver, which results in an underestimation for all estimates at T = 0 s. Furthermore, large error percentages are found for the pitch angle values at T = 0.04 s due to the pitch angle of the validation data crossing zero near T = 0.04 s.

The quadcopter models with the default actuator dynamics generally show an underestimation of the pitch angle and pitch rate with respect to the validation data. This applies for both

the pitch up and pitch down maneuvers. The average errors among all quadcopter configurations at T = 0.1 s for the pitch up and pitch down maneuvers of the pitch angle are 44.39% and 26.84%. The average errors at T = 0.1 s for the pitch up and pitch down maneuvers of the pitch rate are 27.30% and 27.84%.

The quadcopter models with the updated actuator dynamics generally show an overestimation of the pitch rate for both pitch up and pitch down maneuvers. Exceptions include the battery forward configuration and the pitch down maneuver of the battery aft configuration. For all models the pitch angle is overestimated for the pitch down maneuver, and underestimated for the pitch up maneuver. This is as expected since, although undesirable, all validation maneuvers start with a positive initial pitch angle. The absolute differences with the validation data have been reduced substantially compared to the default model. The average errors at T = 0.1 s for the pitch up and pitch down maneuvers of the pitch angle are reduced to 13.75% and 14.70%. The average errors at T = 0.1 s for the pitch up and pitch down maneuvers of the pitch rate are reduced to 12.07% and 11.69%.

To visualize the validation results in the perspective of the reachable set estimates, the results of the pitch down maneuver for the battery neutral configuration are plotted for T = 0.04, 0.08 and 0.1 s together with a realization of the MC simulation reachable set estimate for both the default, Fig. 42, and the updated, Fig. 43, actuator model. The plots in Fig. 42 distinctly show the underestimation of the reachable set on the pitch down maneuver of the quadcopter model with the default actuator model. Note that for the results on T = 0.04 s the pitch angles of the validation data cross zero as the flight maneuvers start at an initial positive nonzero pitch angle, which makes the validation analysis in these time-windows for the pitch angle invalid. The models with updated actuator dynamics in Fig. 43 clearly show an overestimation with respect to the validation data. A more detailed figure on the updated actuator model results can be found in Fig. 44.

To summarize, from the validation analysis it has been found that mainly the quadcopter actuator dynamics are modelled with a too high time constant, as the simulation data show a large underestimation with respect to the validation flight data. Possible explanations include differences between the control mode used to obtain the flight data, such as time-delay and commanded inputs, and possible scaling issues between the commanded and measured rotor speeds. The quadcopter model with updated actuator dynamics (identified on the validation data) show a large decrease in (absolute) error with the validation data compared to the default model, with an average reduction of about 18% at T = 0.1 s. The pitch rate is generally being overestimated, which is expected when comparing an open-loop simulation with closed-loop performed flight maneuvers. Exceptions are the battery forward configuration (both maneuver directions) and the battery aft maneuver (pitch down direction) which underestimate the pitch rate. This could indicate that these models are estimated insufficiently and a re-analysis would be required. For all models the pitch angle is overestimated for the pitch down maneuver, and underestimated for the pitch up maneuver. This is as expected since, although undesirable, all validation maneuvers start with a positive initial pitch angle.

TABLE XV
UPDATED ACTUATOR TIME CONSTANTS IDENTIFIED ON THE VALIDATION FLIGHT DATA.

Motor	τ	$100\mathbf{cov}(\hat{\theta})/\hat{\theta}$	**NRMSE Train**	$\mathbf{R^2}$ **(Train)**
1	0.0262	2.1807 %	0.0634	0.9727
2	0.0332	2.6489 %	0.0720	0.9651
3	0.0229	1.4640 %	0.0539	0.9795
4	0.0256	1.0352 %	0.0550	0.9778

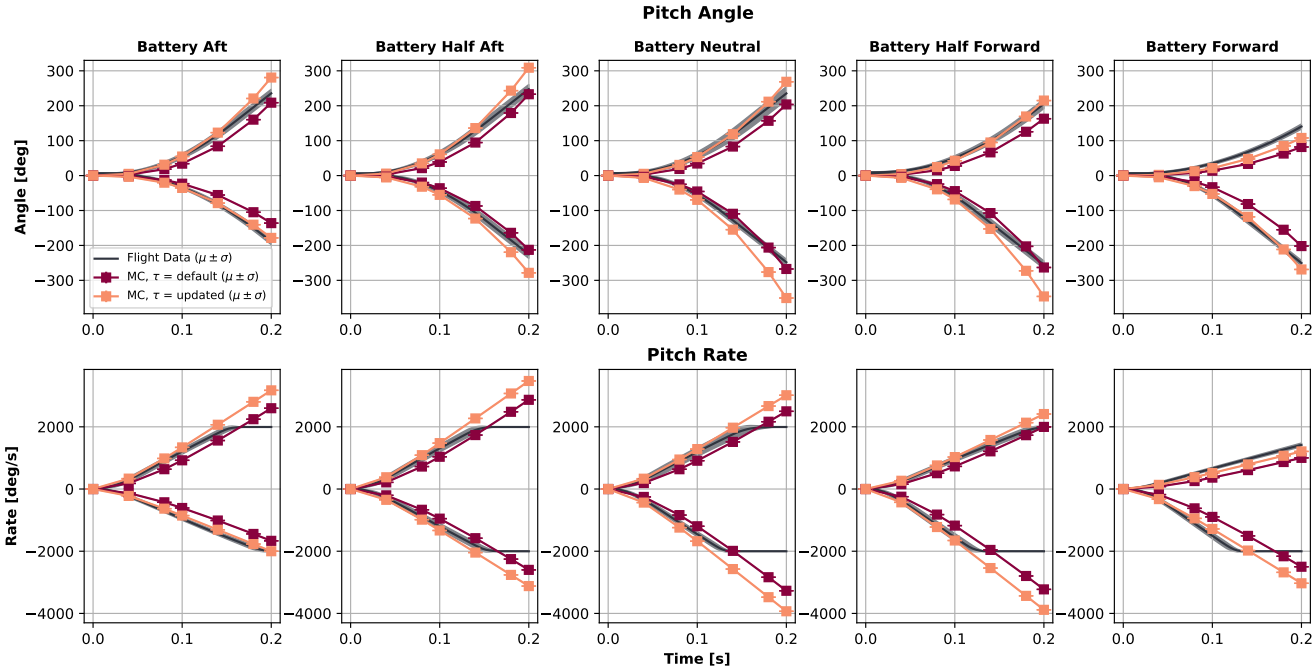

Fig. 40. Validation results showing the measurement data and the estimation from the reachable set over time for all maneuvers and quadcopter configurations. Note that the mean $\pm$ one standard deviation are shown. Also note that the MC reachable set estimates are determined for an integer amount of time-windows, which are interpolated, while the flight data are continuous.

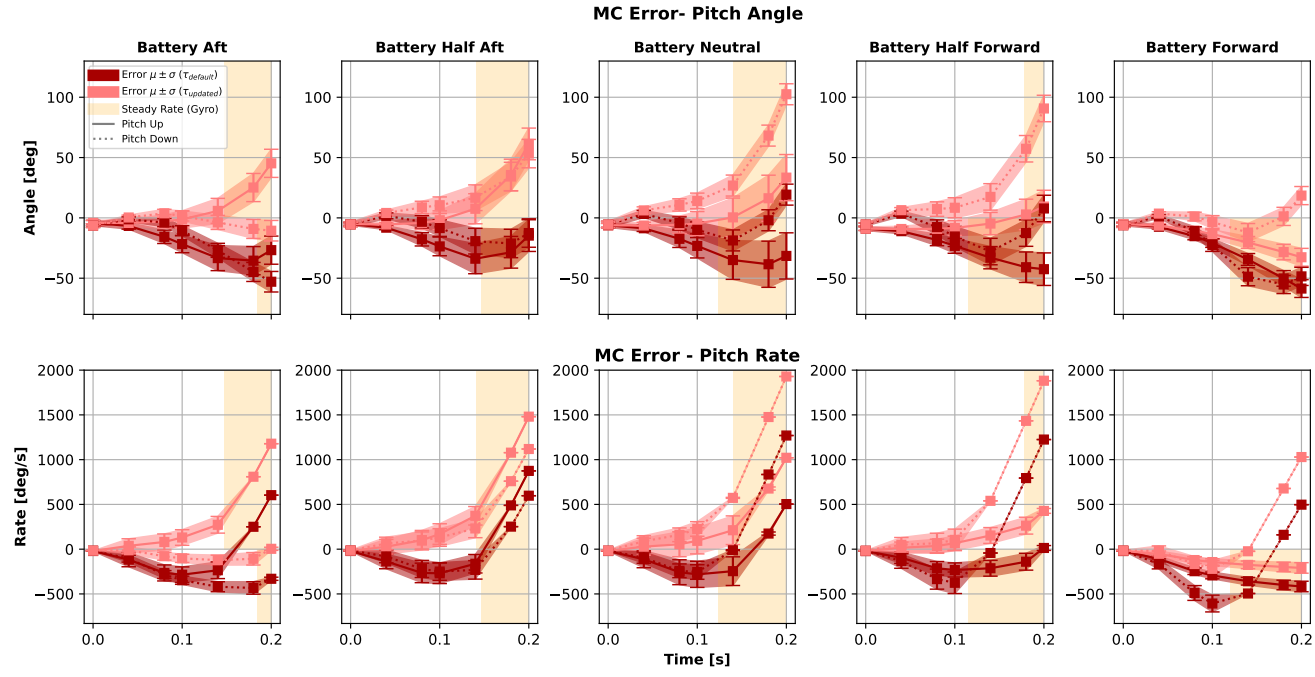

Fig. 41. The validation errors, which are the differences between the MC simulation results and the validation measurements, over time. Note that the regions in which the gyro data have obtained a steady-state value are highlighted since in that case the comparison with the simulation data is invalid. Also note that the variance in the errors (indicated as a bound of one standard deviation) mainly originate from the variations in the validation flight data.

TABLE XVI

SUMMARY OF THE PITCH *ANGLE* VALIDATION RESULTS OF THE *DEFAULT* ACTUATOR MODEL. NOTE THAT THE VALIDATION DATA HAVE AN INITIAL POSITIVE PITCH ANGLE AT THE START OF THE MANEUVER, AS A RESULT THE PITCH DOWN MANEUVER ESTIMATION RESULTS IN AN OVERESTIMATION FOR T = 0.04 S. FURTHERMORE, LARGE PERCENTAGE VALUES ARE FOUND FOR THE PITCH ANGLE VALUES DUE TO THE PITCH ANGLE OF THE VALIDATION DATA CROSSING ZERO NEAR T = 0.04 S.

***ANGLE** [deg]*	**T = 0 [s]**				**T = 0.04 [s]**				**T = 0.08 [s]**				**T = 0.1 [s]**			
Pitch Up	$\mu_{\mathbf{error}}$	%	$\sigma_{\mathbf{error}}$	%	$\mu_{\mathbf{error}}$	%	$\sigma_{\mathbf{error}}$	%	$\mu_{\mathbf{error}}$	%	$\sigma_{\mathbf{error}}$	%	$\mu_{\mathbf{error}}$	%	$\sigma_{\mathbf{error}}$	%
Aft	-4.24	-100.0	2.18	51.31	-6.65	-72.86	2.66	29.13	-15.70	-46.02	5.54	16.25	-21.73	-38.92	7.14	12.79
Half Aft	-5.17	-100.0	0.93	18.01	-8.12	-72.88	1.71	15.33	-17.75	-45.41	5.54	14.18	-23.64	-37.72	7.75	12.37
Neutral	-6.19	-100.0	1.66	26.86	-8.62	-75.76	2.65	23.32	-17.35	-47.78	7.17	19.74	-23.25	-40.25	9.95	17.23
Half Forward	-8.96	-100.0	1.47	16.44	-11.04	-83.29	2.24	16.89	-18.33	-54.68	4.74	14.14	-23.19	-45.63	6.15	12.10
Forward	-5.10	-100.0	1.43	28.02	-7.35	-86.62	1.82	21.47	-15.18	-66.39	2.98	13.01	-20.85	-59.92	3.61	10.37
Pitch Down	$\mu_{\mathbf{error}}$	%	$\sigma_{\mathbf{error}}$	%	$\mu_{\mathbf{error}}$	%	$\sigma_{\mathbf{error}}$	%	$\mu_{\mathbf{error}}$	%	$\sigma_{\mathbf{error}}$	%	$\mu_{\mathbf{error}}$	%	$\sigma_{\mathbf{error}}$	%
Aft	-6.39	-100.0	1.55	24.23	-1.19	-38.96	1.98	65.05	-3.88	23.33	3.34	-20.11	-10.61	31.41	4.13	-12.22
Half Aft	-5.35	-100.0	1.93	35.96	1.72	142.39	2.43	200.82	-3.22	13.88	5.12	-22.10	-8.46	18.92	6.88	-15.39
Neutral	-5.49	-100.0	2.67	48.56	3.24	756.62	2.96	691.19	-4.27	14.57	5.09	-17.34	-9.86	17.81	6.49	-11.72
Half Forward	-5.47	-100.0	1.22	22.33	3.43	-3609.35	2.17	-2278.82	-7.65	23.85	6.01	-18.73	-15.42	25.71	8.31	-13.87
Forward	-6.14	-100.0	1.73	28.21	1.22	96.51	1.55	122.06	-10.89	37.55	3.59	-12.38	-22.56	40.33	5.25	-9.38

TABLE XVII

SUMMARY OF THE PITCH *RATE* VALIDATION RESULTS OF THE *DEFAULT* ACTUATOR MODEL. NOTE THAT THE VALIDATION DATA HAVE AN INITIAL POSITIVE PITCH RATE AT THE START OF THE MANEUVER.

***RATE** [deg]*	**T = 0 [s]**				**T = 0.04 [s]**				**T = 0.08 [s]**				**T = 0.1 [s]**			
Pitch Up	$\mu_{\mathbf{error}}$	%	$\sigma_{\mathbf{error}}$	%	$\mu_{\mathbf{error}}$	%	$\sigma_{\mathbf{error}}$	%	$\mu_{\mathbf{error}}$	%	$\sigma_{\mathbf{error}}$	%	$\mu_{\mathbf{error}}$	%	$\sigma_{\mathbf{error}}$	%
Aft	-20.35	-100.0	1.83	8.98	-117.38	-39.45	79.04	26.56	-265.48	-29.41	89.44	9.91	-285.12	-23.60	86.98	7.20
Half Aft	-20.24	-100.0	1.48	7.32	-137.17	-39.11	81.57	23.26	-265.19	-26.85	109.01	11.04	-269.48	-20.62	114.75	8.78
Neutral	-20.30	-100.0	0.98	4.83	-112.94	-37.08	94.44	31.01	-257.47	-28.81	139.05	15.56	-281.18	-23.61	146.02	12.26
Half Forward	-21.22	-100.0	1.68	7.93	-96.18	-38.51	62.88	25.17	-213.66	-29.57	75.62	10.46	-232.55	-24.21	78.99	8.23
Forward	-20.66	-100.0	1.54	7.47	-109.25	-58.33	32.70	17.46	-246.13	-48.98	36.72	7.31	-293.52	-44.50	37.70	5.72
Pitch Down	$\mu_{\mathbf{error}}$	%	$\sigma_{\mathbf{error}}$	%	$\mu_{\mathbf{error}}$	%	$\sigma_{\mathbf{error}}$	%	$\mu_{\mathbf{error}}$	%	$\sigma_{\mathbf{error}}$	%	$\mu_{\mathbf{error}}$	%	$\sigma_{\mathbf{error}}$	%
Aft	-16.47	-100.0	2.09	12.68	-105.73	45.05	38.40	-16.36	-283.05	39.89	43.95	-6.19	-346.92	36.28	45.83	-4.79
Half Aft	-14.31	-100.0	4.30	30.06	-81.04	28.58	70.59	-24.90	-221.11	24.90	95.59	-10.76	-249.97	20.80	98.85	-8.22
Neutral	-16.57	-100.0	2.09	12.59	-94.58	27.15	62.44	-17.92	-241.44	22.37	76.55	-7.09	-255.14	17.57	81.41	-5.61
Half Forward	-17.10	-100.0	1.58	9.25	-132.49	34.97	81.17	-21.42	-334.47	28.93	112.18	-9.70	-375.37	24.19	120.35	-7.76
Forward	-15.42	-100.0	2.31	15.00	-164.83	47.98	55.70	-16.21	-489.61	44.08	82.60	-7.44	-607.10	40.38	93.83	-6.24

TABLE XVIII

SUMMARY OF THE PITCH *ANGLE* VALIDATION RESULTS OF THE *UPDATED* ACTUATOR MODEL. NOTE THAT THE VALIDATION DATA HAVE AN INITIAL POSITIVE PITCH ANGLE AT THE START OF THE MANEUVER, AS A RESULT THE PITCH DOWN MANEUVER ESTIMATION RESULTS IN AN OVERESTIMATION FOR T = 0.04 S. FURTHERMORE, LARGE PERCENTAGE VALUES ARE FOUND FOR THE PITCH ANGLE VALUES DUE TO THE PITCH ANGLE OF THE VALIDATION DATA CROSSING ZERO NEAR T = 0.04 S.

***ANGLE** [deg]*	**T = 0 [s]**				**T = 0.04 [s]**				**T = 0.08 [s]**				**T = 0.1 [s]**			
Pitch Up	$\mu_{\mathbf{error}}$	%	$\sigma_{\mathbf{error}}$	%	$\mu_{\mathbf{error}}$	%	$\sigma_{\mathbf{error}}$	%	$\mu_{\mathbf{error}}$	%	$\sigma_{\mathbf{error}}$	%	$\mu_{\mathbf{error}}$	%	$\sigma_{\mathbf{error}}$	%
Aft	-4.24	-100.0	2.18	51.31	-4.21	-46.05	2.66	29.13	-2.93	-8.60	5.54	16.25	-1.29	-2.31	7.14	12.79
Half Aft	-5.17	-100.0	0.93	18.01	-5.47	-49.04	1.71	15.33	-4.16	-10.65	5.54	14.18	-1.95	-3.11	7.75	12.37
Neutral	-6.19	-100.0	1.66	26.86	-6.34	-55.72	2.65	23.32	-5.74	-15.80	7.17	19.74	-4.71	-8.16	9.95	17.23
Half Forward	-8.96	-100.0	1.47	16.44	-9.22	-69.55	2.24	16.89	-9.04	-26.99	4.74	14.14	-8.37	-16.47	6.15	12.10
Forward	-5.10	-100.0	1.43	28.02	-6.45	-75.94	1.82	21.47	-10.56	-46.16	2.98	13.01	-13.46	-38.69	3.61	10.37
Pitch Down	$\mu_{\mathbf{error}}$	%	$\sigma_{\mathbf{error}}$	%	$\mu_{\mathbf{error}}$	%	$\sigma_{\mathbf{error}}$	%	$\mu_{\mathbf{error}}$	%	$\sigma_{\mathbf{error}}$	%	$\mu_{\mathbf{error}}$	%	$\sigma_{\mathbf{error}}$	%
Aft	-6.39	-100.0	1.55	24.23	0.32	10.50	1.98	65.05	3.76	-22.64	3.34	-20.11	1.56	-4.62	4.13	-12.22
Half Aft	-5.35	-100.0	1.93	35.96	4.06	336.12	2.43	200.82	8.66	-37.38	5.12	-22.10	10.47	-23.42	6.88	-15.39
Neutral	-5.49	-100.0	2.67	48.56	6.19	1447.77	2.96	691.19	10.73	-36.60	5.09	-17.34	14.05	-25.36	6.49	-11.72
Half Forward	-5.47	-100.0	1.22	22.33	6.37	-6703.97	2.17	-2278.82	7.29	-22.71	6.01	-18.73	8.40	-14.01	8.31	-13.87
Forward	-6.14	-100.0	1.73	28.21	3.55	280.09	1.55	122.06	1.11	-3.84	3.59	-12.38	-3.39	6.06	5.25	-9.38

TABLE XIX

SUMMARY OF THE PITCH *RATE* VALIDATION RESULTS OF THE *UPDATED* ACTUATOR MODEL. NOTE THAT THE VALIDATION DATA HAVE AN INITIAL POSITIVE PITCH RATE AT THE START OF THE MANEUVER

***RATE** [deg]*	**T = 0 [s]**				**T = 0.04 [s]**				**T = 0.08 [s]**				**T = 0.1 [s]**			
Pitch Up	$\mu_{\mathbf{error}}$	%	$\sigma_{\mathbf{error}}$	%	$\mu_{\mathbf{error}}$	%	$\sigma_{\mathbf{error}}$	%	$\mu_{\mathbf{error}}$	%	$\sigma_{\mathbf{error}}$	%	$\mu_{\mathbf{error}}$	%	$\sigma_{\mathbf{error}}$	%
Aft	-20.35	-100.0	1.83	8.98	37.18	12.50	79.04	26.56	80.64	8.93	89.44	9.91	130.38	10.79	86.98	7.20
Half Aft	-20.24	-100.0	1.48	7.32	27.53	7.85	81.57	23.26	100.45	10.17	109.01	11.04	168.95	12.93	114.75	8.78
Neutral	-20.30	-100.0	0.98	4.83	27.95	9.18	94.44	31.01	54.85	6.14	139.05	15.56	93.23	7.83	146.02	12.26
Half Forward	-21.22	-100.0	1.68	7.93	16.37	6.55	62.88	25.17	36.05	4.99	75.62	10.46	66.91	6.97	78.99	8.23
Forward	-20.66	-100.0	1.54	7.47	-53.20	-28.40	32.70	17.46	-121.52	-24.18	36.72	7.31	-143.98	-21.83	37.70	5.72
Pitch Down	$\mu_{\mathbf{error}}$	%	$\sigma_{\mathbf{error}}$	%	$\mu_{\mathbf{error}}$	%	$\sigma_{\mathbf{error}}$	%	$\mu_{\mathbf{error}}$	%	$\sigma_{\mathbf{error}}$	%	$\mu_{\mathbf{error}}$	%	$\sigma_{\mathbf{error}}$	%
Aft	-16.47	-100.0	2.09	12.68	-12.83	5.46	38.40	-16.36	-78.53	11.07	43.95	-6.19	-102.43	10.71	45.83	-4.79
Half Aft	-14.31	-100.0	4.30	30.06	63.45	-22.38	70.59	-24.90	97.16	-10.94	95.59	-10.76	130.60	-10.86	98.85	-8.22
Neutral	-16.57	-100.0	2.09	12.59	87.85	-25.22	62.44	-17.92	160.67	-14.88	76.55	-7.09	225.78	-15.55	81.41	-5.61
Half Forward	-17.10	-100.0	1.58	9.25	49.19	-12.98	81.17	-21.42	66.13	-5.72	112.18	-9.70	103.78	-6.69	120.35	-7.76
Forward	-15.42	-100.0	2.31	15.00	-19.13	5.57	55.70	-16.21	-166.03	14.95	82.60	-7.44	-219.73	14.62	93.83	-6.24

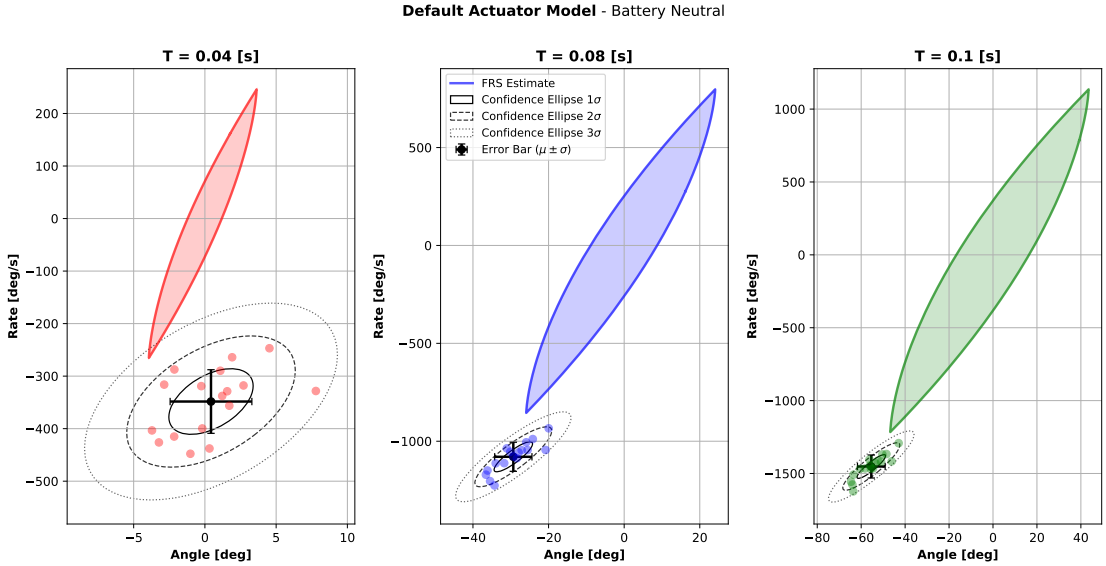

Fig. 42. Validation flight data plotted for T = 0.04, 0.08 and 0.1 s of the pitch down maneuver with the neutral configuration, together with a realization of the MC reachable set estimates from the default actuator model. An error bar of the data points, indicating the mean and one standard deviation bars are plotted, as well as the confidence ellipses (showing that indeed the pitch angle and rate are correlated) for various standard deviation scalings. Note that for the results on T = 0.04 s the pitch angles of the validation data cross zero as the flight maneuvers start at an initial positive nonzero pitch angle, which makes the validation analysis in these time-windows for the pitch angle invalid. The default actuator model results in an underestimation as can be clearly observed.

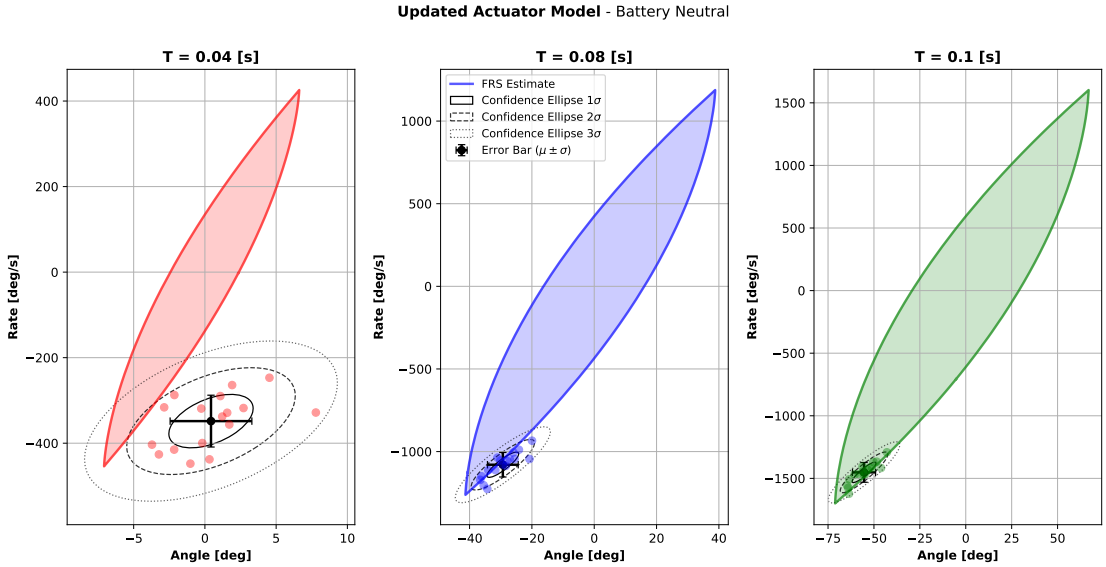

Fig. 43. Validation flight data plotted for T = 0.04, 0.08 and 0.1 s of the pitch down maneuver with the neutral configuration, together with a realization of the MC reachable set estimates from the updated actuator model. An error bar of the data points, indicating the mean and one standard deviation bars are plotted, as well as the confidence ellipses (showing that indeed the pitch angle and rate are correlated) for various standard deviation scalings. Note that for the results on T = 0.04 s the pitch angles of the validation data cross zero as the flight maneuvers start at an initial positive nonzero pitch angle, which makes the validation analysis in these time-windows for the pitch angle invalid. The updated actuator model results in an overestimation as can be clearly observed.

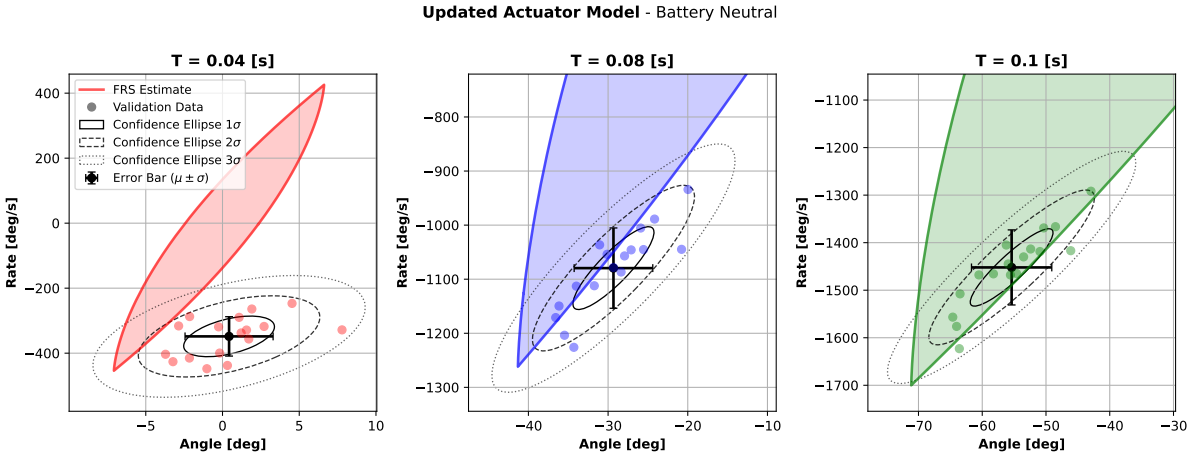

Fig. 44. Zoomed in figure of Fig. 43 which shows the overestimation of the reachable set estimates of the updated actuator model.

X. Conclusions

The use and applications of Unmanned Areal Vehicles (UAV) are expected to grow rapidly in the near future [1]. Currently Loss of control (LOC) is the main cause of failure for UAVs [2], hence in order to improve safety of these systems, development of LOC prevention techniques are of utmost importance. An aircraft operating outside the boundaries of the state-space in which the system can be safely operated is often linked to LOC [3][4]. A way to prevent LOC to occur is by keeping the system within the boundaries of the Safe Flight Envelope (SFE), called flight envelope protection (FEP). The SFE in this work is defined as *the set of states that can be reached, within a certain time-window, for which a trajectory exist to return to a safe flight condition within a predefined time-window* [5][6][7][8]. The aim of this research is to explore the behaviour of the boundaries of the longitudinal SFE of a quadcopter under varying system dynamics. The SFE has been split into a forward reachable set (FRS) and backward reachable set (BRS). The FRS is obtained through a Monte-Carlo (MC) simulation, and the BRS is obtained from the FRS using a minimum-time optimal control routine. Both methods have been verified. An analysis has been carried out on the effects of the center of gravity position, varying time-windows and the effect of actuator dynamics on both reachable sets. Furthermore, the forward reachable sets are experimentally validated. The results from this research add novel knowledge on the behaviour of the reachable sets of quadcopters and contributes to the development of FEP on quadcopter vehicles, thereby contributing to the safety of these systems. The conclusions have been split into the conclusions on the FRS results, BRS results, and the verification and validation part of the research.

A. Conclusions on the Forward Reachable Set

From the results on the FRS, which includes all the states which can be reached from hover condition within a predefined time-window, the following outcomes are found:

- *A larger displacement of the center of gravity from the rotor plane center results in a smaller reachable set area.* This is the direct result of the larger moment of inertia of a quadcopter with a more outer center of gravity location. Consequently, the quadcopter has a larger resistance against a change in angular rotation which results in a smaller reachable set. With respect to the neutral center of gravity position, the area of the reachable set of the aft center of gravity position at T = 0.1 s is reduced by around 45%, while for the forward center of gravity position the area is reduced by around 65%. It is generally favorable to have a center of gravity position near the rotor plane center which results in the largest reachable set.
- *The location of the centroid of the reachable set is a function of the center of gravity offset position.* Due to the center of gravity offset with the rotor plane center, a bias in the pitching moment is induced. Consequently a larger pitching moment can be obtained in the rotation direction of this bias, which shifts the centroid of reachable set accordingly.
- *The reachable set expands as a function of time and is dependent on quadcopter dynamics.* As the time-window increases, the reachable set area expands and the maximum and minimum obtainable pitch angles and rates increase. The extend to which the set grows within a unit of time is dependent on the system dynamics. The area increases more for the larger center of gravity offset positions. The minimum pitch angles and rates increase more for the forward center of gravity position while a larger increase is observed in maximum angles and rates for the aft center of gravity position.

- *The forward reachable set expands in time in a similar fashion as a double integrator system*. This is because the rotational quadcopter dynamics are modelled identical to a double integrator system. Furthermore, the analysis shows that a quadcopter is a very fast system and hence time-windows in the reachability analysis framework should be considered in the order of less than half a second (for the platform as used in this work).
- *Including the modelling of the actuator dynamics reduces the reachable set substantially*. The reachable set area is reduced by about 85% at T = 0.1 s compared to the set without actuator dynamics. Furthermore, the maximum and minimum obtainable pitch angle and rate are reduced by about 60% and 47% respectively. Hence it is essential in any quadcopter analysis to include the actuator dynamics in the modelling. The shrinkage of the reachable set due to the actuator dynamics is independent of center of gravity offset position.

B. Conclusions on the Backward Reachable Set

The BRS contains the time to return to the safe state (hover condition) estimated through an minimum-time optimal control routine for each end state in the FRS. From the results on the BRS, the following outcomes are found:

- *The time to return to the safe state generally requires (substantially) more time than the time-window used to obtain the FRS.* A FRS obtained within a time-window of T = 0.1 s results in a BRS with return times up to 0.7 seconds. This is mainly the result of the maximum control input applied in the FRS estimation, in combination with the actuator dynamics modelling introducing a delay to accelerate back towards the safe state.
- *The distribution of the return time over the entire FRS set is a function of center of gravity offset position.* For the neutral center of gravity position this distribution seems almost symmetric, while for the extreme center of gravity offsets larger return times are found near one of the edges of the FRS. This can be explained by the pitching moment bias as a result of the center of gravity offset with the rotor plane center and the larger moment of inertia. Hence it can be concluded that it is generally favorable to have a center of gravity position near the rotor plane center which results in a BRS with the smallest return time distribution.
- *The return time increases with increasing FRS time-window, until a specific time, after which the return time distribution shows a repeating pattern along the FRS.* The repeating pattern can be explained by the looping of the pitch angle around an arbitrary range in the simulation. And since the commanded input from the optimal control routine depends on the sign of the pitch angle, the found optimal control solution does not always result in the global optimum. It is recommended to loop the pitch angle interval for an integer amount of variations and select the routine resulting in the minimum return time for each end state considered.
- *The BRS without actuator dynamics has a larger FRS with considerably reduced return times.* The quadcopters without actuator dynamics modelling obtain a larger FRS as well as a BRS with considerably lower return times. For a FRS of T = 0.1 s the largest distribution of the return time of the set without actuator dynamics ranges up to only about 0.3 seconds, despite the much larger pitch angles and pitch rates obtained in the FRS. This is because a system without actuator dynamics can apply a change in rotational acceleration instantaneously, while the actuator dynamics introduce a lag, making the system respond slower. Therefore, including the actuator dynamics in the modelling is essential to obtain realistic reachable sets.

C. Conclusions on the Verification

Both the FRS and BRS estimations have been verified with the analytically obtainable reachable sets of the double integrator system [23]. The verification analysis shows that the (system specific) optimized MC simulation approximates the true forward reachable set with high accuracy. The area percentage error ranges from 3.7% at T = 1 s to less than 1.5% at T = 2.5 s for $N_{traj} \geq 2000$. Increasing the number of trajectories results in an improved estimation of the true set up until a certain number of trajectories after which the error converges towards the errors originating from numerical inaccuracies. The accuracy of the converged sets can then be improved by decreasing the numerical integration timestep.

The verification of the BRS shows accurate approximations on estimation of the boundaries of the BRS using the minimum-time optimal control routine. Errors are found in the order of less than 2% to about 0.34% of the total estimated states within the backward reachable sets of time-windows of 1, 1.5, 2 and 2.5 seconds. It should be noted that the performance of the BRS estimation is dependent on the time-step and the margin used around the optimal control curve in the minimum-time optimal control routine. The optimal control routine with a margin of $\pm 2 \cdot dt$ results in the best accuracy performance for the simulation conditions considered in the analysis. Most errors occur near the upper- and lower corners, due to the inability of estimating the control curve on a grid, resulting in incorrect optimal control inputs.

Additionally, the often used *Level-Set Toolbox* [27] has been briefly verified to the analytical sets as well in order to benchmark the performance of the MC simulation with respect to an existing tool which uses the Level-Set method. From the verification it can be concluded that the MC simulation exceeds the performance of the *Level-Set Toolbox* in both accuracy as well as computation time.

D. Conclusions on the Validation

An experimental validation has been performed to validate the estimation of the forward reachable sets from the MC simulation. The edge case scenarios of reaching the maximum and minimum pitch angle and rate (the top and bottom corners of the envelopes) as a function of time were considered. From the validation analysis it can be concluded that the reachable set estimates, as presented in this work, underestimate the sets with respect to the validation flight data. The simulation data show a large underestimation with respect to the validation flight data. The average errors at T = 0.1 s for the pitch up and pitch down maneuvers of the pitch angle are 44.39% and 26.84%. The average errors at T = 0.1 s for the pitch up and pitch down maneuvers of the pitch rate are 27.30% and 27.84%. This underestimation is mainly the result of the quadcopter actuator dynamics which are modelled with too high time constants. A possible explanation of the difference is that the default actuator dynamics are identified on data from a quadcopter flown in "angle mode" while the validation flights have been performed in "rate mode". The "angle mode" has an additional control loop including data from the accelerometer for angle control. The additional control loop possibly results in larger delays, resulting in slower actuator dynamics on the default model. Moreover, the commanded inputs to the rotors may be different as well. The feedback loop oriented "angle mode" controller leads to less aggressive inputs than the feedforward oriented "rate mode" controller. Since the rotor speed commands change faster, the rotor speed output changes more aggressively in "rate mode" and hence a smaller time constant is found. Another possible source for the differences is the observed difference in scaling of the commanded and measured rotor speeds in the flight controller software which directly influences the parameter estimation as well.

The quadcopter models with updated actuator dynamics (identified on the validation data only) show a large decrease in (absolute) error with the validation data compared to the default models. The error is reduced on average by about 18% at T = 0.1 s. This results in an average error at T = 0.1 s for pitch up and pitch down for the pitch angle of 13.75% and 14.70%. The average errors at T = 0.1 s for the pitch up and pitch down maneuvers of the pitch rate are reduced to 12.07% and 11.69%. The pitch rate is generally being overestimated, which is expected when comparing an open-loop simulation with closed-loop performed flight maneuvers. Exceptions are the battery forward configuration (both maneuver directions) and the battery aft maneuver (pitch down direction) which underestimate the pitch rate. This could indicate that these models are estimated insufficiently and a re-analysis would be required. For all quadcopter configuration models the pitch angle is overestimated for the pitch down maneuver, and underestimated for the pitch up maneuver. This is as expected since, although undesirable, all validation maneuvers start with a slightly nonzero positive initial pitch angle (and rate).

XI. Recommendations

The recommendations of this work have been split into the recommendations which follow from the research and recommendations for improving the research itself. Finally recommended follow-up research subjects are proposed.

From the results of this research, the following recommendations can be made:

- To obtain the largest possible forward reachable set (FRS) with smallest return times, defined as the backward reachable set (BRS), it is recommended to place the center of gravity position near the rotor plane center. Any center of gravity offset reduces the reachable set area and increases return times in the BRS.
- The actuator dynamics largely affect the results of the reachable sets obtained, hence it is essential in any quadcopter analysis to include the actuator dynamics in the modelling. The effects of the actuator dynamics show a larger impact on the reachable sets than the effects of the center of gravity offsets. Therefore, it is recommended to further develop the performance of the actuator dynamics as it has a large impact on the reachability of the quadcopter, and thus on the performance of the quadcopter as a whole.
- The quadcopter is a very fast system and hence it is recommended to consider time-windows for reachability analysis in the order of less than or about half a second (for the platform as used in this work).
- For FRS estimation of a quadcopter model, it is recommended to use a Monte-Carlo (MC) simulation rather than the *Level-Set Toolbox* [27], as it has been shown to outperform the toolbox in terms of both accuracy and computation time. Although a more thorough space- and time complexity analysis is recommended. The MC simulation is preferred provided that the system under consideration is control *affine*, such that *bang-bang* control can be used which drastically reduces the sampling space. Additionally, a (system specific optimized) tuning parameter should be used to optimize for boundary estimation, which reduces the required number of trajectories.

The following improvements can be made on the presented research itself:

- The model identification procedures in this work have used signals which have been pre-processed by the flight control software. In particular the gyro data. This directly influences the identified model parameters. Hence, it is recommended to use the raw measurement signals for model identification.
- The data obtained for model identification have been collected from manual piloted (line-of-sight) flights. Consequently the pitching maneuvers, aimed to only excite the pitching moment, are contaminated with unintentional roll- and yaw inputs (although small). Furthermore, manual flights result in a variance among repeated maneuvers. Although in some applications this is desirable as more variations in the input result in exploring a wider range

of the dynamics, in this work the goal was to identify the differences between system dynamics which require identical system inputs. Hence for this analysis it is more desirable to automate flying maneuvers for model identification.

- The reachability analysis has been applied on a quadcopter model without including any (non-rotor) aerodynamic effects. It is recommended to further explore the analysis in the high speed regime and/or include nonlinear effects, such as propwash, to analyse the effects on the reachable sets in extreme flight conditions.
- The pitching moment models do not include the effects of the center of gravity offsets for pitch angles greater than ± 90 degrees (with a pitch angle bounded between $\pm$ 180 degrees). To improve results for envelopes exceeding these angles, model identification on flights with an extended flight regime should be performed. The models could also be extended by for example manipulating the sign of the bias to capture the effects of gravity on the mass unbalance when exceeding ± 90 degrees.
- The validation data show that the quadcopter has an initial nonzero pitch angle and pitch rate at the beginning of the maneuvers. This phenomenon occurred when switching from "angle mode" to "rate mode". To improve future validation analysis it is recommended to eliminate this effect as the validation analysis was designed to start at a zero angle and rate. Furthermore, a consistently larger control moment for the pitch down maneuvers was achieved compared to the pitch up maneuvers. It is recommended to investigate the cause of this asymmetry as symmetrical control moment inputs would benefit the validation analysis. Possible sources are (asymmetrical) differences between the rotor blades and/or motor functionalities. This could be explored by swapping the front and aft blades and/or motors and repeating the flight maneuvers.
- The optimal control routine in this work has been applied around a fixed looping range of pitch angles. Consequently, the trajectory inputs from the control routine do not always provide the global optimum minimum-time solution. In order to find the global optimum, it is recommended to loop the pitch angle range for an integer amount of variations and select the control trajectory resulting in a minimum return time.
- The verification of the BRS has only be performed with respect to the boundary of some selected analytical sets. It is recommended to further verify the estimated return times also within and outside the boundaries of the considered sets. This could be done by for example increasing the amount of analytical sets used in the verification for various time-windows. Furthermore, instead of checking whether the return time estimation is within time-window of the analytical set, the estimated return times can be directly compared to the time-window of the analytical set which intersects the state in question.
- An additional model identification analysis on the actuator dynamics showed substantial different model parameter estimates when using data from a quadcopter flown in "rate mode" only. This motivates further analysis on system identification of the quadcopter model on "rate mode" data only and compare its validation performance. Since the possible explanation of these differences might originate from the differences in control loops, it is recommended to develop a method to perform system identification flights in an open-loop fashion for complete controller-free actuator dynamics model identification.
- The validation analysis has been performed only on the edge cases of the forward reachable sets, which include the maximum and minimum pitch angle and rate of the set. To improve the validation on the FRS, an experiment should be designed which extends to the other edges of the flight envelope as well.
  Furthermore, no validation has been performed on the BRS. A validation experiment could be designed which for example replicates the control inputs from simulation, or implement the *bang-bang* optimal control routine onto the quadcopter, in order to validate the optimal control routine by comparing the time to return to the hover condition from a particular state.
- The results from this work cannot directly be compared to the results from other quadcopter platforms. It is recommended to normalize the states with the dimensions of the platform in order to compare to other platforms. Furthermore, to account for varying flight conditions, a normalization can be done with respect to (aerodynamic) conditions, such as the air density.

To further expand upon the results followed from this research in the framework of reachability analysis of quadcopters, the succeeding follow-up research subjects are proposed:

- In order to apply flight envelope protection (FEP) in the framework of quadcopters, the definition of loss of control (LOC) with respect to the Safe Flight Envelope (SFE) should be better researched and defined. This definition, including the time-window(s) considered, can be very application specific (e.g. how fast the system is and how much "space" is available) and will depend on the safety and performance requirements.
- The optimal control routine, as developed in this work, to return from any end state to hover condition in minimum-time proofs to work in simulation. This optimal control routine can be used to further investigate its application in for example endpoint control and/or implement the routine onto a real quadcopter. The *bang-bang* optimal control in the context of position control has already be proven to work on quadcopters showing improved performance compared to a PID controller [34].
- In extension to the item above, the methods as shown in this work, applied on the pitch channel, can be extended to the roll channel directly. The reachability results could be combined to allow for FEP on both the pitch and roll

channel simultaneously (e.g. in an uncoupled fashion). Position control using the *bang-bang* optimal control can be applied, as done in Westenberger et. al [34], but including a safety guarantee from the FEP system.

- The FRS as a function of time expands in a similar fashion as the double integrator system. For the reachable sets of the double integrator analytical solutions exists [23]. With the results from this research, which adds knowledge on how the sets grow in time, as well as to what extend the actuator dynamics affect the sets, it could be possible to construct an analytical approximation of the reachable set for a quadcopter model including actuator dynamics. This is relevant for example in the framework of a database-driven approach, in which interpolation and/or extrapolation of sets could be beneficial in terms of efficiency and performance for real-time applications [5].
- Besides the attitude state-space domain as investigated in this research, the reachability analysis could be extended to include position and/or velocity envelopes. The envelopes could be used in trajectory planning and/or obstacle avoidance [35]. With the results of this work, the trajectory planning can be extended to not only include the dynamics of the quadcopter, with actuator dynamics, but also add a safety guarantee based on the reachable set analysis in the framework of the SFE (e.g. to guarantee a trajectory change within a specified time-window).

REFERENCES

[1] FAA, "Faa aerospace forecast, fiscal years 2020-2040," FAA, Tech. Rep., 2020. [Online]. Available: https://www.faa.gov/data_research/aviation/aerospace_forecasts/media/FY2020-40_FAA_Aerospace_Forecast.pdf.

[2] C. M. Belcastro, R. L. Newman, J. Evans, D. H. Klyde, L. C. Barr, and E. Ancel, "Hazards identification and analysis for unmanned aircraft system operations," in *17th AIAA Aviation Technology, Integration, and Operations Conference*, Denver, Colorado: American Institute of Aeronautics and Astronautics, Jun. 5, 2017, ISBN: 978-1-62410-508-1. DOI: 10.2514/6.2017-3269. [Online]. Available: https://arc.aiaa.org/doi/10.2514/6.2017-3269.

[3] T. Lombaerts, S. Schuet, D. Acosta, J. Kaneshige, K. Shish, and L. Martin, "Piloted simulator evaluation of safe flight envelope display indicators for loss of control avoidance," *Journal of Guidance, Control, and Dynamics*, vol. 40, no. 4, pp. 948–963, Apr. 2017, ISSN: 0731-5090, 1533-3884. DOI: 10.2514/1.G001740. [Online]. Available: https://arc.aiaa.org/doi/10.2514/1.G001740.

[4] S. R. Schuet, T. Lombaerts, D. M. Acosta, J. T. Kaneshige, K. R. Wheeler, and K. H. Shish, "Autonomous flight envelope estimation for loss-of-control prevention," *Journal of Guidance Control and Dynamics*, vol. 40, pp. 847–862, 2017.

[5] Y. Zhang, "Database-driven online safe flight envelope prediction and protection for enhanced aircraft fault tolerance," Ph.D. dissertation, Delft University of Technology, 2019. DOI: 10.4233/UUID:70778C5C-3F00-4854-A0FB-98B24C9ED1CB. [Online]. Available: http://resolver.tudelft.nl/uuid:70778c5c-3f00-4854-a0fb-98b24c9ed1cb.

[6] E. R. v. Oort, "Adaptive backstepping control and safety analysis for modern fighter aircraft.," Ph.D. dissertation, Delft University of Technology, S.l., 2011. [Online]. Available: https://repository.tudelft.nl/islandora/object/uuid%3A68fd89ff-aad6-4ad8-b280-d2fe8b500d48.

[7] T. Lombaerts, S. Schuet, K. Wheeler, D. M. Acosta, and J. Kaneshige, "Safe maneuvering envelope estimation based on a physical approach," in *AIAA Guidance, Navigation, and Control (GNC) Conference*, Boston, MA: American Institute of Aeronautics and Astronautics, Aug. 19, 2013, ISBN: 978-1-62410-224-0. DOI: 10.2514/6.2013-4618. [Online]. Available: https://arc.aiaa.org/doi/10.2514/6.2013-4618.

[8] M. Yin, Q. P. Chu, Y. Zhang, M. A. Niestroy, and C. C. de Visser, "Probabilistic flight envelope estimation with application to unstable overactuated aircraft," *Journal of Guidance, Control, and Dynamics*, vol. 42, no. 12, pp. 2650–2663, Dec. 2019, ISSN: 1533-3884. DOI: 10.2514/1.G004193. [Online]. Available: https://arc.aiaa.org/doi/10.2514/1.G004193.

[9] G. Terrell and D. Scott, "Variable kernel density estimation," *The Annals of Statistics*, vol. 20, Sep. 1992. DOI: 10.1214/aos/1176348768.

[10] S. Sun, C. C. de Visser, and Q. Chu, "Quadrotor gray-box model identification from high-speed flight data," *Journal of Aircraft*, vol. 56, no. 2, pp. 645–661, 2019. DOI: 10.2514/1.C035135. [Online]. Available: https://doi.org/10.2514/1.C035135.

[11] Y. Zhang and J. Jiang, "Bibliographical review on reconfigurable fault-tolerant control systems," *Annual Reviews in Control*, vol. 32, no. 2, pp. 229–252, Dec. 2008, ISSN: 13675788. DOI: 10.1016/j.arcontrol.2008.03.008. [Online]. Available: https://linkinghub.elsevier.com/retrieve/pii/S1367578808000345.

[12] J. J. van Beers, "Development of a system identification routine, with prediction reliability estimates, suitable for modelling high-speed and aggressive quadrotor flight outdoors [TO BE SUBMITTED]," Delft University of Technology, Dec. 21, 2021. [Online]. Available: https://repository.tudelft.nl/islandora/object/uuid%3A4677f001-bc4f-4990-be0e-4316ec9f8847.

[13] E. J. J. Smeur, Q. Chu, and G. C. H. E. de Croon, "Adaptive incremental nonlinear dynamic inversion for attitude control of micro air vehicles," *Journal of Guidance, Control, and Dynamics*, vol. 39, no. 3, pp. 450–461, Mar. 2016, ISSN: 1533-3884. DOI: 10.2514/1.G001490. [Online]. Available: https://arc.aiaa.org/doi/10.2514/1.G001490.

[14] S. Sun, M. Baert, B. Schijndel, and C. De Visser, "Upset recovery control for quadrotors subjected to a complete rotor failure from large initial disturbances," May 2020, pp. 4273–4279. DOI: 10.1109/ICRA40945.2020.9197239.

[15] M. Baert, "Quadrotor upset recovery after rotor failure," Delft University of Technology, 2019. [Online]. Available: http://resolver.tudelft.nl/uuid:4e1011c7-2db9-4dfe-a910-f2843414b960.

[16] C. Ke, K.-Y. Cai, and Q. Quan, "Uniform fault-tolerant control of a quadcopter with rotor failure," *IEEE/ASME Transactions on Mechatronics*, pp. 1–11, 2022. DOI: 10.1109/TMECH.2022.3202804.

[17] A. Lanzon, A. Freddi, and S. Longhi, "Flight control of a quadrotor vehicle subsequent to a rotor failure," *Journal of Guidance, Control, and Dynamics*, vol. 37, no. 2, pp. 580–591, 2014. DOI: 10.2514/1.59869. eprint: https://doi.org/10.2514/1.59869. [Online]. Available: https://doi.org/10.2514/1.59869.

[18] L. Tang, M. Roemer, J. Ge, A. Crassidis, J. Prasad, and C. Belcastro, "Methodologies for adaptive flight envelope estimation and protection," in *AIAA Guidance, Navigation, and Control Conference*, Chicago, Illinois: American Institute of Aeronautics and Astronautics, Aug. 10, 2009, ISBN: 978-1-60086-978-5. DOI: 10.2514/6.2009-6260. [Online]. Available: https://arc.aiaa.org/doi/10.2514/6.2009-6260.

[19] T. Lombaerts, S. Schuet, D. Acosta, and J. Kaneshige, "On-line safe flight envelope determination for impaired aircraft," in *Advances in Aerospace Guidance, Navigation and Control*, J. Bordeneuve-Guibé, A. Drouin, and C. Roos, Eds., Cham: Springer International Publishing, 2015, pp. 263–282, ISBN: 978-3-319-17517-1 978-3-319-17518-8. DOI: 10.1007/978-3-319-17518-8_16. [Online]. Available: http://link.springer.com/10.1007/978-3-319-17518-8_16.

[20] T. Lombaerts, S. Schuet, D. Acosta, and J. Kaneshige, "Piloted simulator evaluation of safe flight envelope display indicators for loss of control avoidance," *American Institute of Aeronautics and Astronautics*, vol. 40, no. 4, p. 28, 2017.

[21] H. N. Nabi, T. Lombaerts, Y. Zhang, E.-J. Van Kampen, Q. Chu, and C. De Visser, "Effects of structural failure on the safe flight envelope of aircraft," *Journal of Guidance, Control, and Dynamics*, vol. 41, pp. 1–19, Feb. 10, 2018. DOI: 10.2514/1.G003184.

[22] A. Paranjape, N. Sinha, and N. Ananthkrishnan, "Use of bifurcation and continuation methods for aircraft trim and stability analysis - a state-of-the-art," in *45th AIAA Aerospace Sciences Meeting and Exhibit*, Reno, Nevada: American Institute of Aeronautics and Astronautics, Jan. 8, 2007, ISBN: 978-1-62410-012-3. DOI: 10.2514/6.2007-1051. [Online]. Available: https://arc.aiaa.org/doi/10.2514/6.2007-1051.

[23] J. V. Carroll and R. K. Mehra, "Bifurcation analysis of nonlinear aircraft dynamics," *Journal of Guidance, Control, and Dynamics*, vol. 5, no. 5, pp. 529–536, 1982. DOI: 10.2514/3.56198. eprint: https://doi.org/10.2514/3.56198. [Online]. Available: https://doi.org/10.2514/3.56198.

[24] M. Althoff and B. Krogh, "Reachability analysis of nonlinear differential-algebraic systems," *Automatic Control, IEEE Transactions on*, vol. 59, pp. 371–383, Feb. 1, 2014. DOI: 10.1109/TAC.2013.2285751.

[25] I. Kitsios and J. Lygeros, "Launch-pad abort flight envelope computation for a personnel launch vehicle using reachability," in *AIAA Guidance, Navigation, and Control Conference and Exhibit*, San Francisco, California: American Institute of Aeronautics and Astronautics, Aug. 15, 2005, ISBN: 978-1-62410-056-7. DOI: 10.2514/6.2005-6150. [Online]. Available: https://arc.aiaa.org/doi/10.2514/6.2005-6150.

[26] S. Sun and C. De Visser, "Quadrotor safe flight envelope prediction in the high-speed regime: A monte-carlo approach," Jan. 2019. DOI: 10.2514/6.2019-0948.

[27] I. Mitchell and J. Templeton, "A toolbox of hamilton-jacobi solvers for analysis of nondeterministic continuous and hybrid systems," vol. 3414, Mar. 2005, pp. 480–494, ISBN: 978-3-540-25108-8. DOI: 10.1007/978-3-540-31954-2_31.

[28] S. Sun, C. C. de Visser, and Q. Chu, "Quadrotor gray-box model identification from high-speed flight data," *Journal of Aircraft*, vol. 56, no. 2, pp. 645–661, 2019. DOI: 10.2514/1.C035135. eprint: https://doi.org/10.2514/1.C035135. [Online]. Available: https://doi.org/10.2514/1.C035135.

[29] S. Sun, R. Schilder, and C. C. de Visser, "Identification of quadrotor aerodynamic model from high speed flight data," in *2018 AIAA Atmospheric Flight Mechanics Conference*, Kissimmee, Florida: American Institute of Aeronautics and Astronautics, Jan. 8, 2018, ISBN: 978-1-62410-525-8. DOI: 10.2514/6.2018-0523. [Online]. Available: https://arc.aiaa.org/doi/10.2514/6.2018-0523.

[30] J. Svacha, K. Mohta, and V. Kumar, "Improving quadrotor trajectory tracking by compensating for aerodynamic effects," in *2017 International Conference on Unmanned Aircraft Systems (ICUAS)*, 2017, pp. 860–866. DOI: 10.1109/ICUAS.2017.7991501.

[31] C. Powers, D. Mellinger, A. Kushleyev, B. Kothmann, and V. Kumar, "Influence of aerodynamics and proximity effects in quadrotor flight," in Jan. 2013, pp. 289–302, ISBN: 978-3-319-00064-0. DOI: 10.1007/978-3-319-00065-7_21.

[32] M. Athans and P. L. Falb, *Optimal control : an introduction to the theory and its applications / Michael Athans, Peter L. Falb*, English. McGraw-Hill New York ; Sydney, 1966, xiv, 879 p.

[33] A. Adardour, "Non-linear reachability analysis using multivariate b-splines," *[to be published]*, 2016. [Online]. Available: http://resolver.tudelft.nl/uuid:19aab69b-3f58-4519-82e8-20a43146666f.

[34] J. Westenberger, C. D. Wagter, and G. C. H. E. de Croon, "Onboard time-optimal control for tiny quadcopters," *Proceedings of the 12th International Micro Air Vehicle Conference*, [IMAV2021-11], 2021. [Online]. Available: http://www.imavs.org/papers/2021/11.pdf.

[35] H. Seo, C. Youngdong Son, D. Lee, and H. Jin Kim, "Trajectory planning with safety guaranty for a multirotor based on the forward and backward reachability analysis," in *2020 IEEE International Conference on Robotics and Automation (ICRA)*, Paris, France: IEEE, May 2020, pp. 7142–7148, ISBN: 978-1-72817-395-5. DOI: 10.1109/ICRA40945.2020.9196760. [Online]. Available: https://ieeexplore.ieee.org/document/9196760/.

[36] J. J. Van Beers and C. C. De Visser, "Peaking into the black-box: Prediction intervals give insight into data-driven quadrotor model reliability," in *AIAA SCITECH 2023 Forum*, National Harbor, MD & Online: American Institute of Aeronautics and Astronautics, Jan. 23, 2023, ISBN: 978-1-62410-699-6. DOI: 10.2514/6.2023-0125. [Online]. Available: https://arc.aiaa.org/doi/10.2514/6.2023-0125.

[37] S. F. Armanini, M. Karásek, G. C. H. E. de Croon, and C. C. de Visser, "Onboard/offboard sensor fusion for high-fidelity flapping-wing robot flight data," *Journal of Guidance, Control, and Dynamics*, vol. 40, no. 8, pp. 2121–2132, 2017. DOI: 10.2514/1.G002527. eprint: https://doi.org/10.2514/1.G002527. [Online]. Available: https://doi.org/10.2514/1.G002527.

[38] C. Powers, D. Mellinger, A. Kushleyev, B. Kothmann, and V. Kumar, "Influence of aerodynamics and proximity effects in quadrotor flight," in Jan. 2013, pp. 289–302, ISBN: 978-3-319-00064-0. DOI: 10.1007/978-3-319-00065-7_21.

APPENDIX

APPENDIX A
MOMENT OF INERTIA & CENTER OF GRAVITY POSITION MEASUREMENTS

This appendix chapter contains additional information on the moment of inertia measurements in Appendix A-A and center of gravity position measurements in Appendix A-B.

A. Moment of Inertia Measurements

The moment of inertia of the quadcopter configurations has been determined by using a bifilar pendulum set-up. For determination of the moment of inertia around the Y-axis, I_{yy}, for example, the quadcopter has been attached to a chord on two locations on the frame such that the quadcopter would hang parallel with the body X-axis pointing towards the (flat) ground, i.e. the length of the chords (in tension) between the quadcopter and the pendulum frame are the same. See Fig. 45 for an illustration of the pendulum set-up. From the geometry of the pendulum, assuming the small angle approximation and sinusoidal motion, and Newton's second law for rotation, the moment of inertia can be determined by:

$$I = \frac{mgD^2T^2}{16\pi^2 L} \tag{33}$$

With m the mass of the quadcopter, g the gravitational acceleration of 9.81 m/s^2, D the distance between the two chords, T the period of the sinusoidal oscillation and L the length of the two chords. An illustration of the measurement set-up can be found in Fig. 45.

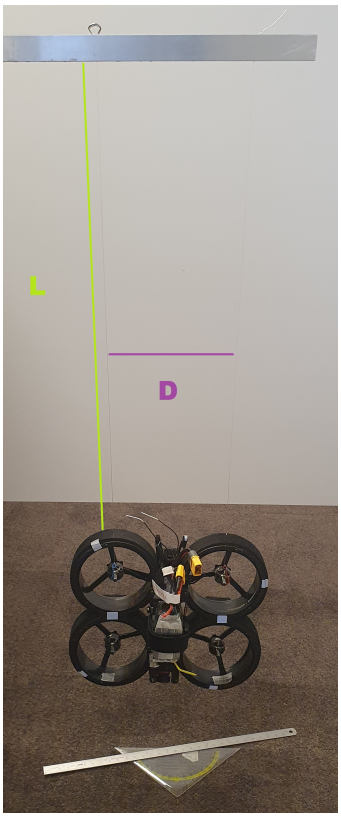

Fig. 45. Set-up for the moment of inertia measurements. In the picture the quadcopter is positioned for measurement of the moment of inertia around the X-axis. Two rulers are used to generate inputs which are within the small angle approximation.

To induce a rotational oscillation, the quadcopter is hold at an angle around the Y-axis ensuring that a pure rotation is induced around this axis only, while respecting the small angle approximation. The quadcopter is then released and the oscillations are logged with the onboard gyro. A summary of the measured moment of inertia around the Y-axis for each quadcopter configuration can be found in Table XX.

The period of the oscillation is estimated by dividing the measurement time by the amount of oscillations counted within the time-window. The amount of oscillations are estimated by fitting a curve through the pitch rate measurements and counting the amount of peaks. An illustration of a representative oscillation can be found in Fig. 46.

TABLE XX
MEASUREMENTS OF THE MOMENT OF INERTIA FOR VARIOUS OSCILLATIONS. THE AVERAGE VALUE HAS BEEN USED AS THE FINAL INERTIA VALUES.

$I_{yy}[kgm^2]$	Aft	Half Aft	Neutral	Half Forward	Forward
1	1.05e-03	1.01e-03	9.54e-04	9.94e-04	1.17e-03
2	1.11e-03	1.01e-03	9.53e-04	7.13e-04	1.32e-03
3	1.14e-03	8.89e-04	9.04e-04	1.06e-03	1.43e-03
4	1.15e-03	8.91e-04	8.59e-04	1.06e-03	1.37e-03
5	1.15e-03		9.08e-04	1.06e-03	1.35e-03
Average	1.12E-03	9.51E-04	9.16E-04	9.79E-04	1.33E-03

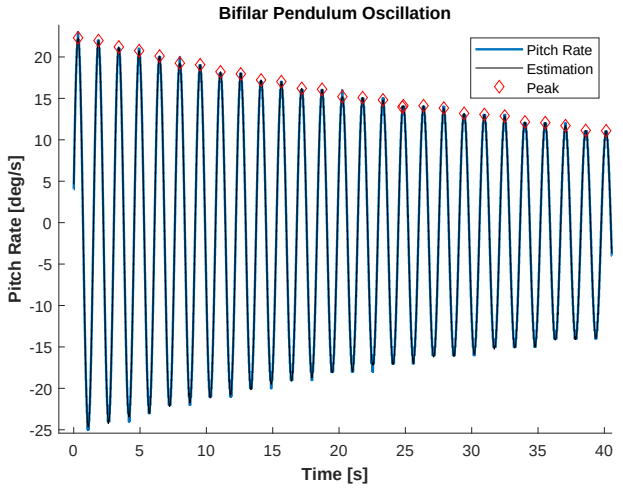

Fig. 46. Example of an oscillation. Both the pitch rate signal and the fitted estimation function are plotted, as well as a highlight of the found peaks.

Both the length of the chords, L (0.524 m), and the distance between the chords, D (0.0096 m), has been measured with a ruler with accuracy of 1 mm. The maximum error due to inaccurate measurements on average amounts to $\pm 4.296e^{-05}$ kgm^2.

It should be noted that due to safety reasons the measurements have been performed with all four propellers removed. The mass of the for set of propellers accounts for 12.46 $gram$, consequently the total mass of the quadcopter (including the battery) used in the moment of inertia measurements amounts to 375.78 $gram$.

An overview of the results from measurements of the moment of inertia around the X-axis and Z-axis can be found in Table XXI. Note that the displacement of the battery along the Y-axis and Z-axis have been limited, hence it is assumed that the I_{xx} remains constant across all quadcopter configurations.

TABLE XXI
FINAL RESULTS FROM THE MOMENT OF INERTIA MEASUREMENTS AROUND THE ROLL AND YAW AXIS.

$I[kgm^2]$	Aft	Half Aft	Neutral	Half Forward	Forward
I_{xx}	8.56e-04	8.56e-04	8.56e-04	8.56e-04	8.56e-04
I_{zz}	1.64e-03	1.57e-03	1.56e-03	1.48e-03	1.77e-03

B. Center of Gravity Position Measurements

The center of gravity location has been determined by attaching the quadcopter to a rope, and by bringing it in a free steady hanging position. The extension of the chord across the frame has been documented, this procedure has been repeated on multiple attachment points. At the intersection of the found lines the center of gravity is located. A visualization of the set-up can be found in Fig. 47. For each quadcopter configuration three attachment points are used, and the measurements were repeated twice. The distance of the center of gravity location to the rotor plane center has been measured with a steal ruler. Hence the reading accuracy is ± 0.5 mm, taking into account for parallax effects.

Errors on the measurements that are expected to largely affect the results originate from the following sources:

- Alignment of the vertical laser with the attachment chord has been done visually, which is prone to induce random errors.
- The vertical laser has been self-leveled with an accuracy of $\pm$ 3 mm per 10 meter.
- The accuracy of documenting the extension of the chord onto the quadcopter frame was affected by unintentionally changing the location of the quadcopter when touching the quadcopter.

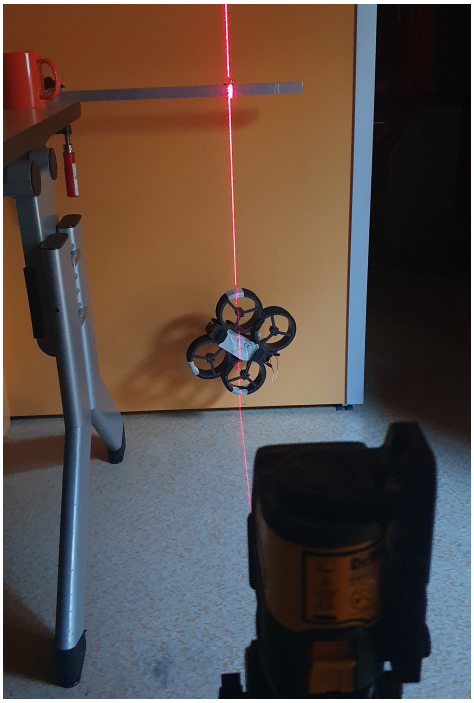

Fig. 47. Set-up for the center of gravity position measurements. The extension of the chord across the quadcopter frame has been determined with the aid of a vertical laser.

APPENDIX B
DATA PROCESSING & FLIGHT DATA RESULTS

The data obtained from the flights are pre-processed and prepared to be used in the system identification process. For the largest part, the data processing and identification code from the work of Van Beers [36] have been used. In order to identify the parameters in the pitching moment model as proposed, the relevant data signals include the data from the gyroscope, containing angular speed measurements, and the rotor speeds. An overview of all the data sources can be found in Table XXII. In this appendix chapter details on the data processing can be found in Appendix B-A, in Appendix B-B an elaborate analysis on the flight data is performed and in Appendix B-C the flight regime in which the flight data have been obtained can be found.

A. Data Processing

Before any data pre-processing is applied, it should be noted that the "raw" data used comes from the onboard logging blackbox which has been filtered before added to the log. The flight software (Betaflight) filters the on-board sensor data (IMU and ESC) in order to remove noise (motor vibration noise and general broadband noise) from the signals which are used in the PID control loop. Filtering of the signals are mostly done on the gyro data and on the D-term in the PID controller in order to obtain a smooth signal for better controller performance. Filtering introduces a delay which could degrade the responsiveness of the quadcopter, hence tuning of the filters involves a trade-off between noise attenuation and time-delay. The primary focus is on filtering the gyro data, which consists of multiple dynamic notch filters which track the peak frequency of the noise using real-time Fast-Fourier Transform analysis. The data used in this analysis are the filtered data from the flight software, as Betaflight logs the data after the filtering process, consequently the data do not contain the pure raw signals from the sensors. It is important to keep in mind that any effects of the filtering have a direct effect on the obtained model parameters. Both the default controller and the default filter settings from BetaFlight Configurator V10.8.0 have been used. The flight data from the on-board gyroscope and the rotor speed data are illustrated in Fig. 48 and Fig. 49.

The onboard sampling rate has been set to 500 Hz, however from inspecting the data, the sampling rate has been varying, see Fig. 50. For this reason all on-board data signals have been linearly interpolated (spline interpolator) and re-sampled at 500 Hz to obtain consistent data signals.

In order to improve the quality of the models, state estimation with an extended Kalman filter (EKF) has been applied in order to mitigate any biases originating from measurement (and/or process) noise. The process equations from Armanin et. al [37] has been used. The bias varies during flight maneuvers, as shown in Fig. 51, which is the result of incorrect dynamics modelling in the equations for state estimation. Consequently, at the beginning of each flight the quadcopter has been kept stationary on the ground, for a few seconds, to

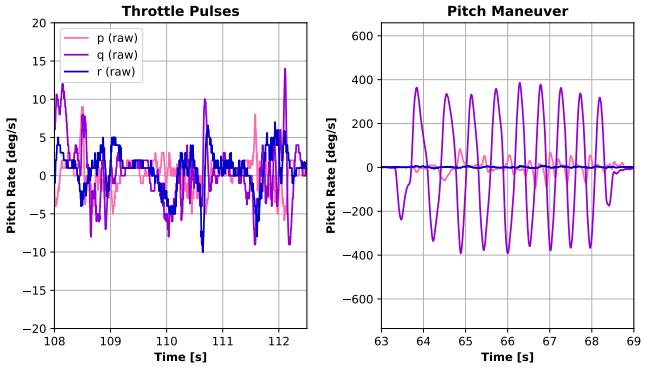

Fig. 48. Illustration of part of the rotational rate measurements from the gyro (battery neutral configuration). Note that, although labeled as raw, these signals come from the pre-filtered data from the flight software.

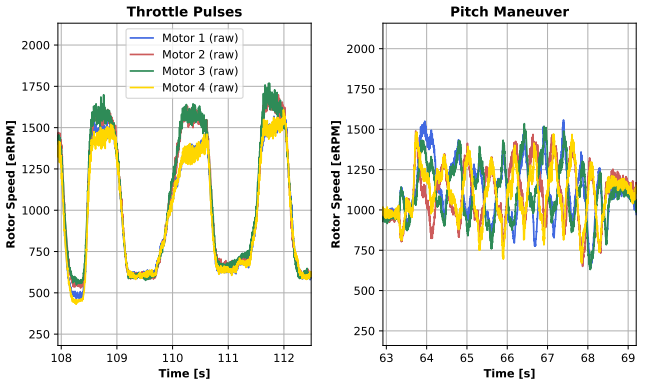

Fig. 49. Illustration of part of the rotor speed measurements from the ESC (battery neutral configuration). Note that, although labeled as raw, these signals come from the pre-filtered data from the flight software.

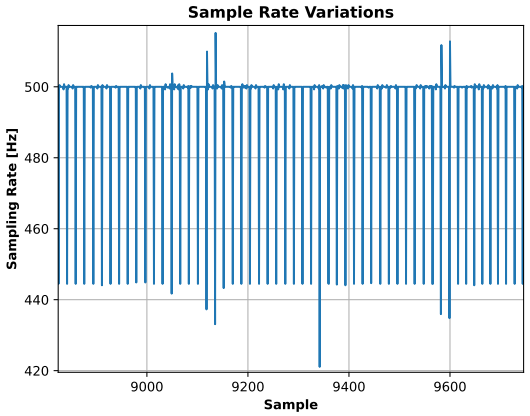

Fig. 50. Sample variations in the datalogging of the on-board IMU. Possible sources on the variations are clock jitter, parallel processes, and clearing the memory buffer.

TABLE XXII
SUMMARY OF THE MEASUREMENT SOURCES. THE OPTITRACK POSITION IS THE POSITION OF THE CENTER OF THE RIGID BODY IDENTIFIED FROM THE MARKERS ON THE QUADCOPTER, OFFSET CORRECTIONS TO THE CENTER OF GRAVITY LOCATION ARE EXCLUDED.

Measurement Device	Data	Sampling Rate	Reference Frame
On-board MEMS Gyroscope	Rotational rate (p, q, r)	500 Hz	Body Frame
On-board MEMS Accelerometer	Specific force (a_x, a_y, a_z)	500 Hz	Body Frame
On-board ESC (Bidirectional DSHOT)	Rotor Speed [eRPM]	500 Hz	
On-board Blackbox	Rotor Speed Commanded	500 Hz	
OptiTrack	Position (X, Y, Z)	120 Hz	OptiTrack Frame
	Attitude (Quaternions)		

allow convergence of the EKF bias estimate. The data from the gyro are corrected for the estimated bias found from this stationary period for each flight.

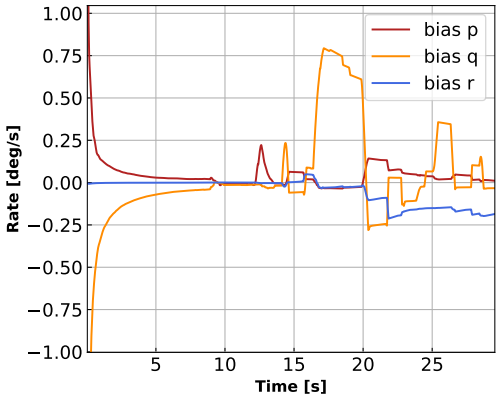

Fig. 51. Bias estimates from the EKF at the beginning of a flight maneuver. For $t > 12$ seconds the quadcopter takes off from the ground.

To further remove any noise on the signal, the unbiased gyro data is additionally filtered with a low pass filter (4rd order Butterworth filter). Since the movement area of a quadcopter is generally between 0 - 80 Hz the cutoff frequency is set at 100 Hz. See Fig. 52 of an illustration of the signals in frequency domain before and after low pass filtering. Note that a zero phase forward-backward filter has been applied.

With the (unbiased) filtered gyro data, and the measured moment of inertia, the pitching moment M can be determined as follows:

$$\mathbf{M} = \mathbf{I} \begin{bmatrix} \dot{p} \\ \dot{q} \\ \dot{r} \end{bmatrix} + \begin{bmatrix} p \\ q \\ r \end{bmatrix} \times \mathbf{I} \begin{bmatrix} p \\ q \\ r \end{bmatrix} \tag{34}$$

The first term accounts for the change of angular rate of the quadcopter around its center of mass, the second term is a compensation for the rotation of the body frame. The rotational acceleration has been obtained by the finite-difference method applied on the rotational rate measurements from the gyro. An illustration of the processed moment signals from a flight can be found in Fig. 53.

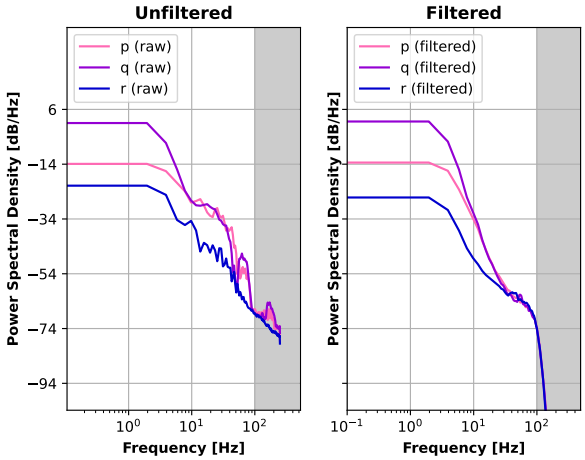

Fig. 52. The power spectral density of the gyro data before and after filtering the signal with a 4rd order Butterworth filter.

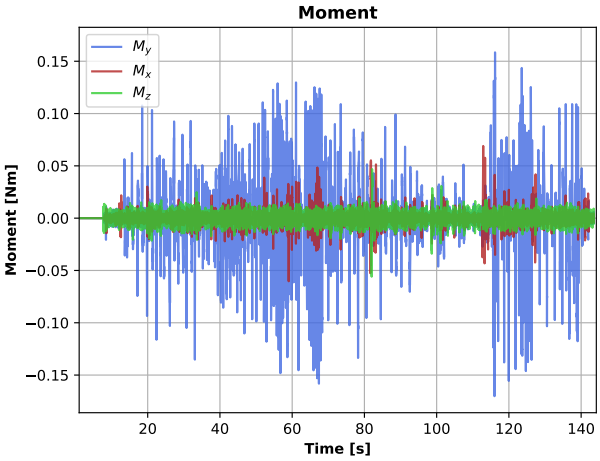

Fig. 53. Illustration of the moment signals of a flight with the battery neutral configuration. The pitching moments are used in the system identification for parameter estimation of the pitching moment models.

B. Flight Data Analysis

The flight data have been analyzed in order to find relevant patterns to be used in the design of the regressor model design. The longitudinal variations of the center of gravity from the rotor plane center causes a change in distribution of rotor speeds among the four motors to obtain a force and moment equilibrium. The data distribution of the rotor speeds of all quadcopter configurations are plotted in Fig. 54, as well as the control pitching moment in Fig. 55. As expected, the center of gravity location closest to the rotor plane center has a more symmetrical distribution while a further displacement center of gravity position causes an increase in rotor speed of the motors near the offset location. This correlation is clearly visible in the control pitching moment data distribution in Fig. 55. When inspecting the data of the control pitching moment and the pitching moment this correlation is visible as well as illustrated in Fig. 56 and Fig. 57. An overview of the correlations of the pitch angle, rate and control moment can be found in Fig. 58. Although the flight regime for the pitch angle and rate are similar among the configurations, different control moments are required to attain them. This supports that including control pitching moment regressor terms enhances the approximation power of the model to capture the effects of the center of gravity offsets.

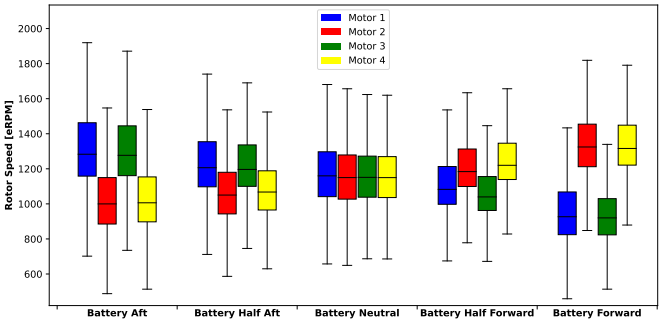

Fig. 54. Data distribution of the rotor speeds of all quadcopter configurations. The closer the center of gravity to the rotor plane center, the more symmetrical the data distribution among the four motors.

C. Flight Regime

The flight regime in which the flight data have been obtained for parameter identification, dictates the ranges of the domain in which the model is valid. For illustration purposes the position trajectory of a flight with the battery neutral configuration is displayed in Fig. 59.

The relevant flight envelope parameters for the pitching moment models as used in this work include the speed regime, the pitching moment, the control pitching moment and both the pitch angles and rates. The velocity profile of all flight data per quadcopter configuration can be found in Fig. 60. The data of the pitching moment are displayed in Fig. 61.

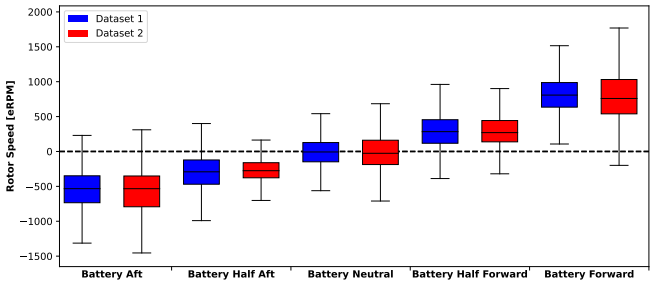

Fig. 55. Data distribution of the control pitching moment of all quadcopter configurations. Data are shown for the two flights per quadcopter configuration separately to show reproducibility of the flight data results.

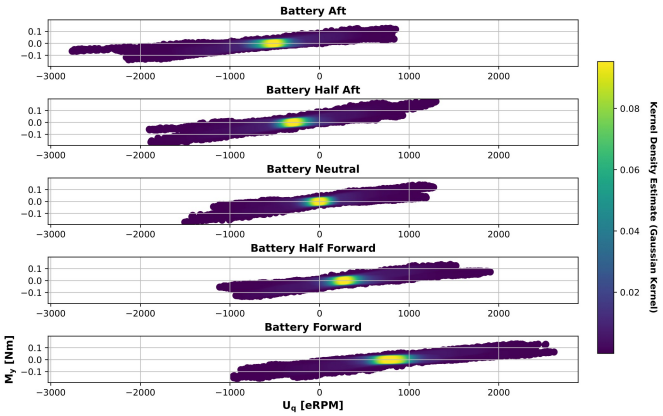

Fig. 56. The control pitching moment versus the pitching moment measured. The correlation between the control pitching moment and center of gravity offset is visible from the location of the highest probability density values. The distribution is estimated using a Kernel Density Estimate with a Scott bandwidth estimation (Gaussian kernel). Note that for more extreme offset positions a higher control pitching moment is required to obtain similar pitching moments. In Fig. 57 the data are illustrated in one figure to show the relative differences between the configurations.

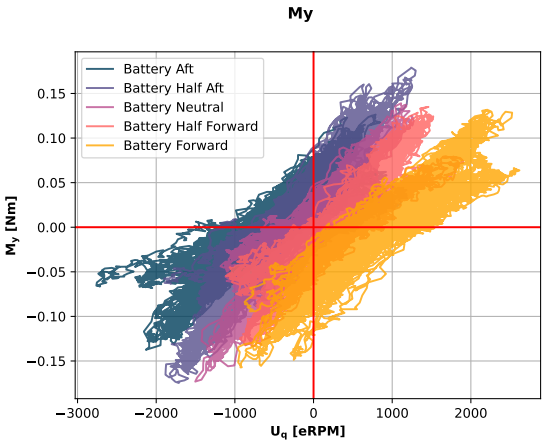

Fig. 57. The control pitching moment versus the pitching moment measured relative to battery configuration. Note that for more extreme offset positions a higher control pitching moment is required to obtain similar pitching moments.

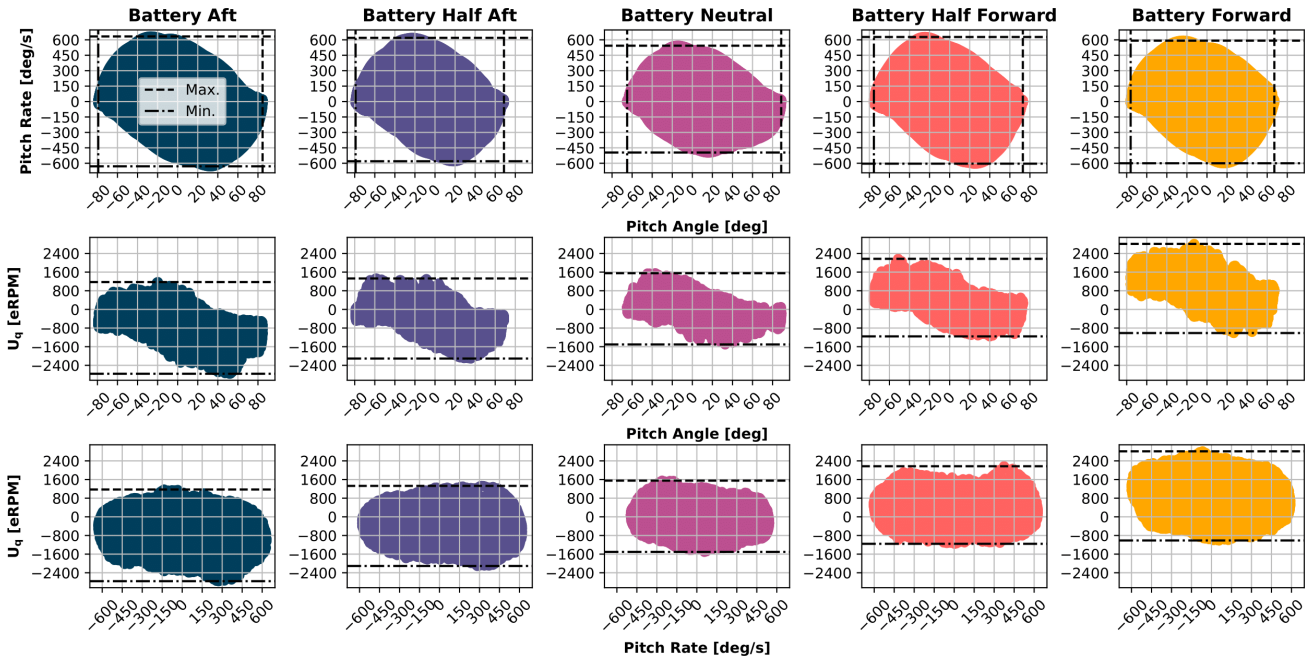

Fig. 58. Plots of the pitch angle, rate and control moment. Note that for more extreme offset positions a higher control pitching moment is required to obtain similar angular position and rates.

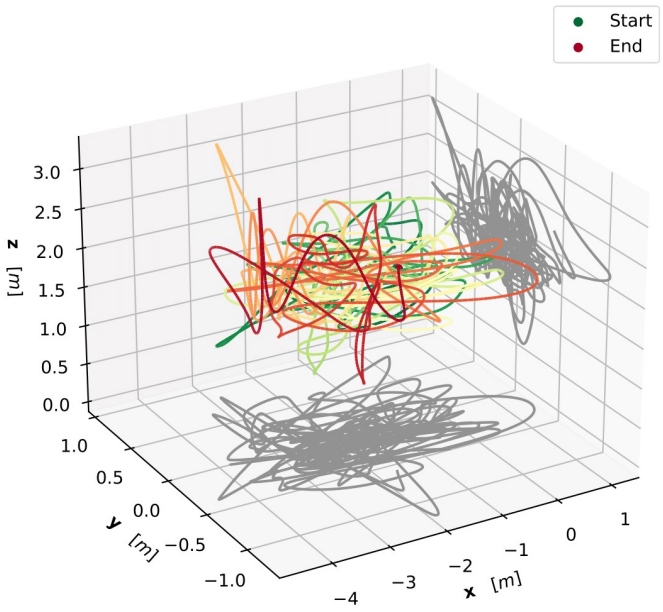

Fig. 59. Position trajectory of a flight with the battery neutral configuration.

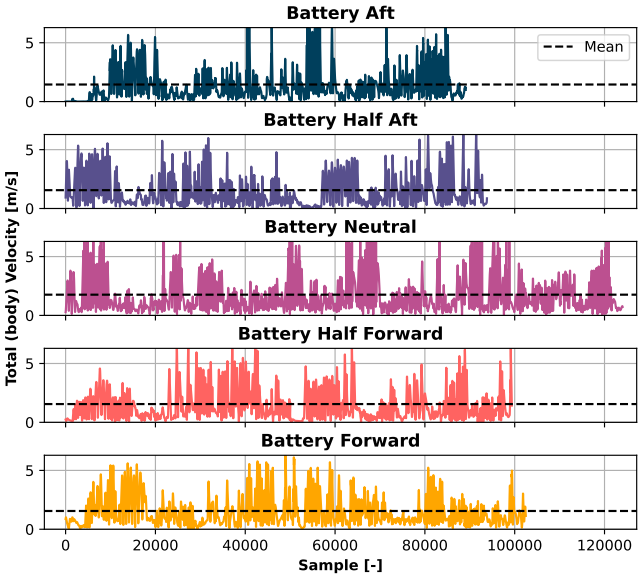

Fig. 60. Total speed computed from the position obtained from the OptiTrack system. It can be observed that the average speed is about 1.5 m/s.

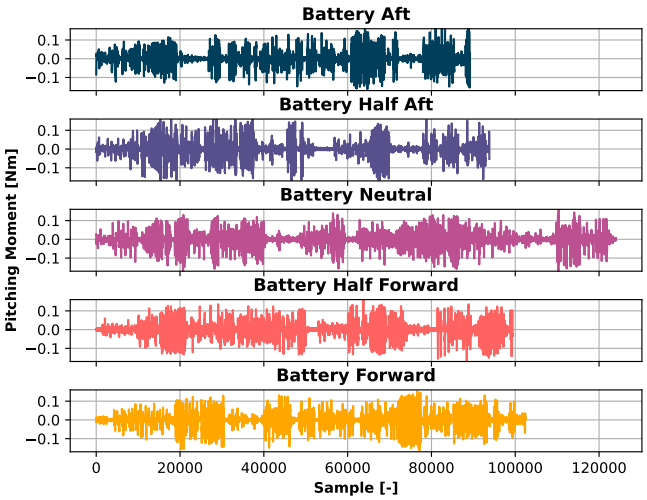

Fig. 61. Pitching moment of all flight data. It can be observed that most data is bounded between $\pm 0.1\ Nm$ for all quadcopter configurations.

APPENDIX C
IDENTIFIED MODEL DETAILS

With the identified parameters the moment models can be used in the quadcopter simulation. A response analysis is done by performing an open-loop control input. The responses of the models to a maximum pitch up and pitch down can be found in Fig. 62 and Fig. 63.

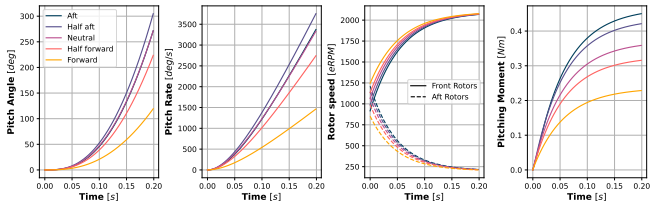

Fig. 62. Response of the quadcopter models to a pitch up maneuver with front rotors commanded to the maximum 2100 eRPM and the aft rotors to the minimum of 200 eRPM. Note the differences in steady-state pitching moment between the quadcopter configurations.

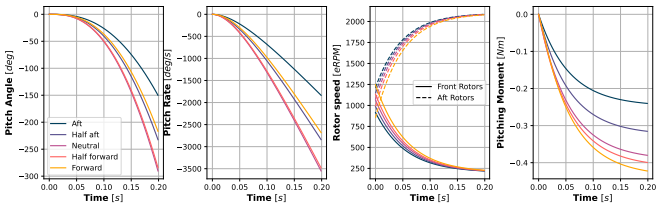

Fig. 63. Response of the quadcopter models to a pitch down maneuver with front rotors commanded to the minimum 200 eRPM and the aft rotors to the maximum of 2100 eRPM. Note the differences in steady-state pitching moment between the quadcopter configurations.

The reachability analysis has been performed from a steady hover condition. In order to obtain a steady hover, the hover

TABLE XXIII
ESTIMATION OF THE HOVER ROTOR SPEEDS PER QUADCOPTER CONFIGURATION [ERPM].

Battery Position	**Front Rotors**	**Aft Rotors**
Aft	916.60	1211.17
Half Aft	988.482	1145.45
Neutral	1064.81	1075.10
Half Forward	1133.55	989.96
Forward	1246.43	852.31

rotor speeds have been determined for each quadcopter configuration model individually. An OLS model identification have been performed with stepwise regression to identify the F_z and F_x models. Note that due to the center of gravity offset with respect to the IMU sensor, a correction on the acceleration measurements have been performed using:

$$a_S = a_B + \dot{\omega}_B \times r + \omega_B \times (\omega_B \times r) \tag{35}$$

With a_s the specific forces measured by the IMU, a_b the "true" body accelerations, ω_b the body rotational rates and r the position vector from the center of gravity position to the IMU sensor. When assuming only a displacement along the X-axis the corrected acceleration reduces to:

$$a_b = a_s + \begin{pmatrix} q^2 + r^2 \\ -(\dot{r} + pq) \\ \dot{q} - pq \end{pmatrix} l \tag{36}$$

With l the distance from the center of gravity to the IMU sensor along the X-axis. The analysis on the data showed that mostly the acceleration in the Z-axis direction was affected by the center of gravity offset due to the large pitching maneuvers. Although, the absolute mean residual was about 6% for the a_Z signals, and hence the effect of the offset on the IMU data can be considered negligibly low.

The models are build up by the regressors selected by the stepwise regression algorithm with a maximum of 15 regressors. This resulted in models with $R^2 > 0.98$ for all quadcopter configurations. A PID controller is implemented to control the quadcopter to maintain zero pitch angle, rate, and zero velocity in the Z-direction. After a steady-state condition had been reached the rotor speeds were documented. A summary of the estimated hover rotor speeds can be found in Table XXIII.

APPENDIX D
SYSTEM IDENTIFICATION

In this appendix chapter more information can be found on the system identification procedure. In Appendix D-A the procedure of regressor selection can be found. Additional information on the stepwise regression and regressor analysis can be found in Appendix D-B. Model performance illustrations can be found in Appendix D-C followed by details on parameter estimation statistics in Appendix D-D. Finally, in Appendix D-E a model residual analysis is performed.

A. Regressor Selection Analysis

For a well-balanced selection of the specific modelling terms (i.e. regressors) the following sources have been addressed:

- **Flight Data** The flight data used in the model identification show relevant patterns which can be used to design regressor terms in order to capture the differences in dynamics between the various battery configurations. The flight data analysis in Appendix B reveals that the relative rotor speeds between front- and aft rotors describe a significant difference in dynamics among the various battery configurations. Furthermore, the control pitching moment shows a distinct correlation with the pitching moment among the different quadcopter configurations in Fig. 57. Hence, based on flight data analysis the control pitching moment term in particular seems to be a promising regressor to capture the relevant dynamics.
- **Stepwise Regression** For obtaining a selection of regressors resulting in the best fit to the flight data, a stepwise regression routine has been applied. Regressors are selected from a pool of regressors resulting in the best fit to the flight data. A model fitting process has been performed using step-wise regression up until fifteen regressor terms. The regressor pool consist of all possible combinations of state terms, constructed as polynomials up to a fourth order degree. The analysis shows that generally after around five regressor terms no large improvements in terms of normalized RMSE and R^2 values can be observed, while the complexity of the regressors increases and terms appear that cannot be directly physically explained. More information on stepwise regression can be found in the succeeding section.
- **Regressor Re-occurence Analysis** Step-wise regression can be considered as a greedy algorithm which selects the regressors based on maximizing data fit. As a result regressors can be selected that are more flight data dependent (i.e. noise dependent) while regressors that physically describe the underlying dynamics are not selected. For this reason an additional analysis is performed which documents the regressors that re-occur during stepwise regression but were not selected in the stepwise regression routine. From the analysis on the pitching model, the control pitching moment term re-occurs at second place among all battery configurations in the first step of the routine. This motivates and confirms that this regressor term plays an important role in modelling the pitching moment to capture the differences in dynamics among the battery configurations. More information on this re-occurence analysis can be found in the succeeding section.
- **Literature** As stated earlier, quadcopters are often modelled by only including the effect of the rotor dynamics while neglecting the aerodynamic effects [28][29]. The pitching moment induced by the rotors can be described by the pitch control and is induced by differential thrust of the motors as follows:

$$\vec{M}_y = l\kappa_0(\omega_4^2 + \omega_2^2 - \omega_3^2 - \omega_1^2) \tag{37}$$

With ω_i the rotor speeds per motor i respectively and l the longitudinal distance along the X-axis to the center of rotation, which is equal to the center of gravity when assuming a uniform gravitational field around the quadcopter. κ_0 is a rotor property coefficient dependent on the air density and can be assumed to be constant [29][30][38]. The parameters in the moment model structure used in this work directly capture the effects of l and κ_0. Moreover a bias is added to include the effects of the center of gravity offset. Note that in this work the control pitching moment does not include the square of the rotor speeds which results in a different scaling of the model parameters.

B. Stepwise Regression Procedure & Details

In stepwise regression an algorithm selects regressors from a pool of regressors resulting in the best fit to the data. For quadcopter model identification Sun et. al [29] uses the stepwise regression procedure to select the model regressors to fit the model to high-speed flight data. The same stepwise regression procedure has been used as described in Sun et. al [29]. The routine consists of a forward step, in which a regressor is selected that improves the accuracy of the model the most. And a backward step, in which the model accuracy is analyzed by removing each regressor one-by-one. The regressor that does not increase the accuracy of the model is then removed (as it became redundant after adding the new regressor). If the regressor reappears in the forward step after being removed the algorithm is stopped to prevent an infinite loop.

The stepwise regression analysis showed that mostly nonlinear terms appeared and after about two to five regressors no large improvements in the R^2 and model error appeared, see Fig. 64. An example of the relative contributions of the selected regressors can be found in Fig. 65.

Furthermore, the re-occurrence analysis, in which the top ten regressors which were *not* selected per regression step were documented, consistently showed the importance of the control pitching moment as regressor term. An example of the documentation of unselected regressors per stepwise regression step can be found in Fig. 66.

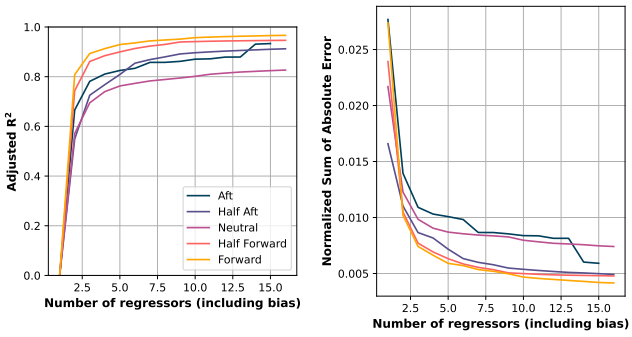

Fig. 64. Adjusted R^2 and normalized error as a function of number of regressors in the model. It can be observed that after five regressors the accuracy of the model starts to converge. Most improvements are made with the first regressor terms. The model results shown have been optimized on a full dataset (without data partitioning).

To keep the models simple and physically explainable, which eases the relative comparison between the quadcopter configurations, it was decided for this work to only select the control pitching moment as regressor in the model. It is recommended when including for example the effects of external aerodynamics interaction, mostly encountered during aggressive and high speed flights, to perform the regressor re-occurence analysis as done in this work. The analysis gives insight into feasible regressors which model the underlying dynamics as the stepwise regression algorithm can be greedy and select the best performing regressor at a cost of higher noise sensitivity.

C. Model Performance Illustration

The performances of the regression models are illustrated for the battery forward configuration on the pitch induced flight maneuvers. These include the low- and high frequency pitching maneuvers (Fig. 67 and Fig. 68), and flying back and forth (Fig. 69).

D. Parameter Estimation Statistics

The extend to which the parameters are sensitive to noise, or the variability of the OLS estimator, can be analyzed by exploring the parameter covariance matrix. The parameter variances, as displayed in Table IV, show that the bias has the largest parameter variance, indicating that this parameter has the largest variability of its estimate with respect to variations in the noise realizations. To analyze the correlation between parameters, the full parameter covariance matrix of all quadcopter models are displayed in Table XXIV (of the validation datasets).

E. Model Residual Analysis

The OLS estimator as used in this work assumes that 1) the error (or model residual) has a constant variance for all measurements and is uncorrelated, and, 2) the residual has zero mean. Thus the model residuals should resemble white noise. These conditions are required to ensure that the estimator is a best linear unbiased estimator (BLUE). In order to quantify the extend to which the model residual resembles white noise, a model residual analysis is performed by exploring the residual signal and the autocorrelation functions. The model residuals of all quadcopter configurations on both training and validation dataset are plotted in Fig. 70. As expected the validation data show a large increase in residual mean value compared to the training datasets, although relatively small. Also most data are within the σ bounds. Hence the estimators can be considered to satisfy 2). In Fig. 71 the autocorrelation functions of the residuals are plotted. It can be observed that, considering the confidence bounds, the residuals do not resemble white noise. However, it should be noted that the confidence bounds are dependent on the number of data points N as follows:

$$conf = \frac{1.96}{\sqrt{N}} \tag{38}$$

This applies to white noise, however when the models are predicting similar maneuvers, similar errors appear while the confidence bound shrinks nonetheless. Indeed, the maneuvers performed to excite the pitching moment are similar and are often repeated. Consequently, similar errors occur, which are observable as "patterns" in the residual data in Fig. 70.

It is highly recommended to perform the same residual analysis on an isolated maneuver or take for example a few seconds before or after a maneuver rather than the full dataset to prevent residual correlations due to repeating or oscillating flight maneuvers.

TABLE XXIV
PARAMETER COVARIANCE MATRICES FOR EACH QUADCOPTER CONFIGURATION. MATRICES ARE ESTIMATED FROM THE VALIDATION DATASETS.

Aft	M_0	M_1	M_2
M_0	4.192893e-08	-9.598106e-11	3.799491e-11
M_1	-9.598106e-11	8.706360e-13	-8.697554e-14
M_2	3.799491e-11	-8.697554e-14	5.214935e-14
Half Aft	M_0	M_1	M_2
M_0	3.580905e-08	-7.155785e-11	4.779818e-11
M_1	-7.155785e-11	5.055205e-13	-9.551595e-14
M_2	4.779818e-11	-9.551595e-14	1.070464e-13
Neutral	M_0	M_1	M_2
M_0	2.832427e-08	-5.007731e-11	4.577028e-11
M_1	-5.007731e-11	2.025016e-13	-8.092184e-14
M_2	4.577028e-11	-8.092184e-14	1.740355e-13
Half Forward	M_0	M_1	M_2
M_0	3.410725e-08	-4.834808e-11	6.664716e-11
M_1	-4.834808e-11	1.096505e-13	-9.447439e-14
M_2	6.664716e-11	-9.447439e-14	4.021293e-13
Forward	M_0	M_1	M_2
M_0	6.472737e-08	-5.017109e-11	1.282646e-10
M_1	-5.017109e-11	5.441901e-14	-9.941969e-14
M_2	1.282646e-10	-9.941969e-14	9.532676e-13

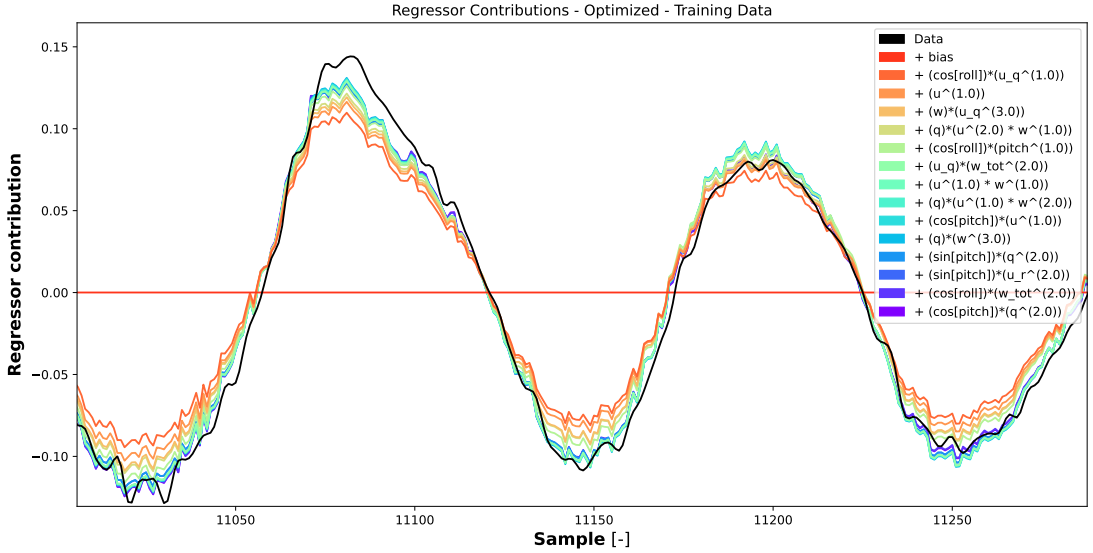

Fig. 65. Relative contributions of the various regressor terms which degrades after about five regressors. Note that the terms are highly nonlinear. The models shown have been optimized on a full dataset (without data partitioning).

Fig. 66. Analysis of the regressors that re-occur among all quadcopter configurations. These regressors are *not* selected by the stepwise regression algorithm but are within the top five of the best performing regressors. Note that in the first selection step the control pitching moment U_q is the first term after the selected regressor that appears in the selection among all quadcopter configurations. This highly suggests that this regressor term captures the underlying dynamics. The models shown have been optimized on a full dataset (without data partitioning).

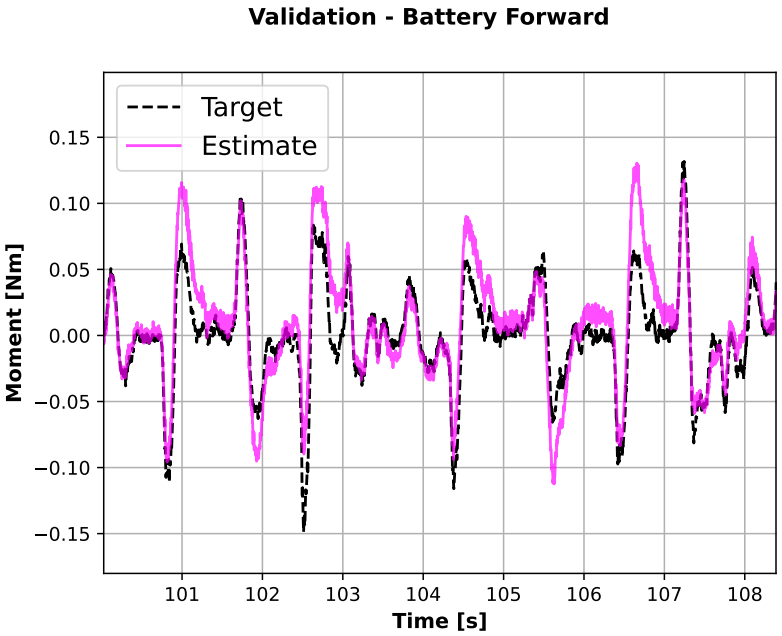

Fig. 67. Performance of the battery forward model on the low frequency pitching maneuvers. The target data concerns the validation dataset.

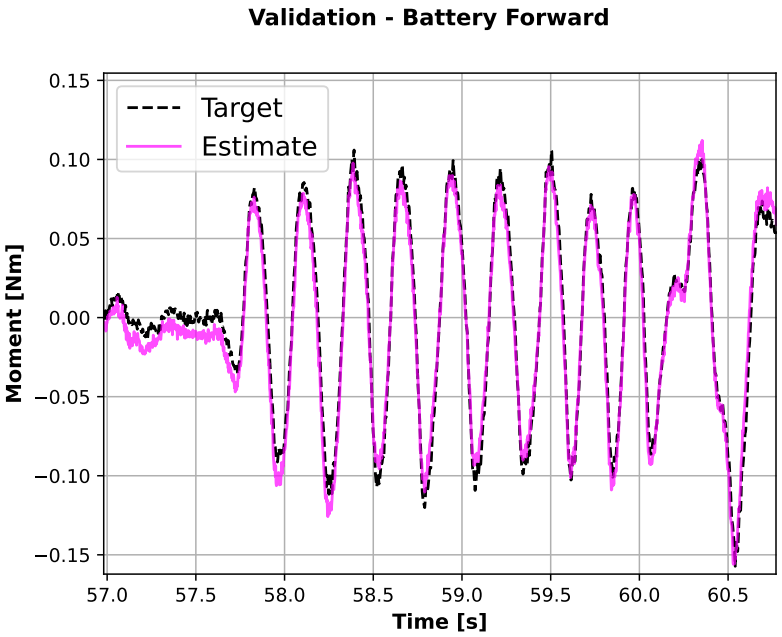

Fig. 68. Performance of the battery forward model on the high frequency pitching maneuvers. The target data concerns the validation dataset.

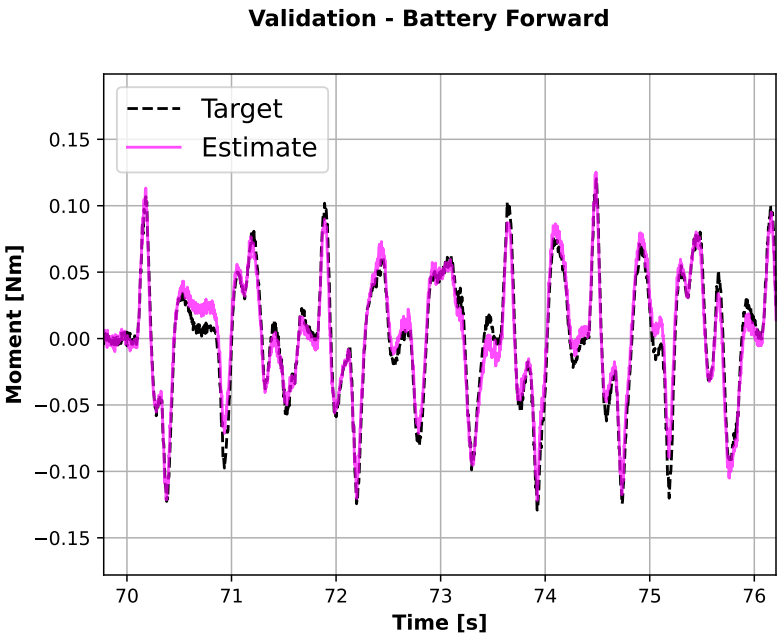

Fig. 69. Performance of the battery forward model on the flying back and forth maneuver. The target data concerns the validation dataset.

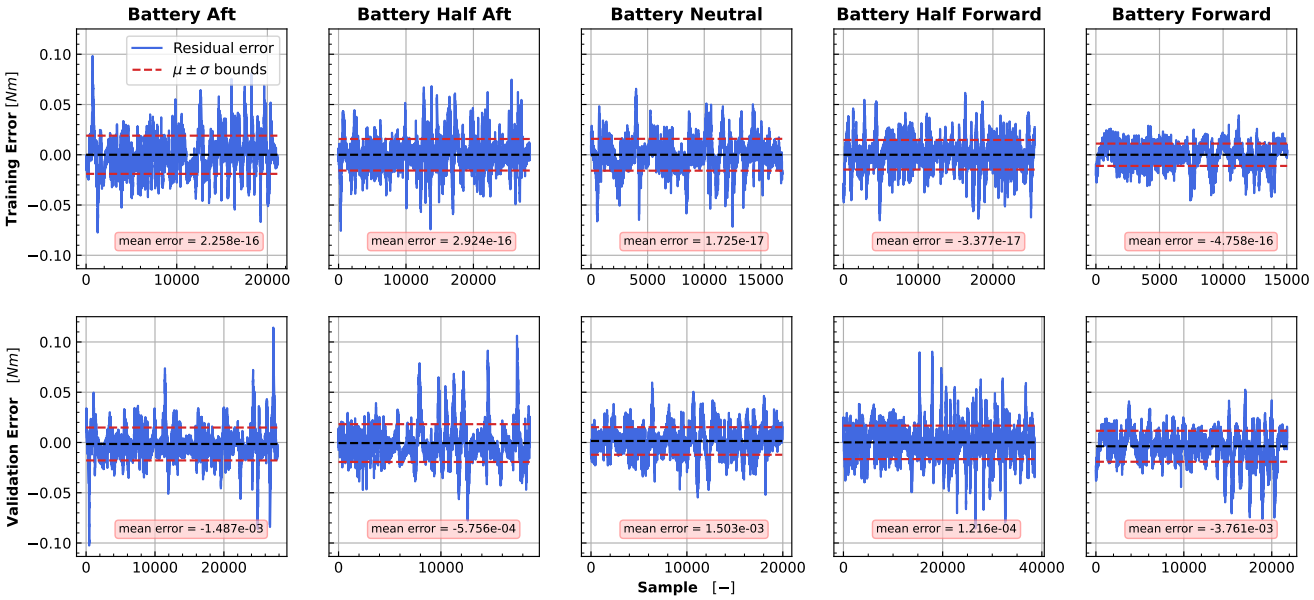

Fig. 70. Model residuals (the difference between the targets and the predictions) for all quadcopter configurations on both the training and validation data. The residual analysis applies on the partitioned datasets.

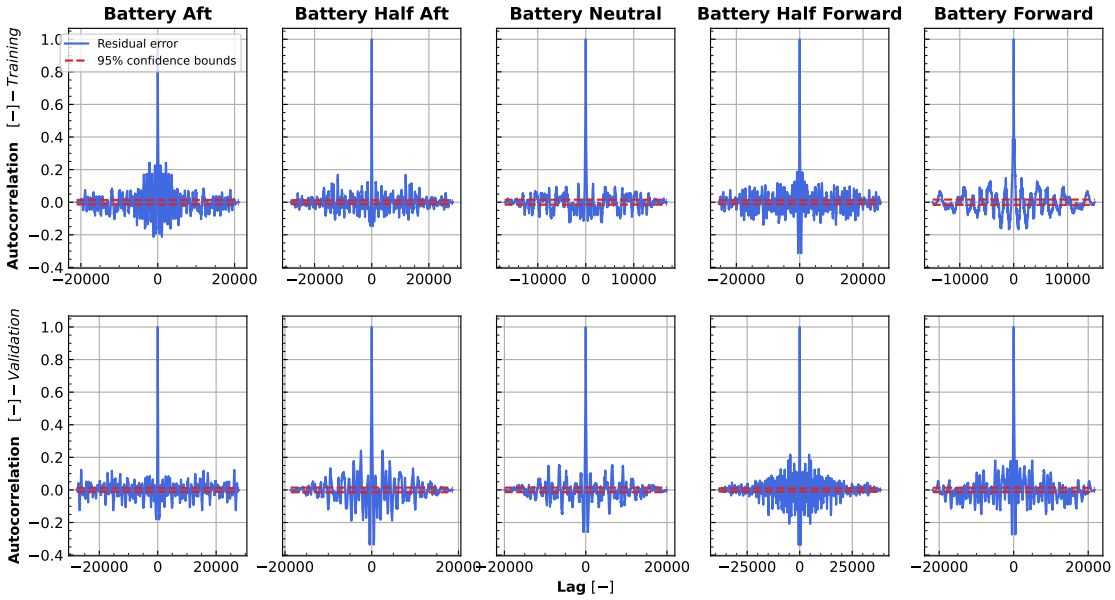

Fig. 71. Autocorrelation functions of the model residuals for all quadcopter configuration on both the training and validation datasets. The 95% bounds are determined by $1.96/\sqrt{N}$, with N the number of data points. The residual analysis applies on the partitioned datasets.

APPENDIX E
VALIDATION EXPERIMENT SET-UP

The validation flights have been performed in the CyberZoo at the faculty over Aerospace Engineering in Delft. The pitching maneuvers have been performed above a net to capture the quadcopter after the maneuver. A picture of the set-up can be found in Fig. 72.

Fig. 72. Validation experiment set-up. The net was necessary to capture the drone after performing the validation flight maneuver.

The procedure for each flight maneuver was as follows:

1) Take-off in “angle mode”.
2) Fly above the net and obtain a steady hover condition.
3) Switch to “rate mode”.
4) Perform a full stick deflection in either the pitch up or pitch down direction while keeping the yaw and roll input zero.
5) Turn off motors after hitting the net and place quadcopter to starting position.
6) Repeat for each quadcopter configuration and pitch direction.

A fully charged battery was used per 15 flight maneuvers, which on average started at about 16.2 Volt (4s battery) and reduced to about 15 Volt.

Since the initial pitch angle at the beginning of the maneuver has to be accurately determined, an external measurement device has been used (OptiTrack). Before the validation flights were performed, the OptiTrack system has been calibrated. This included calibration of the ground plane by placing a calibration square at the origin and levelling it with a level. Furthermore, the maximum sampling rate of 360 Hz has been used to measure the rotations of the quadcopter rigid body. Note that a correction of the offset of the OptiTrack identified rigid body with the quadcopter frame has not been determined nor corrected (if any).

Part II

Literature Review

NOTE:
This part has already been graded under AE4020

3

Introduction Literature Review

Safety in commercial aviation is one of the most important factor taken into account during the design and operation of aircraft. Yet, fatal accidents still occur. From a statistical summary of fatal accidents of commercial jet aircraft occurring from 2011 to 2020 done by the Boeing company it can be concluded that the main cause of fatal accidents is due to loss of control in flight (LOC-I or LOC) [20]. LOC accounts for around 20% of all fatal accidents, and involves most of the fatalities [20]. This has also been confirmed by an accident analysis performed by IATA [21]. Deviation of the aircraft from the nominal flight envelope is a key characteristic of LOC [3][4][5]. Main causes of crossing the flight envelope boundaries are 1) due to pilot unawareness of the envelope 2) lack of guidance for recovery and 3) changes in the flight envelope boundaries which are not identified or monitored (in time) [5]. The first step in preventing LOC includes obtaining knowledge on the dynamic flight envelope. A well known example of a case in which proper knowledge of the (changed) fight envelope could have prevented a fatal accident is the El Al flight 1862 in 1992 [22]. After data analysis of the flight it was found that the aircraft was recoverable even with two engines disattached [23]. This shows the importance of having knowledge on the (updated) flight envelope to prevent entering LOC conditions and hence improving safety.

Besides (commercial jet) aircraft, also a major factor playing a role in safety of Unmanned Aerial Vehicles (UAVs) involves the occurrence of LOC. In Belcastro et al. [2] 100 reported civilian UAV mishaps having a mass less than 25 kg have been analyzed. LOC accounts for the majority of the cases counting 34 mishaps. Also in the analysis of Colgren et al. [12] it was found that 36% of the found UAV mishaps could have been prevented by flight envelope protection and hence has a substantial impact on safety improvement of UAVs. UAVs are being used for various civilian and military applications such as search and rescue missions, delivery of goods, monitoring and other implementations. Since the technology can be considered to be in its early stages, many new applications are expected to arise with their corresponding hazard potentials that come along [2]. The use of (commercial) UAVs has been rising and is expected to grow even more in the future [1]. If no research is done on further improving UAV LOC prevention, the amount of UAV accidents are expected to grow. Hence it is of utmost importance to further develop techniques for UAV safe flight envelope prediction and consequently LOC prevention in order to improve their safety.

The aim of this literature report is to identify areas of improvement for enhancing safety of multirotor UAVs and explore to which extend, and in what form, knowledge can be added to the body of literature to enhance UAV safety. This will be done by means of an extensive literature review on this topic. From the literature review a research objective and research question of the thesis project will formulated. Furthermore, a research methodology will be presented together with a research plan for conducting the proposed thesis project.

The report is structured as follows. In chapter 4 current safety techniques for multirotor UAVs are explored and summarized. In chapter 5 the mainstream and state-of-the-art methods for global flight envelope prediction are identified and described elaborately. With regards to model based prediction techniques, in chapter 6 system identification techniques for multirotor UAVs are investigated. Finally, a conclusion of the literature report is given in chapter 7.

4

Safety of Multirotor UAV

The applications of Unmanned Aerial Vehicles (UAVs) are expected to grow rapidly in the near future [1], however loss of control (LOC) is the main cause of failures for UAVs [2]. In order to improve safety of these systems, development of LOC prevention techniques are of utmost importance. In this chapter current safety techniques with regards to LOC of multirotor UAVs are explored. The goal of this chapter is to summarize current LOC prevention techniques and identify gaps of knowledge that could be further explored to improve safety of multirotor UAVs. In section 4.1 methods for safety improvement of aircraft are described. The definition of the Safe Flight Envelope (SFE) and details regarding the boundary behaviour can be found in section 4.2. In section 4.3 Flight Envelope Protection (FEP) techniques, a method for safety improvement of aircraft, are worked out in more detail. The chapter ends with a conclusion on the findings of this chapter in section 4.4.

4.1. Methods for Safety Improvement

In literature various ways can be distinguished that focus on improving the safety of aircraft. These include fault-tolerant control systems, robust controller and modelling, and safe flight envelope protection and are briefly touched upon below.

1. **Fault-tolerant Control Systems** The development of fault-tolerant control systems consists of a closed-loop control system that is able to (automatically) maintain stability and performance in case an anomaly or failure in the system occurs [24]. This can be done passively, in which a controller is robust against predefined faults, or actively, in which a controller is reconfigurable in case a fault is detected [24]. For the latter an onboard real-time fault detection and diagnostics system is required, which can be model based or applied via data-driven techniques by processing sensor data. Another way of improving safety is by finding ways of recovering from upset conditions. Although not much literature on upset recovery for multirotor UAVs exist, it has been shown that recovering from upset conditions is possible [25][26][27][28].
2. **Robust Controllers and Modelling** A significant amount of multirotor UAV literature (quadcopters in particular) is dedicated towards developing robust controllers [29]. Controllers are designed based on a model of the system which must be an accurate model derived from six degrees of freedom nonlinear system dynamics. Usually (model) uncertainties are not taken into account. Recently there is a trend in developing controllers based on sensor data to relieve the coupling of the controller with the model [30]. Although a model is still required for the control effectiveness. Hence research is still being done on improving (quadcopter) model identification techniques as done in Van Beers [29]. Another method to uncouple controller and model, is through the use of a model-free data-driven system identification. This has been applied to a quadcopter with the use of a fuzzy clustering model in [31].
3. **Safe Flight Envelope Protection** Besides failures that can occur in the system and applying fault-tolerant techniques or develop robust controllers to handle them, another category exist that can cause loss of control. This includes violating the Safe Flight Envelope (SFE) which can be considered as the state space in which an aircraft can be safely operated. Operating outside this envelope is often linked to upset conditions and loss of control, inherently associated with aircraft accident events [32][33][34]. The act of implementing a system that prevents the system to cross

the envelope boundaries is called Flight Envelope Protection (FEP) and requires full knowledge on the flight envelopes. More information on FEP can be found in section 4.3.

Due to the promising nature and still limited research on flight envelopes of multirotor UAVs, this research project will focus on improving and extending knowledge on safe flight envelope prediction and protection techniques. Therefore, the next section will elaborate upon the safe flight envelope, its definition and boundary behaviours.

4.2. The Safe Flight Envelope

The traditional flight envelope definition originates from the (fixed-wing) aircraft literature in which it is defined as the region where the aircraft is constrained to operate, usually described as a function of altitude and airspeed [35]. The usual limiting factors on performance include engine power, stalling, buffet characteristics and structural load [35]. Important to note is that these envelopes consider nominal conditions and only take into account the aircraft performance. An extension to the flight envelope definition is to include environmental conditions and define the flight envelope as the region in the state space in which safe flight is possible. This is referred to as the Dynamic Flight Envelope [6][36] and is defined as the part of the state space for which safe operation of the aircraft and safety of its cargo can be guaranteed and externally posed constraints will not be violated [6]. A definition of the flight envelope with regards to loss of control is the Safe Flight Envelope (SFE), which refers to the set of all the states that can be reached within a certain time-window for which a trajectory exist to return back to a steady-state condition [5][6][7]. This is more formally defined as the intersection of the forward- and backward reachable set, about which more information can be found in the reachability analysis section in chapter 5. The definition for the SFE used in this research is defined as follows:

The Safe Flight Envelope Definition

The Safe Flight Envelope (SFE) is defined as all the possible states which an aircraft can both reach from- and be controlled back to a set of initial flight conditions within a given time-window [8].

Reaching states outside the boundaries of the SFE detriments safe operation and can lead to upset conditions, loss of control (LOC) and eventually a crash. Upset conditions for UAVs can be recovered as seen in Sun et al. [25] and Baert [26], however it is also seen in these literature work that not all conditions can be recovered and eventually the system will enter a LOC condition. The definition of LOC is discussed in the next subsection.

4.2.1. Loss of Control Definition

In Altena [37] an elaborate literature research has been conducted on LOC and its definition. In this work it is concluded that little research has been done on LOC and its prediction, while prevention of LOC can improve the safety of UAVs drastically as it is the main cause of aircraft and UAV accidents[2][12]. The definition of LOC for aircraft is not well defined, and various definitions exist. The traditional flight envelope for fixed-wing aircraft cannot be used to predict LOC of multirotor UAVs because, as identified in Sun et al. [11], multirotor UAVs behave distinctively different than fixed-wing aircraft. Generally, operating outside the SFE as defined in this chapter, is linked to LOC conditions [3][4]. Therefore, this definition will be used for the research project. Two distinct approaches with regards to flight envelope prediction could be identified: focus on predicting boundaries of the SFE locally, and predicting the global SFE. The two approaches are elaborated upon in the next subsection.

4.2.2. Local Envelope Prediction and Global Envelope Prediction

Before LOC prevention techniques can be applied, knowledge is required of the boundaries of the envelope. There are two main approaches that can be taken:

1. **Local Envelope Prediction** This prediction method focuses on local envelope boundary prediction. The idea is to predict whether the system is close towards an envelope boundary and use this information to warn the pilot and/or use a control strategy to stay away from the predicted boundary. A way to predict LOC locally, is by looking at critical transitions. This principle makes

use of warning signals that indicate critical transitions of a system. The most important warning signal is called the critical slowing down principle. The system becomes increasingly slow in recovering from small perturbation as it is approaching a transition [38]. These are called critical thresholds, or tipping points at which the complex system changes from one state to another [38]. This occurs in many complex dynamical systems such as ecosystems and finance, and similar behaviour towards those tipping points are shown for many classes of systems [38]. In case of a multirotor UAV the critical transitions can be seen as transitioning to LOC state. Predicting that a multirotor UAV will transition towards a LOC state can help to employ measures to prevent LOC events to occur. Another way to predict LOC is through the use of neural network models and flight data as done in Altena [37] to predict time to LOC.

2. **Global Envelope Prediction** Global envelope prediction focuses on obtaining full knowledge on envelope boundaries on a global scale. The prediction of the global envelope can be used to develop and implement SFE protection techniques. More details on global boundary prediction methods can be found in chapter 5.

An advantage of having prior knowledge on the global envelope is that SFE protection can be applied. A control strategy can be designed to ensure that the system stays within the SFE in order to preserve the safety of the system by preventing LOC events from occurring. This control strategy could also be exploited by designing it such that the system can be operated close to the boundaries in order to maximize performance. A trade-off between safety and performance can be made for the specific application. Furthermore, on top of the predicted global envelope boundaries, the local boundary prediction methods could be employed in order to locally update the prediction of the globally predicted envelope boundaries. The boundaries of the envelope can be treated as either deterministic or probabilistic as described in next subsection.

4.2.3. Deterministic and Probabilistic Boundaries

In most of the flight envelope literature the boundaries are treated as deterministic bounds in which the envelope is described as a crisp set. See chapter 5 for more details on deterministic envelope prediction methods. Model uncertainties can be taken into account by modelling them as disturbances [39]. However, the safety of a given state depends on various other factors, such as external disturbances, pilot reaction time, actuator dynamics and controller performance [8]. Therefore, it is more realistic to treat the boundaries of the SFE as probabilistic rather than deterministic. In the probabilistic approach the range of possible safe trajectories available can be characterized by this probability [8]. In Yin et al. [8] the definition of the flight envelope has been extended to fuzzy sets with kernel density estimation in order to include a measure for the amount of safety. A visual representation of the difference between deterministic and probabilistic envelopes can be found in Figure 4.1.

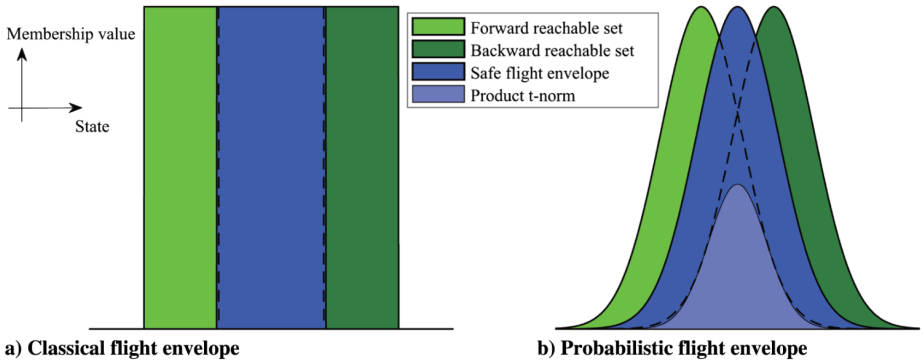

Figure 4.1: Visual representation of the (classical) deterministic flight envelope (a) and probabilistic flight envelope definition for one variable (b) [8]. Formally, the SFE can be defined as the intersection of the forward- and backward reachable set, about which more information can be found in the reachability analysis section in chapter 5.

An advantage of using probabilistic boundaries over deterministic boundaries is that it gives additional information about the safety of a specific point in the envelope. This can be used in flight

envelope protection (FEP) to design the ”aggressiveness” of the protection of the system as a function of the flight envelope [8]. Both in Yin et al. [8] and Sun et al. [11] a Monte-Carlo simulation is used to find the reachable sets of states. However it should be noted that the probability of the input used in the simulation has an effect on the probability distribution of the output as seen in Sun et al. [11]. In the next subsection the sensitivity of the boundaries are discussed.

4.2.4. Envelope Boundary Sensitivity

As indicated in the previous subsection, the boundaries of the flight envelope depend on various factors. In Yin et al. [8] the probabilistic flight envelope of a fixed-wing aircraft has been estimated for various flight conditions, which includes recovery time, equipped control effectors, and mass configurations. It can be seen that when increasing recovery times, the envelope for both angle of attack and pitch angle, and, sideslip angle and yaw rate, expands accordingly while remaining its shape. Whereas a lower mass, enhances agility, and hence the envelope is expanded. The shape has also changed due to center of gravity shifts. It should be noted that in Yin et al. [8] the estimation method has not been validated.

In Brandt et al. [13] a comparison between deterministic and probabilistic reachable sets is made on a simplified aircraft model by adding disturbances. In this paper is it shown that the SFE can shrink substantially when disturbances are included showing that deterministic flight envelopes could lead to dangerously optimistic FEP systems.

4.3. Flight Envelope Protection

Maneuvering within the SFE as defined in section 4.2 will guarantee safe flight and prevent LOC conditions. In order to stay away from the boundaries, protection systems are required which are preferred in both autopilot as well as manual control modes in aircraft [40]. In Lambregts [41] the requirements and approaches for envelope protection design of general aviation and transport aircraft are discussed for both manual and automatic fly-by-wire control. Two main functions of the protection system can be identified, this includes control law design and enhancing pilot awareness [5].

1. **Control Laws** In modern fly-by-wire aircraft limitations of the aircraft imposed by its flight envelope are customary to be implemented in the flight control laws [42]. In this way commands are automatically adjusted when the aircraft is close to LOC [8]. This reduces workload of the pilot [42]. Two types of techniques are *hard limitations* and *soft limitations*. Hard limitations focus on fully limiting the ability of the pilot to fly the aircraft outside the envelope [43], whereas soft limitations still allow pilots to do so [44]. An example of a state that is usually limited in aircraft is the maximum allowed angle of attack [45]. Including a FEP system has been researched in various control configurations which include reconfiguring controllers for fault-tolerant flight control [36], hybrid control [40] and model based predictive control [46].

   In Falkena et al. [46] a flight envelope protection system has been implemented for smaller aircraft for carefree maneuvering. In this paper the following manual FEP approaches are compared:

   - PID Based limiting approach
   - Command limiting approach
   - Constrained Flight Control Law (FCL) using Model Based Predictive Control (MPC)

   An overview of the block diagrams of the FEP control strategies can be found in Figure 4.2. The command limiting is preferred for their application [46]. In Zogopoulos-Papaliakos et al. [47][48] a MPC controller is designed which takes into account the constraints of the trim flight envelope of a fixed-wing nonlinear UAV model. As summarized in Zogopoulos-Papaliakos et al. [47][48] design efforts with regards to dynamic flight envelope protection systems have been employed using MPC. MPC allows to satisfy input- and state constraints hence many fault-tolerant control methods use MPC. However, trade offs between model fidelity and time performance, and, model constraints and feasibility are still an active research area [47].

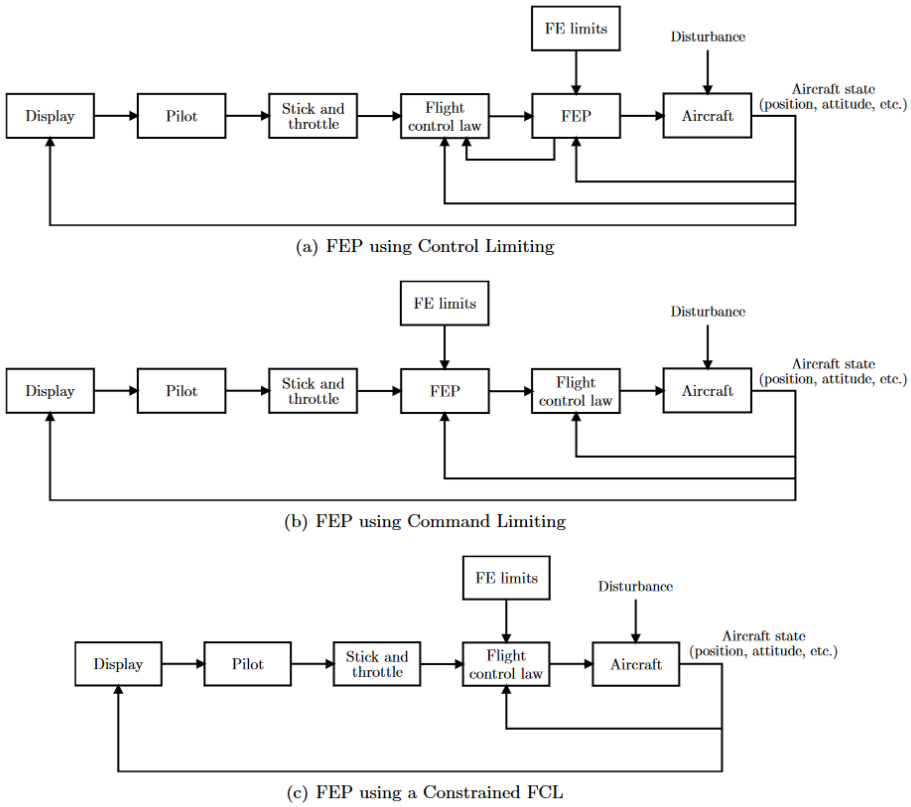

Figure 4.2: Block diagrams for various FEP control strategies to keep the aircraft within the SFE [46].

It should be noted that in traditional general aviation, the protections are implemented for static envelopes. But recently there is a trend in implementing adaptive flight envelope protection systems which use updated envelope limitations [42]. An example of a paper that covers FEP with regards to adaptive flight envelopes includes Tekles et al. [49] which is based on a command limiting approach that accounts for adverse aerodynamics, unusual attitude conditions, and structural integrity. The scheme is implemented around a gain scheduled control law. Another example is Lombaerts et al. [50] in which an adaptive flight envelope is predicted which is used for adaptive FEP in the manual flight control law design to prevent LOC. ”This method is robust with respect to uncertainties in the estimates for the aerodynamic properties.”[50]. Adaptive FEP can also be done by safe switching between flight modes [40]. Local envelope protection can be employed such as avoiding input saturation which is done in Lombaerts et al. [51], however this cannot be considered as a complete protection algorithm.

By adjusting the limitations as defined by the SFE for FEP development, the control law can be designed such to obtain a desired balance between safety and performance for the application of the system.

Instead of using hard limitations, yin et al. [8] proposes to treat the envelope as probabilistic instead of deterministic. As a result the probabilistic boundaries are used to provide additional information. This allows for a novel predictive protection law which can respond earlier and results in gentler protective FEP measures [8]. Instead of hard limiting commands, commands are adjusted during flight [8]. In Yin et al. [8] FEP has been successfully implemented with a novel multiloop nonlinear controller.

2. **Pilot Awareness** Besides control design for preventing operating outside the envelope, another envelope protection technique is by providing cues to the pilot about aircraft limitations. This can be done through a human-machine interface, for example by:

- Displaying visual bounds on a display, e.g. the primary flight display [3][52] .
- Haptic feedback through control loading in the pilot control stick [53][54].

Both above mentioned applications have been implemented in Lombaerts et al. [42] which showed an increase in pilot awareness, a decrease in workload, and a increased amount safety margin used by the pilots preventing LOC in off-nominal conditions.

So far, FEP systems have been discussed with regards to traditional aviation with application to fixed-wing aircraft. In the next subsection envelope protection with regards to multirotor UAV are summarized.

4.3.1. Multirotor UAV Envelope Protection

In Colgren et al. [12] a control system is developed for UAVs with as goal to achieve flight safety during operation as similar to the safety of piloted aircraft. In this paper FEP is proposed that consists of implementing an outer-loop correction for large disturbances that could require maneuver correction, switching of modes or adjusting control inputs to the flight control system. This is implemented with an inner control loop using dynamic inversion methods which enhance the requirements for the outer-loop FEP design. In Vachtsevanos et al. [55] FEP is suggested by a fault detection system in a hierarchical architecture by using sensor fusion and neural network models to detect and identify abnormal situations and switch between modes. The fault-tolerant control system adjusts the available control authority. The mid- and low level controllers are reconfigured accordingly to ensure that the UAV stays within its flight envelope of the selected mode. Another method used for multirotor UAV FEP is through the use of an online trained neural network model for limit prediction and avoidance [56]. Successful avoidance of normal load factor and a rotor stall prediction parameter in a high speed rapid turn in a flight test was achieved [57]. A similar switching between modes strategy is used in Naldi et al. [58] in which a control law is designed for transition maneuvers by using a path following approach with a FEP controller. Obstacle avoidance and operational limit avoidance can be used in parallel by applying them as inequality constraints in a state-space frame in an optimal control solution approach as done for aggressive maneuvers in Moon et al. [59] or through a minimum time approach [60].

The traditional FEP by incorparating (artificial) limits on control system signals as described previously generally results in under-utilization of the operational envelope [61], whereas the extreme maneuverability and agility are the main advantageous characteristics of multirotor UAVs. Hence FEP systems design is required independent of the control system [61]. Finite and time horizon prediction based FEP have been proposed [61]. Finite methods require large modelling and susceptible to model uncertainties, while infinite methods, e.g. the dynamic trim method [62], cannot be used for transient peak limiting [61]. In Unnikrishnan et al. [61] a reactionary approach is developed which modifies system commands to follow a predetermined safe trajectory profile which is close to the boundaries of the envelope. Finite time horizon predictions are estimated through a trained neural network model. Boundary limits are treated as an obstacle to be avoided by moving in the opposite direction. This makes the approach suitable for steady-state and transient peak limiting [61]. This technique is employed to protect load factor limitations and has been verified in simulation and validated in a flight test in an aggressive e-turn maneuver in Unnikrishnan et al. [63].

4.4. Conclusion

The aim of this chapter is to identify areas of improvement for enhancing safety of multirotor Unmanned Aerial Vehicles (UAVs). It is identified that a major factor playing a role in fatal accidents of UAVs involves loss of control (LOC) [2]. Since the use of (commerical) UAVs has been rising and is expected to grow even more in the future [1], it is of utmost importance to prevent LOC conditions to [12]. Operating outside the Safe Flight Envelope (SFE) of an aircraft is linked to loss of control [3][4], which is the main cause of failures for UAVs [2][12]. The SFE is defined as all the possible states which an aircraft can both reach from- and be controlled back to a set of initial flight conditions within a given time-window [8]. A promising technique that prevents the system to cross the envelope boundaries is called flight envelope protection (FEP) and consequently prevents LOC conditions. It is decided to focus on global flight envelope prediction, instead of local prediction. This is because having prior knowledge on the global envelope has as advantage that the FEP system can be developed to balance safety and performance for the specific application. From the literature research it can be concluded

that treating the boundaries as probabilistic is preferred. The reason is because classical deterministic flight envelopes tend to overestimate envelope leading to dangerously optimistic FEP systems [13][14]. Furthermore, in [8] it was shown that the envelope changes shape and size when changing system dynamics, hence in case of system model uncertainties it is more suitable to model the boundaries as probabilistic. Moreover, treating the boundaries as probabilistic allows for earlier responses and gentler protective FEP measures as shown in [8]. Improving techniques and expanding knowledge on (probabilistic) flight envelope prediction could enhance the development of FEP to increase UAV safety as implemented successfully as found in recent UAV literature. Therefore, the next chapter will explore the existing, mainstream and state-of-the-art methods for prediction of the global safe flight envelope.

5

Methods for Predicting the Global Flight Envelope

In literature it is found that in roughly the past ten years there is a trend in developing and investigating methods for determining the (adaptive) Safe Flight Envelope (SFE) for aircraft, usually under various damage case scenarios, see the following references [5][6][36][7][42][50][64][65][66][67][68]. The motivation for improving the techniques for determining the SFE of an aircraft arises from the need for improved flight control in order to enhance safety with regards to post-failure flight due to vehicle damage or abnormal flight conditions [65]. In general, this requires a fault detection and identification system, in order to detect flight anomalies, a method to update the SFE boundaries, and a flight envelope protection system. The application of global SFE determination for multirotor Unmanned Aerial Vehicles (UAVs), however, has only be applied and investigated marginally [11][39][69][70]. This chapter will focus on summarizing the mainstream and state-of-the-art methods for SFE prediction.

Various methods have been used to estimate the global SFE. In the past, due to the lack of analytical tools and simulation capabilities, prediction of solutions to nonlinear aircraft dynamics and control was limited and approximate analytical solutions were used, which were not always reliable [6]. The initial flight envelopes were determined by using windtunnel test and computational fluid dynamics (CFD) analysis, which were verified by expensive flight tests [71]. With improved computational power, the focus turned towards numerical simulations to predict nonlinear (aircraft) dynamics and instabilities. A very important development to allow for flight envelope prediction were the bifurcation and continuation methods introduced by Carroll et al. [72]. With these methods it is possible to compute steady-state solutions for all possible control inputs and was mainly used as analysis during design of flight control laws and flight envelopes [6]. This further branched into the reachability analysis. A state-of-the-art method for determining SFE boundaries are through bio-inspired methods such as artificial neural network models (or neural networks in short) [37][73]. The methods for flight envelope prediction can be roughly divided into two main branches: model based methods and experiment based methods. Although reliable results can be obtained through experiment based methods, they are usually expensive and time-consuming. Hence, model based methods are more extensively applied. A drawback of model based methods is that the results depend on the quality of the model, which always contains differences with the real system. In Figure 5.1 a graphical overview of the in literature identified methods can be found, subdivided over the two main branches.

In section 5.1 model based methods with regards to stability and trim analysis, together with system identification techniques are discussed. Reachability analysis with its corresponding methods are worked out in detail in section 5.2. Neural network models with regards to flight envelope prediction are discussed in section 5.3 and the chapter ends with a conclusion on the findings in section 5.4.

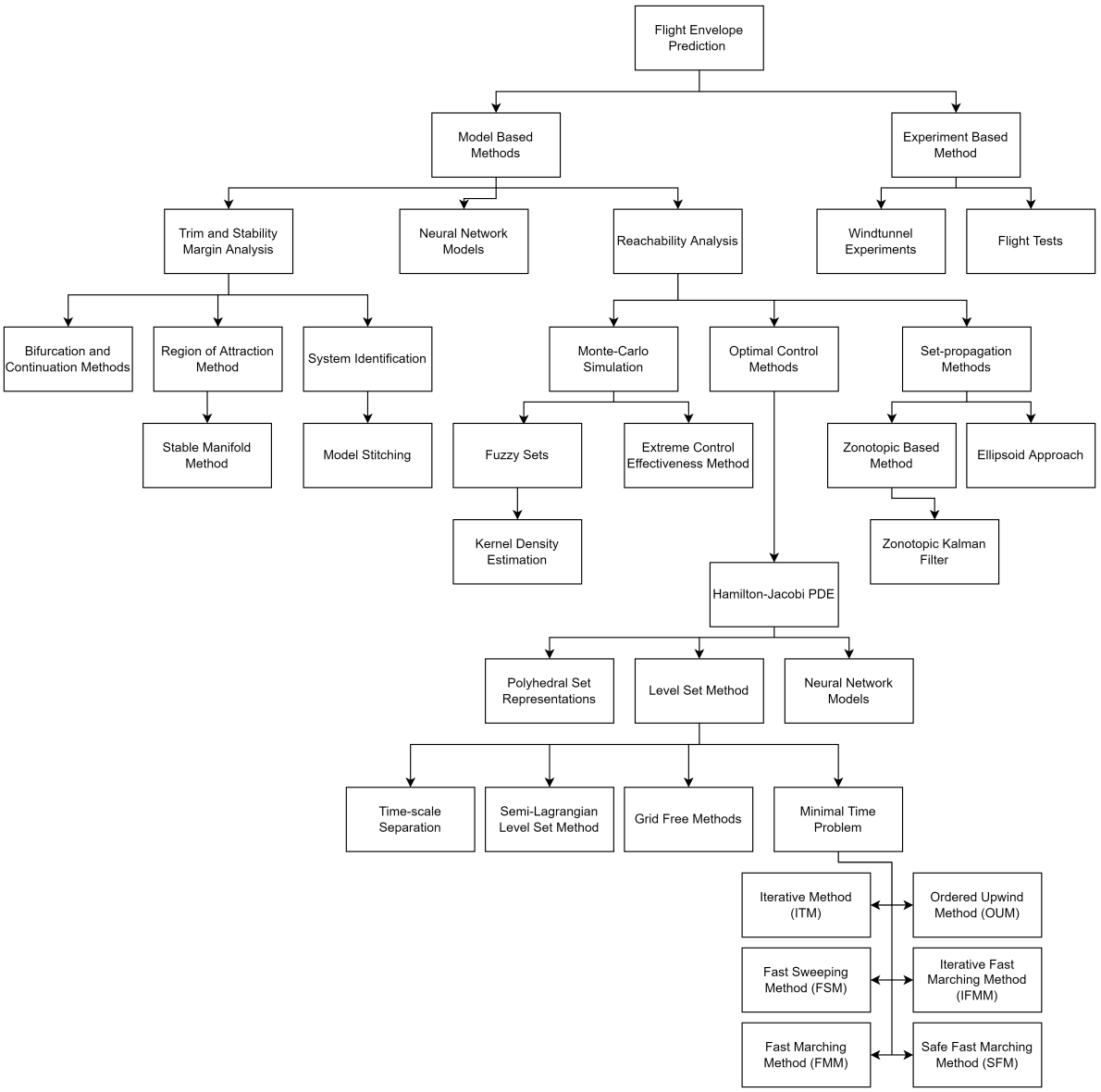

Figure 5.1: An overview of flight envelope prediction techniques with their interconnections.

5.1. Trim and Stability Margin Analysis on High Fidelity Models

The sudden demand of fighter aircraft design pushed the development of aircraft operating outside the linear aerodynamic regions expanding the flight envelope. This introduced challenges regarding nonlinear aircraft dynamics. The introduction of bifurcation and continuation methods by Carroll et al. [72] was a key development to combat this nonlinear dynamics modelling challenge.

5.1.1. Bifurcation and Continuation Methods

The bifurcation and continuation methods have allowed tools to be developed for aircraft stability and trim analysis [71]. An entire set of steady-state (trim) conditions can be calculated for different control inputs, e.g. for elevator deflections in longitudinal dynamics analysis. At each trim condition the dynamics can be linearized and consequently the stability of each trim condition can be computed. The methods can be used to consistently analyze global nonlinear dynamics, to evaluate performance and maneuvering capabilities [74], to verify control laws and flight envelopes [75], to design control inputs to accomplish a desired maneuver [75], to determine operational limits from trim maps that are within system constraints [65] and to analyze the stability of a trim point for prediction and prevention of unsta-

ble nonlinear flight phenomena [76]. Disadvantages of the methods include that they cannot intuitively result in a SFE in state space [77] and it is computationally inefficient to find all trim points for nonlinear dynamics [73]. References to bifurcation analysis applied to flight dynamics can be found in Goman et al. [74] and Yuan et al. [77].

5.1.2. Region of Attraction Method

With the Region of Attraction (ROA) method a stable set of the state space around a trim condition is predicted in which the system is able to return to equilibrium, whereas in reachability analysis all possible reachable states are predicted.

An advantage of ROA methods with regards to safety is that the analysis allows to estimate whether a certain trim point has enough safety margin to ensure recovery to an equilibrium condition in case of a (predefined) disturbance [78]. Hence the larger the ROA for a certain trim point, the higher the disturbance can be to still being able to return to an equilibrium condition. Therefore the size of the ROA can be seen as a measure of the stability of a nonlinear system at a trim condition [78].

A disadvantage of ROA is that computing the exact ROA of nonlinear dynamic systems is challenging and unsolved for higher order systems [78][79]. Significant research has been done on estimating invariant subsets of the ROA, see references in Pandita et al. [78] and Sidoryuk et al. [79]. Often the ROA search is restricted to ellipsoidal approximations [78][79] of which the lower bounds are computed using the Lyapunov function, which is very conservative [77][78]. In Pandita et al. [78] both reachability analysis along with nonlinear ROA is applied on a transport aircraft model. The reachability analysis is used to determine the reachable states, given a control authority, in order to advise the flight crew on possible reachable states and unreachable states. The ROA results can be used to support the guidance algorithm to predict whether future planned trim conditions have enough safety. In Pandita et al. [78] the ROA is estimated by the largest ellipsoid contained in the ROA because determining the best approximation to the ROA is difficult to determine [78], this however leads to conservative results [77]. Similar work has been performed in Chakraborty et al. [80] for control verification and validation and Sidoryuk et al. [79] for aircraft spin mode analysis. In Chen et al. [81] a stability analysis is proposed together with overlapping ROA to evaluate the aircraft stability in case of sudden aerodynamic changes, such as damage to facilitate control design for extreme conditions. Due to the conservative results Yuan et al. [77] employed the stable manifold technique to reduce this conservatism.

Stable Manifold Method In Yuan et al. [77] the stable manifold method is used in order to reduce the previously mentioned conservatism. In the stable manifold method an explicit characterization of the dynamic flight envelope is used which allows computation only on the envelope instead of the entire state space. Compared to the Level Set Method this method is more computationally efficient [77].

Main restrictions of the ROA method is the high computational demand which scales badly with the amount of dimensions of the system [78].

5.1.3. System Identification Techniques

In order to explore and improve the high fidelity dynamical models, the use of system identification has been used extensively in order to model varying dynamics over the flight regime which allows for computation of an updated flight envelope [4][5][36][67][68]. Use of differential vortex lattice algorithm with and extended Kalman filter has been investigated for onboard system identification of impaired aircraft [82]. Furthermore, the concept of model stitching has been employed for quasi-linear parameter varying modelling [83][84][85]. These methods focus on model identification to establish high fidelity models over a flight regime for stability and trim analysis and for design of (adaptive) controllers. More information on system identification can be found in chapter 6.

5.2. Reachability Analysis

A mainstream method that has been applied to various systems with regards to safety verification is called the reachability analysis. Development to adopt the reachability analysis approach originates from the analysis of graphs, to continuous and hybrid system theories in which formal verification of the system is necessary to ensure safety as seen in Althoff et al. [15] and references therein. A way to ensure safety is for instance by staying away from the unsafe set of the state space [86]. Applications

in which reachability analysis is used include safety of flight control (see Lygeros [87] and references therein), autonomous robotic systems [88] and aerobatic UAV maneuver and UAV collision avoidance [39][89]. The main goal of the reachability analysis for most applications is to develop controllers to stay within the safe part of the state space [90].

Determination of the set of all solutions is usually referred to as reachability analysis [15]. In reachability analysis a specific set of the state space of a system is determined that can be reached by the system. Three main sets can be identified: the invariance set, the viability set, and the reachability set. In this chapter the reachability set is defined, see Nabi et al. [66] for an elaboration on the definitions of the other sets.

The reachable set consists of all states for which at least one input exists to bring the system to these states within a given time-window [66]. Thus, the reachable set is a function of the initial condition, the time-window used, and the input constraints [39]. The reachable set can be subdivided into the forward reachable set and the backward reachable set, as the system can be propagated forward and backward in time. In this physical approach a global model of the system is required to model the aerodynamic forces and moments. This allows to estimate the forward- and backward reachable set from a certain trim set. The forward reachable set can be defined as the set of states for which a control input exists such that the system can reach those states within the time-window [66]. The backward reachable set can be defined as the set of all states for which a control input exists such that the system can reach at least one state of the trim set within the given time-window [66]. The intersection of the forward- and backward reachable set is then defined as the SFE which includes all the states that the system, within a time-window and given input constraints, can reach and also safely return to the trim set from which the forward- and backward reachable sets were predicted [11]. A graphical representation of the definition of the SFE can be found in Figure 5.2.

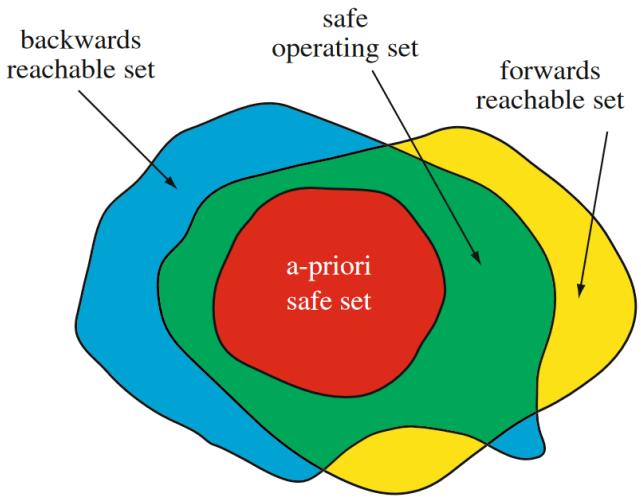

Figure 5.2: The Safe Flight Envelope (SFE) defined as the intersection of the forward- and backward reachable set determined from an initial safe set of states for a given time duration [6].

The advantage of using the reachable set analysis is that it is possible for certain continuous dynamical systems to exactly calculate the reachable states. Consequently tools have been developed to compute the reachable states in an exact manner. For more general systems, methods of numerically approximating these sets have evolved, see Lygeros [87] and references therein. It should be noted that a global model is required to model the (nonlinear) dynamics and the analysis is only valid for this specific model and the corresponding assumptions used. Model uncertainties can be taken into account by modelling them as disturbances [39].

The SFE prediction problem can be constructed into a reachability problem. There are various methods for determining the SFE through reachability analysis. These include through an optimal control problem, a zonotopic based method, and through a Monte-Carlo (MC) simulation. Each method

is described in the succeeding subsections.

5.2.1. Optimal Control Method

Solving the reachability problem may be done by solving for the time-dependent Hamilton-Jacobi-Bellman partial differential equation (HJB PDE) or the Hamilton-Jacobi-Isaac partial differential equation (HJI PDE) in case of disturbances are included in the analysis [14][39][66]. The flight envelope can be described as the intersection of two nonlinear, non-convex reachability problems described by the HJ PDE as supported by Tang et al. [36].

The SFE determination problem can be formulated as a dynamic interaction between control input and disturbances, consequently by using reachability analysis the region of the state space that the system can reach in case of worst case disturbance conditions and the best case controller strategy can be determined [39]. This approach to the reachability analysis uses optimal control methods. The formulation of the reachability problem into an optimal control problem was introduced by Lygeros [87]. The solution can be described by variants of the HJB or HJI PDE and the link between the solution to the PDE and reachability problem is usually established in the framework of the viscosity solutions [87]. It is called the viscosity solution because an artificial viscosity term is added to support stability of the numerical integration for numerically solving the PDE on a grid over time (usually, a Lax-Friedrichs approximation of the Hamiltonian) [91]. It has been proven that by solving for the viscosity solution of a time-dependent HJ PDE the continuous reachable set can be determined since the reachable set is proven to be the zero sublevel set of this viscosity solution [92]. As the level sets of the value function of an optimal control problem can be characterized as the reachable sets, by using dynamic programming without state constraints the value function of the optimal control problem can be identified as the viscosity solution to a first order PDE in the standard HJ form [87][90].

Advantages of the time-dependent HJI PDE over stationary HJI methods include that the viscosity solution is continuous and well-defined [92]. This allows for the application of well developed numerical approximation methods [92][93][94][95]. The solution exists both inside and outside the reachable set, which allows for application of SFE protection [92].

Level Set Method The most popular method for numerically solving for the viscosity solution in the context of reachability analysis is called the Level Set method and has been used to numerically solve for dynamic flight envelopes for (fixed-wing) aircraft [68][66][5][64].The HJ approach to numerical solutions of time-dependent equation for a moving implicit surface has started the development of the Level Set method [91], which adds dynamics to these implicit surfaces [91], as first introduced by Osher et al. [93]. The Level Set method is a subclass of the Euler method in which the state space is discretized in grids and the solution is calculated on each grid point for each dimension [5]. A fundamental disadvantage of the Level Set method is the computational inefficiency. It suffers from the curse of dimensionality as it scales exponential with the number of states and it becomes impractical to use for systems with more than four states [5][11][15][16].

Variants of the Level Set Method Due to limitations of the Level Set Method, various variants of this method have been developed. A complete overview of various variants are summarized in Stapel et al. [14] with relevant references. The following methods are worked out in more detail:

- **Time-scale Separation** In order to combat the curse of dimensionality in Van Oort et al. [64] it was advised to investigate splitting fast and slow dynamics by time-scale separation. Nonlinear aircraft dynamics with higher dimensions can be simplified by using the time-scale separation method [68][16]. In Nabi et al. [66] it was found that time-scale separation is useful for slower dynamics whereas it is not feasible for faster dynamics when considering aircraft control surfaces as inputs.
- **Grid Free Methods** A recent trend in literature is on research to eliminate the use of grids. This idea originates from the exponential cost in both space- and time domain of the Level Set method as the amount of grids increases per dimension. Darbon [96] proposes a method without using grids or numerical approximations but uses classical Hopf formulas. Another method is through the use of neural network models to eliminate grids by using physics-informed neural networks [97].

- **Semi-Lagrangian Method** The semi-Lagrangian method uses semi-Lagrangian time-stepping schemes to overcome timestep limitations, which concerns the Courant-Friedrichs-Lewy-condition [98], as a result of using Euler-methods [6].
- **Minimal Time Problem** In a minimal time problem the reachability problem is not modeled as a differential game, but as a minimal time problem in which a time to reach optimisation is solved. This results into an assigned value of ∞ for those states that cannot be reached [14]. This problem formulation has various numerical schemes as summarized in [14], such as the Iterative Method or non-interative method such as the Fast Marching Method.

Polyhedral Set Representations Besides the Level Set method, polyhedral set representations can be used. "This method scales more favorably with the number of state variables compared to level-set methods, but requires projections of the reachable set onto the constraint manifold determined by the algebraic equations. This projection is computationally expensive and it is not guaranteed that the computed approximation of the reachable set projection onto the manifold is an over-approximation." [99].

Besides the high computational cost and curse of dimensionality that the Level Set suffers from, it also tends to produce conservative results. In Stapel et al. [14] a reachability simulation was performed and "on average the successful trajectories from the Monte-Carlo simulation predict approximately 60% faster arrival times than the Level Set and safe Fast Marching method" [14]. In case of multirotor UAV application this conservativeness may limit protection systems to benefit from the high maneuverability multirotor UAVs have to offer.

5.2.2. Zonotopic Based Methods

Besides optimal control methods, reachability analysis can be applied using set-propagation methods, see Delansnay et al. [100] and references therein. In set-propagation methods the reachable sets in state space are represented by geometric shapes. This method is more efficient even with a larger amount of state variables, and is determined by the type of set representation [100]. A representation can be e.g. ellipsoids [69][101], polytopes and zonotopes. According to Althoff et al. [102] using zonotopes for reachable set calculation is relatively more efficient for higher dimensions and "yields tight results without a wrapping effect" [100]. Furthermore, the accuracy of the sets can be designed by the amount of zonotopes used to balance accuracy and computational time [103][104]. A restriction of zonotopic based methods is that they are not closed under intersection ("i.e. the intersection of zonotopes is not a zonotope in general" [103][104], which is key for reachability analysis of nonlinear and hybrid systems [104]. In Althoff et al. [104] this is bypassed by using zonotopic bundles. Another restriction of the zonotopic based methods is that the system must be linearized [104] which can introduce linearization errors.

In Harno et al. [105] the zonotopic reachability analysis has been applied on helicopters with icing conditions showing the capability for flight envelope estimation (although only the forward reachable set has been used in this paper). In Delansnay et al. [100] a zonotopic reachability analysis is applied on a multirotor UAV using linear model identification, with implementations of algorithms to accomplish underestimated reachable sets as proposed by Hespanha et al. [106] due to safety concerns. Satisfactory results on the forward reachable set can be found when compared to a Monte-Carlo simulation of the linear and nonlinear model [100].

Kalman Filter A new approach for predictive flight envelope monitoring and warning for off-nominal flight conditions is the combination of a Zonotopic Kalman filter (ZKF) and reachability analysis of a closed-loop system for online reachable states prediction. This is presented in Eyang et al. [107]. A ZKF observer can estimate all possible states in terms of zonotopes of the open-loop dynamics, while the reachability analysis consists of computations based on the closed-loop model to predict the future states of the aircraft. This is done over a specified time-window, for the observed set of initial states, and based on assumed (future) control inputs. "In order to get as less conservative as possible reachable regions under various flight conditions, an adaptive set-membership observer minimizes the size of the consistent state sets based on the past measurements." [107]. The initialization of the reachability analysis using the observed states results in more accurate information that is less

conservative [107]. It should be noted that Eyang et al. [107] uses a linear time-variant system, without external atmospheric disturbances, and with bounded disturbances and uncertainties (originating from the model and sensors). This approach results in a prediction of all possible future states and thus gives a prediction of the future behaviour of the aircraft. This can be used to check whether the system remains within a predetermined set of states considered to be safe and support flight crew alertness.

5.2.3. Monte-Carlo Simulation Approach

A recent trend in literature with regards to reachability analysis is the use of a Monte-Carlo (MC) simulation. A MC simulation is a numerical simulation method used for problems that cannot be analytically solved, or in case experiments take too much time and effort. Through the simulation, the behaviour of complex systems can be explored and the simulation can be repeated as often as required [108]. A MC simulation is an algorithm that uses random sampling to obtain system outputs and consequently find an approximation for the probability density function of the system response. A random sequence of input parameters is sampled, consequently, the system dynamics are integrated in time via a system of ordinary differential equations (ODE) to find the system states after the given random input sequence. In this way, the reachable set of a system model can be analyzed. The ODE can be mathematically described as follows:

$$\begin{aligned} \dot{\vec{x}}(t) &= f(t, \vec{x}(t), \vec{u}(t)) \\ \vec{x}(t_0) &= \vec{x_0} \end{aligned} \tag{5.1}$$

With $\vec{x}(t)$ the state vector, $\vec{u}(t)$ the input vector and $\vec{x_0}$ containing the initial states at t_0. Various numerical integration schemes exist, which can be subdivided into explicit methods (e.g. Euler and Adams-Bashfort) and implicit methods (e.g. the Runge-Kutta schemes). Explicit methods are cheaper, however they become unstable for stiff systems and large time-steps. Implicit methods are more expensive but become unstable with large time-steps. Hence careful selection of numerical integration scheme and timestep duration is required to prevent instability. For reachability analysis this can be done by increasing the amount of timesteps used within a certain reachable time-horizon. Note that the time-window used for each trajectory is system dependent.

The trend of using such a simulation originates from evading the high computational inefficiency of the Level Set method which is limited to problems of at most four dimensions [5][11][15][16].

In Sun et al. [11] it is shown that the MC approach can estimate a 6 dimensional reachable set and solve this high dimensional problem more efficiently compared to the Level Set method (in a matter of seconds). The method has been applied to the longitudinal SFE of a quadcopter, including actuator dynamics, using an aerodynamic model identified from high-speed flight data (<16 m/s) and the forward- and backward reachable sets have been validated in a 6 degree of freedom simulation platform.

In Yin et al. [8] a similar method of the MC simulation is applied for generating a probabilistic estimation of the flight envelope of a fixed-wing aircraft by simulating flight trajectories with extreme control effectiveness. In this paper kernel density estimation was used to produce a probabilistic or fuzzy flight envelope in which the final states are assumed to be stochastic variables. It is shown that this method can significantly reduce the computational load compared to previous optimization-based methods and guarantees feasible and conservative envelope estimation of no less than seven dimensions [8].

An advantage of the MC approach is the less computational load with increased number of dimensions compared to the Level Set method. Although in Terrell et al. [9] it was shown that the mean integrated square error of the reachable set is related to the used sample size for each simulated trajectory, which in turn depends on the state dimension. Hence, the MC simulation also suffers from the curse of dimensionality however less than the Level Set method. Moreover, parallel computing can be applied on MC simulations for more efficient code execution.

A disadvantage is that the simulation can be time consuming when applying a random-walk MC simulation approach as many simulations are required (i.e. performing simulations with many random inputs). A bang-bang control is proven optimal to be used in the MC simulation to reach the boundaries of the reachable set and consequently reduce the input space and the amount of simulation time required, although the switching time is still an unknown [8][11]. The bang-bang control as formulated in Sun et al. [11] considers the boundary of the control constraint for each timestep. To further decrease

the amount of trajectories to reach the boundary, in the paper a tuning parameter is set up to control the probability of adapting the control input to and from extreme value inputs [11]. With this parameter the conservativeness is controlled of trajectories reaching the reachable set boundary. Hence, it should be noted that the probability distribution of the input determines the probability distribution of the corresponding output.

Another disadvantage of the MC simulation reachability method is that the output of the simulation results in a discrete point cloud in state-space representing the reachable set. As a result, the boundaries of the envelope are less well defined compared to the result from the Level. Consequently, interpolation between reachable set points is necessary to provide a well-defined reachable set estimate which could be over- or underestimating the boundary. Furthermore, the amount of simulations required to construct the reachable set with a certain level of accuracy is difficult to determine. It should be noted that the quality of the results obtained depends on the model accuracy and input distribution used in the simulation.

5.3. Neural Network Models

A neural network model is generally applied in the framework of modelling system dynamics. The identification of the system dynamics can be done by training a neural network model based on inputs to the system and outputs of the real system. Feedforward neural networks have been implemented successfully for fixed-wing aircraft models [109][110]. Also neural network on quadcopter system identification has been implemented before [111][112][113][114]. A summary of literature work with regards to quadcopters can be found in Pairan et al. [115]. Neural networks can be also be used to capture model residuals in order to improve model accuracy and performance [29][116]. Application of neural networks on flight envelope prediction however is scarce. The main application fields identified include approximating the Level Set method, interpolation of various flight envelopes and using flight data for prediction of (local) envelope boundaries which are described in more detail below.

Approximating the Level Set Method As described earlier, for the Level Set method it is required to solve the viscosity solution of a Hamilton-Jacobi partial differential equation (HJ PDE) which is done by numerically approximating implicit functions over a grid. However, this method suffers from the curse of dimensionality as the amount of grid points increases with the amount of dimensions. In Darbon et al. [97] an attempt is made to overcome this curse by using neural network models. In this paper it is proven that ”some classes of neural networks correspond to representation formulas of the HJ PDE solutions whose Hamiltonians and initial data are obtained from the parameters of the neural networks” [97]. Furthermore, their findings result into efficient neural network models for evaluating solutions of some HJ PDEs in high dimension, in which no grid and numerical approximations are used [97]. In Darbon et al. [97] it is shown that ”some classes of neural network architectures naturally encode the physics contained in some HJ PDEs” [97]. These models are called physics-informed neural networks [117] which have the advantage that less dense grids are required. See Raissi et al. [117] for more information on physics-informed neural networks. However, Campbell et al. [118] questions the obtained accuracy and recommends to use the neural network prediction as reference only.

Flight Envelope Interpolation The high computational load of flight envelope determination techniques mainly restrict the use of real-time implementations of SFE determination. A data-based driven approach is worked out by Zhang [5] in which an aircraft structural failure case is classified based on system identification from flight data. The failure type in combination with the current flight condition allows to select the offline calculated envelopes stored in a database onboard and interpolate those envelopes. This strategy has been researched in Zhang [5], Tang et al. [36], Lombaerts et al. [7][119], Bordeneuve-Guibé et al. [68] and Nabi et al. [66] for aircraft damage cases, in which it was shown that interpolating envelopes that have connections in their physical origins can approximate the result of the Level Set method with high accuracy and interpolation of envelopes result in quick prediction [5]. However, this online interpolation requires carrying databases on board. In Norouzi et al. [73] a method is presented to estimate the global SFE in real-time for unknown failure degree of an aircraft by predicting the interpolation of envelopes based on flight condition and failure degree. Flight envelopes are determined for known failure cases and used as training data for feedforward neural networks. Re-

sults on a aircraft transport model with rudder and aileron failure cases show good approximations of the high fidelity global flight envelopes and fast computation in the order of seconds (only control surface failures are considered) [73]. It should be noted that in Norouzi et al. [73] the maneuvering flight envelope is used which is defined as boundaries containing steady-state maneuvers by determining the region of attraction of equilibrium points. This envelope consists of all (stable or controllable) trim points which are iteratively solved using the nonlinear equations of motion. An advantage of using a trained neural network is the fast output delivery as argued by Norouzi et al. [73] which could be applied in a real-time fashion.

Flight Envelope Prediction using Flight Data Neural networks have been applied on multirotor UAV model identification from flight data [111][115][120] due to their capability of modelling high nonlinearities. Global determination of a flight envelope based on flight data has not yet been done in the past as far as the author is aware. For local boundary detection Altena [37] showed promising results on the generalizability of neural network models based solely on real flight data. It was shown that neural network models can generalise time to loss of control (LOC) prediction for varying quadcopter aerodynamic characteristics from real flight data (”however it is required to compensate the output of the network for expected deviations in predictions in predicted time to LOC” [37]).

A large advantage of using a neural network to predict the flight envelope through flight data is the circumvention of both the need for high fidelity nonlinear models and the use of high computational expensive methods for SFE prediction. These are the main limitations identified from this literature research. To investigate the possibility of using flight data to predict the global SFE, the subsection below will further briefly elaborate on this topic.

5.3.1. Neural Networks and Global Flight Envelope Prediction

To examine ways to predict a SFE of a multirotor UAV based on flight data using a neural network model, first the input and output formats for this application are identified as follows:

- *Input* The input could consist of time-series of sensor data of various parameters such as linear and rotational accelerations, rotor commands, rotor outputs, and heading angle.
- *Output* A flight envelope has a multi-dimensional geometrical shape in state space, which is usually visualized in two- or three dimensions [5][68][7][66]. When using a MC simulation approach, the flight envelope is represented by a multi-dimensional cloud of points [19].

Based on flight data, the neural network has to capture the dynamics of the system based on its response to system inputs and consequently link this to the boundaries of its SFE. The dynamical response of a system is time-dependent as the system responds to a time sequence of control inputs. Therefore a key characteristic of the neural network model is the ability to capture features in time-dependent sequences of its input data.

A challenging design choice with regards to a neural network model is the output format. The network output format has to represent the flight envelope boundary in a multi-dimensional state-space. When using a MC simulation, the boundary is not well defined and consists of an integer number of reachable states. A way of representing the flight envelope is to define it as a geometrical shape in 2D or 3D space. In Romaszko et al. [121] a pipeline was developed to construct 3D Left Ventricular (LV) geometry from cardiac magnetic resonance images using a convolutional neural network (CNN). Due to the high dimensions for both input and output, measures were taken to prevent overfitting and dimension reduction. In this paper principal component analysis (PCA) is carried out on many LV geometries to reduce dimensions [121]. The LV geometries are mapped to a lower dimensional space spanned by some main identified principal components (reduction from 17,000 to 10 dimensions) [121]. Consequently the weights to the output layer of the network are pre-trained and kept fixed, reducing the model complexity due to this added preprocessing step [121]. Each weight (and neuron in the output layer) represents a projection to one principal component. The principal axes coefficient are added together to end up with the final geometry prediction. This is a trade-off between model flexibility (preventing overfitting) but still having enough freedom in the number of dimensions [121]. Another way of predicting a geometry is by defining preset parameters to fully describe the geometry. For example this can be done to predict the bead geometry of a welding technique using a feedforward neural network as done in Manikya Kanti et al. [122] by defining the geometry of the bead by the

width and height. For the application of the so-called parameter variation [123], sufficient amount of distinct geometry parameters must be defined based on the complexity of the geometry and hence prior knowledge is required on the shape and amount of dimensions of the predicted geometry. A more generic approach is to use Fourier Series expansion in which the neural network can predict the coefficients of the series to describe the geometry. This has been done, with a parabolic coordinate system, in Strijhak et al. [124] in which a neural network is used to predict the shape of an airfoil including ice accretion. Another method for outputting geometric shapes is via a 2D pixel representation. Applying neural networks for outputting such shapes are mainly found in the semantic segmentation literature using CNN (see Pohlen et al. [125]). A derivative of this method can be found in Fan et al. [126] where acoustic scattering information is used to predict the 2D shape of (convex) objects with various geometry.

A disadvantage of using neural networks is that preparing training data and training the model are time consuming. Due to training data inefficiency it is very challenging to use in real-world applications. Another disadvantage is due to the lack of a mathematical framework the correctness of the trained model is not guaranteed and is valid only for datasets similar to the training set, which can lead to safety concerns.

5.4. Conclusion

Improving techniques and expanding knowledge on flight envelope prediction could enhance the development of flight envelope protection systems to increase UAV safety. The aim of this chapter was to summarize the mainstream and state-of-the-art methods for Safe Flight Envelope (SFE) prediction methods. SFE prediction can be done in multiple ways as explored in this chapter.

Reachability analysis results in a set of all reachable states for any given time span duration, initial states and control capability. The analysis establishes a firm framework of boundaries within a safe flight is guaranteed. This allows for the development of flight envelope protection systems, such as control law design, to prevent loss of control conditions by preventing the system from crossing the envelope boundaries. Hence, reachability analysis is the preferred method for this research. The reachability analysis comes with an arsenal of well established and widely applied methods such as solving for the Hamilton-Jacobi partial differential equations via the Level Set method. However, due to the high computational load and impracticality for implementation of systems with more than four states [5][11][15][16], application of this method is not preferred for high dimensional multirotor UAV applications. Furthermore, the Level Set method tends to produce underestimated sets [13][14] which are not desirable as it prevents to exploit the ability of highly maneuverable flight which multirotor UAVs have to offer. To conquer these limitations, the Monte-Carlo (MC) simulation seems to be the most promising method to be used as it can be applied on higher dimensional nonlinear systems and is recently successfully applied on quadcopter models [11]. It should be noted that extreme control effectiveness methods, such as bang-bang control, should be employed to mainly reach the boundary states, prevent conservative results and reduce the amount of simulations required. Important to mention is that the time-window (which is system dependent), as well as the input distribution, used for reachability analysis in the MC simulation have a large influence on the obtained results.

Although the Bifurcation and Continuation methods, the Region of Attraction Method and Zonotopic Based Methods seem promising methods, the required trim envelope for nonlinear systems are computational expensive and local linearization of the model limits the analysis of global envelope analysis, while the MC simulation can produce global boundary estimates from the nonlinear model directly. In order to gain insight into SFE prediction of UAVs, a black-box model such as neural network models for envelope prediction will limit this ability and hence does not seem suitable to gain more knowledge on envelope prediction. It should be noted, however, that the use of neural network models for envelope prediction based on flight data seems promising [37][73], and could prevent the two main limitations of mainstream prediction methods which includes the need for high fidelity nonlinear models and the high computational load.

The results from this model-based approach heavily relies on the model quality and model validity used in the reachability analysis. A way of determining high quality models can be done through system identification as already briefly touched upon in this chapter. Hence, next chapter will further elaborate on system identification techniques for multirotor UAV.

6

System Identification of Multirotor UAV Models

This chapter focuses on system identification with the application on multirotor Unmanned Aerial Vehicle (UAV). As seen in the previous chapter, most flight envelope prediction techniques rely on a model based approach. Hence, the quality of the results depends on the model quality and validity as used in the reachability analysis. A way of determining high quality models can be through system identification. As identified in chapter 4 investigating the behaviour and sensitivity of the boundaries of the envelope can enhance probabilistic flight envelope protection (FEP) systems, and consequently the safety of the system. When investigating the behaviour of the envelope on changing system dynamics, the models must be able to capture the resulting differences in dynamics. Therefore, the goal of this chapter is to explore and identify techniques for determining multirotor UAV models. First, basic multirotor UAV dynamics are explored in section 6.1 in which focus is on the widely used quadcopter model configuration. In section 6.2 system identification techniques are described with focus on multirotor UAVs. In section 6.3 excitation maneuvers are identified which can be used to excite the dynamics of a system for model identification. Finally, the chapter ends with a conclusion on the findings in section 6.4.

6.1. Basic Quadcopter Dynamics

For designing a controller in hover flight, often a reduced model of the quadcopter is used. The body reference frame as defined in Figure 6.1 is used. Assuming the quadcopter is a rigid body and using Newton's law of motion the following linear and rotational dynamic equations apply:

$$m \begin{bmatrix} \dot{u} \\ \dot{v} \\ \dot{w} \end{bmatrix} = m \begin{bmatrix} p \\ q \\ r \end{bmatrix} \times \begin{bmatrix} u \\ v \\ w \end{bmatrix} + \vec{G} + \vec{F} \tag{6.1}$$

$$\mathbf{I} \begin{bmatrix} \dot{p} \\ \dot{q} \\ \dot{r} \end{bmatrix} = \begin{bmatrix} p \\ q \\ r \end{bmatrix} \times \mathbf{I} \begin{bmatrix} p \\ q \\ r \end{bmatrix} + \vec{M} \tag{6.2}$$

With m the mass of the quadcopter, u, v, w and $\dot{u}, \dot{v}, \dot{w}$ the body linear speeds and accelerations. $\vec{G}$ and $\vec{F}$ represent the gravity vector and $\vec{F}$ the resultant force vector without gravity in the body frame. p, q, r and $\dot{p}, \dot{q}, \dot{r}$ are the body angular speeds and accelerations. $\vec{M}$ represents the resultant moment vector on the quadcopter in the body frame and $\vec{I}$ represents the inertia matrix.

The forces and moments that act on the quadcopter can be split into the effect from the motors ($\vec{F_r}$ and $\vec{M_r}$) and the aerodynamic effects ($\vec{F_a}$ and $\vec{M_a}$) as follows:

$$\vec{F} = \vec{F_r} + \vec{F_a} \tag{6.3}$$

$$\vec{M} = \vec{M_r} + \vec{M_a} \tag{6.4}$$

The forces of the motors in this simpler hover model is reduced to hover condition:

$$\vec{F}_r = \begin{bmatrix} 0 \\ 0 \\ -T_h \end{bmatrix} = \begin{bmatrix} 0 \\ 0 \\ -\kappa_0 \sum \omega_i^2 \end{bmatrix} \tag{6.5}$$

In which the force T_h is the resultant thrust provided during hover flight, ω_i is the ith motor speed and κ_0 is a rotor property coefficient dependent on the air density and is assumed to be constant [19][127][128]. Any aerodynamic effects on the motors are neglected.

The moment induced by the motors can be described by the roll, pitch and yaw control respectively. The roll control moment $\vec{M}_x$ and the pitch control moment $\vec{M}_y$ are induced by differential thrust of the motors:

$$\vec{M}_x = b\kappa_0(\omega_1^2 - \omega_2^2 - \omega_3^2 + \omega_4^2) \tag{6.6}$$

$$\vec{M}_y = l\kappa_0(\omega_1^2 + \omega_2^2 - \omega_3^2 - \omega_4^2) \tag{6.7}$$

b and l indicate the distance to the center of gravity in the y_b and x_b axis respectively.

The yaw control moment, however, uses moment differences produced by the individual motors, and hence it is configuration dependent [129]. There are two configurations, a "bear-hug" configuration in which motor 1 rotates clockwise, and a "breaststroke" in which motor 1 rotates counter clockwise. In case of the latter configuration, a positive yaw moment is given by:

$$\vec{M}_z = \tau_0(-\omega_1^2 + \omega_2^2 - \omega_3^2 + \omega_4^2) \tag{6.8}$$

τ_0 is the rotor torque coefficient determined from hover measurements and is assumed to be constant. The complete control moment of the motors is then as follows:

$$\vec{M}_r = \begin{bmatrix} b\kappa_0 & -b\kappa_0 & -b\kappa_0 & b\kappa_0 \\ \ell\kappa_0 & \ell\kappa_0 & -\ell\kappa_0 & -\ell\kappa_0 \\ -\tau_0 & \tau_0 & -\tau_0 & \tau_0 \end{bmatrix} \begin{bmatrix} \omega_1^2 \\ \omega_2^2 \\ \omega_3^2 \\ \omega_4^2 \end{bmatrix} \tag{6.9}$$

So far, this simple hover model is only valid in the near-hover regime which is below 2 m/s [17], no aerodynamics are assumed and consequently it is not valid in case of translational velocities.

It has been found that the aerodynamic effects affect the external forces and moments significantly [19][17]. Hence the forces and moments due to the aerodynamic effects $\vec{F}_a$ and $\vec{M}_a$ play a significant role and should be included. Therefore, in order to identify models that are valid in fast forward flight, the main goal of the system identification is to determine the model for $\vec{F}_a$ and $\vec{M}_a$. In Sun et al. [19] this gray-box model has been used and showed great improvements in the prediction ability compared to the basis quadcopter dynamic model.

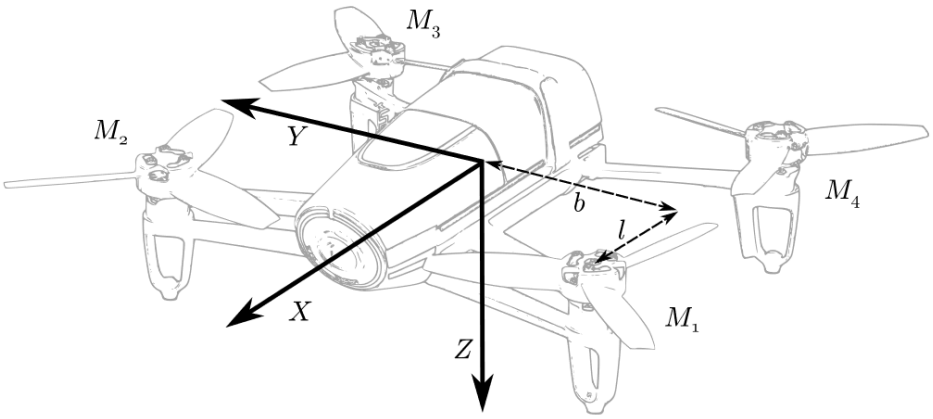

Figure 6.1: Figure of a quadcopter and the body reference frame with origin at the center of gravity [30] (adjusted). Motors are numbered from one to four.

6.1.1. More Advanced Quadcopter Model Dynamics

The basic quadcopter model as described above is only valid for the low-speed regime. The inaccuracies increase when speed increases as a result of aerodynamic effects which are neglected in the hover model. Hence this model detriments significantly in higher speed regimes, as shown in Sun et al. [19]. Various effects can be implemented to extend the hover model:

- **Gyroscopic Moment Effect** Due to the rotation of the propellers a gyroscopic moment is induced on the quadcopter. This moment can be included in which usually it is assumed that the rotors are on the $x_b - y_b$-plane (flat on the z-axis), hence for the rotors it can be assumed that $I_{r_{xz}}$ = $I_{r_{yz}}$ = 0. Furthermore, since generally the propellers do not have a large moment of inertia, the relevant precession terms are those with high rotational speed. The rotors spin around the z-axis, hence it can be assumed that for every ith motor, $\omega_{ix} \ll \omega_{iz}$ and $\omega_{iy} \ll \omega_{iz}$ and thus can be neglected. This also applies to $\dot{\omega_{ix}}$ and $\dot{\omega_{iy}}$ which are neglected. With these assumptions the gyroscopic moment effect is usually implemented as [30][19]:

$$\boldsymbol{M}_{r_i} = \begin{bmatrix} M_{r_{i_i}} \\ M_{r_{iy}} \\ M_{r_{iz}} \end{bmatrix} = \begin{bmatrix} I_{r_{zz}} q \omega_{i_z} \\ -I_{r_{zz}} p \omega_{i_z} \\ I_{r_{zz}} \dot{\omega}_{i_z} \end{bmatrix} \tag{6.10}$$

- **Variations in Thrust** When flying at increasingly high speeds, the thrust is more dependent on the relative velocity of the air with the rotors and the angle of attack of the rotor disks [130][131]. The resulting thrust can be obtained using momentum theory [128] or via blade element theory [132].
- **Blade Flapping** Blade flapping is an aerodynamic phenomenon which effects the attitude control of a quadcopter. Blade flapping occurs due to the difference in relative velocity of a blade going into the direction of the flow while another travels away from the flow. As a result, at every revolution the blades flap up and down due to the imbalance in lift. Consequently, the rotor plane tends to tilt away from the direction of flight. This will introduce a moment when the drone is not flying level [130][131]. Furthermore, there is a net drag force as a result which could be significant for smaller drones [131]. See Mahony et al. [133] for more information on how to model this effect. It should be noted that usually with blade flapping effect modelling [130][133] only conditions at low speeds with no wind (indoors) are examined.

6.2. System Identification Techniques

The goal of system identification is to identify a model that maps input to a desired output behaviour as observed from (training) data or measurements. Hence the technique can be considered as a data-driven approach for model identification. In order to optimize the input-output relation of the model, the parameters of the model are estimated such that the model minimizes the difference between the measured data and the model predicted data (i.e. model residuals). This is called parameter estimation. An estimator estimates these parameters in order to minimize a cost function of the residuals, which is a function of the measurements. It should be noted that the measurements often originate from sensor data, which contain random noise. Hence the estimated parameters should be considered as random variables [134]. The estimator must be defined to estimate the parameters of the chosen model structure to minimize residuals. The way the residuals are minimized is defined in the cost function.

Quadcopter system identification literature consists mainly of identifying forces and moments models of the system. This is often not well understood due to the high nonlinearity and unknown aerodynamic coupling effects that arise, especially in the high speed regime [17]. Hence it should be noted that the resulting model from system identification is only valid for the flight regime from which data was collected to ”train” the model on. In case of traditional aircraft modelling, the aerodynamic model parameters vary with flight condition, which concerns the flight velocity and altitude.

6.2.1. Model Structures

The model, or plant, can be treated as a white-box model, a black-box model or a gray-box model. In a white-box model the model structure is based on first principles which are often well understood (e.g. a physical model). A black-box model maps solely input to output without knowledge on how

this mapping occurs. Whereas a gray-box model uses characteristics of both previously mentioned models.

Many model structures exist and the selection of a certain structure depends on the amount of approximation power required and the allowed computational complexity. The latter is affected by the optimization method of the cost function and the model structure chosen. In literature on quadcopters, the following used model structures are found:

- **Polynomial Models** Polynomial models are white-box models which have the advantage that they are often simple and easy to implement [17]. In the aerospace industry polynomials are often used as a first modelling approach [134]. According to the Weierstrass approximation theorem (1885) every continuous function defined on a closed interval can be approximated as closely as desired by a polynomial function. However, in practice when using higher-order polynomials numerical instability is encountered due to the fact that ordinary polynomials do not have a stable basis. Furthermore, when using polynomial interpolation the approximating function tends to oscillate towards the end of the interval which increases with the degree of the polynomial. This is called the Runge's phenomenon (1991). In order to circumvent these phenomena, the domain can be split into subdomains. For each subdomain, a polynomial of lower order can be fitted. This is called a piecewise interpolation [135]. In quadcopter literature these are mainly implemented with regards to trajectory planning [136]. Piecewise linear polynomials have been implemented in Sun et al. [17].
- **Neural Networks** Neural networks are a type of black-box models which do not depend on a physical based mathematical model. In quadcopter literature the application of feedforward networks with multilayer perceptrons (MLP) have proven to reach good accuracy for nonlinear system identification [111]. Bansal [111] showed the feasibility of feedforward neural networks to approximate a quadcopter model for real flight test data, even with the use of decoupled dynamics. For regression, approximation and forecasting the Radial Basis Functions (RBF) are widely used and show improved accuracy on prediction and training time compared to the MLP models [137] and are successfully applied on quadcopter models [120][138]. Furthermore, Al-Mahasneh et al. [139] explored the use of evolutionary algorithms on quadcopter model prediction, although this turned out to take too much time to be practical for dynamical systems. Proper selection of hyperparameters have a large influence on the performance of the network and finding this optimum can be time consuming when using a trial and error approach. Another disadvantage of using a neural network is the high computational complexity with nonlinear optimization resulting in long required training time.
- **Fuzzy Models** The dynamics of a quadcopter is very nonlinear with time-varying behaviour and uncertainties which make it difficult to model the dynamics mathematically. An advanced way of circumventing this challenge is through the use of model free identification. In Santoso et al. [140] and Ferdaus et al. [31] this is done on a quadcopter by using a fuzzy clustering based system identification technique based on input and output data. In these papers it is shown that fuzzy models can be applied to quadcopter system identification with good accuracy. Besides other black-box approaches such as a neural network, an advantage of a fuzzy system is that is it transparent and hence human readable [141] which allow for insight into the uncertainty.
- **Hybrid Model Structures** As summarized in Sun et al. [17] and Van Beers [29] a quadcopter has many complex interaction effects resulting in highly nonlinear forces and moments compared to when it is in hover flight. In these papers the motivation to use a gray box model (or hybrid model) originates from the possibility to combine prior knowledge of rotorcraft aerodynamics and assumptions in order to select the model structure components, with data observations to model the not well understood interaction effects (at high speeds). In Sun et al. [19] a gray-box model was used combining prior knowledge on quadcopter aerodynamics and stepwise regression was used to identify the model structure. In the paper it was found that the gray-model structure outperforms the standalone physical model and the widely used reduced quadcopter model. However it should be noted that the model was more complex and more independent variables were needed, hence a a trade-off between simplicity and accuracy must be made for the specific application of the model [19]. In Mohajerin et al. [114] a hybrid model was developed consisting of a quadcopter model with a recurrent neural network to account for deviations in the output. Simulations showed that it outperforms the stand-alone model. This motivated Van Beers [29] to couple a polynomial

model with a neural network. In the paper it was found that the polynomial model consistently produced the most useful models and that the hybrid approach as applied in the paper did not achieve better performance than the polynomial model [29].

6.2.2. Model Estimators

The simplest model estimator method is called linear regression in which the goal is to minimize the model residual, which is the error between the output data and the prediction of the regression model. Linear regression requires a linear-in-the-parameters model structure, which can still be used for non-linear in the states models. The linear regression model is generally formulated as follows:

$$\vec{y} = \vec{A}(\vec{x})\vec{\theta} + \vec{\epsilon} \tag{6.11}$$

With $\vec{y}$ an $Nx1$ measurement vector, $\vec{A}(x)$ the Nxn regression matrix, $\vec{x}$ the $mx1$ state vector, $\vec{\theta}$ the $nx1$ parameter vector and $\vec{\epsilon}$ the $Nx1$ model residual vector. The regression matrix consists of regressor functions p:

$$A = \begin{bmatrix} 1 & p_{1,1} & p_{1,2} & \cdots & p_{1,m} \\ 1 & p_{2,1} & p_{2,2} & \cdots & p_{2,m} \\ \vdots & \vdots & \vdots & \ddots & \vdots \\ 1 & p_{N,1} & p_{N,2} & \cdots & p_{N,m} \end{bmatrix} = [1, \mathbf{p}_1, \mathbf{p}_2, \ldots, \mathbf{p}_m] \tag{6.12}$$

The regressor function $p_{N,m}(x(n))$ is a function in terms of the states x and describes the relationship between the state variables. The most widely used regressor functions are polynomials and are often used for aircraft model identification [134][142][143].

Variations on the linear regression method exist, such as the well-known ordinary least-squares (OLS) regression in which a quadratic cost function is used for minimizing the model residual. The OLS estimator for θ can be derived as:

$$\hat{\vec{\theta}} = (\vec{A}^T(\vec{x})\vec{A}(\vec{x}))^{-1}\vec{A}^T(\vec{x})\vec{y} \tag{6.13}$$

Important to note is that the OLS estimator uses the following assumptions in order to be a best-linear unbiased estimator:

1. The residuals have a constant variance for all measurements and are uncorrelated (i.e. they resemble white noise).
2. The residuals have zero mean.
3. No process noise, i.e. the states are deterministic. The measurements are considered to be stochastic.

Very often residuals do not resemble white noise and do not have a constant variance, hence the parameter (co)variances and the residuals must be analyzed to identify correlated parameters. Furthermore, process noise is often present. Hence variants have been developed to extend the regression method, e.g. the weighted least squares, generalized least squares and total least squares estimation.

Besides these linear estimators, in order to take into account correlated residuals, nonlinear regression models have been developed. An example is the maximum likelihood estimation which uses a nonlinear solver. Although less assumptions on the residuals apply, the computational complexity of these methods increases.

In addition to the time domain system identification, the time-series data and model can also be converted to the frequency domain in which model identification and analysis can be performed. More details can be found in Klein [134]. An application of frequency response system identification has been done in Sakulthong et al. [144].

6.2.3. Model Components Selection

In case of a white- or a gray-model structure, the regressor functions within the regression model must be determined which define the relation between the state variables and produce a candidate pool of regressor terms or regressor candidates. As can be seen in Equation 6.13, the regressor function, p, within the regressor matrix, A, have an influence on the complexity of the regressor model.

A higher complexity of the regressor function (and the amount of regressor terms used) will decrease the model residuals at a cost of overfitting (i.e. noise within the data is more strongly captured within the model). Whereas a too simple regressor function (or very little regressor terms are used) will lead to underfitting in which the model cannot capture the dynamics as present in the data. Hence it is important to determine the most suitable regressor function and the selection of regressor terms thereof for the specific system at hand. A selection can be made based on physics theories, experience, or they result from assumptions that are made [19]. A widely applied method is stepwise regression.

Stepwise Regression In Sun et al. [19] a data driven stepwise structure selection method [134] was used, which is called stepwise regression. This technique has been widely used for aircraft models however it has not been widely applied to quadcopter applications [19]. Stepwise regression consists of three steps: the forward selection, backward elimination and stepwise regression. It has as goal to select and eliminate regressor terms from the model in order to improve the accuracy of the model. An elaborate explanation can be found in Klein [134]. Regressor terms are selected from a predesigned pool of regressor candidates produced from a regressor function. The design of the regressor function have an influence on the complexity of the model structure. For example, in Sun et al. [19] it was recommended to further investigate flexible regressor functions to improve the gray-box model performance, which was performed using piecewise polynomial functions [17].

Quadcopter Regressor Functions As identified above, the form of the regressor functions have an influence on the model complexity and hence on its performance. Examples of regressor functions are logarithmic, exponential and polynonial functions. In quadcopter literature not much can be found on system identification using linear regression and covers mostly identification using neural network models. When inspecting a widely used simplified model that is used for designing a controller for hover conditions [19] it can be observed that polynomial functions could be sufficient for describing the relationship between state variables. The literature in which quadcopter system identification is applied using linear regression use indeed polynomial functions as the regressor function [29][19][17].

> **Polynomial Functions** When using polynomial functions as regressor functions, the candidate pool of regressor terms are formed by a combination of state variables which depend on the order of the polynomial and the states selected. For example in case a second order polynomial is used as a function of state x_1 and x_2:
>
> $$\hat{y} = P^2(x_1, x_2) \tag{6.14}$$
>
> The pool of candidates for this regressor function consists of: x_1, x_2, x_1^2, x_2^2, $x_1 x_2$. The candidate pool $\hat{d}$ grows as a function of polynomial degree d and number of independent states n as [145]:
>
> $$\hat{d} = \frac{(d+n)!}{n!d!} \tag{6.15}$$

6.3. Multirotor UAV System Identification Maneuvers

The input must be designed such that it excites all relevant dynamics of the system, hence the input signal must cover sufficient and relevant frequencies as allowed by the experimental set-up. A quadcopter has four motors which are usually located on the same plane facing the same direction. Hence it is important that, in order to identify control effectiveness for each individual motor, the excitation input signals to each motor are uncorrelated [134]. As mentioned before, it should be noted that the identified model is only valid for the flight condition in which the data has been obtained. Quadcopter models are usually determined with respect to a certain airspeed [19]. The airspeeds can be accomplished in either a windtunnel [19] or by (outdoor) free flights [29].

The following maneuvers are identified which have been used in past literature:

- **Classical (fixed-wing) aircraft excitation maneuvers** which include:
  - *Impulses* A spike control input which could be two sided to return to the initial condition. However they are often low energy inputs and hence not always practical [134].

  - *Frequecy sweeps* A continuous input of sinusoids with varying frequency and amplitude resulting in good prediction performance [134]. Piloted inputs are preferred over automated inputs because it introduces some variety in the data enhancing the information content [134]. A challenge of a frequency sweep is keeping the flight condition constant when performing the maneuver. An example in which the frequency sweeps were performed on a quadcopter can be found in Sakulthong et al. [144] in which longitudinal and lateral dynamics were assumed to be decoupled.
  - *Multisines* or (varying-amplitude) orthogonal multisine input signals [146] which is a sum of sinusoids with various frequencies (of interest), amplitudes (to achieve a certain power distribution over the frequency band) and phase angles (usually chosen arbitrarily) [134]. Multisine input signals are used to excite the dynamics such that the information content in the response are maximized while minimizing flight trajectory excursions [146]. The multisines must be designed carefully as described in Alabsi et al. [146] in which four uncorrelated orthonormal multisine signals were generated for each of the four quadcopter motor commands and used for real-time system identification.
  - *Doublets* An approximation of a double sided square wave which produces as wider frequency spectrum than when a single sinusoid was used [134]. A cascade of doublets can be used with various pulse duration based on natural frequencies of the eigenmotions of the system (e.g. 3211 maneuver for fixed-wing aircraft). The amplitude is determined to achieve good signal-to-noise ratio while remaining within the allowable flight condition [134].

- **Multirotor UAV free flights in a windtunnel** which include:

  - *Maneuvers along the wind flow, a horizontal maneuver perpendicular to wind flow, climbing and descend flight and yaw maneuvers [19]* Except for the yaw maneuver, for each excitation maneuver the heading angle changes over time in order to identify cross-coupling between longitudinal and lateral dynamics [19].

- **Multirotor UAV free flights outdoors** using aggressive maneuvers which include [29]:

  - *Sinusoidal Maneuvers* These are sinusoidal inputs along a certain axis while trying to keep other axis unchanged (and remaining at a constant altitude).
  - *Throttle Pulses* Pushing the throttle almost ON and OFF repeatedly.
  - *Acrobat Maneuvers* Such as loopings, barrel rolls and punch outs.

  An important factor in flying outdoors are the uncontrollable factors present, such as wind and gusts, which will have a (stochastic) influence on the measurement data and consequently on the resulting model validity.
- **White noise and pseudo-random binary sequences** Since these have low identification efficiency these signals are not widely used in aircraft system identification [134].

6.3.1. Data Logging and Normalization

For logging flight data, the available sensors introduces constraints on the quality of the obtainable data. A measure on the quality of the measured data is the *signal-to-noise ratio (SNR)*. The measured signal is considered to be deterministic whereas the measurement noise is stochastic. These signals can be separated through an optimal Fourier smoothing method which allows for calculation of the SNR [134]. In case of aircraft response modelling, results are usable with SNR ratios from three to ten (good modelling results) [134].

The following state parameters are usually logged for quadcopter system identification [19]:

- **Position, Velocity and Attitude** These can be obtained through an external motion tracker system.
- **Specific Forces and Angular Rates** These can be obtained through an accelerometer and gyroscope (through an inertial measurement unit (IMU)). The forces can be computed with the known mass of the quadcopter, while for the resultant moments the moments of inertia of the quadcopter are required. Note that IMU data are often noisy and hence a smoothing filter is needed [19]

Normalization Non-dimensionalization of states is often applied in the aircraft literature in order to allow for model comparison between different systems and conditions. Furthermore, aerodynamic forces and moments are often described in non-dimensional coefficients [147]. In Sun et al. [19] a non-dimensionalization approach is described for quadcopters, under the assumption that the aerodynamic forces and moments are produced by the motors.

6.4. Conclusion

Most flight envelope prediction techniques rely on a model based approach. Hence, the quality of the results depends on the model quality used in the reachability analysis. A way of determining high quality models can be through system identification. The goal of system identification is to find the input to output behaviour in terms of a model to capture the dynamics of the system. For multirotor UAV model identification a widely used simplified hover model is often used for quadcopter model identification. In this model the aerodynamic effects are neglected, whereas aerodynamic effects have a significant effect on the forces and moments on the quadcopter, hence the main goal of system identification of multirotor UAV involves the identification of these aerodynamic effects.

As identified in chapter 4 investigating the behaviour and sensitivity of the boundaries of the envelope can enhance probabilistic flight envelope protection systems, and consequently the safety of the system. When investigating the behaviour of the envelope on changing system dynamics, the models must capture the resulting differences in dynamics. Hence it is of utmost importance that the quality between the identified models of various UAV configurations are as similar as possible, such that the differences between the models originate from the difference in the dynamics.

In order to perform an analysis on the obtained models to compare dynamical differences as a result of varying configurations, it is preferred to use a white-box model structure. Polynomial functions seem to be the most promising ones available for the application on multirotor UAV.

To achieve similar model qualities among the multirotor UAV configurations, stepwise regression could be used to meet the desired performance. This can be done by using datasets in which similar or identical system inputs are performed on the configurations. Additionally, polynomial functions used in Sun et al. [19] can be adopted to create a starting regressor candidate pool. Ideally, the same model structure parameters for each multirotor UAV configuration can be used to directly see the effect on the estimated parameters between configurations.

Multirotor UAV models are identified (and hence valid) along a certain airspeed range. For identification of the model, excitation maneuvers should be designed. A trade-off between maximum allowed excursions and capturing the amount of dynamics should be made, which depends on the airspeed in which the models should be valid. In case of low flight speeds, frequency sweeps could be applied starting from a hover condition while keeping a constant altitude. In case of high flight speeds, throttle pulses and multisine signals could be employed. Although in aircraft dynamics identification it is recommended to use piloted inputs, for the identification of multirotor UAV dynamics for various configurations it might be more desirable to program automated control inputs. This is because the same maneuver can be applied on the various configurations, and repeated more easily to reduce the amount of stochastic influences as much as possible. Indoor flights are for similar reasons preferred. If such automated procedures cannot be implemented, manual flights suffice and maneuvers should be repeated as often as possible.

7

Conclusion Literature Study

The aim of this literature report is to identify areas of improvement for enhancing safety of multirotor Unmanned Aerial vehicles (UAVs) and to which extend, and in what form, knowledge can be added to the body of literature to enhance UAV safety. It could be identified that the applications of UAVs are expected to grow rapidly in the near future [1], however loss of control (LOC) is the main cause of failures for UAVs [2]. In order to improve safety of these systems, development of LOC prevention techniques are of utmost importance. A way to prevent LOC is through the use of flight envelope protection (FEP) which enables controllers to keep the system within the Safe Flight Envelope (SFE), which indicates the state space in which the vehicle can be safely operated. Operating outside the SFE is linked to LOC [3][4][5]. The SFE in this research is defined as all the possible states which an aircraft can both reach from- and be controlled back to a set of initial flight conditions within a given time-window [8].

For this research it is decided to focus on global flight envelope prediction (instead of local) because having prior knowledge on the global envelope has the advantage to develop FEP systems to balance safety and performance for the specific application. From the literature research it can be concluded that treating the boundaries of the SFE as probabilistic is preferred. The reason is because classical deterministic flight envelopes tend to overestimate envelopes leading to dangerously optimistic FEP systems [13][14]. Furthermore, in Yin et al. [8] it was shown that the envelopes change shape and size when changing the aircraft system dynamics. Therefore, in case of including system model uncertainties it is more suitable to model the boundaries as probabilistic. Moreover, an advantage of treating the boundaries as probabilistic is that it allows for earlier responses and gentler protective FEP measures [8].

The behaviour of the SFE boundaries of a multirotor UAV under varying configurations is yet to be explored. Therefore, a sensitivity analysis would generate knowledge on the behaviour of the boundaries under varying multirotor UAV configurations which directly adds information to the body of literature of multirotor UAVs. Varying multirotor UAV configurations can be considered as a form of model uncertainty, thus the analysis of the behaviour of the boundaries will generate knowledge on boundary prediction in a probabilistic way. Consequently, this could enhance the integration of SFE protection systems on multirotor UAVs to balance safety and performance with novel probabilistic protection strategies as done in Yin et al. [8]. Furthermore, knowledge on the behaviour of SFE boundaries under varying system dynamics allows for investigation into methods to interpolate envelopes for different configurations of the system. Interpolation of envelopes bypasses the need for recalculation of computational expensive envelope prediction methods and hence could allow for real-time application. It also enables further exploration in the feasibility of the promising database approach for real-time flight envelope prediction for multirotor UAVs as proposed by Zhang [5]. A promising method is through the use of neural network models [73][37].

Focus of the research will be on quadcopter models, for the reason that they are widely used, easily accessible and suitable for conducting (indoor) flight experiments.

The following literature research questions could be answered:

- *How is the Safe Flight Envelope (SFE) defined?*

  The SFE is defined as all the possible states which an aircraft can both reach from- and be controlled back to a set of initial flight conditions within a given time-window [8].
- *Which available method is most suitable for determining the SFE of a quadcopter?*

  The Monte-Carlo simulation approach seems to be the most promising method for quadcopter flight envelope prediction as it can be applied on higher dimensional nonlinear systems [8], it has a lower computational load with increased number of dimensions compared to the mainstream Level Set method [9], and is recently successfully applied on quadcopter models [11].
- *What kind of quadcopter flight maneuvers can be used for identifying quadcopter models?*

  The type of maneuvers that excite all relevant dynamics of the system. To ensure all relevant dynamics are covered various maneuvers should be employed that, together, cover the relevant bandwidth of the system. This depends on the flight speed regime over which the models are identified (answer to subquestion 6a) as the maximum allowed excursions must be met. In low flight speeds this could be frequency sweeps starting from a hover condition while keeping a constant altitude. While for high speed flight throttle pulses and multisines could be employed.
- *What model structure shall be used in the system identification of quadcopter models?*

  In order to perform an analysis on the obtained models, it is preferred to use a white-box model structure. Polynomial functions seem to be the most promising ones available for the application on multirotor UAV. To achieve similar model qualities among the multirotor UAV configurations, stepwise regression could be used to meet the desired performance.

Part III

Closure

8

Conclusions & Recommendations

The aim of this work is to examine the behaviour of the (global) Safe Flight Envelope (SFE) of a quadcopter subjected to varying system dynamics. The definition of the SFE used in this work is defined as *the set of states that can be reached, within a certain time-window, for which a trajectory exist to return to a safe flight condition within a predefined time-window [5][6][7][8]*.

The objective of this research was formulated as follows:

Research Objective

The objective of this thesis work is to assess the behaviour of the boundaries of the Safe Flight Envelope (SFE) of a quadcopter subjected to varying system dynamics.

The effects of longitudinal center of gravity displacements, actuator dynamics and varying time-windows are explored. In this research the SFE is divided into two sets: 1) the forward reachable set (FRS), which defines all the states that the system can reach within a time-window, and, 2) the backward reachable set (BRS), which defines all states from which the system can return to the (initial) safe (set of) state(s) within an arbitrary time-window. For FRS estimation an optimized Monte-Carlo (MC) simulation approach is developed. The BRS is obtained through a minimum-time optimal control routine performed on the end states in the FRS.

With the results of the research presented in Part I the research questions as described in chapter 2 can be answered. The answers to the research questions can be found in section 8.1. Furthermore, the recommendations which follow from this work are presented in section 8.2.

8.1. Conclusions

From the result of this work, the research questions can be answered as follows:

1. How does the FRS vary subjected to:

   (a) *Displacing the center of gravity position?*

   - A larger displacement of the center of gravity from the rotor plane center results in a smaller reachable set area. This is the direct result from the larger moment of inertia of a quadcopter with a more outer center of gravity location, consequently having a larger resistance against a change in angular rotation resulting in a smaller reachable set. With respect to the neutral configuration, the area of the reachable set of the most aft center of gravity position at T = 0.1 s is reduced by around 45%, for the most forward center of gravity position the area is reduced by around 65%.
   - The location of the centroid of the reachable set is a function of the center of gravity offset position. It moves into the direction of the sign of the pitching moment bias. A larger moment can be obtained in the rotation direction of this bias, which shifts the centroid of reachable set accordingly.

(b) *Actuator dynamics?*

- Including the modelling of the actuator dynamics reduces the reachable set substantially. The reachable set area is reduced by about 85% compared to the set without actuator dynamics.

(c) *Varying the time-window of the reachable set analysis?*

- The reachable set expands as a function of time and is dependent on quadcopter dynamics. As the time-window increases, the reachable set area expands and the maximum and minimum obtainable pitch angles and rates increase. The extend to which the set grows within a unit of time is dependent on the system dynamics. The area increases more for the most aft center of gravity position and most forward position. The minimum pitch angles and rates increase more for the most forward center of gravity position while a larger increase is observed in maximum angles and rates for the most aft position.
- The forward reachable set expands in time in a similar fashion as a double integrator system. This is because the rotational quadcopter dynamics are modelled identical to a double integrator system.

2. How does the BRS vary subjected to:

(a) *Displacing the center of gravity position?*

- The distribution of the return time over the entire FRS set is a function of center of gravity offset position. For the neutral position this distribution seems almost symmetric, while for the extreme offset positions larger return times are found near one of the edges of the FRS. This can be explained by the pitching moment bias as a result of the center of gravity offset with the rotor plane center, due to which higher pitching moments are reached into the direction of this bias. Moreover, a higher moment of inertia restricts larger changes in rotational rates, which increases the return time.

(b) *Actuator dynamics?*

- The quadcopters without actuator dynamics modelling obtain larger FRS as well as a BRS with much lower return times. For a FRS of T = 0.1 s the largest distribution of the return time of the set without actuator dynamics ranges up to only about 0.3 seconds, despite the much larger pitch angles and pitch rates obtained. This is because a system without actuator dynamics can apply a change in rotational acceleration instantaneously, while the actuator dynamics introduce a lag, making the system respond slower. Therefore, including the actuator dynamics in the modelling is essential to obtain realistic reachable sets.

(c) *Varying the time-window of the reachable set analysis?*

- The time to return to the safe state generally requires (substantially) more time than the time-window used to obtain the FRS. A forward reachable set, with time-window of T = 0.1 s, results in a BRS with return times up to 0.7 seconds. This is due to the sampling along the maximum input range to estimate the boundary of the FRS. These extreme inputs result in trajectory end states with high rotational rates and accelerations from which the quadcopter needs to recover. Moreover, due to the modelling of the actuator dynamics an additional delay is introduced to change the (direction of the) rotor speeds and generate rotational accelerations towards the safe state.
- The return time increases with increasing FRS time-window, until a specific time, after which the return time distribution shows a repeating pattern along the FRS set. The repeating pattern can be explained by the looping of the pitch angle around an arbitrary range in the simulation. Since the commanded input from the optimal control routine depends on the pitch angle, the found optimal control solution does not always result in the global optimum. It is recommended to loop the pitch angle interval for an integer amount of variations and select the routine resulting in the minimum return time for each end state considered.

3. *To what extend is interpolation of the reachable sets feasible to support a data-base driven approach for (real-time) envelope prediction and protection?*

   The effects of the center of gravity displacements on the FRS mainly affect the set area and the centroid location which can be directly interpolated. From the analysis of the actuator dynamics it was concluded that the area of the envelope has a fixed reduction in area, independent of system dynamics. It could be observed that the set with actuator dynamics seems to represent a set for a smaller time-window compared to the set without actuator modelling. With this knowledge a procedure can be developed which can estimate the set with- and without actuator dynamics. Note that these results are only valid for the actuator time constants used in this work. The FRS as a function of time expands in a similar fashion as the double integrator system. For the reachable sets of the double integrator analytical solutions exists [72]. With the results from this research it could be possible to construct an analytical approximation of the FRS of a quadcopter model, including actuator dynamics, as a function of time.

   Interpolation of the BRS subjected to varying center of gravity position could be done using an approximation of the system specific gradient along the FRS observed in the results. This could also be applied to the influence of the actuator modelling and varying time-windows as well. Moreover, implementation of the optimal control routine as developed in this work could be integrated onto the quadcopter itself. The optimal control surface used in the routine is known in advance and could be efficiently stored onboard and used to apply *bang-bang* control to recover the quadcopter to the safe state.

With an answer provided to all research questions, this concludes the thesis project as the research objective has been achieved.

The results on the FRS and BRS generate knowledge on the capabilities of the quadcopter in the framework of reachability analysis. So far, the reachable sets are separated into the FRS and BRS respectively. In order to determine the SFE, it is required to define the amount of time the quadcopter is allowed to go from- and return to the safe state (hover condition). This particular time-window is application specific and dependent on the safety and performance requirements. For further implementation of the results in the framework of the SFE it is recommended to further investigate the application specific safety requirements (e.g. in terms of time-windows) which can then be co-implemented with a controller for flight envelope protection. More recommendations with regards to this work can be found in the next section.

8.2. Recommendations

The recommendations of this work have been split into the recommendations which follow from the research, recommendations for improving the research itself, and finally recommended follow-up research subjects are proposed.

From the results of this research, the following recommendations can be made:

- To obtain the largest possible forward reachable set (FRS) with smallest return times, defined as the backward reachable set (BRS), it is recommended to place the center of gravity position near the rotor plane center. Any center of gravity offset reduces the reachable set area and increases return times in the BRS.
- The actuator dynamics largely affect the results of the reachable sets obtained, hence it is essential in any quadcopter analysis to include the actuator dynamics in the modelling. The effects of the actuator dynamics show a larger impact on the reachable sets than the effects of the center of gravity offsets. Therefore, it is recommended to further develop the performance of the actuator dynamics as it has a large impact on the reachability of the quadcopter, and thus on the performance of the quadcopter as a whole.
- The quadcopter is a very fast system and hence it is recommended to consider time-windows for reachability analysis in the order of less than or about half a second (for the platform as used in this work).
- For FRS estimation of a quadcopter model, it is recommended to use a Monte-Carlo (MC) simulation rather than the *Level-Set Toolbox* [18], as it has been shown to outperform the toolbox in terms of both accuracy and computation time. Although a more thorough space- and time

complexity analysis is recommended. The MC simulation is preferred provided that the system under consideration is control *affine*, such that *bang-bang* control can be used which drastically reduces the sampling space. Additionally, a (system specific optimized) tuning parameter should be used to optimize for boundary estimation, which reduces the required number of trajectories.

The following improvements can be made on the presented research itself:

- The model identification procedures in this work have used signals which have been pre-processed by the flight control software. In particular the gyro data. This directly influences the identified model parameters. Hence, it is recommended to use the raw measurement signals for model identification.
- The data obtained for model identification have been collected from manual piloted (line-of-sight) flights. Consequently the pitching maneuvers, aimed to only excite the pitching moment, are contaminated with unintentional roll- and yaw inputs (although small). Furthermore, manual flights result in a variance among repeated maneuvers. Although in some applications this is desirable as more variations in the input result in exploring a wider range of the dynamics, in this work the goal was to identify the differences between system dynamics which require identical system inputs. Hence for this analysis it is more desirable to automate flying maneuvers for model identification.
- The reachability analysis has been applied on a quadcopter model without including any (non-rotor) aerodynamic effects. It is recommended to further explore the analysis in the high speed regime and/or include nonlinear effects, such as propwash, to analyse the effects on the reachable sets in extreme flight conditions.
- The pitching moment models do not include the effects of the center of gravity offsets for pitch angles greater than ± 90 degrees (with a pitch angle bounded between $\pm$ 180 degrees). To improve results for envelopes exceeding these angles, model identification on flights with an extended flight regime should be performed. The models could also be extended by for example manipulating the sign of the bias to capture the effects of gravity on the mass unbalance when exceeding ± 90 degrees.
- The validation data show that the quadcopter has an initial nonzero pitch angle and pitch rate at the beginning of the maneuvers. This phenomenon occurred when switching from angle mode to rate mode. To improve future validation analysis it is recommended to eliminate this effect as the validation analysis was designed to start at a zero angle and rate. Furthermore, a consistently larger control moment for the pitch down maneuvers was achieved compared to the pitch up maneuvers. It is recommended to investigate the cause of this asymmetry as symmetrical control moment inputs would benefit the validation analysis. Possible sources are (asymmetrical) differences between the rotor blades and/or motor functionalities. This could be explored by swapping the front and aft blades and/or motors and repeating the flight maneuvers.
- The optimal control routine in this work has been applied around a fixed looping range of pitch angles. Consequently, the trajectory inputs from the control routine do not always provide the global optimum minimum-time solution. In order to find the global optimum, it is recommended to loop the pitch angle range for an integer amount of variations and select the control trajectory resulting in a minimum return time.
- The verification of the BRS has only be performed with respect to the boundary of some selected analytical sets. It is recommended to further verify the estimated return times also within and outside the boundaries of the considered sets. This could be done by for example increasing the amount of analytical sets used in the verification for various time-windows. Furthermore, instead of checking whether the return time estimation is within time-window of the analytical set, the estimated return times can be directly compared to the time-window of the analytical set which intersects the state in question.
- An additional model identification analysis on the actuator dynamics showed substantial different model parameter estimates when using data from a quadcopter flown in rate mode only. This motivates further analysis on system identification of the quadcopter model on rate mode data only and compare its validation performance. Since the possible explanation of these differences might originate from the differences in control loops, it is recommended to develop a method to

perform system identification flights in an open-loop fashion for complete controller-free actuator dynamics model identification.

- The validation analysis has been performed only on the edge cases of the forward reachable sets, which include the maximum and minimum pitch angle and rate of the set. To improve the validation on the FRS, an experiment should be designed which extends to the other edges of the flight envelope as well.

  Furthermore, no validation has been performed on the BRS. A validation experiment could be designed which for example replicates the control inputs from simulation, or implement the *bang-bang* optimal control routine onto the quadcopter, in order to validate the optimal control routine by comparing the time to return to the hover condition from a particular state.
- The results from this work cannot directly be compared to the results from other quadcopter platforms. It is recommended to normalize the states with the dimensions of the platform in order to compare to other platforms. Furthermore, to account for varying flight conditions, a normalization can be done with respect to (aerodynamic) conditions, such as the air density.

To further expand upon the results followed from this research in the framework of reachability analysis of quadcopters, the succeeding follow-up research subjects are proposed:

- In order to apply flight envelope protection (FEP) in the framework of quadcopters, the definition of loss of control (LOC) with respect to the Safe Flight Envelope (SFE) should be better researched and defined. This definition, including the time-window(s) considered, can be very application specific (e.g. how fast the system is and how much space is available) and will depend on the safety and performance requirements.
- The optimal control routine, as developed in this work, to return from any end state to hover condition in minimum-time proofs to work in simulation. This optimal control routine can be used to further investigate its application in for example endpoint control and/or implement the routine onto a real quadcopter. The *bang-bang* optimal control in the context of position control has already be proven to work on quadcopters showing improved performance compared to a PID controller [148].
- In extension to the item above, the methods as shown in this work, applied on the pitch channel, can be extended to the roll channel directly. The reachability results could be combined to allow for FEP on both the pitch and roll channel simultaneously (e.g. in an uncoupled fashion). Position control using the *bang-bang* optimal control can be applied, as done in Westenberger et. al [148], but including a safety guarantee from the FEP system.
- The FRS as a function of time expands in a similar fashion as the double integrator system. For the reachable sets of the double integrator analytical solutions exists [72]. With the results from this research, which adds knowledge on how the sets grow in time, as well as to what extend the actuator dynamics affect the sets, it could be possible to construct an analytical approximation of the reachable set for a quadcopter model including actuator dynamics. This is relevant for example in the framework of a database-driven approach, in which interpolation and/or extrapolation of sets could be beneficial in terms of efficiency and performance for real-time applications [5].
- Besides the attitude state-space domain as investigated in this research, the reachability analysis could be extended to include position and/or velocity envelopes. The envelopes could be used in trajectory planning and/or obstacle avoidance [149]. With the results of this work, the trajectory planning can be extended to not only include the dynamics of the quadcopter, with actuator dynamics, but also add a safety guarantee based on the reachable set analysis in the framework of the SFE (e.g. to guarantee a trajectory change within a specified time-window).

Thesis Report & Literature Review References

[1] FAA, "Faa aerospace forecast, fiscal years 2020-2040," FAA, Tech. Rep., 2020. [Online]. Available: https://www.faa.gov/data_research/aviation/aerospace_forecasts/media/FY2020-40_FAA_Aerospace_Forecast.pdf.

[2] C. M. Belcastro, R. L. Newman, J. Evans, D. H. Klyde, L. C. Barr, and E. Ancel, "Hazards identification and analysis for unmanned aircraft system operations," in *17th AIAA Aviation Technology, Integration, and Operations Conference*, American Institute of Aeronautics and Astronautics, Jun. 5, 2017, ISBN: 978-1-62410-508-1. DOI: 10.2514/6.2017-3269. [Online]. Available: https://arc.aiaa.org/doi/10.2514/6.2017-3269.

[3] T. Lombaerts, S. Schuet, D. Acosta, J. Kaneshige, K. Shish, and L. Martin, "Piloted simulator evaluation of safe flight envelope display indicators for loss of control avoidance," *Journal of Guidance, Control, and Dynamics*, vol. 40, no. 4, pp. 948–963, Apr. 2017, ISSN: 0731-5090, 1533-3884. DOI: 10.2514/1.G001740. [Online]. Available: https://arc.aiaa.org/doi/10.2514/1.G001740.

[4] S. R. Schuet, T. Lombaerts, D. M. Acosta, J. T. Kaneshige, K. R. Wheeler, and K. H. Shish, "Autonomous flight envelope estimation for loss-of-control prevention," *Journal of Guidance Control and Dynamics*, vol. 40, pp. 847–862, 2017.

[5] Y. Zhang, "Database-driven online safe flight envelope prediction and protection for enhanced aircraft fault tolerance," Ph.D. dissertation, Delft University of Technology, 2019. DOI: 10.4233/UUID:70778C5C-3F00-4854-A0FB-98B24C9ED1CB. [Online]. Available: http://resolver.tudelft.nl/uuid:70778c5c-3f00-4854-a0fb-98b24c9ed1cb.

[6] E. R. v. Oort, "Adaptive backstepping control and safety analysis for modern fighter aircraft.," Ph.D. dissertation, Delft University of Technology, S.l., 2011. [Online]. Available: https://repository.tudelft.nl/islandora/object/uuid%3A68fd89ff-aad6-4ad8-b280-d2fe8b500d48.

[7] T. Lombaerts, S. Schuet, K. Wheeler, D. M. Acosta, and J. Kaneshige, "Safe maneuvering envelope estimation based on a physical approach," in *AIAA Guidance, Navigation, and Control (GNC) Conference*, American Institute of Aeronautics and Astronautics, Aug. 19, 2013, ISBN: 978-1-62410-224-0. DOI: 10.2514/6.2013-4618. [Online]. Available: https://arc.aiaa.org/doi/10.2514/6.2013-4618.

[8] M. Yin, Q. P. Chu, Y. Zhang, M. A. Niestroy, and C. C. de Visser, "Probabilistic flight envelope estimation with application to unstable overactuated aircraft," *Journal of Guidance, Control, and Dynamics*, vol. 42, no. 12, pp. 2650–2663, Dec. 2019, ISSN: 1533-3884. DOI: 10.2514/1.G004193. [Online]. Available: https://arc.aiaa.org/doi/10.2514/1.G004193.

[9] G. Terrell and D. Scott, "Variable kernel density estimation," *The Annals of Statistics*, vol. 20, Sep. 1992. DOI: 10.1214/aos/1176348768.

[10] S. Sun, C. C. de Visser, and Q. Chu, "Quadrotor gray-box model identification from high-speed flight data," *Journal of Aircraft*, vol. 56, no. 2, pp. 645–661, 2019. DOI: 10.2514/1.C035135. [Online]. Available: https://doi.org/10.2514/1.C035135.

[11] S. Sun and C. De Visser, "Quadrotor safe flight envelope prediction in the high-speed regime: A monte-carlo approach," Jan. 2019. DOI: 10.2514/6.2019-0948.

[12] R. Colgren and T. Johnson, "Flight mishap prevention for uavs," in *2001 IEEE Aerospace Conference Proceedings (Cat. No.01TH8542)*, vol. 2, 2001, 2/647–2/656 vol.2. DOI: 10.1109/AERO.2001.931244.

[13] R. van den Brandt and C. de Visser, "Safe flight envelope uncertainty quantification using probabilistic reachability analysis," *IFAC-PapersOnLine*, vol. 51, no. 24, pp. 628–635, 2018, ISSN: 24058963. DOI: 10.1016/j.ifacol.2018.09.641. [Online]. Available: https://linkinghub.elsevier.com/retrieve/pii/S240589631832353X.

[14] J. Stapel, C. C. de Visser, E.-J. Van Kampen, and Q. P. Chu, "Efficient methods for flight envelope estimation through reachability analysis," in *AIAA Guidance, Navigation, and Control Conference*, American Institute of Aeronautics and Astronautics, Jan. 4, 2016, ISBN: 978-1-62410-389-6. DOI: 10.2514/6.2016-0083. [Online]. Available: https://arc.aiaa.org/doi/10.2514/6.2016-0083.

[15] M. Althoff and B. Krogh, "Reachability analysis of nonlinear differential-algebraic systems," *Automatic Control, IEEE Transactions on*, vol. 59, pp. 371–383, Feb. 1, 2014. DOI: 10.1109/TAC.2013.2285751.

[16] I. Kitsios and J. Lygeros, "Launch-pad abort flight envelope computation for a personnel launch vehicle using reachability," in *AIAA Guidance, Navigation, and Control Conference and Exhibit*, American Institute of Aeronautics and Astronautics, Aug. 15, 2005, ISBN: 978-1-62410-056-7. DOI: 10.2514/6.2005-6150. [Online]. Available: https://arc.aiaa.org/doi/10.2514/6.2005-6150.

[17] S. Sun, C. C. de Visser, and Q. Chu, "Quadrotor gray-box model identification from high-speed flight data," *Journal of Aircraft*, vol. 56, no. 2, pp. 645–661, 2019. DOI: 10.2514/1.C035135. eprint: https://doi.org/10.2514/1.C035135. [Online]. Available: https://doi.org/10.2514/1.C035135.

[18] I. Mitchell and J. Templeton, "A toolbox of hamilton-jacobi solvers for analysis of nondeterministic continuous and hybrid systems," vol. 3414, Mar. 2005, pp. 480–494, ISBN: 978-3-540-25108-8. DOI: 10.1007/978-3-540-31954-2_31.

[19] S. Sun, R. Schilder, and C. C. de Visser, "Identification of quadrotor aerodynamic model from high speed flight data," in *2018 AIAA Atmospheric Flight Mechanics Conference*, American Institute of Aeronautics and Astronautics, Jan. 8, 2018, ISBN: 978-1-62410-525-8. DOI: 10.2514/6.2018-0523. [Online]. Available: https://arc.aiaa.org/doi/10.2514/6.2018-0523.

[20] B. Company, "Statistical summary of commerical jet airplane accidents, worldwide operations | 1959 – 2020," *IEEE Robotics and Automation Letters*, 2021. [Online]. Available: https://www.boeing.com/resources/boeingdotcom/company/about_bca/pdf/statsum.pdf.

[21] "Loss of control in-flight accident analysis report 2019 edition," *IATA*, p. 44, 2019. [Online]. Available: https://www.iata.org/contentassets/b6eb2adc248c484192101edd1ed36015/loc-i_2019.pdf.

[22] J. M. Maciejowski and C. N. Jones, "MPC fault-tolerant flight control case study: Flight 1862," *IFAC Proceedings Volumes*, vol. 36, no. 5, pp. 119–124, Jun. 2003, ISSN: 14746670. DOI: 10.1016/S1474-6670(17)36480-7. [Online]. Available: https://linkinghub.elsevier.com/retrieve/pii/S1474667017364807.

[23] M. Smaili and J. Mulder, "Flight data reconstruction and simulation of the 1992 amsterdam bijlmermeer airplane accident," in *Modeling and Simulation Technologies Conference*, American Institute of Aeronautics and Astronautics, Aug. 14, 2000. DOI: 10.2514/6.2000-4586. [Online]. Available: https://arc.aiaa.org/doi/10.2514/6.2000-4586.

[24] Y. Zhang and J. Jiang, "Bibliographical review on reconfigurable fault-tolerant control systems," *Annual Reviews in Control*, vol. 32, no. 2, pp. 229–252, Dec. 2008, ISSN: 13675788. DOI: 10.1016/j.arcontrol.2008.03.008. [Online]. Available: https://linkinghub.elsevier.com/retrieve/pii/S1367578808000345.

[25] S. Sun, M. Baert, B. Schijndel, and C. De Visser, "Upset recovery control for quadrotors subjected to a complete rotor failure from large initial disturbances," May 2020, pp. 4273–4279. DOI: 10.1109/ICRA40945.2020.9197239.

[26] M. Baert, "Quadrotor upset recovery after rotor failure," Delft University of Technology, 2019. [Online]. Available: http://resolver.tudelft.nl/uuid:4e1011c7-2db9-4dfe-a910-f2843414b960.

[27] C. Ke, K.-Y. Cai, and Q. Quan, "Uniform fault-tolerant control of a quadcopter with rotor failure," *IEEE/ASME Transactions on Mechatronics*, pp. 1–11, 2022. DOI: 10.1109/TMECH.2022.3202804.

[28] A. Lanzon, A. Freddi, and S. Longhi, "Flight control of a quadrotor vehicle subsequent to a rotor failure," *Journal of Guidance, Control, and Dynamics*, vol. 37, no. 2, pp. 580–591, 2014. DOI: 10.2514/1.59869. eprint: https://doi.org/10.2514/1.59869. [Online]. Available: https://doi.org/10.2514/1.59869.

[29] J. J. van Beers, "Development of a system identification routine, with prediction reliability estimates, suitable for modelling high-speed and aggressive quadrotor flight outdoors [TO BE SUBMITTED]," Delft University of Technology, Dec. 21, 2021. [Online]. Available: https://repository.tudelft.nl/islandora/object/uuid%3A4677f001-bc4f-4990-be0e-4316ec9f8847.

[30] E. J. J. Smeur, Q. Chu, and G. C. H. E. de Croon, "Adaptive incremental nonlinear dynamic inversion for attitude control of micro air vehicles," *Journal of Guidance, Control, and Dynamics*, vol. 39, no. 3, pp. 450–461, Mar. 2016, ISSN: 1533-3884. DOI: 10.2514/1.G001490. [Online]. Available: https://arc.aiaa.org/doi/10.2514/1.G001490.

[31] M. M. Ferdaus, S. G. Anavatti, M. A. Garratt, and M. Pratama, "Fuzzy clustering based nonlinear system identification and controller development of pixhawk based quadcopter," in *2017 Ninth International Conference on Advanced Computational Intelligence (ICACI)*, Feb. 2017, pp. 223–230. DOI: 10.1109/ICACI.2017.7974513.

[32] C. M. Belcastro, J. V. Foster, G. H. Shah, *et al.*, "Aircraft loss of control problem analysis and research toward a holistic solution," *Journal of Guidance, Control, and Dynamics*, vol. 40, no. 4, pp. 733–775, 2017. DOI: 10.2514/1.G002815. eprint: https://doi.org/10.2514/1.G002815. [Online]. Available: https://doi.org/10.2514/1.G002815.

[33] J. Foster, K. Cunningham, C. Fremaux, *et al.*, "Dynamics modeling and simulation of large transport airplanes in upset conditions," in *AIAA Guidance, Navigation, and Control Conference and Exhibit*. DOI: 10.2514/6.2005-5933. eprint: https://arc.aiaa.org/doi/pdf/10.2514/6.2005-5933. [Online]. Available: https://arc.aiaa.org/doi/abs/10.2514/6.2005-5933.

[34] J. Wilborn and J. Foster, "Defining commercial transport loss-of-control: A quantitative approach," in *AIAA Atmospheric Flight Mechanics Conference and Exhibit*. DOI: 10.2514/6.2004-4811. eprint: https://arc.aiaa.org/doi/pdf/10.2514/6.2004-4811. [Online]. Available: https://arc.aiaa.org/doi/abs/10.2514/6.2004-4811.

[35] G. Ruijgrok, *Elements of airplane performance*, English. VSSD, 2009, ISBN: 978-90-6562-203-7.

[36] L. Tang, M. Roemer, J. Ge, A. Crassidis, J. Prasad, and C. Belcastro, "Methodologies for adaptive flight envelope estimation and protection," in *AIAA Guidance, Navigation, and Control Conference*, American Institute of Aeronautics and Astronautics, Aug. 10, 2009, ISBN: 978-1-60086-978-5. DOI: 10.2514/6.2009-6260. [Online]. Available: https://arc.aiaa.org/doi/10.2514/6.2009-6260.

[37] A. Altena, "Quadcopter loss-of-control prediction using recurrent neural networks [TO BE SUBMITTED]," Delft University of Technology, 2022.

[38] M. Scheffer, J. Bascompte, W. A. Brock, *et al.*, "Early-warning signals for critical transitions," *Nature*, vol. 461, no. 7260, pp. 53–59, Sep. 3, 2009, ISSN: 0028-0836, 1476-4687. DOI: 10.1038/nature08227. [Online]. Available: https://www.nature.com/articles/nature08227.

[39] J. H. Gillula, G. M. Hoffmann, H. Huang, M. P. Vitus, and C. J. Tomlin, "Applications of hybrid reachability analysis to robotic aerial vehicles," *The International Journal of Robotics Research*, vol. 30, no. 3, pp. 335–354, Mar. 1, 2011, ISSN: 0278-3649. DOI: 10.1177/0278364910387173. [Online]. Available: https://doi.org/10.1177/0278364910387173.

[40] C. Tomlin, J. Lygeros, and S. Sastry, "Aerodynamic envelope protection using hybrid control," in *Proceedings of the 1998 American Control Conference. ACC (IEEE Cat. No.98CH36207)*, vol. 3, 1998, 1793–1796 vol.3. DOI: 10.1109/ACC.1998.707322.

[41] A. L. Antonius, "Flight envelope protection for automatic and augmented MAnual control," p. 20, 2013.

[42] T. Lombaerts, G. Looye, J. Ellerbroek, and M. R. y. Martin, "Design and piloted simulator evaluation of adaptive safe flight envelope protection algorithm," *Journal of Guidance, Control, and Dynamics*, vol. 40, no. 8, pp. 1902–1924, Aug. 2017, ISSN: 0731-5090, 1533-3884. DOI: 10.2514/1.G002525. [Online]. Available: https://arc.aiaa.org/doi/10.2514/1.G002525.

[43] D. Brière, C. Favre, and P. Traverse, "A family of fault-tolerant systems: Electrical flight controls, from airbus a320/330/340 to future military transport aircraft," *Microprocessors and Microsystems*, vol. 19, no. 2, pp. 75–82, 1995, ISSN: 0141-9331. DOI: https://doi.org/10.1016/0141-9331(95)98982-P. [Online]. Available: https://www.sciencedirect.com/science/article/pii/014193319598982P.

[44] G. Bartley, "Boeing b-777: Fly-by-wire flight controls," 2006.

[45] N. Tekles, J. Chongvisal, E. Xargay, *et al.*, "Design of a flight envelope protection system for nasa's transport class model," *Journal of Guidance, Control, and Dynamics*, vol. 40, no. 4, pp. 863–877, 2017. DOI: 10.2514/1.G001728. eprint: https://doi.org/10.2514/1.G001728. [Online]. Available: https://doi.org/10.2514/1.G001728.

[46] W. Falkena, C. Borst, Q. P. Chu, and J. A. Mulder, "Investigation of practical flight envelope protection systems for small aircraft," *Journal of Guidance, Control, and Dynamics*, vol. 34, no. 4, pp. 976–988, Jul. 2011, ISSN: 0731-5090, 1533-3884. DOI: 10.2514/1.53000. [Online]. Available: https://arc.aiaa.org/doi/10.2514/1.53000.

[47] G. Zogopoulos-Papaliakos and K. J. Kyriakopoulos, "A flight envelope determination and protection system for fixed-wing UAVs," in *2020 IEEE International Conference on Robotics and Automation (ICRA)*, IEEE, May 2020, pp. 9599–9605, ISBN: 978-1-72817-395-5. DOI: 10.1109/ICRA40945.2020.9197433. [Online]. Available: https://ieeexplore.ieee.org/document/9197433/.

[48] G. Zogopoulos-Papaliakos, G. C. Karras, and K. J. Kyriakopoulos, "A fault-tolerant control scheme for fixed-wing UAVs with flight envelope awareness," *Journal of Intelligent & Robotic Systems*, vol. 102, no. 2, p. 46, Jun. 2021, ISSN: 0921-0296, 1573-0409. DOI: 10.1007/s10846-021-01393-3. [Online]. Available: https://link.springer.com/10.1007/s10846-021-01393-3.

[49] N. Tekles, J. Chongvisal, E. Xargay, *et al.*, "Design of a flight envelope protection system for nasa's transport class model," *Journal of Guidance, Control, and Dynamics*, vol. 40, no. 4, pp. 863–877, 2017. DOI: 10.2514/1.G001728. eprint: https://doi.org/10.2514/1.G001728. [Online]. Available: https://doi.org/10.2514/1.G001728.

[50] T. Lombaerts, G. Looye, A. Seefried, M. Neves, and T. Bellmann, "Development and concept demonstration of a physics based adaptive flight envelope protection algorithm**this work was supported by a marie curie international outgoing fellowship (IOF) and the ACROSS project (advanced cockpit for the reduction of stress and workload) within the 7th european community framework program.," *IFAC-PapersOnLine*, vol. 49, no. 5, pp. 248–253, 2016, ISSN: 24058963. DOI: 10.1016/j.ifacol.2016.07.121. [Online]. Available: https://linkinghub.elsevier.com/retrieve/pii/S2405896316303226.

[51] T. Lombaerts, G. Looye, P. Chu, and J. A. Mulder, "Pseudo control hedging and its application for safe flight envelope protection," in *AIAA Guidance, Navigation, and Control Conference*, American Institute of Aeronautics and Astronautics, Aug. 2, 2010, ISBN: 978-1-60086-962-4. DOI: 10.2514/6.2010-8280. [Online]. Available: https://arc.aiaa.org/doi/10.2514/6.2010-8280.

[52] K. A. Ackerman, D. A. Talleur, R. S. Carbonari, *et al.*, "Automation situation awareness display for a flight envelope protection system," *Journal of Guidance, Control, and Dynamics*, vol. 40, no. 4, pp. 964–980, 2017. DOI: 10.2514/1.G000338. eprint: https://doi.org/10.2514/1.G000338. [Online]. Available: https://doi.org/10.2514/1.G000338.

[53] D. Van Baelen, J. Ellerbroek, M. M. (René) van Paassen, and M. Mulder, "Design of a haptic feedback system for flight envelope protection," *Journal of Guidance, Control, and Dynamics*, vol. 43, no. 4, pp. 700–714, 2020. DOI: 10.2514/1.G004596. eprint: https://doi.org/10.2514/1.G004596. [Online]. Available: https://doi.org/10.2514/1.G004596.

[54] R. Helsen, E.-J. van Kampen, C. C. de Visser, and Q. Chu, "Distance-fields-over-grids method for aircraft envelope determination," *Journal of Guidance, Control, and Dynamics*, vol. 39, no. 7, pp. 1470–1480, 2016. DOI: 10.2514/1.G000824. eprint: https://doi.org/10.2514/1.G000824. [Online]. Available: https://doi.org/10.2514/1.G000824.

[55] G. Vachtsevanos, L. Tang, G. Drozeski, and L. Gutierrez, "Intelligent control of unmanned aerial vehicles for improved autonomy and reliability," *IFAC Proceedings Volumes*, vol. 37, no. 8, pp. 852–861, 2004, ISSN: 1474-6670. DOI: https://doi.org/10.1016/S1474-6670(17)32087-6. [Online]. Available: https://www.sciencedirect.com/science/article/pii/S1474667017320876.

[56] I. Yavrucuk, J. V. R. Prasad, and S. Unnikrishnan, "Envelope protection for autonomous unmanned aerial vehicles," *Journal of Guidance, Control, and Dynamics*, vol. 32, no. 1, pp. 248–261, Jan. 2009, ISSN: 0731-5090, 1533-3884. DOI: 10.2514/1.35265. [Online]. Available: https://arc.aiaa.org/doi/10.2514/1.35265.

[57] E. Johnson, D. Schrage, and G. Vachtsevanos, "Software enabled control experiments with university-operated unmanned aircraft," vol. 1, Sep. 2005. DOI: 10.2514/6.2005-6956.

[58] R. Naldi and L. Marconi, "Robust control of transition maneuvers for a class of v/stol aircraft," *Automatica*, vol. 49, pp. 1693–1704, Jun. 2013. DOI: 10.1016/j.automatica.2013.03.006.

[59] J. Moon and J. Prasad, "Aggressive maneuvering for obstacle avoidance with envelope protection for autonomous uavs," *American Helicopter Society International - International Specialists Meeting on Unmanned Rotorcraft 2009*, pp. 351–359, Jan. 2008.

[60] J. Moon and J. Prasad, "Minimum-time approach to obstacle avoidance constrained by envelope protection for autonomous uavs," *Mechatronics*, vol. 21, pp. 861–875, Aug. 2011. DOI: 10.1016/j.mechatronics.2010.10.010.

[61] S. Unnikrishnan and J. Prasad, "Reactionary automatic envelope protection for autonomous unmanned aerial vehicles," in *AIAA Atmospheric Flight Mechanics Conference and Exhibit*, American Institute of Aeronautics and Astronautics, Aug. 16, 2004, ISBN: 978-1-62410-072-7. DOI: 10.2514/6.2004-4819. [Online]. Available: https://arc.aiaa.org/doi/10.2514/6.2004-4819.

[62] J. Horn, A. Calise, and J. Prasad, "Flight envelope cueing on a tilt-rotor aircraft using neural network limit prediction," *Journal of the American Helicopter Society*, vol. 46, pp. 23–31, Jan. 2001. DOI: 10.4050/JAHS.46.23.

[63] S. Unnikrishnan, J. Prasad, and I. Yavrucuk, "Flight evaluation of a reactionary envelope protection system for uavs," *Journal of the American Helicopter Society*, vol. 56, pp. 12 009–1, Jan. 2011. DOI: 10.4050/JAHS.56.012009.

[64] E. van Oort, Q. Chu, and J. Mulder, "Maneuver envelope determination through reachability analysis," English, in *Advances in Aerospace Guidance, Navigation and Control*, F. Holzapfel and S. Theil, Eds. Springer, 2011, pp. 91–102, ISBN: 978-3-642-19816-8.

[65] J. D. Keller, R. M. McKillip, and S. Kim, "Aircraft flight envelope determination using upset detection and physical modeling methods," *American Institute of Aeronautics and Astronautics*, p. 21, 2008.

[66] H. N. Nabi, T. Lombaerts, Y. Zhang, E.-J. Van Kampen, Q. Chu, and C. De Visser, "Effects of structural failure on the safe flight envelope of aircraft," *Journal of Guidance, Control, and Dynamics*, vol. 41, pp. 1–19, Feb. 10, 2018. DOI: 10.2514/1.G003184.

[67] J. Urnes, E. Reichenbach, and T. Smith, "Dynamic flight envelope assessment and prediction," in *AIAA Guidance Navigation and Control Conference*, Aug. 2008, ISBN: 978-1-60086-999-0. DOI: 10.2514/6.2008-6983.

[68] T. Lombaerts, S. Schuet, D. Acosta, and J. Kaneshige, "On-line safe flight envelope determination for impaired aircraft," in *Advances in Aerospace Guidance, Navigation and Control*, J. Bordeneuve-Guibé, A. Drouin, and C. Roos, Eds., Cham: Springer International Publishing, 2015, pp. 263–282, ISBN: 978-3-319-17517-1 978-3-319-17518-8. DOI: 10.1007/978-3-319-17518-8_16. [Online]. Available: http://link.springer.com/10.1007/978-3-319-17518-8_16.

[69] S. Kim, D. Falanga, and D. Scaramuzza, "Computing the forward reachable set for a multirotor under first-order aerodynamic effects," *IEEE Robotics and Automation Letters*, vol. 3, no. 4, pp. 2934–2941, Oct. 2018, ISSN: 2377-3766, 2377-3774. DOI: 10.1109/LRA.2018.2848302. [Online]. Available: https://ieeexplore.ieee.org/document/8387437/.

[70] H. G. Harno and Y. Kim, "Safe flight envelope estimation for rotorcraft: A reachability approach," in *2018 18th International Conference on Control, Automation and Systems (ICCAS)*, 2018, pp. 998–1002.

[71] A. Paranjape, N. Sinha, and N. Ananthkrishnan, "Use of bifurcation and continuation methods for aircraft trim and stability analysis - a state-of-the-art," in *45th AIAA Aerospace Sciences Meeting and Exhibit*, American Institute of Aeronautics and Astronautics, Jan. 8, 2007, ISBN: 978-1-62410-012-3. DOI: 10.2514/6.2007-1051. [Online]. Available: https://arc.aiaa.org/doi/10.2514/6.2007-1051.

[72] J. V. Carroll and R. K. Mehra, "Bifurcation analysis of nonlinear aircraft dynamics," *Journal of Guidance, Control, and Dynamics*, vol. 5, no. 5, pp. 529–536, 1982. DOI: 10.2514/3.56198. eprint: https://doi.org/10.2514/3.56198. [Online]. Available: https://doi.org/10.2514/3.56198.

[73] R. Norouzi, A. Kosari, and M. H. Sabour, "Real time estimation of impaired aircraft flight envelope using feedforward neural networks," *Elsevier*, 2019. DOI: 10.1016/j.ast.2019.04.048. [Online]. Available: https://reader.elsevier.com/reader/sd/pii/S1270963818311751?token=92CE52CD78CDAF07F241B15D73056F95ABD570CF079AFC06AD30237047AF447DCC96662645F8B13BA74984E1575D9B73&originRegion=eu-west-1&originCreation=20220510125204.

[74] M. G. Goman, A. V. Khramtsovsky, and E. N. Kolesnikov, "Evaluation of aircraft performance and maneuverability by computation of attainable equilibrium sets," *Journal of Guidance, Control, and Dynamics*, vol. 31, no. 2, pp. 329–339, Mar. 2008, ISSN: 0731-5090, 1533-3884. DOI: 10.2514/1.29336. [Online]. Available: https://arc.aiaa.org/doi/10.2514/1.29336.

[75] A. K. Khatri, J. Singh, and N. K. Sinha, "Aircraft maneuver design using bifurcation analysis and sliding mode control techniques," *Journal of Guidance, Control, and Dynamics*, vol. 35, no. 5, pp. 1435–1449, Sep. 2012, ISSN: 0731-5090, 1533-3884. DOI: 10.2514/1.56361. [Online]. Available: https://arc.aiaa.org/doi/10.2514/1.56361.

[76] Q. Xin and Z. Shi, "Prediction and recovery of aircraft unstable nonlinear phenomena using bifurcation analysis and backstepping method," *Journal of Computational and Nonlinear Dynamics*, vol. 11, no. 6, Jul. 22, 2016, ISSN: 1555-1415. DOI: 10.1115/1.4034049. [Online]. Available: https://doi.org/10.1115/1.4034049.

[77] G. Yuan and Y. Li, "Determination of the flight dynamic envelope via stable manifold," *Measurement and Control*, vol. 52, no. 3, pp. 244–251, Mar. 1, 2019, ISSN: 0020-2940. DOI: 10.1177/0020294019830115. [Online]. Available: https://doi.org/10.1177/0020294019830115.

[78] R. Pandita, A. Chakraborty, P. Seiler, and G. Balas, "Reachability and region of attraction analysis applied to GTM dynamic flight envelope assessment," in *AIAA Guidance, Navigation, and Control Conference*, American Institute of Aeronautics and Astronautics, Aug. 10, 2009, ISBN: 978-1-60086-978-5. DOI: 10.2514/6.2009-6258. [Online]. Available: https://arc.aiaa.org/doi/10.2514/6.2009-6258.

[79] M. E. Sidoryuk and A. N. Khrabrov, "Estimation of regions of attraction of aircraft spin modes," *Journal of Aircraft*, vol. 56, no. 1, pp. 205–216, Jan. 2019, ISSN: 0021-8669, 1533-3868. DOI: 10.2514/1.C034936. [Online]. Available: https://arc.aiaa.org/doi/10.2514/1.C034936.

[80] A. Chakraborty, P. Seiler, and G. J. Balas, "Nonlinear region of attraction analysis for flight control verification and validation," *Control Engineering Practice*, vol. 19, no. 4, pp. 335–345, Apr. 2011, ISSN: 09670661. DOI: 10.1016/j.conengprac.2010.12.001. [Online]. Available: https://linkinghub.elsevier.com/retrieve/pii/S0967066110002595.

[81] J. Chen, C. Ma, and D. Song, "Stability analysis of aircraft's sudden damage process with roa overlapping," *Aircraft Engineering and Aerospace Technology*, vol. 90, pp. 00–00, Jan. 2018. DOI: 10.1108/AEAT-08-2016-0127.

[82] P. Menon, J. Kim, P. Sengupta, V. Vaddi, B.-J. Yang, and J. Kwan, "Onboard estimation of impaired aircraft performance envelope," in *AIAA Guidance, Navigation, and Control Conference*, American Institute of Aeronautics and Astronautics, Aug. 8, 2011, ISBN: 978-1-60086-952-5. DOI: 10.2514/6.2011-6688. [Online]. Available: https://arc.aiaa.org/doi/10.2514/6.2011-6688.

[83] M. B. Tischler and E. L. Tobias, “A model stitching architecture for continuous full flight-envelope simulation of fixed-wing aircraft and rotorcraft from discrete point linear models:” Defense Technical Information Center, Fort Belvoir, VA, Apr. 1, 2016. DOI: 10.21236/AD1008448. [Online]. Available: https://apps.dtic.mil/sti/citations/AD1008448.

[84] A. Gong, F. C. Sanders, R. A. Hess, and M. B. Tischler, “System identification and full flight-envelope model stitching of a package-delivery octocopter,” in *AIAA Scitech 2019 Forum*, American Institute of Aeronautics and Astronautics, Jan. 7, 2019, ISBN: 978-1-62410-578-4. DOI: 10.2514/6.2019-1076. [Online]. Available: https://arc.aiaa.org/doi/10.2514/6.2019-1076.

[85] H. N. Nabi, C. C. d. Visser, M. D. Pavel, and G. Quaranta, “Development of a quasi-linear parameter varying model for a tiltrotor aircraft,” *CEAS Aeronautical Journal*, vol. 12, no. 4, pp. 879–894, Nov. 2021, ISSN: 1869-5582, 1869-5590. DOI: 10.1007/s13272-021-00539-1. [Online]. Available: https://link.springer.com/10.1007/s13272-021-00539-1.

[86] R. Alur, T. Henzinger, G. Lafferriere, and G. Pappas, “Discrete abstractions of hybrid systems,” *Proceedings of the IEEE*, vol. 88, no. 7, pp. 971–984, Jul. 2000, ISSN: 0018-9219, 1558-2256. DOI: 10.1109/5.871304. [Online]. Available: http://ieeexplore.ieee.org/document/871304/.

[87] J. Lygeros, “On reachability and minimum cost optimal control,” *Automatica*, vol. 40, no. 6, pp. 917–927, Jun. 2004, ISSN: 00051098. DOI: 10.1016/j.automatica.2004.01.012. [Online]. Available: https://linkinghub.elsevier.com/retrieve/pii/S0005109804000263.

[88] S. Bansal, “Safe and data-e□cient learning for robotics: A control theoretic approach,” Electrical Engineering and Computer Sciences, University of California, Berkeley, Nov. 24, 2020.

[89] S. Kim, D. Falanga, and D. Scaramuzza, “Computing the forward reachable set for a multirotor under first-order aerodynamic effects,” *IEEE Robotics and Automation Letters*, vol. 3, no. 4, pp. 2934–2941, 2018. DOI: 10.1109/LRA.2018.2848302.

[90] K. Margellos and J. Lygeros, “Hamilton-jacobi formulation for reach-avoid differential games,” *IEEE Transactions on Automatic Control*, vol. 56, Nov. 24, 2009. DOI: 10.1109/TAC.2011.2105730.

[91] S. Osher and R. P. Fedkiw, *Level set methods and dynamic implicit surfaces*. New York: Springer, 2003, ISBN: 978-0-387-22746-7.

[92] I. Mitchell, A. Bayen, and C. Tomlin, “A time-dependent hamilton-jacobi formulation of reachable sets for continuous dynamic games,” *IEEE Transactions on Automatic Control*, vol. 50, no. 7, pp. 947–957, Jul. 2005, ISSN: 0018-9286. DOI: 10.1109/TAC.2005.851439. [Online]. Available: http://ieeexplore.ieee.org/document/1463302/.

[93] S. Osher and J. A. Sethian, “Fronts propagating with curvature-dependent speed: Algorithms based on hamilton-jacobi formulations,” *Journal of Computational Physics*, vol. 79, no. 1, pp. 12–49, Nov. 1988, ISSN: 00219991. DOI: 10.1016/0021-9991(88)90002-2. [Online]. Available: https://linkinghub.elsevier.com/retrieve/pii/0021999188900022.

[94] J. A. Sethian, “A fast marching level set method for monotonically advancing fronts.,” *Proceedings of the National Academy of Sciences of the United States of America*, vol. 93, no. 4, pp. 1591–1595, Feb. 20, 1996, ISSN: 0027-8424. [Online]. Available: https://www.ncbi.nlm.nih.gov/pmc/articles/PMC39986/.

[95] I. Mitchell, A. M. Bayen, and C. J. Tomlin, “Validating a hamilton-jacobi approximation to hybrid system reachable sets,” in *Hybrid Systems: Computation and Control*, M. D. Di Benedetto and A. Sangiovanni-Vincentelli, Eds., red. by G. Goos, J. Hartmanis, and J. van Leeuwen, vol. 2034, Berlin, Heidelberg: Springer Berlin Heidelberg, 2001, pp. 418–432, ISBN: 978-3-540-41866-5 978-3-540-45351-2. DOI: 10.1007/3-540-45351-2_34. [Online]. Available: http://link.springer.com/10.1007/3-540-45351-2_34.

[96] J. Darbon, “Algorithms for overcoming the curse of dimensionality for certain hamilton–jacobi equations arising in control theory and elsewhere,” p. 26, 2016.

[97] J. Darbon, G. P. Langlois, and T. Meng, "Overcoming the curse of dimensionality for some hamilton–jacobi partial differential equations via neural network architectures," *Research in the Mathematical Sciences*, vol. 7, no. 3, p. 20, Sep. 2020, ISSN: 2522-0144, 2197-9847. DOI: 10.1007/s40687-020-00215-6. [Online]. Available: https://link.springer.com/10.1007/s40687-020-00215-6.

[98] R. Courant, K. Friedrichs, and H. Lewy, "Über die partiellen differenzengleichungen der mathematischen physik," *Mathematische Annalen*, vol. 100, pp. 32–74, 1928.

[99] T. Dang, A. Donzé, and O. Maler, "Verification of analog and mixed-signal circuits using hybrid system techniques," in *Formal Methods in Computer-Aided Design*, A. J. Hu and A. K. Martin, Eds., red. by D. Hutchison, T. Kanade, J. Kittler, *et al.*, vol. 3312, Berlin, Heidelberg: Springer Berlin Heidelberg, 2004, pp. 21–36, ISBN: 978-3-540-23738-9 978-3-540-30494-4. DOI: 10.1007/978-3-540-30494-4_3. [Online]. Available: http://link.springer.com/10.1007/978-3-540-30494-4_3.

[100] G. Delansnay, A. V. Wouwer, H. G.Harno, and Y. Kim, "Zonotopic reachability analysis of multirotor aircraft," in *2021 25th International Conference on System Theory, Control and Computing (ICSTCC)*, Oct. 2021, pp. 576–581. DOI: 10.1109/ICSTCC52150.2021.9607056.

[101] A. A. Kurzhanskiy and P. Varaiya, "Ellipsoidal techniques for reachability analysis of discrete-time linear systems," *IEEE Transactions on Automatic Control*, vol. 52, no. 1, pp. 26–38, 2007. DOI: 10.1109/TAC.2006.887900.

[102] M. Althoff, G. Frehse, and A. Girard, "Set propagation techniques for reachability analysis," *Annual Review of Control, Robotics, and Autonomous Systems*, vol. 4, no. 1, pp. 369–395, 2021. DOI: 10.1146/annurev-control-071420-081941. eprint: https://doi.org/10.1146/annurev-control-071420-081941. [Online]. Available: https://doi.org/10.1146/annurev-control-071420-081941.

[103] M. Althoff, O. Stursberg, and M. Buss, "Computing reachable sets of hybrid systems using a combination of zonotopes and polytopes," *Nonlinear Analysis*, p. 17, 2010.

[104] M. Althoff and B. H. Krogh, "Zonotope bundles for the efficient computation of reachable sets," in *IEEE Conference on Decision and Control and European Control Conference*, IEEE, Dec. 2011, pp. 6814–6821, ISBN: 978-1-61284-801-3 978-1-61284-800-6 978-1-4673-0457-3 978-1-61284-799-3. DOI: 10.1109/CDC.2011.6160872. [Online]. Available: http://ieeexplore.ieee.org/document/6160872/.

[105] H. G. Harno and Y. Kim, "Flight envelope estimation for helicopters under icing conditions via the zonotopic reachability analysis," *Aerospace Science and Technology*, vol. 102, p. 105 859, Jul. 2020, ISSN: 12709638. DOI: 10.1016/j.ast.2020.105859. [Online]. Available: https://linkinghub.elsevier.com/retrieve/pii/S1270963820305411.

[106] A. Girard, C. Le Guernic, and O. Maler, "Efficient computation of reachable sets of linear time-invariant systems with inputs," in *Hybrid Systems: Computation and Control*, J. P. Hespanha and A. Tiwari, Eds., vol. 3927, Berlin, Heidelberg: Springer Berlin Heidelberg, 2006, pp. 257–271, ISBN: 978-3-540-33170-4 978-3-540-33171-1. DOI: 10.1007/11730637_21. [Online]. Available: http://link.springer.com/10.1007/11730637_21.

[107] E. Eyang, C. Combastel, and A. Zolghadri, "Determination of reachable flight regions: A zonotopic approach," *IFAC-PapersOnLine*, vol. 50, no. 1, pp. 4014–4020, Jul. 2017, ISSN: 24058963. DOI: 10.1016/j.ifacol.2017.08.716. [Online]. Available: https://linkinghub.elsevier.com/retrieve/pii/S240589631731162X.

[108] R. L. Harrison, "Introduction to monte carlo simulation," *AIP Conference Proceedings 1204*, p. 6, 2010.

[109] J. Harris, F. Arthurs, J. V. Henrickson, and J. Valasek, "Aircraft system identification using artificial neural networks with flight test data," *2016 International Conference on Unmanned Aircraft Systems (ICUAS)*, pp. 679–688, 2016.

[110] N. Peyada and A. Ghosh, "Aircraft parameter estimation using neural network based algorithm," in *AIAA Atmospheric Flight Mechanics Conference*. DOI: 10.2514/6.2009-5941. eprint: https://arc.aiaa.org/doi/pdf/10.2514/6.2009-5941. [Online]. Available: https://arc.aiaa.org/doi/abs/10.2514/6.2009-5941.

[111] S. Bansal, A. K. Akametalu, F. J. Jiang, F. Laine, and C. J. Tomlin, *Learning quadrotor dynamics using neural network for flight control*, Oct. 19, 2016. arXiv: 1610.05863[cs,math]. [Online]. Available: http://arxiv.org/abs/1610.05863.

[112] N. A. Bakshi and R. Ramachandran, "Indirect model reference adaptive control of quadrotor uavs using neural networks," in *2016 10th International Conference on Intelligent Systems and Control (ISCO)*, 2016, pp. 1–6. DOI: 10.1109/ISCO.2016.7727123.

[113] A. J. Al-Mahasneh, S. G. Anavatti, and M. Garratt, "Nonlinear multi-input multi-output system identification using neuro-evolutionary methods for a quadcopter," in *2017 Ninth International Conference on Advanced Computational Intelligence (ICACI)*, 2017, pp. 217–222. DOI: 10.1109/ICACI.2017.7974512.

[114] N. Mohajerin, M. Mozifian, and S. Waslander, "Deep learning a quadrotor dynamic model for multi-step prediction," in *2018 IEEE International Conference on Robotics and Automation (ICRA)*, 2018, pp. 2454–2459. DOI: 10.1109/ICRA.2018.8460840.

[115] M. F. Pairan, S. S. Shamsudin, and M. F. Zulkafli, "Neural network based system identification for quadcopter dynamic modelling: A review," *Journal of Advanced Mechanical Engineering Applications*, vol. 1, no. 2, pp. 20–33, Nov. 5, 2020, ISSN: 2716-6201. [Online]. Available: https://penerbit.uthm.edu.my/ojs/index.php/jamea/article/view/6993.

[116] F. Jiang, F. Pourpanah, and Q. Hao, "Design, implementation, and evaluation of a neural-network-based quadcopter uav system," *IEEE Transactions on Industrial Electronics*, vol. 67, no. 3, pp. 2076–2085, 2020. DOI: 10.1109/TIE.2019.2905808.

[117] M. Raissi, P. Perdikaris, and G. Karniadakis, "Physics-informed neural networks: A deep learning framework for solving forward and inverse problems involving nonlinear partial differential equations," *Journal of Computational Physics*, vol. 378, Nov. 2018. DOI: 10.1016/j.jcp.2018.10.045.

[118] N. H. Campbell, M. J. Acheson, and I. M. Gregory, "Dynamic vehicle assessment for intelligent contingency management of urban air mobility vehicles," in *AIAA Scitech 2021 Forum*. DOI: 10.2514/6.2021-1001. eprint: https://arc.aiaa.org/doi/pdf/10.2514/6.2021-1001. [Online]. Available: https://arc.aiaa.org/doi/abs/10.2514/6.2021-1001.

[119] T. Lombaerts, S. Schuet, D. Acosta, and J. Kaneshige, "Piloted simulator evaluation of safe flight envelope display indicators for loss of control avoidance," *American Institute of Aeronautics and Astronautics*, vol. 40, no. 4, p. 28, 2017.

[120] J. Wu, H. Peng, Q. Chen, and X. Peng, "Modeling and control approach to a distinctive quadrotor helicopter," *ISA transactions*, vol. 53, Sep. 2013. DOI: 10.1016/j.isatra.2013.08.010.

[121] L. Romaszko, A. Borowska, A. Lazarus, *et al.*, "Neural network-based left ventricle geometry prediction from CMR images with application in biomechanics," *Artificial Intelligence in Medicine*, vol. 119, p. 102 140, Sep. 2021, ISSN: 09333657. DOI: 10.1016/j.artmed.2021.102140. [Online]. Available: https://linkinghub.elsevier.com/retrieve/pii/S0933365721001330.

[122] K. Manikya Kanti and P. Srinivasa Rao, "Prediction of bead geometry in pulsed GMA welding using back propagation neural network," *Journal of Materials Processing Technology*, vol. 200, no. 1, pp. 300–305, May 2008, ISSN: 09240136. DOI: 10.1016/j.jmatprotec.2007.09.034. [Online]. Available: https://linkinghub.elsevier.com/retrieve/pii/S0924013607008205.

[123] C. Zimmerling, D. Trippe, B. Fengler, and L. Kärger, "An approach for rapid prediction of textile draping results for variable composite component geometries using deep neural networks," presented at the PROCEEDINGS OF THE 22ND INTERNATIONAL ESAFORM CONFERENCE ON MATERIAL FORMING: ESAFORM 2019, 2019, p. 020 007. DOI: 10.1063/1.5112512. [Online]. Available: http://aip.scitation.org/doi/abs/10.1063/1.5112512.

[124] S. Strijhak, D. Ryazanov, K. Koshelev, and A. Ivanov, "Neural network prediction for ice shapes on airfoils using iceFoam simulations," *Aerospace*, vol. 9, no. 2, p. 96, Feb. 12, 2022, ISSN: 2226-4310. DOI: 10.3390/aerospace9020096. [Online]. Available: https://www.mdpi.com/2226-4310/9/2/96.

[125] T. Pohlen, A. Hermans, M. Mathias, and B. Leibe, "Full-resolution residual networks for semantic segmentation in street scenes," Nov. 2016.

[126] Z. Fan, V. Vineet, C. Lu, and K. McMullen, *Prediction of object geometry from acoustic scattering using convolutional neural networks*, Oct. 2020.

[127] J. Svacha, K. Mohta, and V. Kumar, "Improving quadrotor trajectory tracking by compensating for aerodynamic effects," in *2017 International Conference on Unmanned Aircraft Systems (ICUAS)*, 2017, pp. 860–866. DOI: 10.1109/ICUAS.2017.7991501.

[128] C. Powers, D. Mellinger, A. Kushleyev, B. Kothmann, and V. Kumar, "Influence of aerodynamics and proximity effects in quadrotor flight," in Jan. 2013, pp. 289–302, ISBN: 978-3-319-00064-0. DOI: 10.1007/978-3-319-00065-7_21.

[129] D. Mellinger, N. Michael, and V. Kumar, "Trajectory generation and control for precise aggressive maneuvers with quadrotors," *International Journal of Robotic Research - IJRR*, vol. 31, Apr. 2012. DOI: 10.1177/0278364911434236.

[130] G. Hoffmann, H. Huang, S. Waslander, and C. Tomlin, "Quadrotor helicopter flight dynamics and control: Theory and experiment," in *AIAA Guidance, Navigation and Control Conference and Exhibit*. 2012. DOI: 10.2514/6.2007-6461. eprint: https://arc.aiaa.org/doi/pdf/10.2514/6.2007-6461. [Online]. Available: https://arc.aiaa.org/doi/abs/10.2514/6.2007-6461.

[131] H. Huang, G. M. Hoffmann, S. L. Waslander, and C. J. Tomlin, "Aerodynamics and control of autonomous quadrotor helicopters in aggressive maneuvering," in *2009 IEEE International Conference on Robotics and Automation*, 2009, pp. 3277–3282. DOI: 10.1109/ROBOT.2009.5152561.

[132] W. Johnson, *Helicopter Theory* (Dover Books on Aeronautical Engineering Series). Dover Publications, 1994, ISBN: 978-0-486-68230-3. [Online]. Available: https://books.google.nl/books?id=SgZheyNeXJIC.

[133] R. Mahony, V. Kumar, and P. Corke, "Multirotor aerial vehicles: Modeling, estimation, and control of quadrotor," *IEEE Robotics Automation Magazine*, vol. 19, no. 3, pp. 20–32, 2012. DOI: 10.1109/MRA.2012.2206474.

[134] V. Klein and E. Morelli, *Aircraft System Identification: Theory And Practice*. Aug. 2006. DOI: 10.2514/4.861505.

[135] C. de Boor, *A Practical Guide to Spline*. Jan. 1978, vol. Volume 27. DOI: 10.2307/2006241.

[136] N. A. Alqahtani and H. Najjaran, "Control system of a terrain following quadcopter under uncertainty and input constraints: A review and research framework," Nov. 2017.

[137] L. Saud and Z. Abbas, "A comparison between multi-layer perceptron and radial basis function networks in detecting humans based on object shape," *Ibn AL- Haitham Journal For Pure and Applied Science*, vol. 31, p. 210, Sep. 2018. DOI: 10.30526/31.2.1950.

[138] H. Zhong, S. Li, Y. Wang, and H. Liu, "Adaptive robust rbfnns-based model estimator for a small quadrotor aircraft robot," in *2016 12th IEEE/ASME International Conference on Mechatronic and Embedded Systems and Applications (MESA)*, 2016, pp. 1–6. DOI: 10.1109/MESA.2016.7587103.

[139] A. J. Al-Mahasneh, S. G. Anavatti, and M. Garratt, "Nonlinear multi-input multi-output system identification using neuro-evolutionary methods for a quadcopter," in *2017 Ninth International Conference on Advanced Computational Intelligence (ICACI)*, IEEE, Feb. 2017, pp. 217–222, ISBN: 978-1-5090-4726-0. DOI: 10.1109/ICACI.2017.7974512. [Online]. Available: http://ieeexplore.ieee.org/document/7974512/.

[140] F. Santoso, M. A. Garratt, and S. G. Anavatti, "Fuzzy system identification for the dynamics of the AR.drone quadcopter," p. 8, 2016.

[141] Q. Zhang and M. Mahfouf, "Fuzzy modelling using a new compact fuzzy system: A special application to the prediction of the mechanical properties of alloy steels," in *2011 IEEE International Conference on Fuzzy Systems (FUZZ-IEEE 2011)*, 2011, pp. 1041–1048. DOI: 10.1109/FUZZY.2011.6007730.

[142] C. De Visser, "Global nonlinear model identification with multivariate splines," Ph.D. dissertation, Jul. 2011. [Online]. Available: http://resolver.tudelft.nl/uuid:6bc0134a-0715-4829-903d-6479c5735913.

[143] M. Tischler and R. Remple, *Aircraft and Rotorcraft System Identification: Engineering Methods with Flight Test Examples* (AIAA education series). American Institute of Aeronautics and Astronautics, 2012, ISBN: 978-1-60086-820-7. [Online]. Available: https://books.google.nl/books?id=lYUvLgEACAAJ.

[144] S. Sakulthong, S. Tantrairatn, and W. Saengphet, "Frequency response system identification and flight controller tuning for quadcopter UAV," in *2018 Third International Conference on Engineering Science and Innovative Technology (ESIT)*, Apr. 2018, pp. 1–6. DOI: 10.1109/ESIT.2018.8665114.

[145] C. De Visser, J. Mulder, and Q. Chu, "Global nonlinear aerodynamic model identification with multivariate splines," in *AIAA Atmospheric Flight Mechanics Conference*, Aug. 2009. DOI: 10.2514/6.2009-5726.

[146] M. I. Alabsi and T. D. Fields, "Real-time closed-loop system identification of a quadcopter," *Journal of Aircraft*, vol. 56, no. 1, pp. 324–335, Jan. 2019, ISSN: 0021-8669, 1533-3868. DOI: 10.2514/1.C034219. [Online]. Available: https://arc.aiaa.org/doi/10.2514/1.C034219.

[147] H. J. Allen, "Estimation of the forces and moments acting on inclined bodies of revolution of high fineness ratio," 1949.

[148] J. Westenberger, C. D. Wagter, and G. C. H. E. de Croon, "Onboard time-optimal control for tiny quadcopters," *Proceedings of the 12th International Micro Air Vehicle Conference*, [IMAV2021-11], 2021. [Online]. Available: http://www.imavs.org/papers/2021/11.pdf.

[149] H. Seo, C. Youngdong Son, D. Lee, and H. Jin Kim, "Trajectory planning with safety guaranty for a multirotor based on the forward and backward reachability analysis," in *2020 IEEE International Conference on Robotics and Automation (ICRA)*, Paris, France: IEEE, May 2020, pp. 7142–7148, ISBN: 978-1-72817-395-5. DOI: 10.1109/ICRA40945.2020.9196760. [Online]. Available: https://ieeexplore.ieee.org/document/9196760/.